Dispersion and self-assembly of anisotropic plasmonic nanoparticles in liquid crystalline media

By: Julian Evans

B.S., Harvey Mudd College, 2008

A thesis submitted to the

Faculty of the Graduate School of the

University of Colorado in partial fulfillment

of the requirement for the degree of

Doctor of Philosophy

Department of Physics

2013

This thesis entitled:

Dispersion and self-assembly of anisotropic plasmonic nanoparticles in liquid crystalline media

written by Julian Evans

has been approved for the Department of Physics

_____

Ivan Smalyukh, Ph.D

_____

Noel Clark, Ph.D.

Date_____

The final copy of this thesis has been examined by the signatories, and we find that both the content and the form meet acceptable presentation standards of scholarly work in the above mentioned discipline.

Abstract

Evans, Julian (Ph.D., Physics)

Dispersion and self-assembly of anisotropic plasmonic nanoparticles in liquid crystalline media

Thesis directed by Professor Ivan Smalyukh

Noble metal nanoparticles possess extraordinary optical properties due to their plasmon modes that make them desirable for inclusion into materials. Non-dipolar plasmon modes are one of the simplest known ways to control the magnetic properties of a material; consequently gold nanoparticles are one of the most promising systems to produce metamaterials. In order to fully utilize the properties of gold nanoparticles for device applications, one needs to control the interparticle spacing, distribution, and orientation of anisotropic gold nanoparticles within a material. Liquid crystalline host materials can allow for alignment and self-assembly of nanoparticles through viscoelastic forces. In this thesis, I demonstrate the feasibility of incorporating nanoparticles into liquid crystals and assembling complex architectures through elasticity mediated interaction.

First, we explore the dispersion of nanoparticles of various size and shape in a few different liquid crystalline systems. 20nm thick gold nanorods can be dispersed at reasonably high concentrations in micellar lyotropic systems, but show qualitatively different self-assembly behavior depending on their length. 10 micron wide, 5nm thick polygonal platelets produce elastic distortions in thermotropic and lyotropic systems, while behaving like “molecular” inclusions in a graphene oxide based discotic phase.

Next, we look at the elastic interactions between colloids of various shapes and sizes and topological defects. Homeotropically aligned glass microspheres produce a hyperbolic hedgehog

point defect or Saturn ring which attract and align nanoparticles in different manners depending on the surface chemistry, size and shape of the nanoparticle. We have also optically generated topological defects in frustrated cholesteric cells which contain similar hyperbolic hedgehog point defects that eliminates the need of microsphere inclusions. We have produced elastomeric cylinders with photothermal response enhanced by gold nanospheres that allow for an arbitrary particle shape to be generated *in situ* to explore the rich physics associated with arbitrary nematostatic and cholesterostatic dipoles.

This work extends our understanding of colloidal inclusions in liquid crystals to the regime where the mesogen size and colloidal inclusion have sizes within a couple orders of magnitude of each other and potentially allows for the development of an exciting new class of nanocomposite liquid crystalline materials.

Acknowledgements

First and foremost, I would like to thank my advisor Ivan Smalyukh for his unwavering support throughout my graduate school career, incredible energy and motivation for writing papers, and copious opportunities to do interesting research and attend international conferences. Additionally I would like to thank my thesis committee members Noel Clark, Wounjhang Park, Daniel Schwartz, Jao van de Lagemaat, and David Walba for their insightful feedback and support. I would like to thank Jeanne Nijhowne for making the paperwork associated with graduate school as painless as possible.

I would like to thank ICAM for the exchange award that allowed me to spend three months researching in the Netherlands

I would like to all the members of the Smalyukh group. In particular Qingkun Liu for helping me quickly start doing interesting stuff with nanorods as well as Paul Ackerman, Corinne Beier, Budhadipta Dan, Dennis Gardner, Bohdan Senyuk, and Yaoran Sun for direct collaborations that became chapters in this thesis and Michael Varney for his knowledge of Microsoft word.

Finally I'd like to thank my parents for all the support over the years and the freedom to spend my time making small assemblies of blocks well into my twenties. I couldn't do it without you.

TABLE OF CONTENTS

List of Tables

List of Figures

List of Abbreviations

3PEFPM- 2-photon epi-fluorescence polarizing microscopy

3PEFPM- 3-photon epi-fluorescence polarizing microscopy

A-Analyzer

AFM- Atomic force microscopy

BCC- Bent cylinder colloid

BPF- Band Pass Filter

CARS-PM- Coherent anti-Stokes Raman Scattering polarizing microscopy

CLC- Cholesteric liquid crystal

CNC- Cellulose nanocrystals

CTAB- Cetyl trimethylammonium Bromide

D-diameter

d-thickness

DMOAP- [3-(trimethoxysilyl)propyl]octadecyl-dimethylammonium chloride

DNA-Deoxyribonucleic acid

FCPM- Fluorescence confocal polarizing microscopy

FFTEM- Freeze-fracture transmission electron microscopy

GGO- Giant Graphene Oxide

GNR- Gold nanorod

GNP- Gold nanoparticle

GNS- Gold nanosphere

ITO- Indium Tin Oxide

L-length

LC-Liquid Crystal

LCE- Liquid Crystal Elastomer

MG- Microgold

mPEG- methoxy Polyethylene Glycol

n, **N(r)**- director

NA- numerical aperture

NB-Nanoburst

P-Polarizer

p-pitch

PI- Polyimide

POM- Polarizing Optical Microscopy

PVP- Polyvinyl Pyrrolidone

QD- quantum dot

QR- quantum rod

R-Retardation Plate

SDS- Sodium Decyl Sulfate

SDdS- Sodium Dodecyl Sulfate

SEM- Scanning electron microscope

SF- Starfruit

sGNR- small gold nanorod (10x45nm with polystyrene capping)

SPR- Surface Plasmon Resonance

SWNT-single-walled carbon nanotube

TEM-Transmission electron microscope

TIC- Translationally Invariant Configuration

TOAB- Tetraoctyl Ammonium Bromide

TPL-Two-photon luminescence

χ-cholesteric helical axis

Chapter 1: Introduction

Since Pendry's seminal work[1] in the year 2000, demonstrating the feasibility of engineering magnetic material properties, there has been a massive effort to develop optical metamaterials. Metamaterials, or negative index materials, offer the potential of sub-diffraction limit far field optical imaging[2] that could revolutionize microscopy in the physical and biological sciences.

Spherical noble- metal nanoparticles are an ancient technology used by Roman and medieval artisans to produce a variety of colored glasses used in ceramics and cathedral windows. The colors associated with noble metal nanoparticles are due to plasmon resonance which occurs in nanospheres when $\varepsilon_{nanoparticle}+2\varepsilon_{medium}=0$ [3], where ε is the dielectric permitivity. For gold, silver, and copper nanospheres, the plasmon resonance condition is met at 525nm, 420nm, and 580nm yielding red, yellow, and green glasses respectively. Guided plasmon modes allow for non-trivial engineering of magnetic permeability within the optical and near-IR spectral regions making concentrated noble metal nanoparticle dispersions a highly promising system for producing bulk optical metamaterials[4]. In recent decades several well-controlled syntheses of rod[5], platelet[6], and platonic solid shaped [7] noble- metal nanoparticles have been developed, yielding particles with multiple plasmonic modes that are associated with different orientations of the nanoparticle.

In order to produce device scale materials that benefit from shape-dependent plasmonic engineering, one must produce long range alignment of these anisotropic nanoparticles. Liquid crystal(LC) phases produce long-range alignment of anisotropic building blocks and would be a logical way of aligning high aspect ratio nanoparticles, however the most nanoparticles with longitudinal plasmon modes in the visible do not have sufficient aspect ratio to form an LC phase on their own. Low aspect ratio particles can be aligned in a guest-host system[8]. Furthermore

visco-elastic forces associated with colloidal inclusions in a liquid crystal could potentially allow for periodic assembly of colloidal inclusions into a Wigner crystal and other forms of self-assembly. However these viscoelastic inclusions are energetically costly making the production of highly concentrated dispersions non-trivial, especially when the nanoparticles are significantly larger than the LC mesogens.

This work focuses on producing highly concentrated dispersions of nanoparticles in a LC and harnessing the viscoelastic properties of the LC to produce complex nanoparticle architectures. In Chapter 2 I discuss the feasibility of LC-nanoparticle based metamaterials, provide evidence suggesting the formation of a Wigner crystal. In Chapter 3 I describe the synthesis of aspect ratio 2000 nanoplatelets and the surface boundary conditions produced by those platelets in small molecule thermotropic and chromonic LCs. In Chapter 4, I describe bulk dispersion of those nanoplatelets in a giant graphene oxide based discotic phase. In Chapter 5, I explore the elastic interactions of single nanoparticles and microspheres, then describe the hierarchical self-assembly of microparticle-nanoparticle dimers. In Chapter 6, I use a confined cholesteric LC to generate well-controlled elastic traps that do not require the presence of a microsphere and use a partially-polymerizable system to allow for fully 3-dimensional preparation of elastic scaffolding. In Chapter 7, I describe the preparation of elastomeric colloids containing gold nanospheres that impart enhanced photothermal response. In Chapter 8, I dynamically change the shape of elastomeric colloids dispersed in a short-pitch cholesteric LC to explore the distortions associated with various types of dipoles and further inform our choice of shapes for future LC-nanoparticle composite materials. In chapter 9 I describe the infiltration of solid anisotropic structures with gold nanorods namely, cross-linked polymer lyotropic phases and carbon

nanotube structures. In chapter 10 I describe the preparation of solid materials from cellulose based LC phases containing gold nanorods. In chapter 11 I provide some concluding remarks.

1.2 References

1. J.B. Pendry. *Phys Rev. Lett.*, 85, 3966, (2000).

2. J. Valentine, S. Zhang, T. Zentgraf, E. Ulin-Avila, D. Genov, G. Bartal, X. Zhang. *Nature*, 455, 376, (2008).

3. G. Colas de Francs, S. Derom, R. Vincent, A. Bouhelier, A. Dereux, *International Journal of Optics* **2012**, 175162 (2012).

4. A. V. Kabashin, P. Evans, S. Pastkovsky, W. Hendren, G. A. Wurtz, R. Atkinson, R. Pollard, V. A. Podolskiy, and A. V. Zayats *Nature Materials* **8**, 867 - 871 (2009)

5. C. Murphy, T. Sau,A. Gole, C. Orendorff, J. Gao, L. Gou, S. Hunyadi, T. Li. *J. Phys. Chem. B* **109***,* 13857-13870 (2005**).**

6. M. Grzelezak, J. Juste, P. Mulvaney, L. Liz-Marzan. *Chem. Soc. Rev.* **37**, 1783-1791 (2008).

7. C. Huang , P. Chiu, Y. Wang, W. Chen, and T. Meen *J. Electrochem. Soc*. **153**, 8, D129-D133 (2006)

8. Q. Liu, Y. Cui, D. Gardner, X. Li, S. He, I.I. Smalyukh, I.I. *Nano Lett*, 10, 1347, (2010).

Chapter 2: Metamaterials, nanoparticle Self-Alignment, and defect patterning in Liquid Crystals

Adapted from: *Mol. Cryst. Liq. Cryst.* **545**, 1227 (2011)

Chapter Overview

We explore the nanoscale colloidal self-assembly and self-alignment in liquid crystals. We use model particles with controlled shapes and sizes, including quantum dots, quantum rods and metal nanoparticles in the form of spheres, rods, and polygonal platelets. To study these composites on the scales ranging from nanometers to millimeters and to motivate their use in metamaterial fabrication, we utilize optical microscopies, freeze-fracture transmission electron microscopy, and cryogenic transmission electron microscopy. We discuss the long-range alignment and assembly of anisotropic nanoparticles imposed by the orientational elasticity of liquid crystals, showing that these composites provide a powerful platform for self-assembly of metamaterials.

2.1. INTRODUCTION

Optical metamaterials are a new class of man-made materials with the potential for a broad range of breathtaking applications that range from nanoscale diffraction-unlimited optical imaging with "perfect" lenses to invisibility cloaking [1-25]. They are composed of ordered arrays of predesigned structural units different from those in the conventional matter and allow for the engineering of unprecedented material properties. These ordered structures of predesigned anisotropic nanoparticles play the role of "building blocks" similar to that of molecules and atoms in conventional condensed matter systems [1-25]. Metamaterials allow for engineering of unprecedented physical properties not encountered in naturally occurring materials, such as negative refraction of light [1,2]. However, for these applications to come within reach, large-

scale fabrication approaches are needed [5,15].

Hybrid nanostructured materials based on nanoparticles and liquid crystals (LCs) are a class of composites poised to revolutionize scientific instruments, technologies, and devices, and may enable self-assembly-based approaches for fabrication of metamaterials [15]. LCs may enable reconfigurable and switchable self-assembly of dispersed nanoparticles directed by the nanoscale molecular ordering in these anisotropic fluids with a broad range of mesomorphic phases. Control of the colloidal and molecular structural organization and ensuing composite properties may be achieved by using intrinsic liquid crystalline self-assembly and re-assembly into various mesomorphic phases (including phases that have not been encountered previously), applying external electric, magnetic, mechanical, and optical fields, varying temperature, and changing surface treatment at the nanostructured solid-LC interfaces [26]. However, the nanoscale interactions between colloidal nanoinclusions in LC media remain poorly understood. There is a need to explore the fundamental organizing principles of this type of LC-directed self-assembly arising from the controlled structuring of switchable liquid crystalline order and nanoparticles of various shapes and chemical composition.

In this chapter, we discuss the nanoscale colloidal self-assembly and self-alignment in LCs probed for a variety of model particles with controlled shapes and sizes. External magnetic and electric fields and shearing allow for alignment and realignment of the LC matrix with the ensuing reconfigurable long-range orientational order of the dispersed nanoparticles that can be kept dispersed or made to self-organize into structures such as chains and periodic lattices. The device-scale bulk nanoparticle self-alignment and self-assembly may enable optical metamaterial

mass production and control of their properties arising from combining the switchable nanoscale structure of LCs and the so-called Surface Plasmon Resonance (SPR) properties of the plasmonic nanoparticles [15]. Potential applications of these man-made artificial materials include "perfect" lenses for imaging with sub-wavelength resolution, better optical tweezers, wide-angle non-mechanical beam steering devices, novel band gap materials, high-density optical data storage, stealth technology (i.e., invisible warfare), and many other applications [1-33]. Metamaterials also provide an incredible range of untouched fundamental science problems and engineering challenges which greatly stimulate the development of novel nanoparticle synthesis approaches, techniques for nanoparticle dispersion and assembly, etc. [34-49].

This chapter will show that the LC colloidal nanoparticle dispersions provide a powerful platform for self-assembly-based tunable optical metamaterial fabrication and may allow their potential applications to come within reach. We provide the motivation and a brief introduction to the fundamental aspects of metamaterials in the next section 2.2 and then proceed with the description of the used materials and experimental techniques in the section 2.3. The main results are described in section 2.4, followed by a brief discussion (section 2.5), and concluding remarks (section 2.6).

2.2. STRUCTURE AND POTENTIAL APPLICATIONS OF METAMATERIALS

In terms of resolution, optical imaging of long-range molecular orientation patterns had only incremental improvements over a century of its use, even though it is one of the most important and frequently used techniques in the LC research. Novel approaches of imaging of structural self-assembly in LCs with improved resolution are needed to further the collective understanding

of these media on the nanoscale. Therefore, motivating this work with the current state-of-the-art of nanoscale LC imaging is a convincing way of presenting the importance and the need for the development of optical metamaterials. Fig. 2.1 shows nanoscale images of a chromonic lyotropic LC obtained by a cryogenic transmission electron microscope (TEM), a powerful nanoscale imaging technique that is rarely available to researchers. Because of the need to freeze the samples and a number of other limiting factors, this technique is incapable of revealing the dynamics of the nematic and columnar hexagonal ordering of the constituent molecular stacks. Despite of the recent interest in the lyotropic chromonic LCs, they remain poorly understood, and even the types of molecular organization into chromonic stacks still need to be clarified for some of the most common materials. Cryogenic TEM images in Fig. 2.1 show that molecular stacking in nematic and columnar hexagonal phases is qualitatively different. Nematic-phase stacks possess multiple kinks and can relatively easily bend or branch into multiple stacks (Fig. 2.1(a,b)). Columnar stacks in the hexagonal phase are much more regularly structured and highly ordered as compared to those in the nematic phase (Fig. 2.1(c)). These images give the average length of the molecular aggregates of molecules of Cromolyn Sodium which is 50-100nm in the nematic phase and even longer (hundreds of nanometers) in the columnar hexagonal phase as well as high values (0.8-0.95) of the orientational order parameter in these phases [50]. However, cryogenic TEM fails to reveal the temporal evolution of the molecular stacks and how they change and rearrange during phase transitions, switching by external fields, etc. On the other hand, noninvasive diffraction-limited optical imaging in different modes [51-57] lacks the nanoscale resolution of the order of 1nm needed to address this problem. Although there have been recent developments in optical imaging that allow overcoming the diffraction limit [58-60],

their use is typically restricted to very specific chromophores and would not be easily applicable for imaging of soft matter systems such as choromonic LCs.

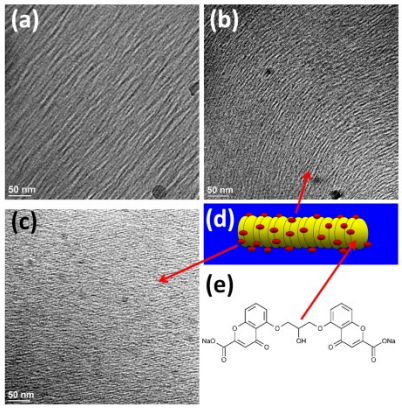

FIG. 2.1 Nanoscale imaging of a chromonic lyotropic LC by means of the Cryogenic Transmission Electron Microscopy. a-c) Cryogenic TEM images obtained for an aqueous solution of cromolyn sodium in (a,b) nematic and (c) columnar hexagonal phases. d) a schematic representation of a columnar stack that is a building block of both columnar hexagonal and nematic phases of the chromonic lyotropic LC. e) Chemical structure of cromolyn sodium used to obtain the studied LC in its aqueous solutions (section 2.3.2).

Recently, a bulk of theoretical and experimental research showed the feasibility of diffraction-unlimited optical imaging by use of simple optical elements based on metamaterials with a negative index of refraction. Theoretical works of Veselago [1] and Pendry [2], followed by numerous theoretical and experimental papers [3-33], have demonstrated that the diffraction limit of conventional lenses (Fig. 2.2(a)) is not a limiting factor for the focusing of light by a lens made of a flat slab of metamaterial with a negative index of refraction (Fig. 2.2(b)), often referred to as a "super-lens" or a "perfect lens." Improved resolution of the negative-index super-lens is due to the transmission of the evanescent surface waves, which (unlike in the case of conventional lenses) are not lost. Being first considered theoretically over four decades ago by Veselago [1], metamaterials (also called "left-handed materials") have never been encountered in

nature or fabricated until the theoretical work of Pendry provided important physical insights into how these unusual materials can be realized [2].

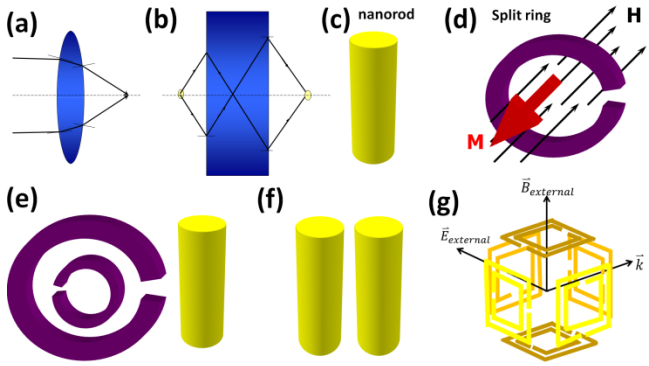

FIG. 2.2 Motivation for the development of optical metamaterials and common designs of their structural units. a,b) comparison of light focusing by lenses made of a) conventional materials and b) a flat slab of the metamaterial with a negative index of refraction. Structural elements of metamaterials: c) plasmonic nanorods for negative electric response, d) split nanorings for negative magnetic resonance, e) double split nanorings paired with nanorods to provide negative electric and magnetic response, f) coupled nanorods also capable of providing negative electric and magnetic response in certain conditions, g) a unit cell of a three-dimensional optical metamaterial composed of double split rings [1-33].

Metamaterials are composed of structural units much smaller than the wavelength of incident light, so they appear homogeneous to the waves. To obtain metamaterials with a negative refractive index, one has to achieve simultaneous negative electric and magnetic response in the artificial nanofabricated composite material. At optical frequencies close to the SPR peaks, the electric response can be negative. Therefore, achieving negative electric response (dielectric constant) is relatively easy when using metal nanoparticles, because they show SPR peaks dependent on material composition and shape. For example, gold nanospheres have one SPR peak at ~525nm and silver nanospheres exhibit SPR at ~420nm, while metal nanorods and particles of more complex shapes have more than one SPR peak with the spectral locations dependent on the shapes and aspect ratios of these nanoparticles. For nanorods, there are two resonance modes, transverse & longitudinal, both of which can be located within the visible

spectral range. To have different SPR peaks within the visible spectrum, one typically needs to use nanoparticles with fairly small (1.5-3) aspect ratios as the larger the aspect ratio, the longer is the wavelength of the longitudinal peak and the wavelength of the transverse peak is fixed and similar to that of spheres. Achieving strong negative magnetic response at optical frequencies, however, is more difficult than obtaining negative electrical response (considered being impossible until about a decade ago). This was part of the reason why Veselago's left-handed materials have not attracted much attention in the scientific and engineering communities until recently. Pendry proposed that split-ring resonators could produce a strong negative magnetic response (Fig. 2.2(d)) [2], inspiring a bulk of experimental and theoretical research that led to confirmation of his theoretical predictions and to a "metamaterial rush" in the optics and materials research communities [2-33]. The predesigned structural units of metamaterials can be built out of nanoparticles designed to provide negative electric and magnetic response. Popular metamaterial designs involve pairs of double-split rings and rods (Fig. 2.2(e)), coupled rods (Fig. 2.2(f)), and three-dimensional structures composed of multiple double-split rings (Fig. 2.2(g)) [2-33].

Various nanofabrication approaches have been successfully utilized to produce nanoscale structures exhibiting metamaterial properties. Metamaterials working in the infrared and visible spectral ranges have been recently proposed and realized, with the so-called "fishnet metamaterials" being perhaps the most successful example. However, as already mentioned in the introduction, for practical applications of these artificial materials to come within reach, self-assembly-based approaches for mass production of large-scale three-dimensional metamaterials need to be developed [5, 15, 33]. LCs with the intrinsic long-range orientational and partial

positional ordering can provide several critical components in this effort, including self-assembly and self-alignment of nanoparticles, their spatial self-positioning and chiral arrangement, as well optical, electric, magnetic, thermal and other means of control and switching applied to LC-incorporated particles of pre-designed shapes and composition.

2.3. MATERIALS AND EXPERIMENTAL TECHNIQUES

2.3.1. Synthesis of Gold Nanoparticles

Although gold nanoparticles have been used in red stained glass in cathedrals for centuries and have been studied extensively starting from the works by Faraday, their potential use in metamaterials requires a precise control of particle shapes and their spatial structuring on length scales much smaller than the wavelength of visible light. This sets new fundamental research and engineering challenges from the standpoint of their synthesis, dispersion, and controlled structural organization. The synthesis of colloidal gold nanoparticles typically occurs through the reduction of gold cations in the presence of a certain capping agent. The size and shape of the nanoparticles are determined by the kinetics of nucleation, the ratio of gold and capping agent, and the stabilization of different crystallographic faces by the capping agents [61]. To produce spherical particles, fast reduction with no preferential surface stabilization is ideal. For example, in the Brust-Schiffrin method, chloroauric acid is complexed with tetraoctylammonium bromide (TOAB) and toluene to enter the organic phase [62]. It is then reduced by sodium borohydride in the presence of excess thiol to produce 2nm spheres (Fig. 2.3(a)). If no thiol is added, TOAB stabilizes the formation of 20nm spheres (Fig. 2.3(b)).

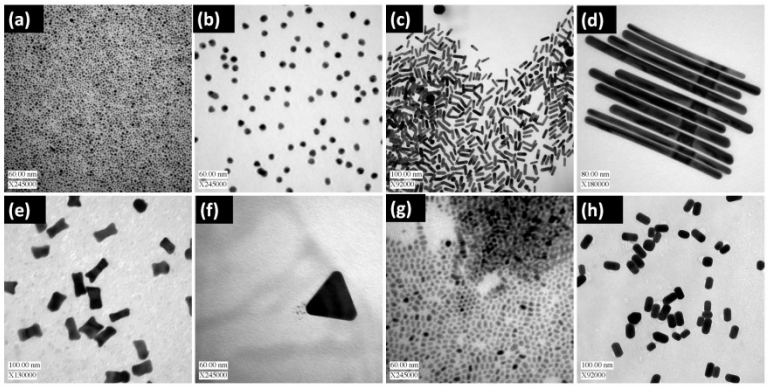

FIG. 2.3 Examples of nanoparticles of different material composition, shapes, and sizes. a) Gold nanospheres of 2-3nm in diameter. b) gold spheres of 20nm in diameter. c) CTAB capped gold nanorods with an aspect ratio of about 3. d) CTAB capped gold nanorods with aspect ratios ranging from 15 to 20. e) dog-bone-shaped gold nanoparticles. f) PVP capped silver triangle synthesized by photoreduction. g) CdSe quantum rods with aspect ratio of about 2. h) short gold nanorods obtained from NanoPartz.

The growth of non-spherical nanoparticles requires slower reduction and preferential selection of crystal facets. One of the best known examples of synthesis of non-spherical metal nanoparticles is the synthesis of nanorods capped by cetyl trimethylammonium bromide (CTAB) [63,64]. In the synthesis procedure, spherical seeds are produced by reducing chloroauric acid with sodium borohydride in the presence of sodium citrate or CTAB. These spherical seeds are then transferred to a growth solution with more CTAB, chloroauric acid, and ascorbic acid that produces a mild reduction on the <110> facets of the seed particles [65] (Fig. 2.3(c,d)). If the ascorbic acid is too active, then the ends can get overgrown producing anisotropic nanoparticles with shapes resembling “dog bones” [66] (Fig. 3(e)). Triangular platelets can be synthesized using various methods such as photoreduction (Fig. 3(f)) [67] and biosynthesis [68]. These triangles and dog bones mentioned above are of special interest for the metamaterial applications because the SPR that they exhibit is enhanced by sharp corners. CdSe quantum dots and rods

were obtained as described in ref. [48,60] and provided by P. Prasad. Gold Nsol rods were obtained from Nanopartz Inc. (Loveland, Colorado, USA).

2.3.2. Nanoparticle Dispersion in LCs and Cell Preparation

Before introducing nanoparticles into the thermotropic LC host they are first dispersed in an organic solvent. Then the particles are continuously added (2μl at a time) to the LC while the mixture is rapidly stirred by a magnetic stir bar. The LC with the added nanoparticles is kept at an elevated temperature (above the boiling point of the used solvent) overnight to evaporate the solvent. For example, the sample is kept overnight at 80 ^{o}C in the case of hexane (above its boiling point) to assure that the solvent is fully removed from the sample through evaporation. After the solvent is evaporated, the sample is vigorously stirred for three minutes using a VWR Analogue Vortex Mixer, sonicated for three minutes by a Branson 250 Sonifier, and finally sonicated for 3 minutes in a Cole Parmer 8891 ultrasonic bath to ensure the nanoparticles are well dispersed in the LC.

The dispersion of nanoparticles in lyotropic LCs is limited to nanoparticles functionalized or capped with surfactants. For example, the synthesis procedure of the gold nanorods yields CTAB-capped rods dispersed in an aqueous solution. We add more CTAB (surfactant) and benzyl alcohol (cosurfactant) to this aqueous nanorod dispersion to obtain the desired lyotropic LC phase according to the phase diagram of aqueous mixtures of surfactant CTAB and co-surfactant benzyl alcohol previously studied without adding nanoparticles [15, 69, 70]. For example, the LC-nanorod dispersion in the columnar hexagonal phase is prepared using a composition of 25% CTAB, 5% benzyl alcohol (both from Aldrich, used as supplied) and 70%

of aqueous suspension of CTAB-capped GNRs. The nematic phase is prepared in a similar way, but consists of 25% CTAB and 75% of aqueous suspension of CTAB-capped GNRs. This preparation is typically followed by centrifugation at 3000 rpm for 10 min. The obtained LC-nanoparticle composites are sonicated in the ultrasonic bath for two hours to ensure homogeneous mixing and dispersion.

For optical microscopy observations, the LC-nanoparticle dispersions are filled into a rectangular capillary or glass cell by use of capillary action. The glass cells are typically made of a clean microscope slide and a cover slip. The microscope slide and cover slip are glued together using UV-curable glue mixed with glass spacers that set the cell gap. Typically, the substrates have no alignment layers. The cell substrates are sealed using a 5-min epoxy.

2.3.3. Optical microscopy and spectroscopy

Optical imaging of nanoparticle-LC composites is performed using an Olympus BX-51 upright optical polarizing microscope with a fluorescent attachment. The dispersion quality (i.e., absence of micron-scale or larger nanoparticle aggregates) is assessed by means of the transmission-mode bright-field imaging. The phase behavior and LC alignment is studied by the same microscope in the polarizing optical imaging mode using 10×, 20×, and 50× air objectives (all from Olympus) with numerical aperture NA=0.3-0.9 as well as a Spot 14.2 Color Mosaic Camera (from Diagnostic Instruments, Inc.). In addition, we have used an inverted microscope IX81 with a fluorescence attachment, a confocal microscopy scanning unit, and a NA=1.4 objective (all from Olympus). The SPR extinction spectra are measured using a USB-2000 microspectrometer (Ocean Optics) mounted on the optical microscope.

2.3.4. Nanoscale imaging of Nanoparticles in Liquid Crystals

The images of the synthesized nanoparticles, such as those shown in Fig. 2.3, are obtained using a Philips CM10 TEM (FEI, Inc.) operating at 80kv. However, regular TEM is not appropriate for probing the structural assembly and alignment of nanoparticles in LCs because, in addition to many other reasons, the vacuum levels at which the conventional TEM operates cause LC evaporation. To overcome this problem, and to get insights into the nanoscale structural assembly in nanoparticle-doped LCs, we use a technique known as Freeze Fracture Transmission Electron Microscopy (FFTEM) that has been widely used in the studies of LCs.

The sample preparation for FFTEM imaging starts by taking a small quantity (2-4μl) of the sample and sandwiching it between two thin copper substrates. This sample between the copper

plates is then rapidly quenched in liquid propane to temperatures below -183 ^{o}C. The copper sandwich is loaded into a BalTec freeze etch machine at a temperature of -140 ^{o}C and pressure of 10^{-6} mbar. The copper sandwich is then fractured in the cold vacuum. The exposed fractured surfaces are shadowed with ~2nm of a platinum-carbon (Pt-C) alloy at 45° and ~30nm of carbon normal to the fractured plane. The Pt-C alloy is deposited for image contrast and the layer of carbon is used to improve mechanical stability. The shadowed sample is removed from vacuum, and gradually warmed to room temperature. It is then washed in deionized water, ethanol, and ethyl acetate to remove the LC host and nanoparticles leaving behind Pt-C replicas of the fracture plane. The Pt-C replicas are imaged using the TEM revealing the structural assembly and alignment of nanoparticles in the LC at the fractured plane. We also used an alternative method of FFTEM sample preparation. In this method, a sample of volume ~2-4μl is placed in a small copper bowl instead of sandwiching it between two copper plates. The sample in the bowl is frozen and inserted into the freeze etch machine as described above. Fracturing of the frozen sample is then done with a special knife. The rest of the preparation/imaging procedure is the same as described above.

2.4. RESULTS

2.4.1. LC-Nanoparticle Interactions Probed Using Fluorescence

To explore the basic properties of nano-scale interactions of LC host fluids with nanoparticle inclusions, we use fluorescent Cadmium Selenide Quantum Dots (QDs) [60]. Spatial location of these nanoparticles in the samples can be directly visualized by use of fluorescence signals in fluorescence microscopy or fluorescence confocal polarizing microscopy. We explore the

behavior of nanoparticles as the LC sample is subjected to temperature changes causing phase transitions. To perform these experiments, the dispersion of QDs in hexane is added to a commercial thermotropic nematic mixture E7 (EM Chemicals) at a concentration of 0.001% by weight. The cell with the QD-E7 dispersion is then placed into an Instec STC200 heating stage mounted on a fluorescent microscope. A 10x objective is used with a 488 nm argon laser to obtain monochromatic transmission optical microscopy images between crossed polarizers and corresponding fluorescent images of the sample. The transmission and fluorescence images are overlaid to visualize the nanoparticle spatial locations and interactions (Fig. 2.4a).

To explore the differences in the behavior of particles in isotropic vs. nematic LC hosts, the temperature to which the sample is subjected in the heating stage is first increased to 80 ^{o}C and then cooled at 0.5 ^{o}C/s to room temperature. In the isotropic phase, the QDs are well dispersed and undergo Brownian motion. However, when the LC sample transitions to the nematic phase, the QDs are expelled from the nucleated and growing nematic domains into their isotropic surroundings. This expulsion is due to the elastic energy costs associated with the distortions of the LC director by QDs. Retaining QDs in the isotropic phase is energetically favorable because there is no elastic energy cost associated with the isotropic phase while the nanoparticle-induced distortions in the nematic host correspond to the elastic free energy of the order of $KL \geq K_B T$ per nanoparticle, where K~10pN is the average Frank elastic constant and L is the average size of nanoparticles. Fig. 2.4(a) shows a series of images taken as the E7 transitions from isotropic to the nematic phase. The highlighted QDs are expelled from the nematic domain and remain at the isotopic-nematic phase boundary as long as possible, until the isotropic region of the sample disappears. This expulsion often leads to the transition-induced aggregation of colloidal

inclusions. Furthermore, this clearly demonstrates that dispersion of nanoparticles in LC fluids is more challenging as compared to the isotropic solvents and even the nanoparticles that disperse well in isotropic melts of certain materials may aggregate as a result of a transition to the mesophase.

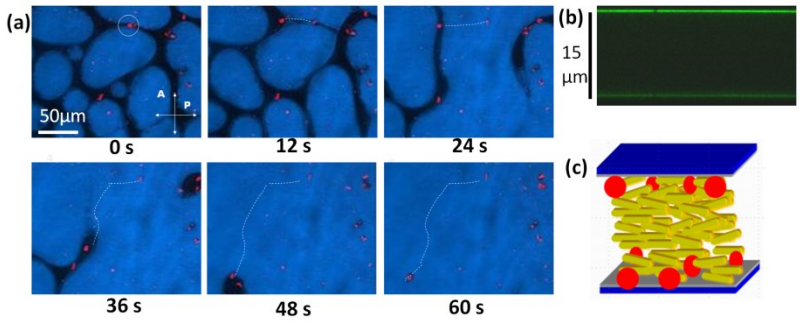

FIG. 2.4 Nanoparticle expulsion from the LC. a) a series of color-coded superimposed images taken in polarizing and fluoresce microscopy modes. The white circle in the image at time t=0 highlights QDs expelled from the LC while remaining in the isotropic melt of the sample until disappearing. The dashed white lines in the images highlights the movement of QDs along about 200μm-long trajectory across the sample over the course of 1 min. Using Fluoview software of the confocal microscope, the grayscale transmission-mode images with the fluorescence from QDs are color-coded so that the bright areas appear blue, the dark areas appear black, and the strong fluorescence signals from QDs appear red. b) a vertical cross section of nematic LC cell obtained using fluorescence confocal microscopy. Fluorescence from the QD nanoparticles is shown in green. c) a schematic showing QDs expelled to the glass-LC interface.

2.4.2. Expulsion of Fluorescent Nanoparticles to Confining Substrates

Partial expulsion of nanoparticles from the LC hosts is also observed for samples deep in the nematic phase. After being kept for several hours in the nematic LC, the fluorescent QDs partially segregate to the nematic-glass interface. The same effect is observed for Quantum Rods (QRs) (Fig. 2.3(g)) [43]. Using the dispersion techniques described above, the QRs are dispersed in the nematic mixture ZLI-2806 (obtained from EM Chemicals) at the doping concentration of 0.01% by weight. This nematic has low birefringence, which makes it ideal for imaging by means of a confocal microscope. QRs are excited using a 488nm Argon laser and imaged using

the confocal microscope. Cross sections of the sample are shown in Fig. 2.4(b). The fluorescence from the QRs is colored green and can be seen throughout the sample, but is the strongest at the nematic-glass boundary, indicating the segregation of the majority of the nanoparticles onto the substrate. Fig. 2.4(c) shows a schematic representation of the phase separation. Much like the expulsion of QDs from the nematic nuclei into the surrounding isotropic melt discussed above, the nematic LC expels the distortion-causing QRs to the glass/nematic boundary where this elastic distortion is minimized in size and energy cost. Although this experiment highlights an additional challenge of obtaining long-term-stable nanoparticle dispersions in LCs, it also shows the feasibility of stable dispersion of nanoparticles in the LC as somewhat weaker fluorescent signals also come from the individual QRs in the bulk of the LC which do not segregate (Fig. 2.4(b)).

2.4.3. Entrapment of nanoparticles by defect networks

To show that LC defects can be utilized for spatial patterning of nanoparticles, we use a cholesteric LC. Doping the nematic mixture ZLI-4788 with a chiral agent ZLI-811 (both from EM Chemicals) yields a room temperature cholesteric LC with pitch that depends on the amount of the chiral additive. QRs are added to such a mixture with cholesteric pitch of 1μm at 0.1% concentration by weight. An Olympus BX51 fluorescent microscope is used to obtain epi-fluorescence images as well as transmission-mode polarizing microscopy images. Fig. 2.5(a) shows the typical oily streak texture of this cholesteric LC when infiltrated into a cell with untreated glass substrates. Fig. 2.5(b) shows the same area of the sample imaged with fluorescence microcopy. The fluorescence from the QRs is the strongest in the vicinity of oily streaks, indicating that the nanoparticles spatially localize within the defect cores. The self-

assembly of the QRs into the defects is driven by the reduction of elastic free energy costs when the nanoparticles are in the defect core as the particles replace energetically costly regions of the defects. Similar to the case of larger colloids [71], the studied QRs stabilize the network of oily streak defects. Since the nanoparticles now tend to stay within the defects, they are less susceptible to segregation to the bounding glass plates.

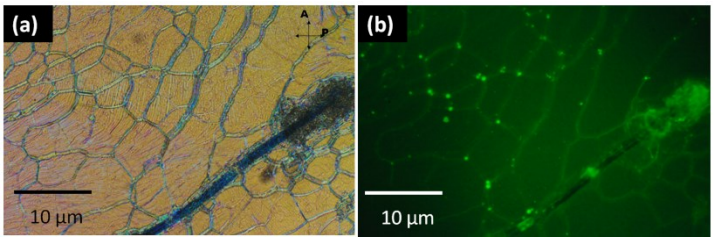

FIG. 2.5 Entrapment of nanoparticles by defects. a) polarizing microscopy image obtained with crossed polarizers showing the cholesteric oily streaks in the planar system of cholesteric layers. b) Fluorescent microscopy images of the LC doped with quantum rods shows that these nanoparticles have self-assembled into the oily streaks making these defects appearing more luminous than the surrounding LC with a uniform cholesteric structure.

2.4.4. Direct Nanoscale Imaging of Well-Dispersed Nanoparticles in Liquid Crystals

To demonstrate that certain types of nanoparticles can disperse in the ground-state samples of LCs without aggregating or localizing into defects, we perform FFTEM imaging of the TI-827 doped with gold nanospheres (shown in Fig. 2.3(b)) at 10% concentration by weight. Fig. 2.6(a,b) shows the FFTEM image of the sample having 300 nm pitch with the nanoparticles well-dispersed in the LC, as clearly seen from the high-magnification inset of the same area in the sample. Similar high-quality dispersion of the nanoparticles is seen throughout the sample except in a few areas (Fig.2.6(c)) where local aggregation may be “seeded” by much larger nanoparticles. The larger nanoparticles create stronger distortions in the LC molecular alignment that may trap surrounding nanoparticles to reduce the elastic distortion costs. Further

experiments are needed to investigate how nanoparticle dispersions depend on particle size distribution.

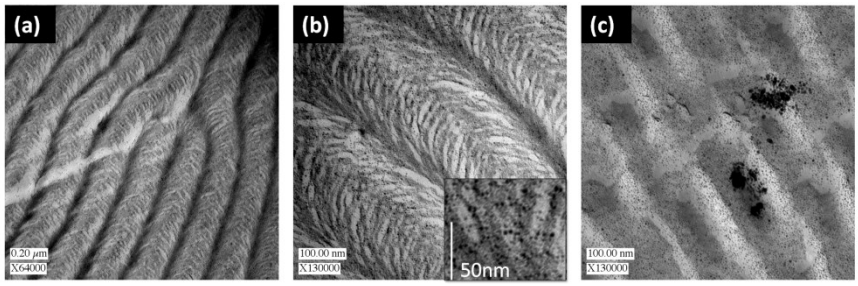

FIG. 2.6 Nanoscale imaging of nanoparticles dispersed in a cholesteric LC. Freeze fracture TEM images of a) 2-3 nm thiol-capped gold nanospherers dispersed in a short pitch cholesteric and b) a magnified image of (a) showing the high-quality dispersion of the nanoparticles; the inset shows the details of the nanoparticle-doped sample at even higher magnification. c) Local aggregation of nanoparticles seeded by larger nanospheres occasionally present in the sample.

2.4.5. Nanoparticle Dispersion, Alignment, and Self-Assembly in CTAB-based Lyotropic Liquid Crystals

We have previously demonstrated that gold nanorods can be well dispersed and aligned in both nematic and columnar hexagonal lyotropic LCs [15], even at high concentrations when inter-rod distances are comparable to their length. However, other types of behavior of nanorods are possible too, depending on the sizes, shapes, capping of nanorods, as well as the details of their dispersion into the LC hosts. Fig. 2.7 shows FFTEM images obtained for nanorods with length ~400 nm and diameter ~20 nm dispersed in a surfactant-based lyotropic LC similar to that used in our previous studies [15]. Doping these rods (having rather high aspect ratios) into the LC in a columnar hexagonal phase typically causes nano-scale polydomain structure (Fig. 2.7). By varying the concentration of these nanorods in the LC, we see their periodic self-assembly (Fig. 2.7 (b,c)), a percolating network of nanorods with a ~200 nm mesh (Fig. 2.7 (d,e)), and dispersed nanorods aligning along the domain boundaries (Fig. 2.7 (f)). The observed structures are a result of medium-nanorod interactions minimizing elastic distortions in the nanoparticle-doped LC in

the hexagonal phase by eliminating distortions at the nanorod ends (as schematically shown Fig. 2.7(a)) or localizing these nanoparticles within the LC domain boundaries. These observations show a great potential for forming nanoparticle self-assemblies of interest for fabrication of metamaterials and other structured nanocomposites. The addition of these and other nanoparticles to LCs may not only result in their nanoscale self-assembly or simple segregation but also may lead to new complex thermodynamic phases not exhibited by these constituents themselves, such as in the case of lipid-biopolymer composites [72].

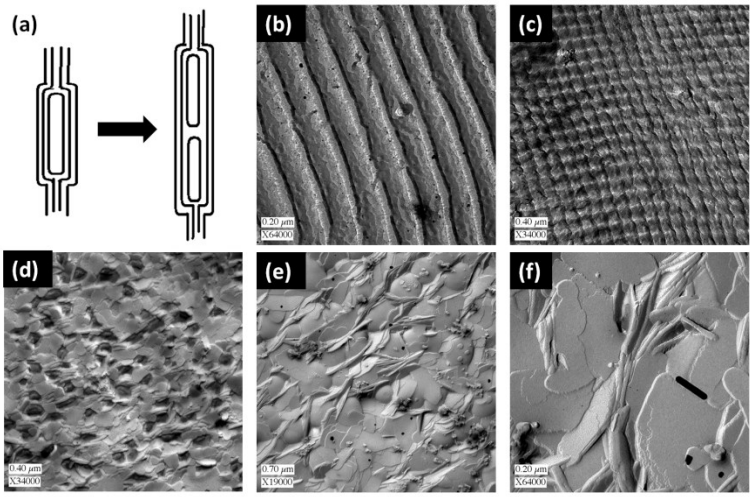

FIG. 2.7 Spatial nanoscale structuring of nanorods dispersed in the 70% water, 25% CTAB, 5% BnOH hexagonal LC hosts. a) Rods in an aligned LC may form chains to reduce elastic energy due to the distortions at their ends. Freeze fracture transmission electron microscopy images of b) long rods forming chains and c) periodic structure in the plane orthogonal to the chains. d,e,f) different 3D networks of nanorods f) aligning along the domain walls between the nanoscale domains in the columnar hexagonal phase of the lyotropic LC.

Optical dark field imaging of these lyotropic LC provides further evidence of the qualitative differences in nanoparticle behavior depending on the dimensions of the nanoparticle. In fig. 2.8(a), the 50nmx20nm GNR are well-dispersed and do not aggregate to any features of the hexagonal columnar domain structure. In fig. 2.8(b), the 400nmx20nm GNR are self-assembled within the hexagonal columnar domain structure. In the left half of fig. 2.8(b), the rods are wholly excluded from some domains and included in the bulk of other domains potentially corresponding to figs 2.7(d,e) while in the right half of the image the rods are entirely aggregated to the domain barriers potentially corresponding to fig 2.7(f).

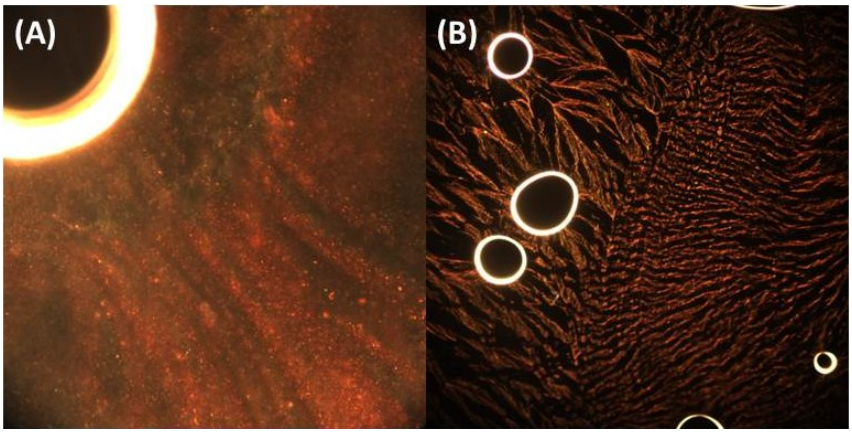

Fig. 2.8: Dark Field imaging showing in (a) that 50nmx20nm disperse well in hexagonal columnar phase while in (b) 400nmx20nm rods tend to assemble in domain boundary defects

2.4.6 Nanoparticle self-assembly in similar hexagonal columnar phases

Whether nanorod inclusions in an LC host disperse or self-assemble depends on several factors including the absolute size of the nanorod, the aspect ratio of the nanorod, and the chemistry of the LC host and nanorod surface. Since CTAB stabilized nanorods are not stable in tetradecyltrimethyl ammonium bromide (TTAB) based LC hosts and small molecule thermotropic discotic phases, 10x45nm mPEG stabilized GNR from Nanopartz were dispersed in a hexagonal lyotropic phase prepared with 35% TTAB, 10% NaBr, and 55% water. Mesogen capped rods from P. Prasad were added to a small molecule thermotropic discotic SK-76 (Fig. 2.10(a)) provided by Sandeep Kumar

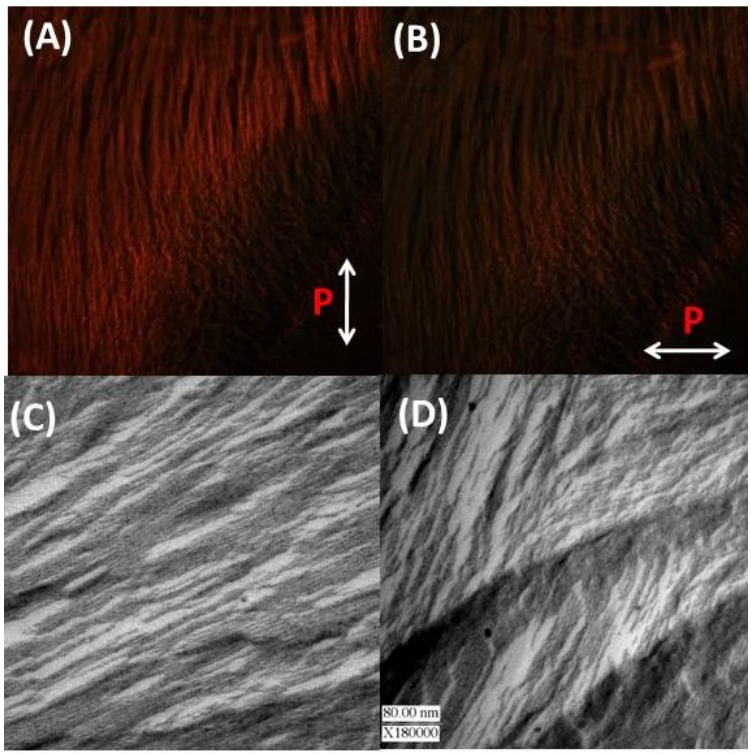

Fig. 2.9: TTAB based hexagonal columnar shows polarization dependent assembly of 10nm x 45nm. Polarized dark field imaging with polarization a) 90 degrees b) 0 degrees show that nanorods preferentially align within domain barriers. c,d) Freeze fracture imaging reveals a periodic structure of individual micelles with c) a gold nanorod aligned with the micelles and d)potentially domain barriers associated with the hexagonal columnar phase.

The nanorods in the TTAB based lyotropic align with the far-field director and disperse throughout most of the sample with a few domains that entirely exclude the nanorods(fig 2.9). There appears to be mild aggregation of nanorods at domain barriers. Whereas in the small molecule thermotropic discotic the nanorods almost exclusively decorate the domain barriers(fig 2.10). These two systems demonstrate that there is not a sharp transition between dispersion and defect-driven self assembly of nanorods

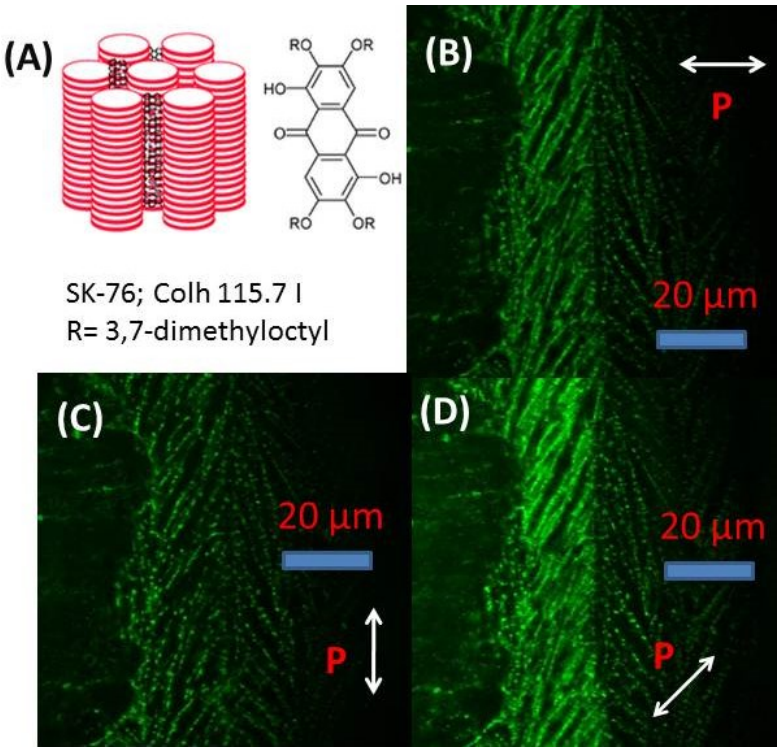

Fig. 2.10: Polarized two-photon luminescent imaging of nanoparticles in discotic hexagonal phase schematically depicted in a) at polarizations of 0,90,45 degrees in b,c,d) respectively shows a strong dependence suggesting that the rods in the left half of the image are aligning with the domain boundary lines. In the right half of the sample the rods are potentially coming out of the page since this is the edge of a droplet.

2.5. DISCUSSION

Our experimental results presented in this work (and also those published elsewhere [27-31]) show that LC host media allow for multiple ways of structural self-assembly and self-alignment [33] of nanoparticles. However, before the LC media can be used as "smart" host fluids for the self-assembly-based fabrication of metamaterials, there is a need for deeper fundamental understanding of the inter-particle forces in LCs and nanoparticle-LC interactions as well as finding ways of dealing with numerous technical challenges. One of the main challenges is the robust stabilization of colloidal nano-scale dispersions in various LC phases. Fig. 2.4 shows that even nanoparticles that are well dispersed in the isotropic phase of LC can aggregate and be

expelled out due to their interactions with the host fluid once it transitions into the ordered viscoelastic LC phase. This expulsion from a host fluid in the nematic phase is caused by the elastic free energy cost of the nanoscale director distortions introduced by the inclusion. Expulsion of a nanoparticle into the isotropic melt (Fig. 2.4(a)) of the LC reduces the overall free energy by the energy cost of distortions, typically of the order of KL, where K is the average elastic constant and L is the average size of the inclusion. When the nanoparticles are expelled to surfaces (Fig. 2.4(b,c)), one obtains a similar reduction of the elastic energy as the nanoparticle-induced distortions partially disappear while the colloids localize at the surfaces.

The enhanced aggregation of nanoparticles in the LC hosts is often facilitated by the elasticity-mediated inter-nanoparticle interactions. Studies of colloidal micro-particles in nematic LCs reveal strongly anisotropic long-range interactions that can be of both attractive and repulsive nature [73,74]. These interactions typically depend on topological defects and director distortions occurring around the particles and are mediated by orientational elasticity of the surrounding LC. In the case of micron-sized inclusions embedded in a nematic LC, both dipolar and quadrupolar configurations can occur, depending on the surface anchoring. When the orientation of the "easy axis" of the director is normal to the surface of the particle, linear colloidal chains are typically formed owing to the long-range dipolar attraction between elastic dipoles formed by particles and hyperbolic point defects. The short range repulsive interactions associated with the presence of the hyperbolic point defects close to the colloids prevent aggregation. When the surface anchoring at the LC-colloid interface is weak-vertical or planar, more complex structures form due to director distortions of quadrupolar symmetry, such as the ones involving Saturn ring disclinations or surface point defects called boojums [28]. These interactions often result in

aggregation of particles into chains at a certain angle with respect to the far-field LC director. When the particle size is ~50nm or smaller, their size is comparable or smaller than the typical surface anchoring extrapolation length for the case of strong surface boundary conditions, and all spherical particles induce director distortions of quadrupolar symmetry; thus, elasticity mediated forces in anisotropic fluids like nematics may facilitate their irreversible anisotropic aggregation. This suggests several approaches for overcoming the problems of irreversible aggregation discussed below.

One approach is to impose strong vertical boundary conditions or use particles of low-symmetry shapes so that dipolar rather than quadrupolar director distortions form around the LC colloids [31]. Relatively large nanoparticles (~50 nm and larger) or nanoparticles of well-controlled specific shapes can be stabilized using this method. The other approach is to use LCs with partial positional ordering, such as smectic and columnar LCs, as successfully realized in our previous works [15, 29, 30]. The layered or columnar structures with one-dimensional or two-dimensional positional ordering, respectively, restrict particle motion to the directions in which the LC is fluid and the nanoparticles can then be stabilized even by use of the very same elasticity-mediated quadrupolar interactions that can be repulsive in the directions in which colloids are allowed to move [15, 29, 30]. Yet another approach is to make the inter-particle interactions sufficiently weak and comparable in strength to that of thermal fluctuations. In this case, the particles properly stabilized in isotropic melt of the thermotropic LC or in the dilute aqueous solutions will be also stable in the thermotropic or lyotropic mesophases, respectively. Fig. 2.6 demonstrates how this is achieved for small nanoparticles of size ~2 nm in the same cholesteric LC in which larger particles aggregate. The smaller nanoparticles are well dispersed because,

due to their size, they barely perturb the ground-state LC structure and the elastic energy cost of the surrounding distortions is negligible or comparable to the thermal energy. Increasing the size of similar particles to 10-15 nm already makes them unstable as the cost of elastic energy distortions increases with the particle size. Particles of larger size can be stabilized in lyotropic nematic LCs made of cylindrical micelles [15] due to the fact that elastic constants of these LCs are about an order of magnitude smaller than in the case of thermotropic LCs. Interestingly, even in the cases when the elasticity-mediated interactions are weak, nanoparticle orientation with respect to the LC director can be controlled and depends on the symmetry of nanoparticle shape, its surface treatment, and the mesophase of the LC host [15, 31].

The very same nanoparticle-induced elastic distortions that make their colloidal stabilization more difficult compared to that in isotropic fluids can be utilized for the controlled spatial patterning of nanoparticles. The nanoinclusion-induced distortions give rise to the elasticity-mediated interactions of the particles with defects and other distortions that can be deliberately induced by external fields and beams of light or pre-defined by ground states of certain phases, such as blue phases. The oily streak defects in the cholesteric phase, for example, attract the surrounding CdSe nanoparticles (Fig. 2.5), so that the defects in the doped samples strongly fluoresce, giving direct evidence for the location of particles in the defect cores (with the majority being concentrated in the defect nodes).

In addition to the spatial localization and patterning of nanoparticles, we have recently demonstrated aggregation-free elastic self-alignment of nanorods dispersed in LCs and their realignment by shearing and magnetic fields [15]. The orientational self-ordering of gold nanorods is a result of the elastic interaction of nanorods with the surrounding matrix of a

uniformly aligned LC. The elastic energy is minimized for the nanorod alignment parallel to the far-field director because the elastic distortions in this case occur only at the rod ends. In the case of gold nanorods, this self-alignment gives rise to the strong polarization sensitivity of SPR, showing the potential for LC-mediated oriented self-assembly of bulk optical metamaterials with tunable and switchable properties [15]. External magnetic/electric fields and shearing allow for alignment and realignment of the liquid crystal matrix with the ensuing reconfigurable long-range orientational order of the dispersed nanoparticles that can be kept well dispersed during this process. A number of interesting structures can be achieved as a result of elasticity-mediated spatial patterning of nanoparticles in different LCs, ranging from the aligned nematic-like arrangements of well-dispersed nanorods [15] to translationally periodic chains and arrays of nanorods, and to the percolating three-dimensional network of these nanoparticles (Fig. 2.7). The experiments show a very broad spectrum of self-assembly phenomena that depend on the size and shape of nanoparticles, the type of LC used, etc. For example, the formation of long periodically-spaced chains shown in Fig. 2.7b allows the elimination of the strong elastic distortions induced at the opposite particle ends or share some of the distortions (Fig. 2.7a). Clearly, the long nanorods show a distinctly different behavior as compared to the case of short nanorods and either assemble into long chains or cause a nanoscale polydomain structure of the surrounding lyotropic LC and segregate into the domain walls, forming a three-dimensional percolating network of nanorods in the LCs.

2.6. CONCLUSIONS

In conclusion, we have demonstrated dispersion, self-alignment, and self-assembly of plasmonic metal nanoparticles in liquid crystals. Since the LC-mediated alignment and assembly of plasmonic nanoparticles gives rise to a switchable polarization-sensitive plasmon resonance (exhibiting stark differences from that of the same nanoparticles in isotropic fluids [15]), the LCs with self-assembled and self-aligned anisotropic nanoparticles are of interest for fabrication of tunable optical metamaterials. Furthermore, once the understanding and control of the underlying physical processes are improved, the device-scale bulk nanoparticle self-alignment and self-assembly may enable optical metamaterial mass production and control of their properties arising from combining the switchable nanoscale structure of LCs and the surface plasmon resonance properties of the plasmonic nanopartricles.

2.7 REFERENCES

1. V.G. Veselago. *Soviet Physics Uspekhi*, 10, 509, (1968).

2. J.B. Pendry. *Phys Rev. Lett.*, 85, 3966, (2000).

3. D.H. Werner, D.H. Kwon, I.C. Khoo, A.V. Kildishev, V.M. Shalaev. *Optics Express,* 15, 3342, (2007).

4. A. Minovich, D.N. Neshev, D.A. Powell, I.V. Shadrivov, Y.S. Kivshar. *Appl. Phys. Lett.,* 96, 193103, 2010.

5. C.M. Soukoulis, Linden, S., Wegener, M. *Science,* 315, 47, (2007).

6. T. Li, Y.Q. Li, F.U. Wang, Q.J. Wang, H. Liu, S.N. Zhu, Y.Y. Zhu. *Appl. Phys. Lett.*, 90, 251112, (2007).

7. J. Valentine, S. Zhang, T. Zentgraf, E. Ulin-Avila, D. Genov, G. Bartal, X. Zhang. *Nature*, 455, 376, (2008).

8. E. Kim, F. Wang, W. Wu, Z. Yu, Y.R. Shen. *Phys. Rev. B.*, 78, 113102, (2008).

9. A. Minovich, D.N. Neshev, D.A. Powell, I.V. Shadrivov, M. Lapine, I. McKerracher, H.T. Hattori, H.H. Tan, C. Jagadish, Y.S. Kivshar. *Phys, Rev. B.*, 81, 115109, (2010).

10. S. Zhang, W. Fan, N.C. Panoiu, K.J. Malloy, R.M. Osgood, S.R.J. Brueck. *Phys. Rev. Lett.*, 95, 1347404, (2005).

11. G. Dolling, C. Enkrich, M. Wegener, C.M. Soukoulis, S. Linden. *Science*, 312, 892, (2006).

12. W. Wu, E. Kim, E. Ponizovskaya, Y. Liu, Z. Yu, N. Fang, Y.R. Shen, A.M. Bratkovsky, W. Tong, C. Sun, X. Zhang, S.Y. Wang, R.S. William. *Appl. Phys A: Matter. Sci. Process.*, 87, 143, (2007).

13. U.K. Chettiar, A.V. Kildishev, H.K. Yuan, W. Cai, S. Xiao, V.P. Drachev, V.M. Shalaev. *Optics Letters*, 32, 1671, (2007).

14. E. Plum, J. Zhou, J. Dong, V.A. Fedotov, T. Koschny, C.M. Soukoulis, N.I. Zheludev. *Phys. Rev. B*, 79, 03540, (2009).

15. Q. Liu, Y. Cui, D. Gardner, X. Li, S. He, I.I. Smalyukh, I.I. *Nano Lett*, 10, 1347, (2010).

16. J. Yao, Z. Liu, Y. Liu, Y. Wang, C, Sun, G. Bartal, A.M. Stacy, X. Zhang, X. *Science*, *321*, 930, (2008).

17. I.C. Khoo, D.H. Werner, X. Liang, A. Diaz. *Optics Letters*, 31, 2592, (2006).

18. S. Zhang, Y.S. Park, J. Li, X. Lu, W. Zhang, X. Zhang. *Phys. Rev. Lett.*, 102, 023901, (2009).

19. V.A. Podolskiy, A.K. Sarychev, V.M. Shalaev. *J. Nonlinear Optical Phys. and Mater. Sci*, 11, 65, (2002).

20. V. Podolskiy, A. Sarychev, V. Shalaev. *Optics Express*, 11, 735, (2003).

21. V. Shalaev, W. Cai, U.K. Cettiar, H.K. Yuan, A.K. Sarychev, V.P. Drachev, A.V. Kildishev. *Optics Letters*, 30, 3356, (2005).

22. S. Linden, C. Enkrich, M. Wegener, J. Zhou, T. Koschny, C.M. Soukoulis. *Science*, 306, 1351, (2004).

23. S. Zhang, W. Fan, B.K. Minhas, A. Frauenglass, K.J. Malloy, S.R.J. Brueck. *Phys. Rev. Lett.*, 94, 037402, (2005).

24. D.R. Smith, W.J. Padilla, D.C. Vier, S.C. Nemat-Nasser, S. Schultz. *Phys. Rev. Lett.,* 84, 4184, (2000).

25. J.D. Baena, L. Jelinek, R. Marques. *Phys. Rev. B*, 76, 245115, (2007).

26. C. Lapointe, T. Mason, I.I. Smalyukh. *Science,* 326, 1083, (2009).

27. N. Liu, H. Liu, S. Zhu, H. Giessen. *Nature Photonics, 3*, 157, (2009).

28. C. Lapointe, S. Hopkins, T.G. Mason, I.I. Smalyukh. *Phys. Rev. Lett.,* 105, 178301, (2010).

29. I.I. Smalyukh. *Proc. Nat. Acad. U.S.A.,* 107*,* 3945, (2010).

30. R. Pratibha, W. Park, I.I. Smalyukh. *J. Appl. Phys.,* 107, 063511, (2010).

31. R. Pratibha, K. Park, I.I. Smalyukh, W. Park. *Optics Express*, 17, 19459, (2009).

32. I.C. Khoo, D.H. Werner, X. Liang, A. Diaz. *Optics Letters., 31*, 2592, (2006).

33. K.J. Stebe, E. Lewandowski, M. Ghosh. *Science, 325*, 159, (2009).

34. A. Swami, P.R. Selvakannan, R. Pasricha, M. Sastry. *J. Phys. Chem. B., 108*, 19269, (2004).

35. M. Fukuto, R.K. Heilmann, P.S. Pershan, A. Badia, R.B. Lennox. *J. Chem. Phys., 120*, 3446, (2004).

36. R. Shenhar, T.B. Norsten, V.M. Rotello. *Advanced Materials*, *17*, 657, (2005).

37. J. Perez-Juste, B. Rodrigues-Gonzalez, P. Mulvaney, L. Liz-Marzan. *Adv. Funct. Mater.*, 15, 1065, (2005).

38. R. Elghanian, J.J. Storhoff, R.C. Mucic, R.L. Letsinger, C.A. Mirkin. *Science, 277*, 1078, (1997).

39. T. Hegmann, H. Qi, V.M. Marx. *J. Inorg. Organomet. Polym. Mater.*, *17*, 483, (2007).

40. J. Perez-Juste, L.M. Liz-Marzan, S. Carnie, D.Y.C. Chan, P. Mulvaney. *Adv. Funct. Mater.*, *14*, 571, (2004).

41. M.D. Lynch, D.L. Patrick, D.L. *Nano Letters*, 2, 1197, (2002).

42. J.L. Baker, A. Widmer-Cooper, M.F. Toney, P.L. Geissler, A.P. Alivisatos. *Nano Letters*, 10, 195, (2010).

43. C. Sonnichsen, A.P. Alivisatos. *Nano Letters, 5*, 301, (2005).

44. W. Ahmed, E.S. Kooij, A. van Silfhout, B. Poelsema. *Nano Letters,* 9, 3786, (2009).

45. S. Zhang, G. Leem, L. Srisombat, T.R. Lee. J. *Am. Chem. Soc.*, *130*, 113, (2008).

46. B. Halle, P.O. Quist, I. Furó. *Phys. Rev. A*, *45*, 3763, (1992).

47. K.J. Wu, K.C. Chu, C.Y Chao, Y.F. Chen, C.W. Lai, C.C. Kang, C.Y. Chen, P.T. Chou. *Nano Letters,* 7, 1908, (2007).

48. K.T. Yong, Y. Sahoo, M. Swihart, P. Prasad. *Advanced Materials,* 18, 1978, (2006).

49. H. Yoshida, Y. Tanaka, K. Kawamoto, H. Kubo, T. Tsuda, A. Fujii, S. Kuwabata, H. Kikuchi, M. Ozaki. *Applied Physics Express*, 2, 121501, (2009).

50. J. Lydon. *Current Opin. Colloid & Interface Sci.* 3, 458, (1998).

51. A.V. Kachynski, A.N. Kuzmin, P.N. Prasad, I.I. Smalyukh, I.I. *Optics Express,* 16, 10617, (2008).

52. A. Kachynskii, A. Kuzmin, P.N. Prasad, I.I. Smalyukh. *Appl. Phys. Lett.,* 91, 151905, (2007).

53. I.I. Smalyukh, D. Kaputa, A.V. Kachynski, A.N. Kuzmin, P.N. Prasad. *Optics Express,* 15, 4359, (2007).

54. P.S. Salter, G. Carbone, E.J. Botcherby, T. Wilson, S.J. Elston, E.P. Raynes, E. P. *Phys. Rev. Lett.* 103, 257803, (2009).

55. I.I Smalyukh, S. Shiyanovskii, O.D. Lavrentovich. *Chem. Phys. Lett.* 336, 88-96, (2001).

56. T. Lee, R.P. Trivedi, I.I. Smalyukh. *Opt. Lett., 35 3447,* (2010).

57. A. Xie, D.A. Higgins. *Appl. Phys. Lett.* 84, 4014, (2004).

58. M.J. Rust, M. Bates, X. Zhuang. *Nature Methods,* 3, 793, (2006).

59. E. Betzig, G.H. Patterson, R. Sougrat, O.W. Lindwasser, S. Olenych, J.S. Bonifacino, M.W. Davidson, J. Lippincott-Schwartz, H.F. Hess. *Science,* 313, 1642, (2006).

60. P.N. Prasad. *Nanophotonics*. Wiley: Hoboken, US, (2004).

61. M. Grzelezak. J. Juste, P. Mulvaney, L. Liz-Marzan. *Chem. Soc. Rev*., 37, 1783, (2008).

62. M. Brust, M. Walker, D. Bethell, D. Schiffrin, R.J. Whyman. J. *Chem. Soc., Chem. Commun.*, 801, (1994).

63. C. Murphy, T. Sau, A. Gole, C. Orendorff, J. Gao, L. Gou, S. Hunyadi, T.J. Li. *Phys. Chem. B*, 109, 13857, (2005).

64. C. Wang, T. Wang, Z. Ma, Z. Su. *Nanotechnology*, 16, 2555, (2005).

65. N.R. Jana, L. Gearheart, C.J. Murphy. *Langmuir*, 17, 6782, (2001).

66. B. Nikoobakht, M.A. El-Sayed. *Chem. Mater.,* 15, 1957, (2003).

67. B. Pietrobon, V. Kitaev. *Chemistry of Materials*, 20, 5186, (2008).

68. S. Chandran, M. Chaudhary, R. Pasricha, A. Ahmad, M. Sastry. *Biotechnol Prog.*, 22, 577, (2006).

69. J.S. Clawson, G.P. Holland, T.M. Alam. *Phys. Chem. Chem. Phys.*, 8, 2635, (2006).

70. G. Montalvo, M. Valiente, E.J. Todenas. *Colloid Interface Sci*., 172, 494, (1995).

71. M. Zapotocky, L. Ramos, P. Poulin, T.C. Lubensky, D.A. Weitz. *Science*, 283, 209, (1999).

72. I. Koltover, T. Salditt, J.O. Radler, C.R. Safinya. *Science*, 281,78, (1998).

73. P. Poulin, H. Stark, T.C. Lubensky, D.A. Weitz. *Science* 275, 1770, (1997).

74. T.C. Lubensky, D. Pettey, N. Currier, H. Stark. *Phys Rev E* 57, 610, (1998).

Chapter 3: Biosynthesis of high-aspect ratio colloidal gold nanoplatelets and their alignment in nematic liquid crsytals

Adapted from: *J. Appl. Phys.* **110**, 033535 (2011)

Chapter overview

In the previous chapter we described the potential applications of LC nanoparticle composites and the feasibility and challenges associated with producing highly concentrated nanorod dispersions. In this chapter we study elasticity-mediated alignment of highly anisotropic gold platelets in liquid crystals to better understand the elastic forces associated with micro and nano scale colloids. Colloidal gold particles of controlled shapes (spheres, rods, and polygonal platelets) and sizes are prepared using biosynthesis techniques with varying solvent conditions. When introduced into liquid crystalline structured solvents, these gold particles impose tangential or vertical surface boundary conditions for the liquid crystal molecules or building blocks such as chromonic molecular aggregates. This allows for multiple types of their controlled alignment in both lyotropic and thermotropic liquid crystals and is of interest for self-assembly-based fabrication of tunable nanostructured composite materials.

3.1. Introduction

Composite materials comprised of nano-sized and micro-sized colloidal particle dispersions in structured host media have attracted a great deal of interest [1-10]. The plasmonic properties of noble metallic particles make them desirable structural units of a number of novel composites

such as optical metamaterials [11-14]. In these artificial materials, also often referred to as “left-handed materials” [11-14], ordered structures of predesigned anisotropic nanoparticles play the role of ‘‘building blocks’’ similar to that of molecules and atoms in conventional matter [13], allowing for the engineering of unprecedented properties not encountered in naturally occurring materials [14], such as negative refractive index. Control of particle shape and size is essential for engineering the needed surface plasmon resonance (SPR) properties for the development of optical and near-infrared metamaterials. The synthesis of functionalized spheres through thiol linkages [15], the seed-mediated growth of nanorods,[16] and a variety of polyhedral and platelet-shaped [17] particle syntheses are well understood and broadly used, although obtaining micro-sized gold colloids through conventional wet chemical synthesis is limited by the high density of gold (causing sedimentation of larger particles due to gravity) and rarely accomplished. [15-21] Previous studies have shown that aqueous solutions of a variety of polyol containing biological materials such as Aloe Vera extract,[18] Bovine Serum Albumin,[19] Lemon Grass extract,[20] and Cellulose [21] provide effective means for obtaining gold triangular platelets of various lateral sizes and thicknesses. Post-synthetic manipulation of morphology has been described previously in the context of many-particle to one-particle transformation through lengthy refluxing.[22] However, the potential uses of biosynthesized gold nanoparticles to form tunable and reconfigurable nanostructured composites have not been explored. This is despite of the fact that they are of particular interest for such applications because of the simplicity of synthesis and the feasibility of obtaining nanoparticles with a broad range of controlled shapes and sizes.

In this chapter, we report dispersion of high-aspect ratio biosynthesized gold platelets in both thermotropic and lyotropic liquid crystals (LCs). We manipulate particles' shapes and sizes

through redispersion in different solvents and show that the gold platelet particles can impose both tangential and vertical surface boundary conditions for the liquid crystalline molecular alignment. This allows for several different types of elasticity-mediated self-alignment of polygonal gold platelets in LC host fluids, which are of interest and importance for both fundamental and applied research on LC colloidal dispersions.

3.2. Materials and Methods

3.2.1 Preparation of gold nanoparticles

A typical gold particle synthesis was performed by dissolving 3.9 mg of gold(III) chloride hydrate in 9 mL of the solvent, adding 1mL of aqueous Aloe Vera extract solution, and leaving the mixture at room temperature overnight. Aloe Vera extract was prepared by finely cutting 30g of a 2 lb Aloe Vera leaf (obtained from Aloe Farms Inc.) and boiling it in 100mL of deionized water. According to previous studies, the reductant necessary for the nanoparticle synthesis is likely a hydrophilic aldose, or aldehyde, or ketone present in Aloe Vera [17]. The used solvents and gold(III) chloride hydrate were obtained from Sigma Aldrich and used without further purification, except deionized water was obtained from the Barnstead/Thermolyne E-pure system (>17 MΩcm).

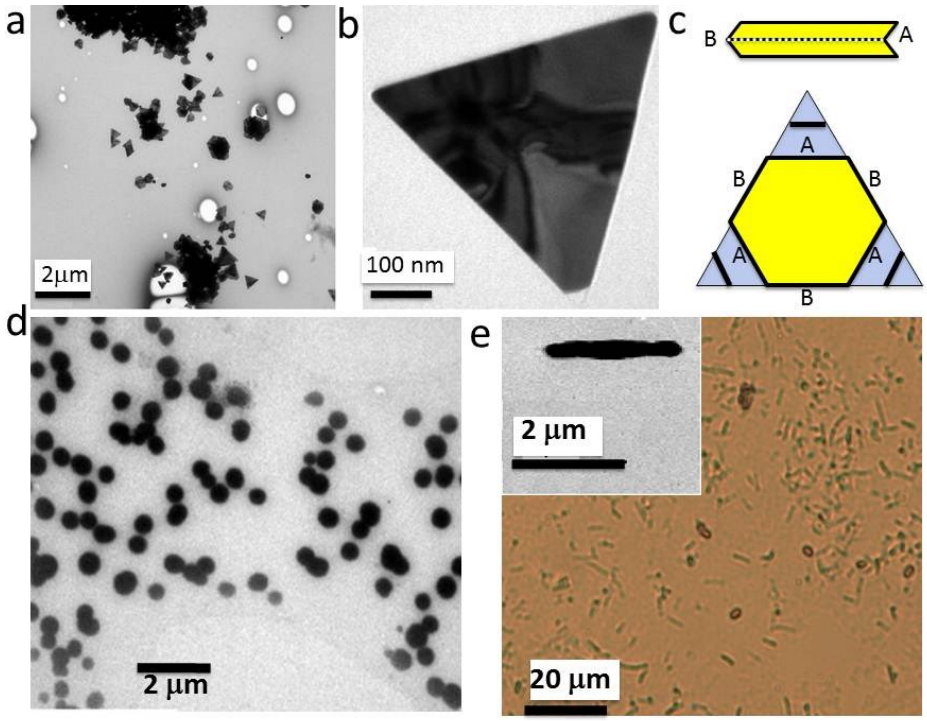

Fig. 3.1. Triangular colloidal platelets synthesized using Aloe Vera and gold(III) chloride hydrate and water, toluene, or ethanol as solvents. a) A large-area image showing colloidal triangles of about 300nm in the lateral dimensions, along with a smaller number of particles of other polygonal platelet shapes and of different sizes obtained by use of water as a solvent. b) a magnified image of a 300 nm triangular platelet similar to the ones shown in (a). c) a schematic showing the single twin growth mechanism responsible for the formation of the triangular platelets; the concave and convex edges of the platelet are marked with "A" and "B", respectively. The gray regions and lines illustrate the kinetics of the nanoparticle growth process. d) Colloidal spheres of about 150 nm in diameter grown in toluene. e) Colloidal gold rods of about two micrometers in length grown in ethanol.

During the nanoparticle synthesis, we used water as the solvent to produce 300nm by 5nm triangles and hexagons (Fig. 3.1(a,b)), following the procedure previously reported by Sastry *et al.* [18,20] Using toluene instead of water produces 150nm spheres (Fig. 3.1(d)) and using ethanol produces 2 μm by 300nm rods (Fig 3.1(e)). Using methanol as the solvent produces highly polydisperse triangles, hexagons, and nonagons (Fig 3.2(a)) with 5nm thickness (Fig. 3.2(b,c)) and side lengths up to 10 microns. These platelets appear to be relatively rigid in solution as thermal fluctuations of their shape (when dispersed in a solvent) are not readily

observable. Triangular platelets are formed when there is one twinning plane parallel to the plane of the platelet resulting in one set of fast growing concave edges marked by "A" in Fig. 3.1(c), following the silver halide model [17,23]. Hexagonal platelets are the result of two twinning planes yielding more highly symmetric growth [17,23] (Fig. 3.2(e)). The nonagons are likely the result of particle growth with three twinning planes producing one doubly concave edge and one singly concave edge (Fig. 3.2(f)). In the primary growth phase the doubly concave edge grows faster which results in an asymmetric hexagonal shape (Fig. 3.2(c)). Upon filling the original concavities the doubly concave edges become singly concave, which allows for a secondary growth that produces the final nonagon shape (Fig. 3.2(g)). This secondary growth is occurring only from the central twinning plane; it does not follow the overall crystallography of the particle and can result either in relatively small triangular platelet growths off of three sides (Fig. 3.2(c)), or proceed further to produce nonagons, or go to completion to produce non-equilateral hexagons (Fig. 3.2(d) inset). The simple replacement of water with less polar solvents in these well understood biosynthesis procedures results in dramatic and robust changes of the obtained particle shapes and sizes.

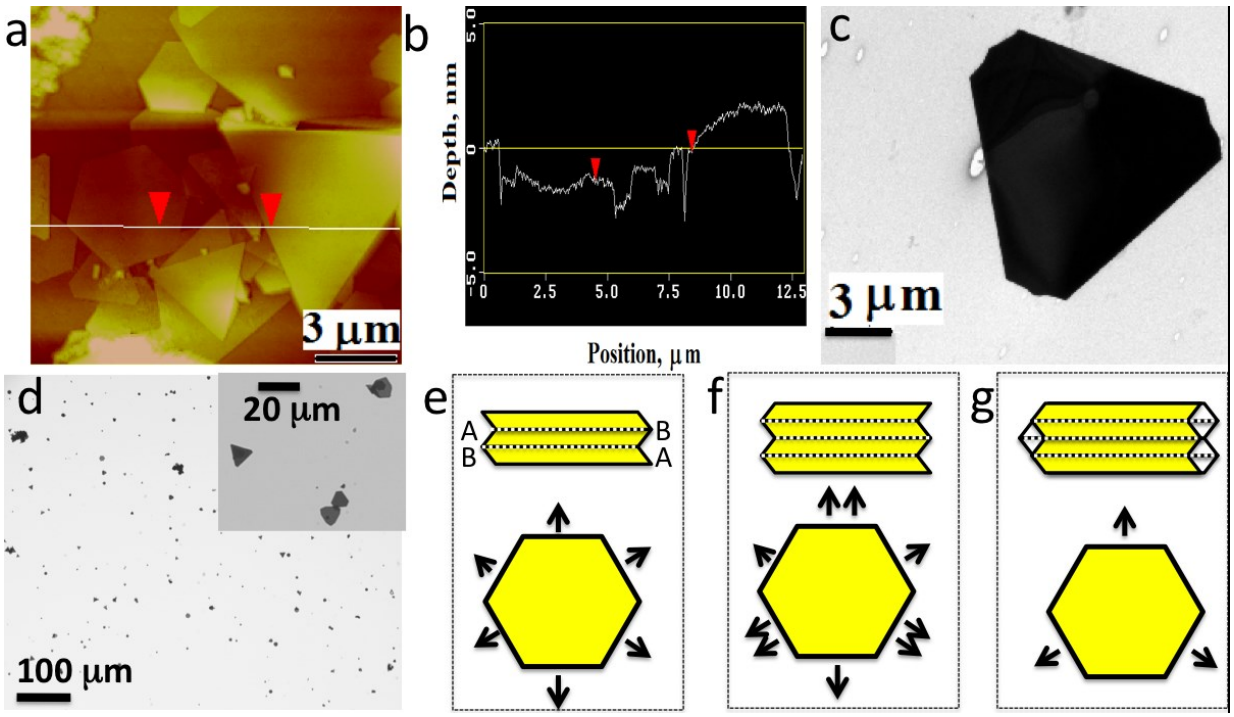

Fig. 3.2. Colloidal platelets obtained by use of methanol as a solvent. a) AFM image of the surface profile and b) the depth profile across the platelets indicate that the polygonal particles are about 5nm in thickness. c) Enlarged image of a colloidal platelet. d) Optical micrograph showing predominantly colloidal triangles (with some hexagons and nonagons) obtained after drying the dispersion on a glass cover slide. Schematic illustrations of the e) double-twinned growth mechanism of hexagons, f) triply twinned primary growth mechanism of non-equilateral hexagons, and g) secondary growth on triply twinned particles that yields nonagons or non-equilateral hexagons.

3.2.2 Characterization

Transmission electron microscopy (TEM) imaging samples are prepared by pipetting 2 µl of solution onto a formvar coated copper grid. TEM characterization is performed using a Philips CM10 system with an accelerating voltage of 80kV. For the atomic force microscopy (AFM) imaging, the samples are prepared by drying 2 µL of the solution on a silica wafer. AFM images are obtained using a Digital Instruments' Nanoscope III with non-conductive silicon nitride contact mode tips from Veeco (model MLCT-AUHX). The vertical displacement profiles are measured using AFM in the contact imaging mode. For example, representative AFM images of

gold platelets reveal that their thickness is about 5 nm (Fig. 3.2(a,b)). Optical images are obtained in bright field and polarizing imaging modes using the Olympus BX51 upright polarizing optical microscope. To obtain optical micrographs, we also use Spot 14.2 Color Mosaic Camera (from Diagnostic Instruments, Inc.) and microscope objectives with magnifications of 10, 20, and 50x of numerical aperture NA=0.1-0.5 (Olympus). For optical imaging, dispersions of particles are either dried on glass microscope slides or imaged directly in the dispersions in the bulk of glass cells. SEM samples are prepared by drying 5 μL of the dispersion on a silica wafer. Scanning Electron Microscopy (SEM) images were taken by use of JSM-6480LV SEM operating in high vacuum mode with 5 kV accelerating voltage.

3.2.3 Liquid Crystal Sample Preparation

The studied samples were designed to probe alignment of gold nanoparticles in the bulk and at surfaces of both thermotropic and lyotropic liquid crystals. The room-temperature thermotropic nematic LC mixture E31 is purchased from EM Industries and used as supplied. The lyotropic chromonic LCs are formed by solutions of cromolyn (from Sigma, purified by use of filters with pore size of 0.2 μm) in deionized water at 13-14 wt.% to insure a room-temperature nematic phase. By means of solvent drying and solvent exchange, the polygonal platelets are introduced into the thermotropic nematic LC mixture E31 and the water-based lyotropic chromonic LC mixture.

To study gold nanoparticles in the LC bulk, the glass cells are prepared using 1mm-thick plates separated by spherical spacers to set the cell gap within the range of 10-20 μm and sealed using epoxy. The glass cells are then infiltrated with LC dispersions using capillary action. For vertical (homeotropic) surface alignment of the director of thermotropic LCs, we treat confining

substrates of the cells with [3-(trimethoxysilyl)propyl]octadecyl-dimethylammonium chloride (DMOAP, obtained from Aldrich). The other cells where formed using plasma-cleaned glass plates without further treatment.

In the experiments designed to probe platelet alignment at LC surfaces, 5 µl of an aqueous dispersion of polygonal platelets is placed atop of a thin layer of glycerol (obtained from Aldrich) so that, after water-glycerol mixing, some particles are trapped at the glycerol-air interface with orientation of their large-area faces parallel to the interface. Upon placing a 2 µl droplet of E31 atop of the glycerol, the platelets remained confined at the LC-glycerol interface and their alignment and stability was explored using optical microscopy.

3.3. Results and Discussion

3.3.1. Self-alignment of anisotropic nanoparticles in liquid crystals

The biosynthesized polygonal platelets impose vertical boundary conditions for the thermotropic nematic LC director [24]. In a homeotropic cell of E31, the colloidal platelets align with their large-area faces orthogonally to the vertical (homeotropic) far-field director, as shown in Fig. 3.3 for the case of a triangular particle. A particle induces a disclination loop encircling it in the plane of the platelet. In some places around the platelet, the defect loop is pinning to the platelet's edge, thus transforming into a surface disclination, and then becoming a bulk defect line again. The details of director distortions around such a platelet will need to be explored further, however, experiments suggest that the observed defect line is a half-integer disclination of strength s=-1/2, as shown in the schematic drawing in Fig. 3.3(d). A similar disclination loop, also known as a "Saturn ring" defect line [2], can be observed around spherical particles with vertical boundary conditions. [2,30] Because of the homeotropic surface anchoring, the

alignment of the thin gold platelet with the large-area faces orthogonal to the far-field director and the observed disclination loop are expected to correspond to the minimum-elastic-energy alignment and director structure. Since the normal vector of the platelet plane is parallel to **n**(**r**), the induced director distortions ideally have the D_N symmetry of the polygonal platelet with N edge faces. However the spontaneous pinning of the defect line to the edge faces of the platelet may break the D_N symmetry. This spontaneous formation of topological defect lines around the colloids could lead to qualitatively different elasticity- and defect-mediated modes of colloidal self-assembly than those seen for platelets with tangential boundary conditions [25, 26] and spherical particles [1, 2, 27]. From the elastic energy standpoint, the orientations of the gold triangular platelets with the induced distortions around them are invariant with respect to rotations around an axis parallel to the far field director and orthogonal to the platelet's large-area faces.

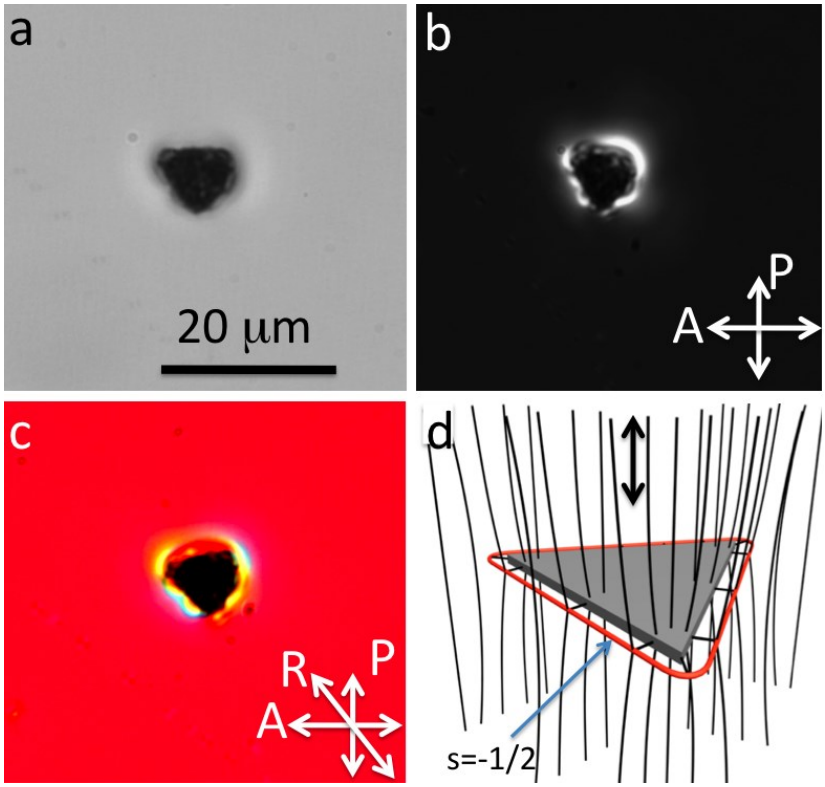

Fig. 3.3 Triangular platelet of gold in the bulk of a thermotropic nematic LC mixture E31. a-c) co-located optical microphotographs of a triangular platelet in a homeotropic LC cell filled with E31 obtained in a) bright-field transmission microscopy mode, b) polarizing microscopy mode between crossed polarizer labeled as "P" and analyzer labeled as "A", and c) polarizing microscopy mode with an additional retardation plate labeled "R" inserted at 45 degrees between the crossed polarizers. d) a schematic showing **n**(**r**)-structure around a triangular platelet encircled by a loop of a disclination of strength s=-1/2; the platelet self-aligns orthogonally to the far-field LC director marked by a black double arrow.

Alignment of similar gold platelets in a lyotropic chromonic LC has qualitatively different features from that in a thermotropic LC discussed above (Fig. 3.4): (a) bulk defects around the particles are not observed and (b) boundary conditions for **n**(**r**) imposed by platelet surfaces are tangential. Observation of many particles in a sample with non-uniform texture and director distortions on the scales much larger than the size of the particles leads to the conclusion that thin triangular platelets (Fig. 3.4(a)) align with the large-area faces parallel to the far-field director, barely perturbing local **n**(**r**) at their edges (Fig. 3.4(b)). Although the system of a

platelet nanoparticle in the LC does not have rotational symmetry with respect to the normal to the large-area faces of the platelet, the elastic energy cost of director distortions at the edge faces of 5nm-thick platelets is relatively small. Therefore, the observed rotations of such a platelet around the axes marked by red double arrows shown in Fig. 3.4(a) preserve the alignment of the large-area faces parallel to the far-field director (black double arrow in Fig. 3.4(a)) but show no specific alignment of the edge faces with respect to the far-field director. This is likely due to the fact that the changes of bulk elastic and surface anchoring energies associated with the rotations of such a 5nm-thick platelet around the normal to the large-area faces are comparable or smaller than the thermal energy.

A schematic in Fig. 3.4(c) shows a thicker triangular platelet with edge faces inducing well-defined boundary conditions for the **n**(**r**): the orientations that minimize the overall free energy require the large-area faces and one edge face aligning parallel along the **n**(**r**), similar to the case of our previous studies on lithographically generated polygonal platelets. [25] The ensuing **n**(**r**)-distortions have dipolar symmetry dictated by the boundary conditions at the surfaces of the faceted particle with low-symmetry shape.[25] The elastic dipole moment of a structure shown in Fig. 3.4(c) is aligned orthogonally to the far-field director and its orientation is invariant with respect to the rotations around the axis parallel to the far-field director and one edge face. Although an instantaneous elastic dipole can be defined also for the structure shown in Fig. 3.4(a), its orientation with respect to the far-field director is not stable, unlike in the case of the other dipolar structure shown in Fig. 3.4(c). The experimental optical micrographs shown in Fig. 3.4(d-f) suggest that both aligned and unaligned with **n**(**r**) elastic dipoles due to triangular platelets (Fig. 3.4(c) and Fig. 3.4(a), respectively) can be observed in a very same lyotropic LC sample. Generalizing these observations and analysis to particles of other shapes, polygonal gold

platelets with an even number of edge faces (hexagons) are expected to induce quadrupolar distortions of **n**(**r**), while the ones with an odd number of edge faces (triangles and nonagons), induce dipolar distortions. This is reminiscent of the behavior of lithographically generated polygonal platelets that we studied previously, [25, 26] however, the ability of inducing homeotropic surface boundary conditions for **n**(**r**) (in addition to tangential ones) as well as much larger aspect ratios of platelet's lateral sizes to their thickness, allow one to achieve several new types of platelet alignment in the LC bulk with respect to the uniform far-field director, as shown in Figs. 3.3 and 3.4. The thicker platelets interact with elastic distortions in unaligned LC samples (Fig. 3.4(d-f)), which may provide means for their spatial patterning in LCs by use of deliberately introduced elastic distortions by means of surface treatment and topography, external fields, light, etc.

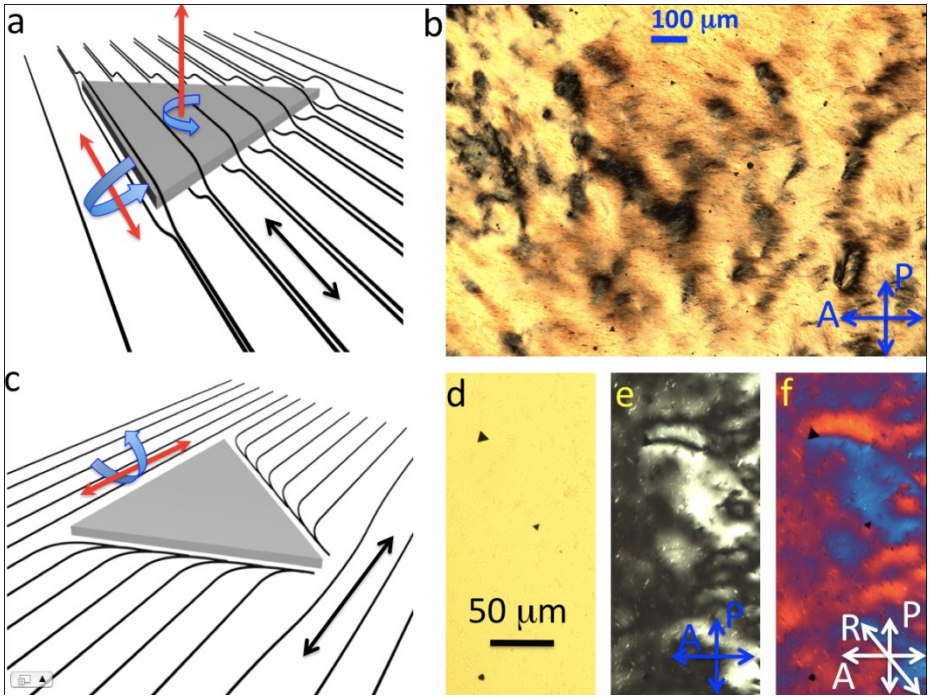

Fig. 3.4. Gold polygonal platelets of varying lateral size and thickness in a lyotropic chromonic LC of the aqueous solution of cromolyn. a) a schematic illustration showing a thin triangular platelet aligning with the large-area faces parallel to the far-field director and barely perturbing the director field at its edge faces; the allowed rotations of the platelet around the axes marked by red double arrows preserve the alignment of the large-area faces parallel to the far-field director (marked by the black double arrow). b) polarizing microscopy texture of the LC-sample with non-uniform **n**(**r**) obtained between crossed polarizer "P" and analyzer "A" and showing polygonal platelets at orientations having large-area faces following **n**(**r**). c) a schematic showing a triangular platelet with edge faces inducing a well-defined tangential surface anchoring; the orientations that minimize the overall free energy require that the large-area faces and one edge face align parallel to **n**(**r**). Transmission optical microscopy images obtained in d) bright field mode, polarizing microscopy modes with e) crossed polarizer and analyzer and f) with an additional retardation plate (marked "R") between the polarizers; the images show that the largest platelet is co-located with the deformed **n**(**r**) while the two smaller ones do not induce detectable distortions of **n**(**r**), similar to the schematics shown in c) and a), respectively.

An interesting open question is whether the elasticity-mediated forces between platelets (due to the elastic distortions that they induce) can be utilized for colloidal self-assembly? Because of the small thickness of gold platelets, both dipolar and quadrupolar elastic interaction between platelets of different shapes having tangential surface anchoring are expected to be weak, overcoming thermal fluctuations only at small distances. This is due to the weak elastic

distortions induced by such thin particles, reminiscent of weak elastic interactions between rod-like nanoparticles studied previously [28]. Consequently, self-assembled structures of such aligned polygonal platelets in the studied LCs are not observed (Fig. 3.4(b,e-f)). Since biosynthesized gold triangular platelets reported in the literature have thicknesses of 3-8 nm when obtained using Aloe Vera [18], 15-20 nm when using Lemon Grass [20] and Bovine Serum Albumin [19] and 200-800 nm when using Cellulose [21], their dispersions in chromonic LCs is a good system for exploring how inter-particle interactions and their self-assembly depend on thickness and aspect ratio of these platelets.

The platelets residing at the interface of glycerol and thermotropic LC E31 impose tangential surface boundary conditions for the director at the large-area faces (Fig. 3.5). This is a likely consequence of the platelets being "coated" by glycerol (known to produce tangential surface anchoring [2]), which may also explain the long-term-stability of these platelets at the interface of polar glycerol and nonpolar LC. Colloidal assembly and defect transformations around spherical colloidal particles have recently attracted a great deal of attention because of the possibility of chemo-responsive control of colloidal interactions that can be tuned from dipolar attractive to repulsive.[29,30] The used polygonal platelets can produce weak director distortions of both dipolar and quadrupolar symmetry, however, they do not exhibit a well defined alignment with respect to the far-field director at the interface, because of the weak coupling of $\mathbf{n}(\mathbf{r})$ to the glycerol-submerged edge faces of the particles. However, the platelets at the interface of glycerol and a LC droplet with concentric configuration of $\mathbf{n}(\mathbf{r})$ often tend to localize either in the center of the droplet (Fig. 3.5), a location of the surface point defect (the so-called boojum) induced by the geometry of the director pattern in the droplet, or next to the droplet's contact

line.

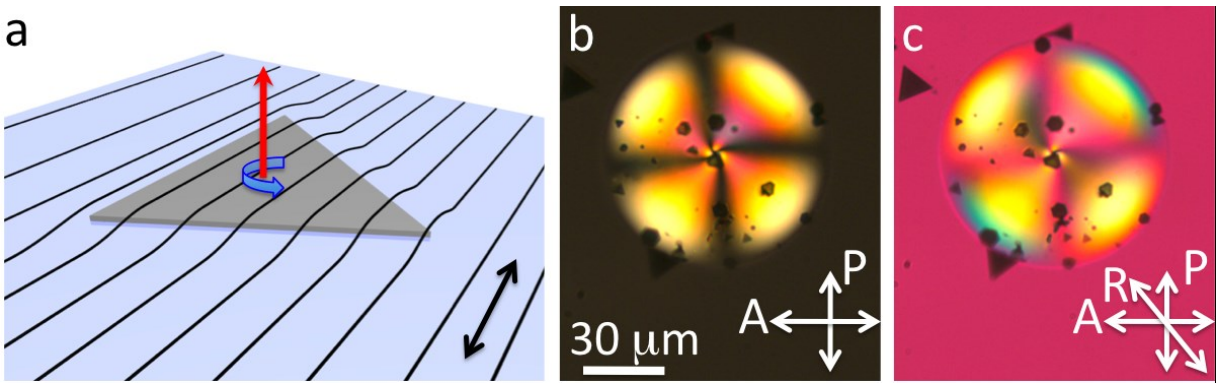

Fig. 3.5. Gold polygonal platelets at the thermotropic LC-glycerol interface. a) a schematic showing a platelet partially submerged in glycerol that induces tangential surface boundary conditions for **n**(**r**) and barely perturbs the uniform director structure; since the free energy cost of rotations around the red axis orthogonal to the platelet is small, the platelets are found at various possible orientations of their edges with respect to **n**(**r**). b,c) polarizing optical microscopy textures obtained for a sample between crossed polarizer "P" and analyzer "A" b) without and c) with an additional retardation plate "R"; the platelets within and outside of the area covered by a small LC droplet display arbitrary orientations of edge faces while having their large-area faces parallel to the LC-glycerol interface.

Our studies of biosynthesized gold platelets in the bulk and at surfaces of LCs suggest the possibility of controlling surface boundary conditions for molecular alignment in LCs and may further expand the possible use of elasticity-mediated alignment, [25, 26, 28, 33] electrical and magnetic switching [26,28], and assembly of complex-shaped particles in liquid crystals [25]. These self-alignment studies may be expanded to the case of other biosynthesized gold particles with anisotropic shapes, such as rods and ribbons (Figs. 3.1 and 3.6). In particular, rod-shaped gold colloids that induce tangential surface anchoring boundary conditions for the LC have been observed to align along the far-field director, consistent with the literature observations [28,31]. Possible applications of LC-gold nanoparticle composites include the design and fabrication of self-assembled optical metamaterials and enhancement of conversion efficiencies of solar energy to electricity in organic-inorganic hybrid solar cells [25, 26, 28, 30, 32-36].

3.3.2 Shape stability of nanoparticles

Since particles of different size and shape are naturally produced by different solvent conditions, it is important to consider the effects of changing solvents when preparing LC-nanoparticle composites. This is especially important since the redispersion of these nanoparticles into LCs often requires involving intermediate solvents. We observe that, upon phase transfer, single nanoparticles can change shape and maintain their size or retain both shape and size (Fig. 3.6). For example, the methanol synthesized microtriangles are stable for several days in water, glycerol (Fig. 3.6(d)), and chromonic LCs. The shapes of methanol-synthesized gold platelets are also short-term stable (for about one day, typically becoming somewhat rounded after several days and eventually spherical) in the bulk of thermotropic and rather nonpolar E31 nematic mixture. However, transferring 300 nm by 3-8 nm equilateral triangular platelets [18] (Fig. 3.1(a,b)) from water into ethanol results in the formation of 400-700 nm by 20 nm rods (Fig. 3.6(a,b)). These rods have similar volumes to the starting nanotriangles, which suggests individual particle-to-particle shape transformations. The fact that the particles become rods of a different size than the rods obtained directly via synthesis in ethanol further supports the hypothesis that this is an individual particle transformation process.

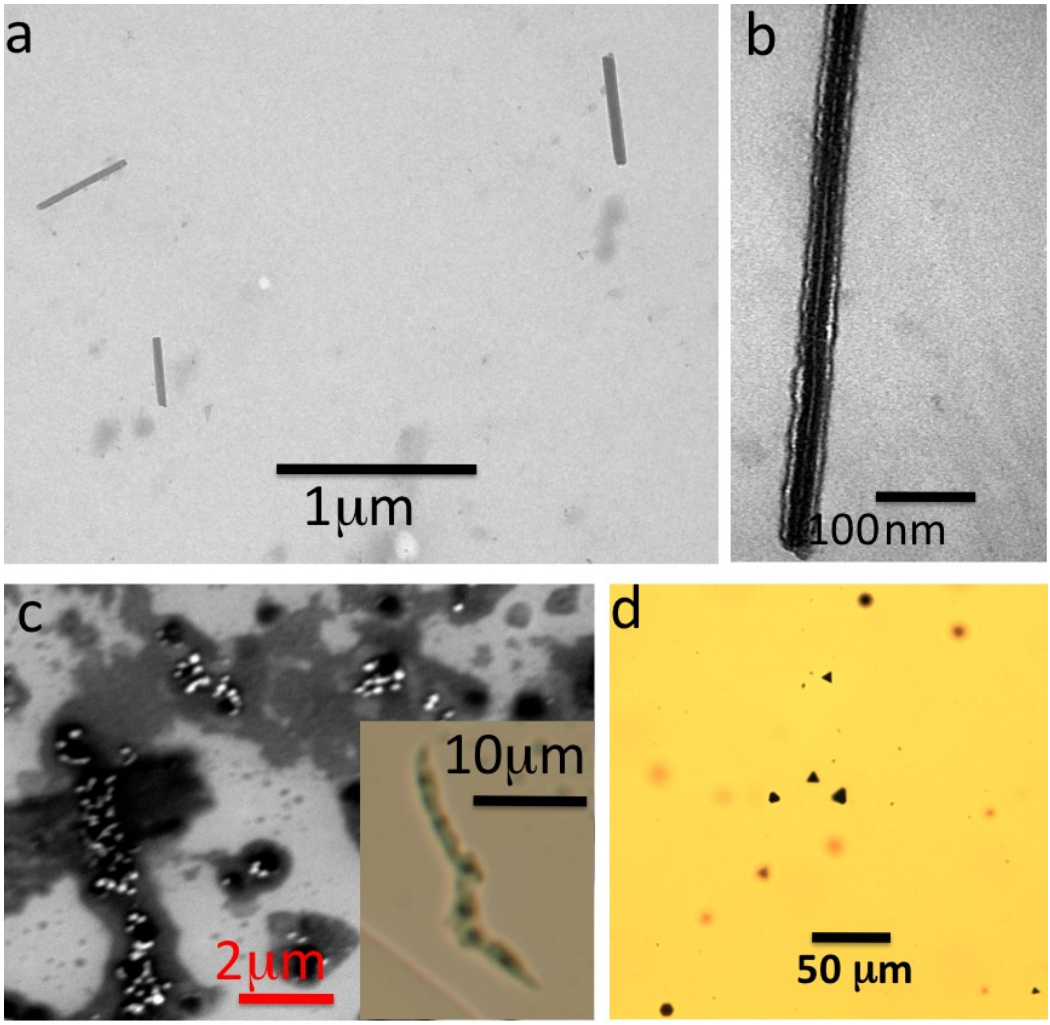

Fig. 3.6. Post-synthetic shape stability of gold particles in different solvents. a) a TEM image of 700nm x 20nm rods obtained by re-dispersing 300 nm triangular platelets in ethanol. b) A high-magnification TEM image of a single 700nm x 20nm rod showing a well pronounced line along its center. c) a SEM image showing colloidal gold spheres originally obtained in toluene that aggregate in an anisotropic fashion when redispersed in ethanol to eventually produce ribbons optical micrograph of which is shown in the inset. d) optical micrograph showing that the shape of polygonal colloidal platelets remains intact when the platelets are re-dispersed from methanol to glycerol.

Transferring particles from toluene to ethanol appears to produce ribbons (inset of Fig. 3.6(c)). We have used Scanning Electron Microscopy to get insights into the process of formation of these ribbons. Similar to the process described in the literature [37], we see that at the onset of the ribbon formation, several spheres assemble in an anisotropic fashion to eventually transform

into the ribbon (Fig. 3.6(c)). Although the apparent shape plasticity of some of the used biosynthesized nanoparticle systems may be a limitation from a device development standpoint (since well defined shapes easily change with changing solvents), it can be also purposefully utilized in the design of structured composites, provided that these shape transformations are well understood and controlled.

3.4. Conclusions

To conclude, we have demonstrated that biosynthesized particles of desired shapes can be dispersed in liquid crystal host fluids and can impose well-defined vertical or tangential surface boundary conditions for the molecular alignment. These well-defined tangential or vertical boundary conditions, in turn, allow for achieving several different types of controlled long-range self-alignment of the anisotropic colloids in the bulk of LCs directed by the long-range orientational order of these anisotropic fluids that are of interest for the design of novel composite materials and metamaterials [25, 26, 28, 36]. We also show that the biosynthesized Aloe Vera capped nanoparticles show extraordinary shape plasticity as a function of solvent but can also be dispersed in certain liquid crystalline and other solvents without the shape transformation.

3.5 REFERENCES

1. P. Poulin, H. Stark, T.C. Lubensky and D.A. Weitz. *Science* **275,** 1770 (1997).

2. H. Stark. *Phys Rep,* **351,** 387 (2001).

3. P. Poulin and D.A. Weitz. *Phys. Rev E* **57,** 626 (1998).

4. C. L. van Oosten, C. W. M. Baastiansen, and D. J. Broer *Nature Mater*. **8** 677-682 (2009).

5. I.I. Smalyukh, A.V. Kachynski, A.N. Kuzmin, and P.N. Prasad. *Proc. Nat. Acad. U.S.A.* **103**, 18048 (2006).

6. Y. Gu and N.L. Abbot, *Phys. Rev. Lett.* **85**, 4719 (2000).

7. C.D. Santangelo and R.D. Kamien. *Phys. Rev. Lett.* **91**, 045506-1 (2003).

8. S. J. Woltman, D. G. Jay, and G. P. Crawford. *Nature Mater.* **6**, 929-938 (2007).

9. J. Yamamoto and H. Tanaka. *Nature Mater.* **4**, 75-80 (2005).

10. I.I. Smalyukh, Y. Lansac, N. Clark, R. Trivedi. *Nature Mater.* **9**, 139-145 (2010).

11. N. Engheta. *Science* **317**, 1698 (2007).

12. V. G. Veselago. *Sov. Phys. Usp.* **10**, 509 (1968).

13. D. A. Pawlak, *et al. Adv. Funct. Mater.* **20**, 1116-1124 (2010).

14. J. B. Pendrey. *Phys. Rev. Lett.* **85**, 3966 (2000).

15. M. Brust, M. Walker, D. Bethell, D. Schiffrin, R. Whyman. *J. Chem. Soc. Chem. Commun.,* 801-802 (1994).

16. C. Murphy, T. Sau,A. Gole, C. Orendorff, J. Gao, L. Gou, S. Hunyadi, T. Li. *J. Phys. Chem. B* **109***,* 13857-13870 (2005**).**

17. M. Grzelezak, J. Juste, P. Mulvaney, L. Liz-Marzan. *Chem. Soc. Rev.* **37**, 1783-1791 (2008).

18. S. Chandran, M. Chaudhary, R. Pasricha, A. Ahmad, M. Sastry. *Biotechnol Prog.* **22**, 577-583 (2006).

19. J. Xie, J. Y. Lee and D. Y. C. Wang. *J. Phys. Chem. C* **111**,10226 (2007).

20 S. Shankar, A. Rai, B. Ankamwar, A. Singh, A. Ahmad, M. Sastry. *Nature Mater.* **3**, 482-488 (2004).

21. Z. Li, A. Friedrich, A. Taubert. *Journal of Materials Chemistry* **18**, 1008-1014 (2007).

22. S. Stoeva, V. Zaikovski, B. Prasad, B. Stoimenov, C. Sorensen, K. Klabunde. *Langmuir* **21**, 10280-10283 (2005).

23. C. Lofton, W. Sigmund. *Adv. Funct. Mater.* **15**, 1197-1208 (2005)

24. M. Zapotocky *et al.*. *Science* **283**, 209 (1999).

25. C. Lapointe, T. Mason, I.I. Smalyukh. *Science* **326**, 1083-1086 (2009).

26. C. Lapointe, S. Hopkins, T.G. Mason, and I.I. Smalyukh. *Phys. Rev. Lett.* **105**, 178301 (2010).

27. T. Yamamoto, Y. Tabe, and H. Yokoyama. *Colloids and Surfaces A-Physicochemical and Engineering Aspects* **334**, 155 (2009).

28. Q. Liu, Y. Cui, D. Gardner, X. Li, S. He, and I.I. Smalyukh. *Nano Lett.* **10**, 1347-1351 (2010).

29. G.M. Koenig , I.-H. Lin, N.L. Abbott. *Proc. Natl. Acad. Sci. USA* 2010, **107**, 3998–4003.

30. I. I. Smalyukh. *Proc. Nat. Acad. Sci. U.S.A.* **107**, 3945-3946 (2010).

31. I. I. Smalyukh, J. Butler, J. D. Shrout, M. R. Parsek, and G.C.L. Wong. *Phys. Rev. E* **78**, 030701(R) (2008).

32. T. H. Reilly III, R.C. Tenent, T. M. Barnes, K. L. Rowlen, and J. van de Lagemaat. *ACS Nano* **2**, 615-624 (2010).

33. J. C. Johnson, T. H. Reilly III, A. C. Kanarr and J. van de Lagemaat. *J. Phys. Chem. C* **113**, 6871–6877 (2009).

34. H. A. Atwater and A. Polman. *Nature Materials* **9**, 205-213 (2010).

35. M. J. Romero, A. J. Morfa, T. H. Reilly III, J. van de Lagemaat, and M. Al-Jassim. *Nano Lett.*, **9**, 3904–3908 (2009).

36. M. R. Jones, R. J. Macfarlane, B. Lee, J. Zhang, K. L. Young, A. J. Senesi, and C. A. Mirkin. *Nature Mater*. **9**, 913-917 (2010).

37. Y. Tan, J. Lee, D. Wang. *Journal of Physical Chemistry C* **112**, 5463-5470 (2008).

Chapter 4: Discotic Nematic Liquid Crystals of Aqueous, Giant Graphene Oxide Flakes as a host for biosynthetic gold nanoplatelets

Adapted from: *Soft Matter*, **7**, 11154 (2011)

Chapter Overview

In the previous chapter we observed the dispersion of extremely high aspect ratio gold nanoplatelets in conventional liquid crystals. In this chapter we describe novel liquid crystalline gels formed by giant graphene oxide flakes (aspect ratio above 10,000) suspended in water which can potentially serve as a better host material for these gold platelets. As their concentration increases, the flakes undergo transitions from an isotropic dispersion to a biphasic system and then to a discotic nematic liquid crystal. The gel-like liquid crystal displays an unusual defect-free uniform director alignment over hundreds of micrometers. We characterize the nematic order parameter, optical birefringence and elastic properties of this novel mesomorphic system.

4.1 Introduction

Colloidal suspensions of anisotropic particles have been the subject of continued research for over 100 years, owing to their rich variety of liquid crystalline phases and fascinating phase transitions.[1] Initial studies on the orientational ordering, optical, and elastic properties of liquid crystals (LCs) were performed primarily on suspensions of rod-like particles.[2-5] Onsager[4] noted that liquid crystallinity is not restricted to only rod-like building blocks, but should also extend to other anisotropic shapes, like disks and platelets. Experimental realization of disk and platelet LC systems, however, was achieved much later[6] and has been a topic of intense

research since that time.[7-8] In the mid 1960s, mesophases of disk-like molecules were observed during the high temperature carbonization of graphitizable substances such as petroleum and coal tar pitches.[9] Their complex, polydisperse composition, consisting of multi-component polyaromatic molecules, likely impeded a detailed investigation of this naturally occurring "carbonaceous mesophase". The first experimental observation of discotic mesophase in a pure, single-component organic molecule system was reported in 1977 by Chandrasekhar et al.[6] They prepared a number of benzene-hexa-*n*-alkanoates, compounds with rigid aromatic cores and flexible aliphatic side chains, and used optical and X-ray studies to unambiguously demonstrate the existence of discotic LCs.

During the last three decades, more than 50 different organic cores and 3000 derivatives have been shown forming discotic LCs.[8] Most molecules are a single atomic layer thick (thickness h < 1 nm) and a few nanometers in diameter (D), i.e., of typical aspect ratios $D/h \sim 5$. A majority of these aromatic-core based compounds demonstrate columnar discotic LC phases, where strong π-π interactions allow the disk-like molecules to assemble into cylindrical structures which in turn act as mesogens. A nematic mesophase, which is the prevalent mesophase observed in calamitic molecules, is not common among discotic organic molecules.[10] Lyotropic LC phases have been observed in colloidal dispersions of inorganic platelets.[11-13] Isotropic to discotic nematic, and columnar LC phase transitions have been reported in dispersions of several systems including nickel hydroxide[14], gibbsite[15-16], and layered double hydroxide.[17-18] The mineral platelets are typically larger in size ($D \sim$ hundreds of nanometers). However, an accompanying higher thickness often limits the highest achievable aspect ratio to only $D/h \sim 20$.

Recently, Behabtu et al.[19] reported the liquid crystallinity of graphene suspensions in chlorosulfonic acid at high graphene concentration (2 wt%). While the present work was under

preparation and submission, Kim et al.[20] and Xu and Gao[21] reported discotic nematic fluid behavior in aqueous suspensions of graphene oxide, qualitatively similar to graphene in strong acids.[19] In this work, we explore the lyotropic phase behavior of high aspect ratio ($D/h \sim 10^4$ and higher) giant graphene oxide (GGO) flakes in aqueous suspension; discotic building blocks with the highest aspect ratio and largest lateral dimensions to our knowledge and an order of magnitude higher than the previous reports. We demonstrate that higher aspect ratio leads to a dramatic change in the mesomorphic behavior; GGO dispersions form gel-like liquid crystal instead of fully fluid nematics reported previously for both graphene[19] and graphene oxide[20,21] and mesomorphic behavior is observed at concentrations an order of magnitude lower than what has been achieved for discotic mesogens. Optical methods are used to reveal the alignment of GGO flakes in the ordered phase, and measure the birefringence and order parameter; scaling law provides an estimate for the Frank elastic constant of this novel discotic LC system. Controlled confinement and colloidal inclusions are employed to induce LC defects and elastic distortions in the GGO director field.

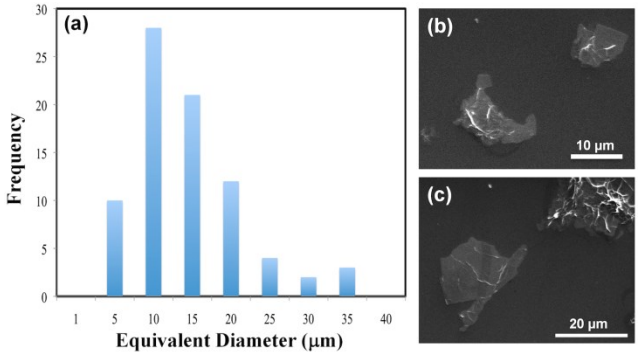

Fig. 4.1 (a) Size distribution of monolayer GGO flakes obtained through SEM and TEM imaging. (b,c) Representative SEM images of flakes prepared by spin coating dilute aqueous GGO suspension on silicon substrates.

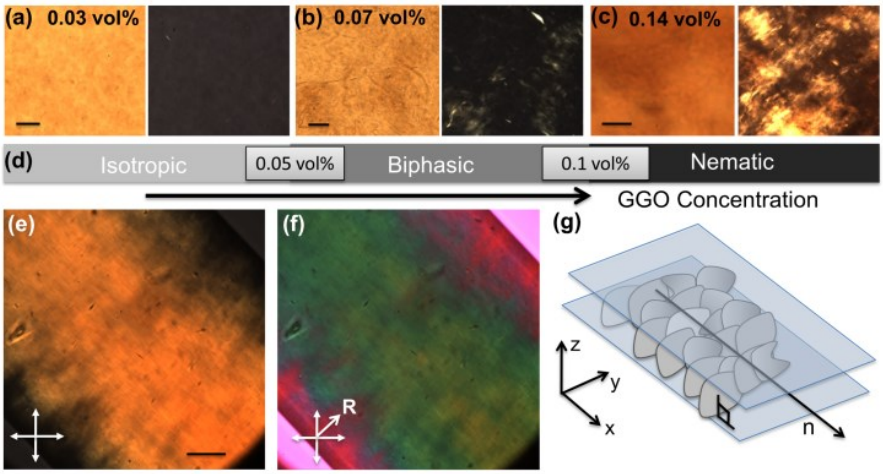

Fig. 4.2: (a-c) Optical microscopy images obtained without analyzer (left) and between crossed-polarizers (right) of GGO aqueous suspensions, demonstrating phase behavior vs. concentration: (a) isotropic (0.03 vol%), (b) biphasic (0.07 vol%) and (c) nematic (0.14 vol%). The scale bar in (a-c) is 10 μm. (d) Phase behavior vs. concentration. (e,f) Polarizing microscopy images of GGO nematic phase, inside a capillary, obtained with and without retardation plate, respectively; uniform birefringence indicates uniform alignment of director over large length scales. The scale bar in (e) is 20 μm and "R" in (f) marks the slow axis of phase retardation plate. (g) Schematic showing the alignment of flakes.

Much like in the case of polymers and single wall carbon nanotubes (SWNTs), liquid crystalline phase of graphene and graphene oxide is an important precursor for fabrication of high performance multifunctional aligned fibers. Discotic LCs of graphitic hydrocarbons are also

attractive for applications in advanced electronics.[22] Both mechanical and electrical properties of such graphene based macrostructures are expected to improve with increasing aspect ratio of individual molecules; similar scaling has already been demonstrated for the structurally similar SWNTs.[23] Therefore, LC suspensions of high aspect ratio graphene are of strong practical interest. From a fundamental point of view, these systems could be the closest experimental realization of theoretical models based on infinitely thin and high aspect ratio rigid platelets.[24,25]

4.2 Materials and methods

The GGO flakes were prepared by the method of Ref.[26] These monolayer GGO flakes tend to have a more regular structure and larger continuous regions of intact basal plane, compared to graphene oxide produced using other conventional techniques like Hummer's method.[27] The presence of functional groups such as epoxy, hydroxyls, carbonyls, and carboxylates render the flakes hydrophilic. The average size and polydispersity of GGO flakes was characterized using transmission electron microscopy (TEM) and scanning electron microscopy (SEM), as shown in Fig. 4.1. The GGO flakes had irregular polygonal shapes with a few ribbon-like structures. They had a number-average equivalent diameter $\langle d \rangle$ of 12 μm with relative standard deviation $\sigma_d = \left(\langle d^2 \rangle - \langle d \rangle^2 \right)^{1/2} / \langle d \rangle$ of 59%. The median aspect ratio of flakes was 10^4; in comparison, aspect ratio of graphene and graphene oxide in previous reports were: Behabtu et al. ~ 700, Kim et al. ~ 1200 and Xu and Gao ~ 2600.

The phase behavior of aqueous suspensions of GGO flakes was investigated for a concentration range of 0.01-0.14 vol%. Drops from suspensions with different GGO concentrations were squeezed between a cover slip and a glass slide whose edges were sealed

with epoxy glue. These samples were examined using a bright field transmission-mode optical polarizing microscope (Olympus BX51) with 50x and 100x oil immersion objectives and between crossed-polarizers. The dilute suspensions (< 0.05 vol%; assuming density of GGO ~ 2000 kg/m^3)[28] appeared dark and featureless under crossed-polarizers, as shown in Fig. 4.2(a). Lack of visible aggregates indicated a stable suspension. Suspensions with GGO concentration above ~ 0.05 vol% displayed regions with weak birefringence, indicating onset of ordering and a biphasic system (Fig. 4.2(b)). The fraction of ordered phase in the sample, as detected under crossed-polarizers, increased with GGO concentration. Above ~ 0.1 vol%, the entire sample appeared birefringent at different stages of sample rotation under crossed-polarizers, indicating a single-phase LC state (Fig. 4.2(c)). Our observations are consistent with theoretical predictions for a colloidal system comprised of infinitely thin and monodisperse disk-like particles, which is expected to transition from isotropic to nematic at a volume fraction of $\Phi_{iso} = 4\ h/D$.[24] Φ_{iso} = 0.04 vol% for GGO flakes, in good agreement with the experiments (Fig. 4.2(a-d)). The existence of a rather wide biphasic region (0.05 – 0.1 vol%) can be partially attributed to the polydispersity in flake size, although even monodisperse flakes can exhibit biphasic behavior.

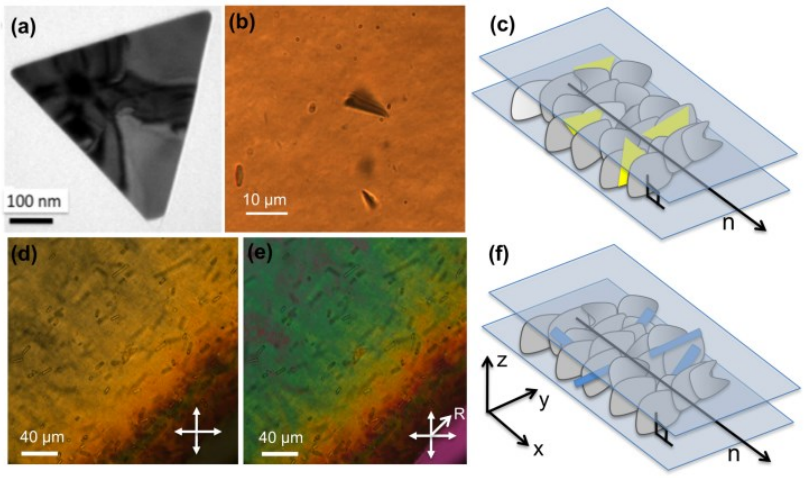

Fig. 4.3: Anisotropic colloidal particles and their spontaneous alignment in GGO nematic LC. (a) TEM image of an anisotropic gold triangular platelet. (b) Bright-field transmission-mode image showing triangular platelets with up to 10 μm side length and 5 nm thickness as they spontaneously align parallel to GGO flakes of the LC. (c) Schematic diagram of the GGO flake and gold platelet alignment. Polarizing microscopy images showing spontaneous alignment of glass micro-rods in the GGO LC observed under crossed polarizers with (d) and without (e) an additional retardation plate. (f) Schematic showing the alignment of micro-rods in the LC.

The high-concentration GGO suspensions had a gel-like consistency (Fig. 4.2(c)). Gelation has been observed previously in several other lyotropic discotic LC systems; most notably clay, whereby upon increasing the concentration, suspensions transition from an isotropic liquid to an isotropic gel to a birefringent gel.[29-31] Uniformly aligned nematic domains of GGO were prepared by dipping one end of a rectangular glass capillary tube (50 μm thick and 0.5 mm wide, inner dimensions, obtained from Vitrocom) in dilute isotropic GGO suspension (~ 0.03 vol%), causing spontaneous filling due to capillary action. Subsequent slow evaporation of water through the capillary ends led to a continuous increase of concentration of GGO flakes in the suspension. Upon observation of birefringent textures, the tube ends were sealed with epoxy glue to prevent further drying. Fig. 4.2(e) shows an optical micrograph under crossed polarizers of a high concentration GGO suspension prepared using this procedure. Uniform brightness across the entire field of view indicates a well-aligned director, ***n***, over large length scales (hundreds of

microns or more). Moreover, it indicates that the GGO flakes are oriented perpendicular to the wide top and bottom sides of the rectangular capillary (since flakes parallel to the top and bottom sides of the capillary would not produce birefringent textures). It is important to note that the observed flake alignment with respect to the top and bottom sides of capillary is likely metastable as it is partly driven by the kinetics of sample preparation procedure. The kinetics of the sample preparation process likely aids in the uniform director alignment as well, in addition to the intrinsic elasticity of the sample which is discussed in further details later.

The direction of in-plane orientation for GGO flakes was determined by inserting a full wave retardation plate (530 nm), also called "red plate", between the sample and analyzer, with its slow axis oriented at 45º with respect to the polarizer. For a GGO flake, the axis along the basal plane represents slow axis while the normal to plane is the fast axis. Therefore, the appearance of bluish-green color (Fig. 4.2(f)), which in the case of GGO flakes (with negative birefringence) indicates addition of phase retardations of the sample and the red plate,[32] shows that the GGO flakes are also oriented normal to the length of the capillary. The above analysis yields the overall arrangement and orientation of GGO flakes and the nematic director in the LC phase shown in Fig. 4.2(g).

4.3 Results and Discussion

Remarkably, uniform director orientation over ~ 1 mm length scales was achieved without any surface alignment layer, such as typically required for small molecule LCs; this likely indicates high elastic constant values. Indeed, according to density functional theory based models for nematic discotic systems, the average Frank elastic constant (K) of a nematogen can be expressed as:[33]

$$K \propto Q^{2/3}(Q^{-2}+2)S^2 \qquad (1)$$

where $Q = D/h$ is the aspect ratio of nematogens and S is the nematic scalar order parameter. For disk-shaped nematogens, $Q >> 1$ and the average elastic constant scales as $K \propto Q^{2/3}$. Previous studies on discotic nematics with average aspect ratios of $Q \sim 5$ have reported average elastic constants on the order of 1 pN.[34-36] Because the elasticity coefficients of nematogens are mainly sensitive to the average molecular dimensions,[33] the average elastic constant of GGO ($Q \sim 10^4$) was estimated to be $K_{GGO} \sim 100$ pN, at least one order of magnitude higher than that of most previously studied discotic nematics.

The highly uniform samples prepared in rectangular capillaries enabled characterization of the GGO LC parameters, such as the optical birefringence (Δn) and the order parameter (S). The optical birefringence was measured by use of a Berek compensator. Measurements were performed at several different locations, giving an average birefringence of $\Delta n = -0.0017 \pm 0.0005$ for the GGO LC. For comparison, the absolute values of birefringence of other discotic nematics are much larger, typically, −0.05 for polyacrylates[37] and −0.02 for disodium cromoglycate and −0.01 for violet-20 chromonic LC.[38] The order parameter of GGO flakes in the nematic phase was estimated using optical absorption anisotropy, as described in Ref.[38] .

Liquid crystalline GGO in a 50 μm thick capillary was placed on a microscope stage between *parallel* polarizers, and illuminated with monochromatic green light. The transmittance through the sample was measured for director orientations of 0º, 45º, and 90º with respect to the polarizers (referred to as t_0, t_{45} and t_{90}, respectively). Corresponding absorption indices, k_0, k_{45} and k_{90}, were obtained from the expression $t_i = \exp(-4\pi k_i d/\lambda)$, where i = 0, 45, 90 is indexed corresponding to director orientations of 0º, 45º, and 90º, respectively, at λ = 550 nm and d = 50 μm. For an ordered phase of disk-like molecules with the molecular planes oriented perpendicular to the director, if the shape of absorption spectrum is independent of molecular orientation and the birefringence is small (both conditions hold true for GGO), the scalar order parameter can be expressed as:[38]

$$S = \frac{1-\Delta}{1+\Delta/2} \qquad (2)$$

where $\Delta = k_0/k_{90}$ is the linear dichroic ratio. The above expression evaluated at several different locations along the sample yields an average S = 0.43±0.15, which is lower than what has been measured for other discotic nematic LCs. In comparison, typical order parameter values measured in other LCs include ~ 0.9 for hexa-*n*-hexyloxytriphenylene,[7] 0.6-0.85 for 2,3,7,8,12,13-hexa-*n*-decanoyloxytruxene (H10TX) and 2,3,6,7,10,11-hexa-*n*-pentyloxytriphenylene (H5T),[39] and 0.8 for gibbsite particles.[40]

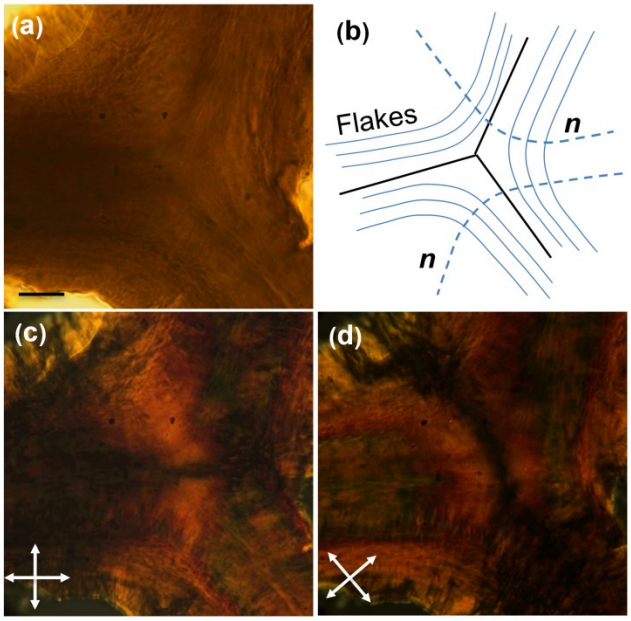

Fig. 4.4: A half-integer s= –1/2 disclination in the director field of GGO LC observed when the nematic phase was attained by solvent evaporation under the confinement of a glass slide and cover slip. (a) Transmission-mode bright field image. (b) Schematic of the arrangement of GGO flakes, Polarizing microscopy images of the same region obtained (c) between vertical and horizontal crossed polarizers and (d) with crossed-polarizers at 45º and 135º with respect to horizontal side of the image. The scale bar in (a) is 20 μm.

Optical absorption anisotropy provides an independent estimate of the birefringence. The phase retardation of transmitted light traversing an anisotropic sample is:[38]

$$\Delta\varphi = \cos^{-1}\left(\frac{4t_{45} - (t_0 + t_{90})}{2\sqrt{t_0 t_{90}}}\right) \qquad (3)$$

The phase retardation is related to optical birefringence as $\Delta n = \Delta\varphi \cdot \lambda / 2\pi d$. Calculations using this method yield an optical birefringence of Δn = –0.0018±0.0009, in good agreement with the value obtained via Berek compensator measurements.

Dispersion of colloidal particles in various types of LCs has been widely used for enhancement of LC properties, assembly of anisotropic structures, and alignment of anisotropic particles such as rods and discs.[41-49] We use anisotropic colloidal inclusions for direct visualization of

orientation of GGO flakes in the nematic phase. Two types of particles were chosen for this purpose: gold microtriangles, 5 nm in thickness and up to 10 μm in side length, (Fig. 4.3(a)) prepared using a biosynthesis technique,[50] and glass micro-rods, 3 μm diameter and 10 μm long (from Duke Scientific). Gold triangular platelets spontaneously oriented inside the GGO nematic phase with their large-area faces perpendicular to ***n*** and parallel to GGO flakes, as shown in Fig. 4.3(b,c), and consistent with cross-polarized optical images. Glass micro-rods spontaneously aligned with their long axes perpendicular to ***n*** and parallel to the GGO flakes, as shown in Fig. 4.3(d-f)**.** The ability of GGO LC to disperse and align anisotropic colloidal particles is important from an applications perspective. For example, the large scale ordering and alignment of anisotropic plasmonic nanoparticles such as gold, silver and palladium nanorods by means of dispersion in a LC is a valuable route for development of optoelectronic devices and metamaterials.[49]

Given the natural propensity of our GGO flakes to form large LC domains with uniform ***n***, the samples rarely exhibited defects. In order to induce defects, drops of dilute GGO suspension with circular footprints were trapped between a glass slide and cover slip, separated by 60 μm spacers and evaporated slowly to achieve a nematic phase. The recession of meniscus from all directions forces the formation of a defect at the center of drop. Interestingly, in most cases, the circular drops transformed into roughly Y-shaped structures as the drop radii became sufficiently small, likely due to the high elastic constant of GGO nematogens. The optical transmission image of an $s = -1/2$ defect, observed at the center of such Y-shaped nematic structures, is shown in Fig. 4.4(a). The arrangement of GGO flakes and director field around the defect is shown schematically in Fig. 4.4(b). Fig. 4.4(c-d) show the polarizing optical micrographs of the defect structure with crossed-polarizers in 0˚-90˚ and at 45˚-135˚ orientations, respectively; the

orientation of two dark brushes parallel to one of the polarizers is consistent with the schematically shown model of the defect structure.

Elastic distortions and defects in LCs can be also induced by inclusion of colloidal particles. Colloidal spheres suspended in nematics lead to particle size-dependent dipolar and quadrupolar distortions in the surrounding director field.[42-48] Minimization of the ensuing elastic energy due to distortions induced by these inclusions often results in spontaneous assembly of colloidal particles into anisotropic colloidal structures. In our study, we used melamine resin colloidal microspheres with diameters ranging from 2 μm to 15 μm. Aqueous microspheres (< 1 vol%) were mixed in the dilute GGO suspension, followed by capillary filling and solvent evaporation. Interestingly, small diameter particles (≤ 3 μm) did not produce detectable distortions (Fig. 4.5(a)), while larger particles (4 - 15 μm) produced distinct distortions in the director field, (Fig. 4.5(b-d)). Optical analysis of these distortions using the "red plate" revealed "homeotropic" surface anchoring for ***n***, i.e. GGO flakes exhibit tangential alignment to the melamine resin particles. The orientation of GGO flakes around melamine resin particles is likely influenced by acid-base interactions between the $-NH_2$ and =N– groups on melamine resin and acidic hydrophilic functional groups on GGO flakes.

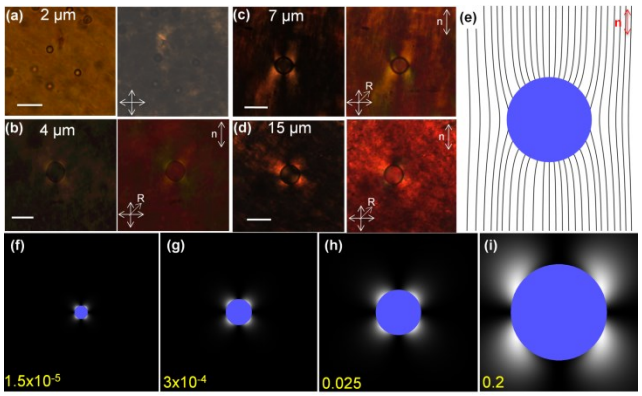

Fig. 4.5: Quadrupolar distortions in nematic director field around spherical inclusions, demonstrating homeotropic surface anchoring of the director. (a) Transmission-mode bright field (left) and between crossed polarizers (right) images of GGO LC. (b-d) Images of sample between crossed-polarizers (left) and with a retardation plate (right). Scale bars are 10 μm (a), 5 μm (b), 10 μm (c), 20 μm (d). Particle sizes, and orientations of crossed polarizers and retardation plates marked on the images. Computer-simulated (e) director field and (f-i) polarizing microscopy textures for particle sizes 2, 4, 7, and 15 μm, respectively. The values shown in (f-i) in yellow color are the ratios of maximum transmitted and incident light intensities for the corresponding computer-simulated images.

The particle size-dependent distortions observed in GGO LC provide important insights into the interplay of bulk elastic and surface anchoring energies, which often determine whether a colloidal inclusion in a nematic LC will induce defects in the director field or barely perturb it.[41-48] For example, a spherical colloidal inclusion with homeotropic anchoring induces a pattern of director equivalent to that around a point defect with charge +1, known as a "radial hedgehog".[42] Therefore, the distortions around the particle, should be accompanied by a hyperbolic hedgehog or a half-integer "Saturn ring" disclination loop, (both having topological charge of –1) in order to conserve the total topological charge in the sample with a uniform far-field alignment.[42,47] On the other hand, nanoparticles of size only somewhat larger than that of the LC molecules and microparticles with weak surface anchoring typically produce either weak or no elastic distortions of the LC director field.[49] In the case of melamine resin particles

suspended in GGO LC, no accompanying bulk or surface topological defects are observed (Fig. 4.4). The director distortions have quadrupolar symmetry, reminiscent of that formed around microparticles with weak homeotropic surface anchoring, suggesting that $K/W>R$, where R is particle radius and W is the polar surface anchoring coefficient.[42,48,49] Equivalently, the nematic director at the LC-colloid interface deviates from the "normal" orientation (Fig. 4.5(e)), in order to minimize elastic distortions and reduce the elastic energy at the expense of surface anchoring energy cost. The director distortions become less pronounced as R decreases, being barely noticeable for the 2 μm particles.

We have simulated the expected nematic director structure surrounding the particles and corresponding polarizing microscopy textures using the *ansatz* for LC director structure proposed by Ruhwandl and Terentjev[48] (Fig. 4.5(e)) and the Jones matrix method.[51] In the simulations, we have used estimated values of the elastic constant $K=10^{-10}$ N, an optical anisotropy of $\Delta n = -0.0017$ and a polar anchoring coefficient of $W = 10^{-5}$ J/m^2, typical of lyotropic LCs.[49] The LC sample, with a colloidal inclusion and director distortions around it, was split into a set of thin slabs with known orientation of the optical axis ($\equiv \boldsymbol{n}$). In each pixel of a simulated polarizing microscopy texture (similar to those in Fig. 4.5(f-i)), intensity of the light after propagation through the cell was obtained by successive multiplication of the Jones matrices corresponding to a polarizer, the thin nematic slabs, and the analyzer. The computer simulated textures closely match the experimental results (Fig.4.5). Interestingly, although the particle diameters and the lateral GGO flake sizes are comparable, the director structures around the colloidal inclusions can still be understood based on simple considerations of the interplay between bulk elastic and surface anchoring energies originally developed for small-molecule LCs.

The melamine resin microspheres suspended in GGO LC are practically immobile and show no tendency to self-assemble into anisotropic structures, even at long time scales (several days), as has been reported in other nematic systems.[42-47] This is unexpected for anisotropic nematic fluids, given the distortions induced by the particles and the high elastic constant of GGO. The lack of particle motion and any noticeable interaction among the microspheres could be due to chemical interactions between the microspheres and flakes, a gel-like networked structure among the flakes and/or an extremely high viscosity at high GGO concentrations. Future studies are needed to decipher the nature of the forces responsible for the particle immobility.

4.4 Conclusions

In summary, we have shown that, with increasing concentration, aqueous suspensions of GGO flakes exhibit well-defined isotropic, biphasic and nematic LC behavior. Preparation of the nematic phase by slow evaporation of solvent from the isotropic phase yields large domains with uniform directors and minimal defects. Such large domains are consistent with estimated Frank elastic constant that is about one hundred-fold higher than in low-molecular-weight discotic nematics. Optical characterization yields a birefringence of $\Delta n \sim -0.0017$ and order parameter $S = 0.43$. We show that defects and elastic distortions can be deliberately induced by means of confinement and by colloidal inclusions. The studied spherical inclusions induce quadrupolar distortions of the director field and anisotropic particles self-align at a well-defined orientation with respect to the director and reveal the director structures. The liquid crystalline behavior from this new class of extremely high aspect ratio ($\sim 10^4$ and larger) disk-like building blocks could broadly impinge on both fundamental and applied aspects of discotic liquid crystals.

4.5 References

1. P. de Gennes and J. Prost, *The physics of liquid crystals*, Oxford University Press, USA, 1995.

2. H. Zocher, *Zeitschrift Fur Anorganische Und Allgemeine Chemie*, 1925, **147**, 91-U15.

3. F. C. Bawden, N. W. Pirie, J. D. Bernal and I. Fankuchen, *Nature*, 1936, **138**, 1051-1052.

4. L. Onsager, *Annals of the New York Academy of Sciences*, 1949, **51**, 627-659.

5. G. J. Vroege and H. N. W. Lekkerkerker, *Reports on Progress in Physics*, 1992, **55**, 1241-1309.

6. S. Chandrasekhar, B. K. Sadashiva and K. A. Suresh, *Pramana*, 1977, **9**, 471-480.

7. S. Chandrasekhar and G. S. Ranganath, *Reports on Progress in Physics*, 1990, **53**, 57-84.

8. H. K. Bisoyi and S. Kumar, *Chemical Society Reviews*, 2010, **39**, 264-285.

9. J. D. Brooks and G. H. Taylor, *Nature*, 1965, **206**, 697-699.

10. D. Dunmur, A. Fukuda, G. Luckhurst and I. o. E. Engineers, *Physical properties of liquid crystals: nematics*, INSPEC, 2000.

11. F. M. van der Kooij, K. Kassapidou and H. N. W. Lekkerkerker, *Nature*, 2000, **406**, 868-871.

12. A. S. Sonin, *Journal of Materials Chemistry*, 1998, **8**, 2557-2574.

13. J. C. P. Gabriel and P. Davidson, *Advanced Materials*, 2000, **12**, 9-20.

14. A. B. D. Brown, C. Ferrero, T. Narayanan and A. R. Rennie, *European Physical Journal B*, 1999, **11**, 481-489.

15. F. M. van der Kooij and H. N. W. Lekkerkerker, *Journal of Physical Chemistry B*, 1998, **102**, 7829-7832.

16. D. van der Beek and H. N. W. Lekkerkerker, *Europhysics Letters*, 2003, **61**, 702-707.

17. S. Y. Liu, J. Zhang, N. Wang, W. R. Liu, C. G. Zhang and D. J. Sun, *Chemistry of Materials*, 2003, **15**, 3240-3241.

18. M. C. D. Mourad, E. J. Devid, M. M. van Schooneveld, C. Vonk and H. N. W. Lekkerkerker, *Journal of Physical Chemistry B*, 2008, **112**, 10142-10152.

19. N. Behabtu, J. R. Lomeda, M. J. Green, A. L. Higginbotham, A. Sinitskii, D. V. Kosynkin, D. Tsentalovich, A. N. G. Parra-Vasquez, J. Schmidt, E. Kesselman, Y. Cohen, Y. Talmon, J. M. Tour and M. Pasquali, *Nature Nanotechnology*, 2010, **5**, 406-411.

20. J. E. Kim, T. H. Han, S. H. Lee, J. Y. Kim, C. W. Ahn, J. M. Yun and S. O. Kim, *Angewandte Chemie International Edition*, 2011, **50**, 3043-3047.

21. Z. Xu and C. Gao, *ACS Nano*, 2011, **5**, 2908–2915.

22. L. Schmidt-Mende, A. Fechtenkotter, K. Mullen, E. Moons, R. H. Friend and J. D. MacKenzie, *Science*, 2001, **293**, 1119-1122.

23. N. Behabtu, M. J. Green and M. Pasquali, *Nano Today*, 2008, **3**, 24-34.

24. M. A. Bates and D. Frenkel, *Journal of Chemical Physics*, 1999, **110**, 6553-6559.

25. R. Eppenga and D. Frenkel, *Molecular Physics*, 1984, **52**, 1303-1334.

26. D. C. Marcano, D. V. Kosynkin, J. M. Berlin, A. Sinitskii, Z. Z. Sun, A. Slesarev, L. B. Alemany, W. Lu and J. M. Tour, *ACS Nano*, 2010, **4**, 4806-4814.

27. W. S. Hummers and R. E. Offeman, *Journal of the American Chemical Society*, 1958, **80**, 1339-1339.

28. D. A. Dikin, S. Stankovich, E. J. Zimney, R. D. Piner, G. H. B. Dommett, G. Evmenenko, S. T. Nguyen and R. S. Ruoff, *Nature*, 2007, **448**, 457-460.

29. J. C. P. Gabriel, C. Sanchez and P. Davidson, *Journal of Physical Chemistry*, 1996, **100**, 11139-11143.

30. A. Mourchid, A. Delville, J. Lambard, E. Lecolier and P. Levitz, *Langmuir*, 1995, **11**, 1942-1950.

31. A. Mourchid, E. Lecolier, H. Van Damme and P. Levitz, *Langmuir*, 1998, **14**, 4718-4723.

32. E. E. Wahlstrom, *Optical crystallography*, John Wiley & Sons Inc., 1979.

33. M. A. Osipov and S. Hess, *Molecular Physics*, 1993, **78**, 1191-1201.

34. B. Tjiptomargo, G. T. Evans, M. P. Allen and D. Frenkel, *Journal of Physical Chemistry*, 1992, **96**, 3942-3948.

35. T. Haven, D. Armitage and A. Saupe, *Journal of Chemical Physics*, 1981, **75**, 352-364.

36. N. H. Phuong, G. Germano and F. Schmid, *Journal of Chemical Physics*, 2001, **115**, 7227-7234.

37. C. D. FavreNicolin and J. Lub, *Macromolecules*, 1996, **29**, 6143-6149.

38. Y. A. Nastishin, H. Liu, T. Schneider, V. Nazarenko, R. Vasyuta, S. V. Shiyanovskii and O. D. Lavrentovich, *Physical Review E*, 2005, **72**, 041711.

39. T. S. Perova and J. K. Vij, *Advanced Materials*, 1995, **7**, 919-922.

40. D. van der Beek, P. Davidson, H. H. Wensink, G. J. Vroege and H. N. W. Lekkerkerker, *Physical Review E*, 2008, **77**, 031708-031716.

41. F. Brochard and P. G. D. Gennes, *Journal De Physique*, 1970, **31**, 691.

42. P. Poulin, H. Stark, T. C. Lubensky and D. A. Weitz, *Science*, 1997, **275**, 1770-1773.

43. P. Poulin, N. Frances and O. Mondain-Monval, *Physical Review E*, 1999, **59**, 4384-4387.

44. J. C. Loudet, P. Barois and P. Poulin, *Nature*, 2000, **407**, 611-613.

45. C. P. Lapointe, T. G. Mason and Smalyukh, II, *Science*, 2009, **326**, 1083-1086.

46. P. Poulin and D. A. Weitz, *Physical Review E*, 1998, **57**, 626-637.

47. Smalyukh, II, A. V. Kachynski, A. N. Kuzmin and P. N. Prasad, *Proceedings of the National Academy of Sciences*, 2006, **103**, 18048-18053.

48. R. W. Ruhwandl and E. M. Terentjev, *Physical Review E*, 1997, **55**, 2958-2961.

49. Q. K. Liu, Y. X. Cui, D. Gardner, X. Li, S. L. He and Smalyukh, II, *Nano Letters*, 2010, **10**, 1347-1353.

50. J. S. Evans, C. N. Beier and I. I. Smalyukh, *J. Appl. Phys.* **110**, 033535 (2011)

51. P. Yeh and C. Gu, *Optics of Liquid Crystal Displays*, John Wiley & Sons, Inc., 1999.

Chapter 5: Elastic trapping of single plasmonic nanoparticles by topological defects and hierarchical self-assembly of colloidal dimers in liquid crystals

Adapted from: Nano Lett. ***12**, 955-963 (2012)*

Chapter Overview

In the previous 3 chapters, we have demonstrated a variety of interesting materials produced through simple inclusion of gold nanocolloids in a liquid crystal. In this chapter we explore the architectural complexity that can be achieved through including multiple sizes of colloid and optically assisting their assembly. We demonstrate scaffolding of plasmonic nanoparticles by topological defects induced by colloidal microspheres to match their surface boundary conditions with a uniform far-field alignment in a liquid crystal host. Displacing energetically costly liquid crystal regions of reduced order, anisotropic nanoparticles with concave or convex shapes not only stably localize in defects but also self-orient with respect to the microsphere surface. Using laser tweezers, we manipulate the ensuing nanoparticle-microsphere colloidal dimers, probing the strength of elastic binding and demonstrating self-assembly of hierarchical colloidal superstructures such as chains and arrays.

5.1 Introduction

Starting from the development of facile synthetic methods, gold nanoparticles have been the focus in the quest for understanding and exploiting their extraordinary optical properties arising from the localized surface plasmon resonance (SPR).[1-3] Strong absorption and local field enhancement observed in such nanoparticles are of great interest for applications in

nanophotonics, solar cells[4], photothermal therapies, and imaging.[2-3] Nonspherical particles can exhibit SPR tunable throughout the visible and near-infrared spectral regions[3,5] and their plasmonic properties can be further enhanced by the collective behavior when the inter-particle separation becomes comparable to their size.[2] For example, multipole SPRs[6] and well-defined assemblies[7] of nanoparticles give simple ways of obtaining a non-trivial magnetic response, making plasmonic colloidal systems useful for the preparation of metamaterials.[8] Near-field proximity of plasmonic nanoparticles can also alter the fluorescent behavior of semiconductor and dielectric particles as well as molecular dyes.[9-11] Precise arrangement of metal nanoparticles can yield highly desirable functionality for applications such as nanoantennas.[12-14] These examples demonstrate the great potential of non-contact manipulation and trapping techniques that would allow for precise positioning of plasmonic and other particles with respect to each other in fluid host media.

Although spatial manipulation of colloids of most compositions can be accomplished using optical trapping, this technique requires continuous focusing of high-intensity laser beams and has diffraction-limited minimum inter-particle distance (typically hundreds of nanometers) at which two particles can be stably localized with respect to each other. Furthermore, optical trapping of metal nanoparticles[15-18] is limited by heating[17], the relationship between trapping and SPR wavelengths[18], poor control of anisotropic particle orientation, and other factors. In anisotropic fluids such as liquid crystals (LCs)[19], which are of great interest for introducing tunability into the dispersions of plasmonic nanoparticles[12,20-22], manipulation becomes even more complicated as the electric field of the trapping beam can cause local realignment and induce phase transitions in the LC host.

In this chapter, we use topological singularities (defects) for elastic scaffolding of small plasmonic nanoparticles next to bigger colloidal microspheres. These microparticle-induced defects in a nematic LC elastically trap nanoparticles with concave and convex anisotropic shapes. Nanoparticles are attracted to defects to displace the energetically costly defect core regions of reduced order parameter surrounded by strong long-range elastic distortions of the LC. By means of dark-field microscopy and polarization-sensitive two-photon luminescence (TPL) imaging, we demonstrate that anisotropic gold colloids such as nanoplatelets and elongated rod-like octagonal, pentagonal, and starfruit-like prisms not only self-localize within topological defects, but also exhibit well-defined orientation with respect to the neighboring microparticle and the uniform far-field LC alignment. Using laser tweezers, we manipulate the dielectric colloidal microspheres along with the defect-bound plasmonic nanoparticles next to them. We explore the strength of nanoparticle-defect interaction forces and show hierarchical self-assembly of metal and dielectric colloids into chains and two-dimensional arrays. The demonstrated control of position and orientation of the plasmonic nanoparticles allows for the creation of new nanoscale systems with interesting potential applications in the areas of nanoscale imaging and nanoscale energy conversion.

5.2 Materials and Methods

We use a single-compound LC material 4-pentyl-4'-cyanobiphenyl (5CB, obtained from Frinton Labs, Inc.) and nanoparticles with different anisotropic shapes, dimensions (characterized by the axial diameter D_{np} and length L_{np}), and surface chemistry (Table 5.1). Ethanol dispersions of Microgolds (MGs), Starfruits (SFs), Nanobursts (NBs) and nanorods (GNRs) with NSol(akyl acrylate) polymer conjugation (Fig. 5.1(a-d)) were obtained from Nanopartz, Inc. (Colorado,

USA). The smallest gold nanorods (sGNRs) with polystyrene capping were obtained by means of an esterification reaction between mercaptophenol-functionalized nanorods and carboxyl-terminated polystyrene (MW = 5000 g/mol) as described elsewhere.[23,24] Silica microspheres of 3 μm in diameter were obtained from Duke Scientific as a powder and treated with a surfactant [3-(trimethoxysilyl)propyl]octadecyl-dimethylammonium chloride (DMOAP) to set vertical surface boundary conditions for the LC molecular alignment.[25] Melamine resin spherical particles of 2 μm in diameter and with tangential surface boundary conditions[26] were obtained in an aqueous dispersion (from Sigma-Aldrich) and turned into a powder via slow water drying. These microparticles were then dispersed in the LC by direct mixing and a 15-30 min sonication to break apart pre-existing colloidal aggregates. Gold nanoparticles were dispersed from ethanol to toluene and then added to the mixture of LC and microspheres; toluene was evaporated afterwards. This colloidal dispersion was sonicated for 30-60 min while slowly changing the samples' temperature from isotropic to the LC state to obtain isolated microspheres and metal nanoparticles in the nematic host. Using capillary forces, LC colloidal dispersions were filled into ~ 5-10 μm thick cells formed by substrates spaced by glass fiber spacers and treated to provide planar or vertical boundary conditions. In order to set homogeneous planar boundary conditions, glass plates were spin-coated with polyimide PI2555 (HD MicroSystem) on their inner surfaces, unidirectionally rubbed, and then glued together by epoxy while aligned to have "antiparallel" rubbing directions at the opposite plates. Surface treatment of substrates with DMOAP was used to set the vertical surface boundary conditions for the LC molecules.

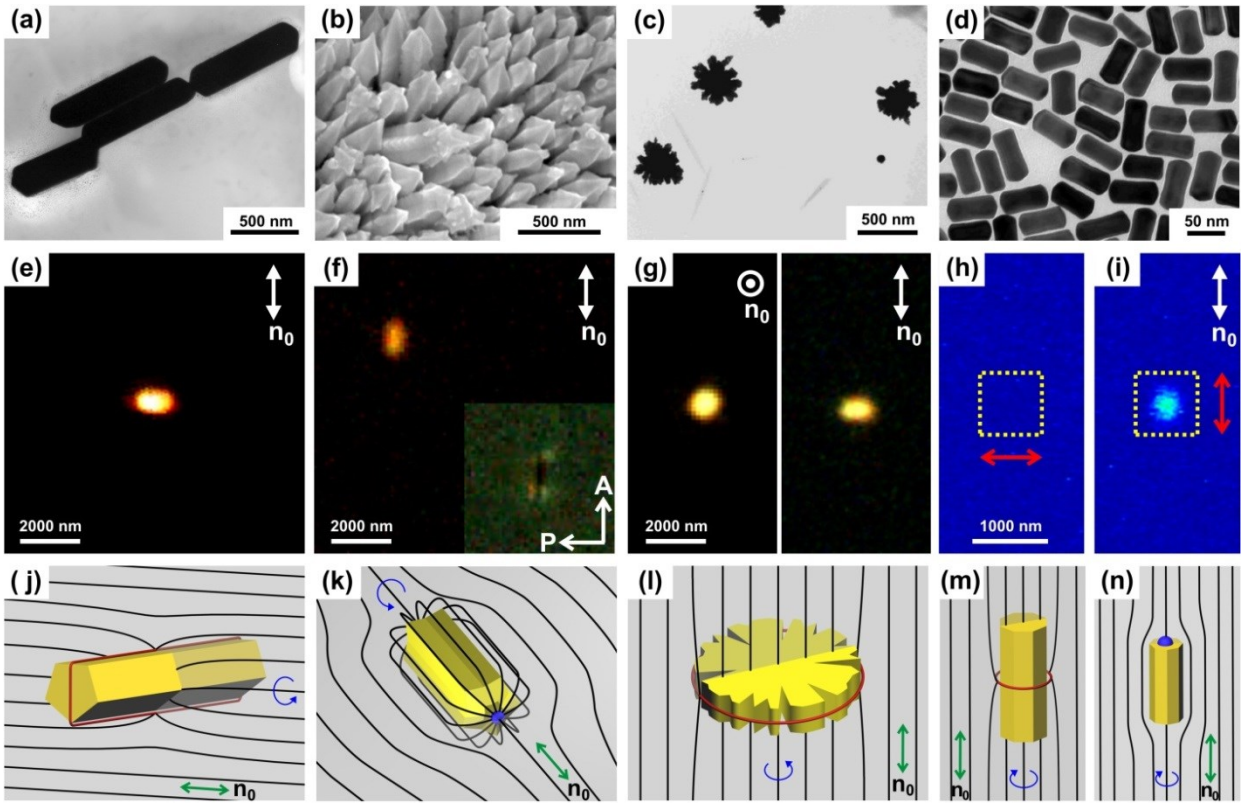

Fig. 5.1. Gold nanoparticles in a nematic LC. (a, c, d) TEM images of MG, NB and GNR nanoparticles, respectively. (b) SEM image of SF nanoparticles. (e-g) Dark-field microscopy images of MGs, SFs and NBs in 5CB, respectively. Inset in (f) shows the texture of director distortions around SF between crossed polarizer "P" and analyzer "A". (h, i) TPL images of an sGNR nanoparticle (in the area outlined by yellow dashed line) taken with the polarization of excitation beam (λ_{exc} = 850 nm) perpendicular (h) and parallel (i) to $\mathbf{n_0}$. (j-n) Schematic diagrams of **n(r)** (black lines) around MG, SF, NB, GNR and sGNR nanoparticles, respectively. Red lines in (j, l, m) and blue semispheres in (k, n) show a k = -1/2 defect line and an m = -1 boojum point singularities, respectively. Green and white double arrows show the in-plane direction of the far-field director $\mathbf{n_0}$; white circle with the point in the middle show $\mathbf{n_0}$ normal to the field of view. Red double arrows in (h,i) show the polarization direction of the excitation beam. Blue arrows in (j-n) show the allowed rotations of aligned nanoparticles.

We have used dark-field, bright-field, and polarizing modes of optical imaging with an inverted Olympus microscope IX81 integrated with a holographic optical trapping (HOT) setup[27] operating at wavelength λ = 1064 nm. The strong scattering of metal nanoparticles[28] in the dark-field microscopy[20,29] (Fig. 5.1(e-g)) allowed us to visualize individual colloids of size

smaller than the diffraction limit. The adjustable numerical aperture (NA) of the high magnification oil objective 100× was selected to be smaller (NA = 0.6) than the NA of the dark-field condenser (NA_{cond} = 1.2). The interaction between gold nanoparticles and topological defects was monitored with a PointGrey CCD camera at a frame rate of 15 fps using dark-field microscopy, enabling a direct measurement of elastic interaction forces.[29]

Orientation-sensitive imaging of sGNRs and GNRs was performed using their polarized TPL.[30,31] We used a tunable (680-1080 nm) Ti:sapphire oscillator (140 fs, 80 MHz, Chameleon Ultra-II, Coherent) to generate TPL from sGNRs and GNRs (Fig. 5.1(h,i)). To enhance the polarization dependence of TPL, the excitation of gold nanorods was performed at wavelengths in the proximity of the longitudinal SPR peak (850 nm for sGNR and ~ 650 nm for GNR), and the TPL signal from a single nanorod was detected within the spectral range of 400-700 nm by a photomultiplier tube (Hamamatsu). The in-plane position of the focused excitation beam was controlled by a galvano-mirror scanning unit (FV300, Olympus) and its polarization was varied using a half-wave retardation plate mounted immediately before the 100× oil objective. The average power of fast-scanning excitation beam in the sample plane was ~ 100-200 μW, low enough to be insufficient to change the temperature of LC and affect its local ordering due to the laser-induced heating of gold nanoparticles.[17]

5.3 Results and Discussion

The unique property of colloidal dispersions of all studied anisotropic gold nanoparticles in LCs is that they exhibit well-defined alignment with respect to the uniform far-field director $\mathbf{n_0}$ that can be controlled on large scales via treatment of confining substrates (like in flat-panel LC displays). Nanoparticle shape and capping can promote vertical or tangential alignment of the LC

molecules at its surface. Particles disturb the initially uniform average local molecular alignment along the LC director **n** describing the average local orientation of the rod-like molecules,[19] and induce spatial distortions described by the director field **n(r)** and dependent on the type and strength of anchoring at their surfaces. The ensuing equilibrium orientation of anisotropic nanoparticles depends on their size and the type and strength of surface anchoring, and can be characterized by a dimensionless parameter[32,33] $\omega \sim R_{np}W_a/K$, where W_a is a surface anchoring coefficient at the nanoparticle-nematic interface, $R_{np} = D_{np}/2$ is a radius of nanoparticle and K is an average Frank elastic constant.[19] Taking typical values of $K \approx 10$ pN and $W_a \sim 10^{-6}$-10^{-4} J/m^2 and sizes of studied nanoparticles, we find that $\omega \sim 0.001$-1 varies within a wide range. Although NSol coatings at flat surfaces promote vertical boundary conditions while polystyrene coatings promote planar boundary conditions at flat LC-solid interfaces, the resulting spatial distortions of **n(r)** due to nanoparticles also depend on their shape (i.e., concave vs. convex). Since the ensuing **n(r)**-structures appear on submicrometer scales, their details cannot be resolved by polarizing optical microscopy. However, by means of dark-field microscopy, we directly observe nanoparticles as bright diffraction-limited scattering spots on a dark background of the non-scattering aligned LC (Figs. 5.1(e-g)). Dark-field imaging reveals the orientation of nanoparticles: pentagonal MG nanorods (Fig. 5.1(a)) align perpendicular to the far-field director $\mathbf{n_0}$ (Fig. 1(e)) while SFs align along $\mathbf{n_0}$ (Fig. 5.1(f)) and NBs align with their large-area flat faces normal to $\mathbf{n_0}$ (Fig. 5.1(g)).

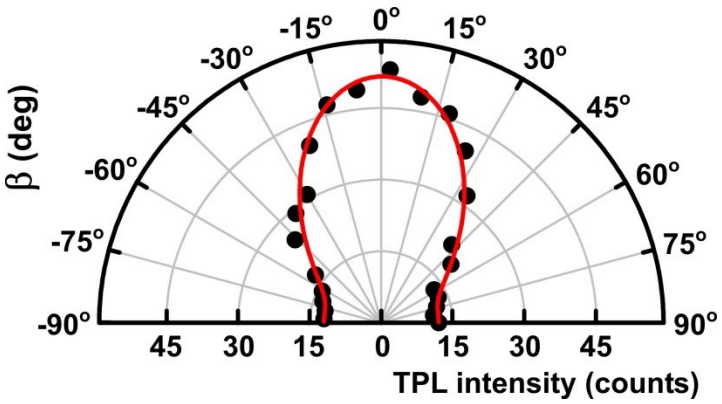

Fig. 5.2. TPL intensity from a sGNR nanorod in a nematic LC vs. the angle β between its long axis and the polarization of excitation beam, revealing its alignment along $\mathbf{n_0}$. The red line shows the best fit of experimental data (black filled circles) with the expected angular dependence of TPL ~ $\cos^4\beta$.

The orientation of small octagonal sGNR and GNR nanorods was determined using polarized TPL (Figs. 5.1(h,i) and 5.2). The TPL intensity from these particles depends on the polarization direction of the excitation beam as $\cos^4\beta$, where β is the angle between the long axis of the nanorod and the polarization of the excitation light.[30] Fig. 5.2 shows a polar plot of TPL intensity vs. β for a nanorod aligned along $\mathbf{n_0}$. The TPL intensity from both sGNR and GNR particles is at minimum for the polarization of excitation light perpendicular to $\mathbf{n_0}$ (Fig. 5.1(h)) and maximum for their parallel orientation (Fig. 5.1(i)), allowing us to unambiguously establish that sGNRs and GNRs align parallel to $\mathbf{n_0}$ (Fig. 5.1(m,n)). Figs. 5.1(j-n) show the corresponding schematics of $\mathbf{n(r)}$ and defects induced in the LC by studied gold nanoparticles, as established based on the known boundary conditions at their surface and the comparative analysis of different types of optical images, such as the dark-field and polarizing microscopy images shown in Fig. 5.1(f) for the case of SFs shown in Fig. 5.1(b). MG nanoparticles (Fig. 5.1(a)) have the shape of a pentagonal prism and align in the nematic LC with their long dimension L_{np} normal to $\mathbf{n_0}$ (Fig. 5.1(j)). Due to the homeotropic surface anchoring, they are encircled by a disclination

loop of strength k = -1/2 (Fig. 5.1(j)), where k is defined as a number of director turns by 2π when the defect core is circumnavigated once. MGs freely rotate around $\mathbf{n_0}$. NB nanoparticles have NB nanoplatelets (Fig. 5.1(c)) with multiple irregular sharp edges and vertical surface boundary conditions align with their flat sides normal to $\mathbf{n_0}$, inducing a k = -1/2 disclination loop around their perimeter (Fig. 5.1(l)). The SFs have complex elongated shape with the concave base in the form of a star (Fig. 5.1(b)). They align with their long axes along $\mathbf{n_0}$ and, as can be seen from polarizing microscopy textures (inset of Fig. 5.1(f)), induce **n(r)** of quadrupolar symmetry with two surface point defects called "boojums" at their ends (Fig. 5.1(k)). This **n(r)**-structure can be explained by the grooved surface relief of the rod-like SF nanoparticles with star-shaped base (Fig. 5.1(b)). Bulk elastic energy is minimized when the LC director locally follows these groves instead of satisfying antagonistic surface boundary conditions exerted by the complex ribbed surface relief of these nanoparticles (Fig. 5.1(f,k)), explaining the observed **n(r)**-configuration. GNR and sGNR particles have octagonal cross-sections. GNRs promote vertical alignment of LC molecules at their surface and align with their long axes along $\mathbf{n_0}$ with the k = -1/2 disclination loop encircling them in the plane normal to their long axis (Fig. 5.1(m)). Since ω is small, one can expect that this disclination loop is "virtual" or located at the particle surface.[32-34] The anchoring at sGNR polystyrene-capped surfaces is tangential, causing weak **n(r)**-distortions of quadrupolar symmetry with two boojums (Fig. 5.1(n)). These findings for complex-shaped colloids are consistent with the studies of colloidal cylinders in LCs,[32-33,35-37] which showed that their orientation can be both along and perpendicular to $\mathbf{n_0}$ for normal boundary conditions and that rods with tangential boundary conditions typically align parallel to $\mathbf{n_0}$.

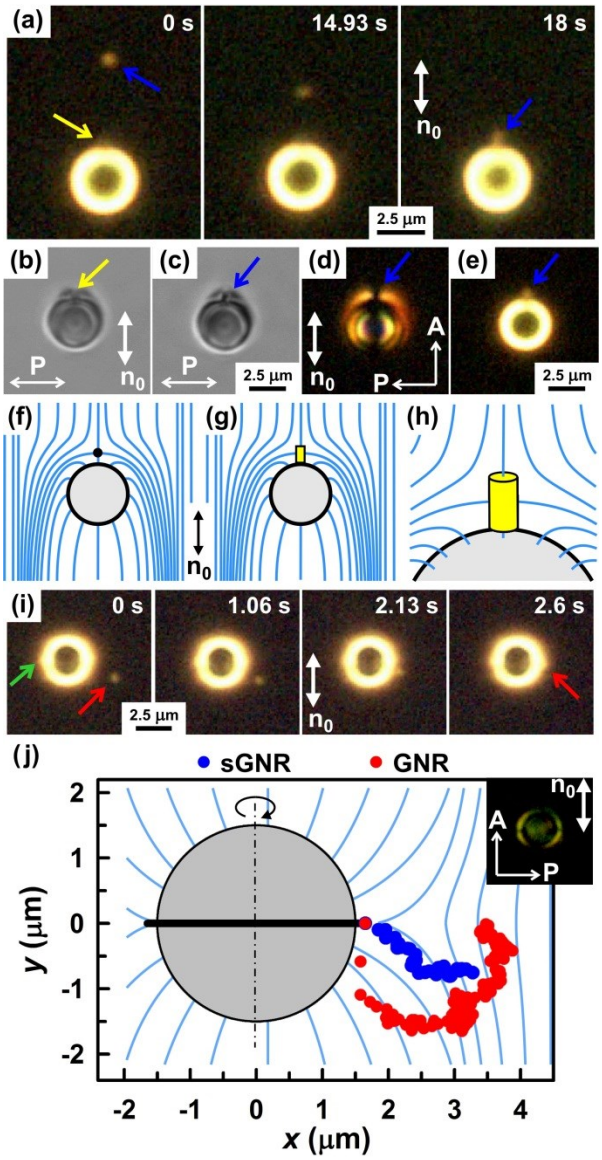

Fig. 5.3. Attraction of GNRs and sGNRs to topological singularities in a nematic LC. (a) A sequence of dark-field images showing an sGNR nanorod (marked by a blue arrow) moving into an $N = -1$ point defect (marked by a yellow arrow) near the microsphere. (b) A bright-field image of the microsphere with the point defect. (c-e) Bright-field, polarizing, and dark-field images, respectively, of silica microsphere with the point defect displaced by an sGNR. (f) A schematic diagram of the dipolar **n(r)** around the microsphere; black filled circle shows the point defect. (g) A schematic diagram of **n(r)** with the nanorod (yellow) displacing the defect. (h) An enlarged schematic view of the nanorod (yellow cylinder) in the defect. (i) Dark-field images showing attraction of a GNR (marked by a red arrow) to a "Saturn ring" defect (marked by a green arrow). (j) Trajectories of GNR (red filled circles) and sGNR (blue filled circles) nanoparticles attracting to the "Saturn ring" (black line). $\mathbf{n_0}$ is shown by white double arrows and **n(r)** in (f-h,j)

is shown by blue lines. Inset in (j) shows the polarizing microscope texture of the microsphere with the "Saturn ring" defect.

To enable and control spatial localization of fluid-borne nanoparticles of varying sizes and shapes, we use colloidal microspheres also dispersed in the LC. These solid microspheres induce much stronger distortions of **n(r)** compared to the nanoparticles, causing well-defined singular point and line defects.[38-39] Depending on the strength,[40] the vertical surface anchoring at silica spheres causes either dipolar distortions of **n(r)** with a hyperbolic point defect[19] of topological charge $N = -1$ (Fig. 5.3(a,b,d,f)) or quadrupolar distortions of **n(r)** with $k = -1/2$ disclination loop ("Saturn ring")[41] encircling the sphere along its equator in the plane normal to $\mathbf{n_0}$ (Fig. 5.3(i,j)). In our experiments, spherical particles with the hedgehog defect were commonly observed in thicker 10 μm-thick cells and particles with the "Saturn ring" defect were observed predominantly in thinner 5 μm-thick cells.[42] In dark-field microscopy, the hyperbolic point defect is seen as a weakly scattering spot near a strongly scattering silica sphere (Fig. 5.3(a) and Fig. 5.4(a), marked by a yellow arrow). The "Saturn ring" (Fig. 5.3(j)) appears as a weakly scattering line that is clearly seen at the microsphere edges (Fig. 5.3(i), marked by a green arrow).

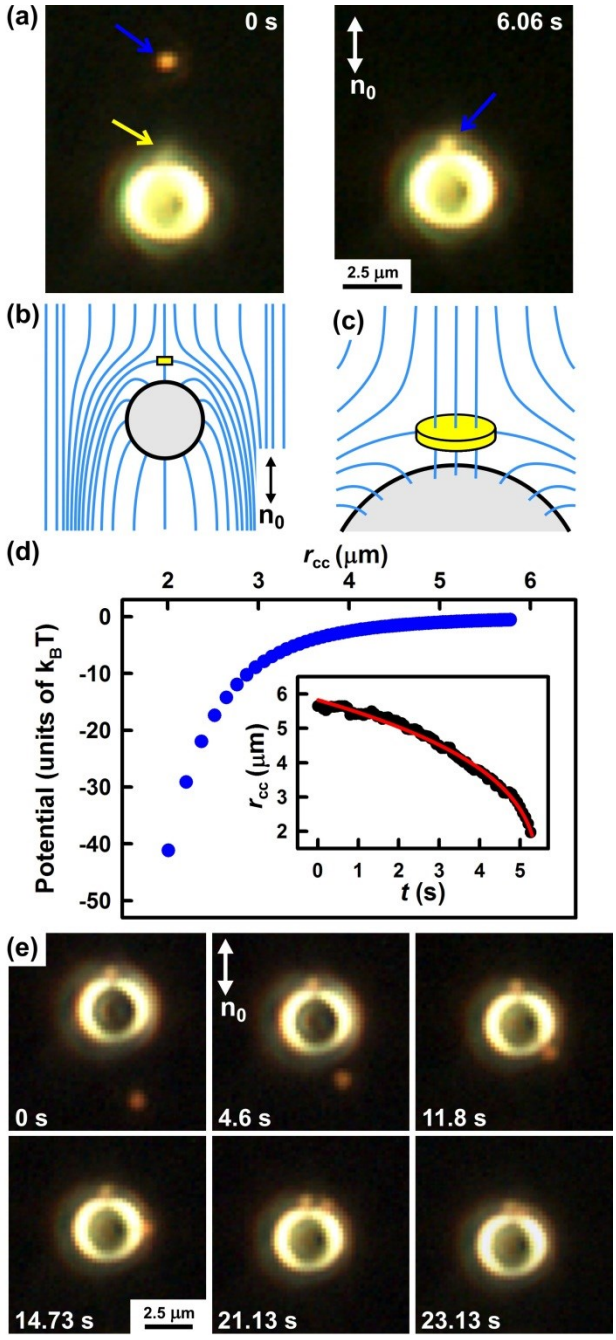

Fig. 5.4. Attraction of a NB nanoplatelet to a microsphere-induced point defect in a nematic LC. (a) Dark-field images show the NB (marked by a blue arrow) moving toward the point defect (marked by a yellow arrow). (b) A schematic diagram of dipolar **n(r)** with NB nanoparticle (yellow) displacing the defect. (c) An enlarged schematic view of the NB platelet in the trap. (d) The elastic interaction potential as a function of a center-to-center separation between particles r_{cc}, derived from the inset plot of r_{cc} vs. time t. (e) Dark-field video frames showing motion of NB to a point defect from the initial position "behind the microsphere," with its sliding around the microsphere surface towards the defect.

Colloidal particles suspended in LCs experience anisotropic interaction forces[38-39] that arise due to minimization of the elastic free energy driven by sharing of director distortions introduced by neighboring particles. Attraction of nanoparticles into topological singularities induced by microspheres is of similar nature and arises due to the displacement of energetically costly regions of distorted **n(r)** and "melted" isotropic defect cores by the nanoparticles. We have used the HOT system[27] to translate the microspheres to the vicinity of metal nanoparticles. Dark-field video microscopy then tracked the motion of colloids after releasing the microparticles in the vicinity of nanoparticles. The sGNRs, GNRs (Fig. 5.3(a,i)) and NBs (Fig. 5.4(a)) were attracted towards point and line defects within a couple microns and eventually trapped by them (Figs. 5.3(a,c,e,g,h) and 5.4(a-c)). Figs. 5.3(a) and 5.4(a) show such nanoparticles being attracted into the point defect in the direction roughly along $\mathbf{n_0}$. The entrapment of nanorods by the "Saturn ring" defect around microsphere is demonstrated in Fig. 5.3(i,j). At large distances, the directionality of the elastic interactions between the microsphere and GNR is similar to that of two quadrupolar LC colloids with "Saturn rings" and the same curvature of **n(r)**-distortions,[38,39,42] repelling at center-to-center separation vectors parallel and perpendicular to $\mathbf{n_0}$ but attracting at intermediate angles.[38,39,42] Even when released with center-to-center vector orientation corresponding to repulsion (Fig. 5.3(j)), the GNR slowly drifts to the attractive angular sector and attracts toward the microsphere roughly along the expected direction of maximum attraction between such quadrupoles.[38,39,42] Once in the vicinity of the microsphere, the GNR slides around its surface by continuously displacing increasingly stronger director distortions and eventually localizes in the defect (Fig. 5.3(j)). In contrast, the directionality of the elastic interactions between microsphere with the "Saturn ring" and sGNR

with two boojums (Fig. 5.3(j)) is similar to the case of two quadrupolar LC colloids having opposite distributions of defect signs and opposite curvature of **n(r)**-distortions,[43] attracting at center-to-center separation vectors parallel and perpendicular to $\mathbf{n_0}$ but repelling at the intermediate angles. When released having the center-to-center separation vector perpendicular to $\mathbf{n_0}$, sGNRs head straight to the disclination until entrapped (Fig. 5.3(j)). Once trapped in the point defect, sGNRs and GNRs spontaneously orient orthogonally to the sphere surface and along $\mathbf{n_0}$, as revealed by polarized TPL. GNRs and sGNRs trapped in disclinations align along the defect lines, minimizing the total free energy by maximizing the volume of melted defect core that they displace at this orientation.

Fig. 5.4 shows that NB nanoplatelets are attracted to the point defect not only from close proximity (Fig. 5.4(a)) but even when released at distant initial locations on the side of the microsphere opposite to that of the defect, moving down the path corresponding to the strongest gradient of $\mathbf{n}(\mathbf{r})$ (Fig. 5.4(e)). Defect-trapped NBs orient to have their large-area faces locally parallel to the surface of the microsphere (Fig. 5.4(b,c)). Several NBs can be collected in the region of the point defect simultaneously while preserving this orientation with respect to the microsphere (Fig. 5.4(e)).

By tracking positions of colloids with video microscopy (Fig. 5.3(i)), one can measure the time dependent center-to-center separation $r_{cc}(t)$ between the nanoparticle and the microsphere (inset of Fig. 5.4(d)). In the regime of low Reynolds numbers (Re << 10^{-7} in our case), the inertia effects are negligible and the attractive elastic force is balanced by the viscous drag force[37,44] $F_d = c_d \cdot v_r(t)$, where c_d is an average drag coefficient in an anisotropic fluid and $v_r(t) = dr_{cc}/dt$ is a relative velocity of the nanoparticle with respect to the center of the microsphere. To estimate c_d, we have measured self diffusion constants $D_{\parallel}$ and $D_{\perp}$ of the nanoparticle for the diffusion

directions along and perpendicular to $\mathbf{n_0}$, respectively.[44] Using estimated c_d and measured $v_r(t)$ (see, for example, the inset in Fig. 5.4(d)), one determines the separation-dependent attractive potential (Fig. 5.4(d)), minimum of which yields the attraction energy W_0 of a nanoparticle to the defect before being entrapped in the defect core; the interaction energies increase with the nanoparticle size (Table 5.1).

Table 5.1. Properties of gold nanoparticles in a nematic liquid crystal

Nanoparticles	Capping	axial diameter D_{np} (nm)	length L_{np} (nm)	elastic energy of distortions in an "equivalent" sphere ΔW (k_BT)	attraction energy near contact with point/line defects W_0 (k_BT)
Microgold (MG)	NSol(akyl acrylate)	150	800	235	-
Starfruit (SF)	NSol(akyl acrylate)	100	500	153	-
Nanoburst (NB)	NSol(akyl acrylate)	~500	100	262	~40/-
nanorods (GNR)	NSol(akyl acrylate)	25	60	30	(3-5)/20
nanorods (sGNR)	polystyrene	10	45	15	(3-5)/20

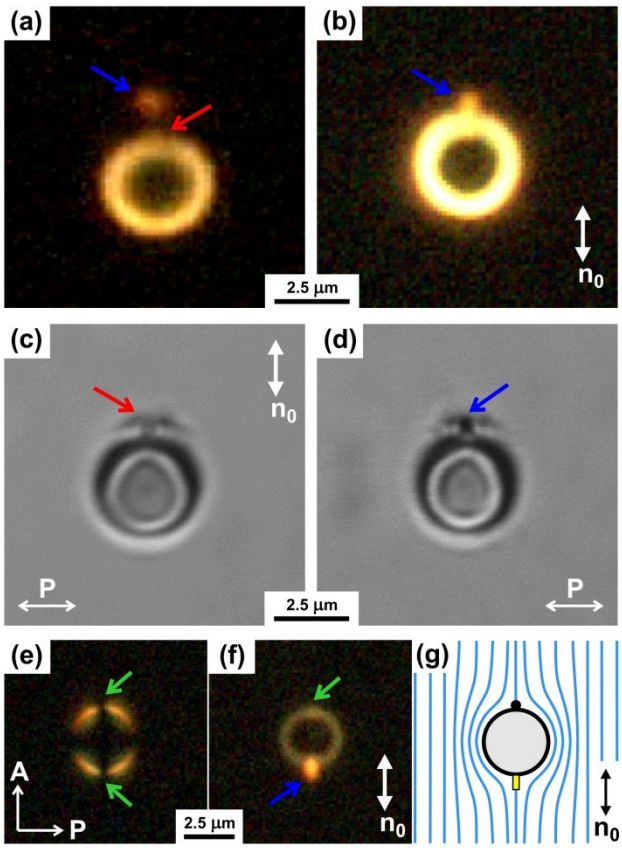

Fig. 5.5. Entrapment of MGs and SFs by point singularities assisted by optical tweezers. (a) Dark-field image showing MG (marked by a blue arrow) in the initial local-minimum-energy location away from a bulk point defect (marked by a red arrow). (b) A dark-field image of MG nanoparticle stably trapped in a point defect region after the use of optical tweezers to overcome the elastic energy barrier. (c) A bright-field image of the microsphere with dipolar **n(r)** and a point defect. (d) A bright-field image of a MG nanorod (pointed by a blue arrow) displacing the bulk point defect. (e) A polarizing microscopy image showing the quadrupolar **n(r)** around melamine resin microsphere. (f) A dark-field image of SF nanorod (marked by the blue arrow) entrapped by a surface point defect (the boojum is marked by a green arrow) with the assistance of optical tweezers. (g) A schematic of **n(r)** (blue lines) around a microsphere with tangential anchoring and SF nanoparticle (yellow) corresponding to (e) and (f); the black filled semicircle in (g) shows the boojum.

MG and SF colloids also experience attraction toward the silica microsphere (Fig. 5.5(a)). However, in contrast to GNRs, sGNRs and NBs, they do not self-localize into the hyperbolic hedgehog core but rather in the region of distorted **n(r)** at a distance to the point defect comparable to their size, forming weakly bound microsphere-nanoparticle pairs with the r_{cc}

changes due to central fluctuations within ~0.5μm. The same is true in the vicinity of boojum defects induced by melamine resin microparticles (Fig. 5.5(e,f)): SFs do not localize in the boojum regions, but stay elastically bound in the nearby region with strongly distorted **n(r)**, with r_{cc} also changing due to thermal fluctuations up to ~0.5μm. Their behavior is consistent with the elastic dipole-qudrupole and quadrupole-quadrupole interactions that was previously explored for microspheres.[27,38,39,43] To locate MG and SF nanoparticles more precisely within the defects, we have used optical manipulation. Laser beams of moderate power (20-50 mW) focused between the point defect and the nanoparticle lead to trapping of MGs and SFs at the bulk point defects (Figs.5.5(b,d)) or surface boojums (Figs.5.5(f,g)). Dark-field microscopy (Fig. 5.5(b,f)) reveals that defect-trapped MGs and SFs orient perpendicular to the microsphere surface.

The shape- and size-dependent oriented attraction and trapping of metallic nanoparticles by topological defects are driven by the minimization of director distortions and corresponding elastic energies. They can be qualitatively understood by comparing anisotropic particle dimensions R_{np}, L_{np} and the so-called surface extrapolation length $l_a = K/W_a \sim$ 0.1-10 μm.[19] The surface anchoring effects are negligible for particles with $R_{np} < l_a$, so that they are simply driven towards regions with the strongest gradients of **n(r)** and eventually trapped while displacing LC regions with increasingly stronger and stronger elastic distortions. One can roughly estimate the maximum free energy reduction $\Delta W \sim K \cdot R_{eqs}$ due to replacing the energetically costly volume of the distortions by a particle of volume $V_{np} = \pi D_{np}^2 L_{np} / 4$ as the elastic energy of distortions in the region limited by an "equivalent" sphere of volume V_{np} and radius R_{eqs} (Table 5.1). As expected, the estimated energy reduction ΔW is larger or comparable to the attraction energy W_0 between the sGNR, GNR ($R_{eqs} < l_a$) and defects measured near the

contact with the singularity at a distance limited by a ~10 nm resolution of videotracking (Table 5.1). When $R_{eqs} \gtrsim l_a$, the director field around the nanoparticle is highly dependent on the boundary conditions at its surface, and such a nanoparticle may induce additional elastic distortions if placed into the region with the non-uniform **n(r)**, so that the superposition of pre-existing and nanoparticle-induced director distortions may not always lead to lower elastic energy. This is the case for MG and SF nanoparticles, which are driven toward the region with strongly distorted **n(r)** around the microparticles (Fig. 5.4(a)) until the mismatch of **n(r)** around the microparticle and nanoparticles causes an energetic barrier > k_BT and localizes them next to the topological singularity in a location which is likely a metastable state. Laser tweezers help to overcome this energetic barrier when the trapping beam is placed in the region between the point defect and MG or SF, further distorting **n(r)** and dragging MGs and SFs into the stable trapping position coinciding with the core of the point defect (Figs. 5.5(b,d,f,g)). Although R_{eqs} of NBs is comparable to that of MGs and SFs, NB colloids spontaneously localize in the defect cores, which is because the elastic distortions induced by these nanoparticles are weak and distributed around their perimeter, so that they do not result in significant elastic energy barriers as the particle traverse toward defect cores. This finding indicates that oriented trapping of nanoparticles by topological defects is highly dependent on their shape, in addition to the particle size.

Topological singularities entrap nanoparticles with nanoscale precision on the order of the defect core radius (~ 10 nm) with respect to the center of the defect core, better than in the conventional optical traps (dependent on laser power but on the order of the diffraction limit, i.e., about hundreds of nanometers) and even better than in the case of plasmonic optical traps.[45] The changes of the center-to-center distance between the microsphere and entrapped nanoparticles

are smaller or comparable to the 10 nm resolution with which we can localize the centers of these colloids by means of video microscopy. At short distances < R_{np}, the topological defect trapping force F_{tdt} is expected to increase linearly with the displacement[26,27] Δr of the nanoparticle from the equilibrium position in the elastic trap following Hooke's law $F_{tdt} = \kappa_{tdt} \Delta r$, where κ_{tdt} is a trap stiffness. F_{tdt} is maximized when $\Delta r \sim R_{eqs}$, and can be called a "trap escape force" F_{te} in analogy with the case of optical trapping.[26,27] This escape force for the point defect trap can be determined using the energy ΔW_R cost of displacing the nanoparticle from the elastic trap by a distance R_{eqs}. The reduction energy ΔW_R is equal to the sum of the defect core energy and the elastic energy of director distortions in a volume of the defect occupied by the nanoparticle. In the case of the hyperbolic point defect (Fig. 5.3(f)), ΔW_R can be estimated using the expression $W_{hp} = \frac{8}{3}\pi K\left(R_{eqs} - r_{pc}\right) + \gamma r_{pc}^3$, where W_{hp} is the elastic energy of the hedgehog defect, $\gamma \sim 10^5$ J/m^3 is the energy density of the isotropic core and $r_{pc} = \sqrt{(8/9)(\pi/\gamma)K} \approx 13\,\text{nm}$ is its radius.[19] The first term in W_{hp} corresponds to the elastic contribution and the second term describes the energy of a "melted" isotropic core. In the case of the "Saturn ring" defect (Fig. 5.3(i,j)), ΔW_R can be estimated as an elastic energy of a wedge disclination loop of the strength k = -1/2, $W_{sr} = \pi k^2 K L \ln\left(R/r_{dc}\right) + W_{dc}$, where R is a characteristic dimension of the considered system, L is the disclination length, $r_{dc} \sim$ 10 nm and W_{dc} are the radius and the energy of the disclination core, respectively.[19] For R_{np} comparable to the defect core size, the energy reduction is mostly due to the energy of the displaced isotropic defect core, but the contribution of the elastic part of the defect energy increases further with increasing R_{np}. Using calculated reduction energy ΔW_R for different nanoparticles and defects (Table 5.2), one can roughly estimate the order of magnitude of the corresponding trap escape forces as $F_{te} \sim \Delta W_R / R_{eqs}$

(Table 5.2). Consistent with the range of obtained values, optical tweezers at moderate laser powers of about 50 mW (corresponding optical trapping forces of up to ~ 20 pN[27]) at the sample plane do not exert optical trapping forces that would be strong enough to remove nanoparticles from the topological defect traps once they are entrapped. The stiffness of these topological defect traps is $\kappa_{tdt} \geq k_{\mathrm{B}}T/\Delta r^2$, where Δr ~ 10 nm is the maximum experimentally observed displacement of the nanoparticle from the center of the defect trap, precise measurement of which is limited by the resolution of videomicroscopy. The estimated stiffness κ_{tdt} for different studied nanoparticles is 20-100 pN/nm, which is significantly larger than the stiffness of optical tweezers trapping gold nanoparticles at relatively high laser powers[15-17] and plasmonic optical traps.[45]

Table 5.2. Properties of topological defect traps for different gold nanoparticles

Nanoparticles	reduction energy ΔW_{R} ($k_{\mathrm{B}}T$)		trap escape force F_{te} (pN)	
	point defect	line defect	point defect	line defect
MG	1854	3817	51	105
SF	1170	2335	49	99
NB	2078	4318	51	107
GNR	132	334	29	73
sGNR	59	136	27	62

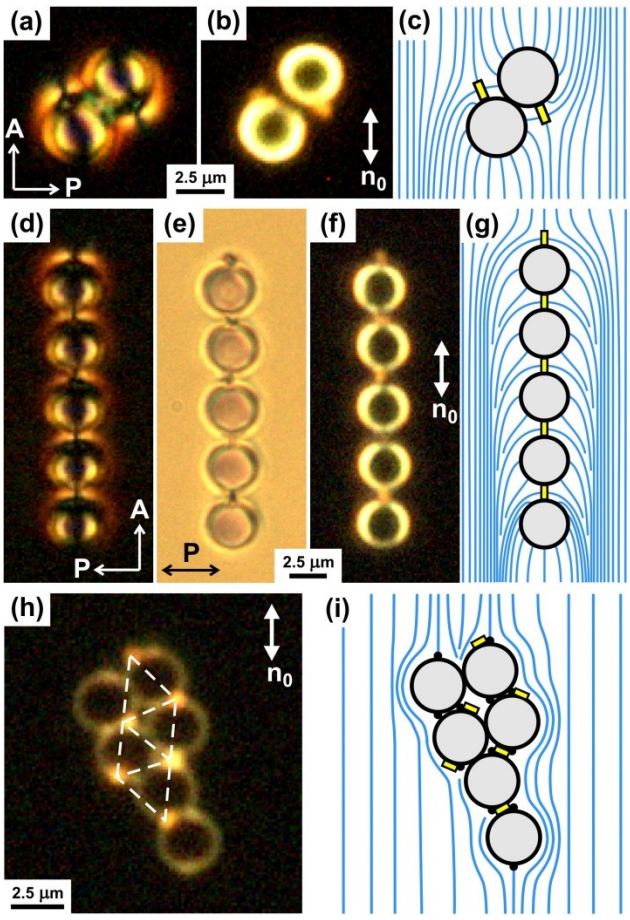

Fig. 5.6. Colloidal superstructures of gold nanoparticles and dielectric microspheres. (a-c) Polarizing and dark-field microscopy images and a schematic diagram showing microsphere-MG pairs assembled in anti-parallel direction, respectively. (d-g) Polarizing, bright-field, and dark-field microscopy images and a schematic diagram showing chains of microsphere-MG dimers aligned along $\mathbf{n_0}$, respectively. (h, i) A dark-field image and a schematic diagram of an array (accentuated by a dashed line) formed by SF nanorods trapped in distorted regions next to melamine resin microspheres.

The mobility of nanoparticle-microsphere dimers in the LC can be used to assemble desired photonic structures. Fig. 5.6 shows examples of such assemblies levitating in the LC bulk because of the repulsive elastic interactions between the colloidal dimers and confining substrates. Once nanoparticles are trapped by defects, the dimers of plasmonic and dielectric particles can assemble into patterns dictated by elastic interactions in the LC. For example, Figs.

5.6(a-c) show a pair of MGs trapped into the hedgehogs due to two microspheres. Figs. 5.6(d-g) shows a chain of MG-microsphere pairs along $\mathbf{n_0}$; the 3μm spacing between MGs is defined by the diameter of microspheres. Nanoparticles can be also assembled into two-dimensional arrays, such as the one composed of SF nanoparticles trapped into boojums (Fig. 5.6(h,i)). Interestingly, the alignment of SFs often changes as multiple microparticles self-assemble into more complex structures, which may be promoted by sharing of individual anisotropic nanoparticles by two boojums induced by the two interacting microspheres (Fig. 5.6(i)). The distance between nanoparticles and their alignment in such structures can be controlled by using microspheres with different size and surface chemistry, depending on the need of specific photonic applications. Although the surface boojums localize nanoparticles in a direct contact with the surface of the microspheres, the bulk point and line defects can localize nanoparticles at a well-controlled distance and orientation with respect to the surface of the microsphere. The distance from the center of microsphere to the hyperbolic point defect is known to be ~ 1.2a,[38-39] where a is the radius of the microsphere, while the radius of the "Saturn ring" defect is typically ~ 1.1a.[41] By controlling the size of the colloidal microspheres in the submicrometer and micrometer ranges as well as controlling the size and shape of entrapped nanoparticles, one can use the demonstrated scaffolding of nanoparticles to form two-particle nanoantennas with the distance between the surfaces of bigger and smaller colloids controlled within 10-100 nm. One can also envision the assembly of ring-shaped structures of multiple plasmonic nanoparticles entrapped and oriented in the "Saturn ring" defect line encircling a bigger metallic or dielectric colloidal sphere. In addition to microspheres, one can utilize bigger particles of other shapes, like platelets and rings that are known to induce different types of defects.[44] Importantly, all of these fluid-borne colloidal microparticles with scaffolded nanoparticles can be further used for

self-assembly or light-guided hierarchical superstructures with a host of potential applications, such as fabrication of novel types of tunable metamaterials.

5.4 Conclusions

In conclusion, we have demonstrated oriented trapping of plasmonic gold nanoparticles by topological singularities in nematic LCs. The defect traps induced by colloidal microspheres allow for highly precise, oriented spatial localization, strong maximum trapping potentials of 100-5000 k_BT, and large trap stiffnesses that depend on the shape and size of trapped nanocolloids and are of great interest for fundamental studies in nanophotonics and plasmonics. The demonstrated elastic scaffolding of smaller nanoparticles by elastic distortions and defects due to bigger microparticles yields an interesting colloidal system with the anisotropic nanoparticles at well-defined orientation with respect to the surface of microparticles and the far-field LC director. The ensuing colloidal dimers of plasmonic metal nanoparticles and dielectric microparticles can be assembled into a number of one- and two- dimensional arrays of desired configuration, as needed for applications in nanoscale photonics and plasmonics. The use of metal microparticles instead of dielectric ones may enable applications in nanoantennas as well as in nanoscale energy conversion systems. Similar approaches may be used for nanoscale trapping of other types of nanoparticles, like semiconductor nanocrystals, which are important for imaging and energy conversion. Since self-assembled structures of plasmonic nanoparticles can exhibit a broad range of magnetic and electric resonances,[7] plasmonic nanoparticle self-assemblies in a fluid LC medium with facile response to electric fields may offer a means for low-voltage control of their optical response and enable self-assembly-based fabrication of tunable bulk metamaterials.

5.5 REFERENCES

1. Lal, S.; Link, S.; Halas, N. J. *Nat. Photonics* **2007**, *1*, 641-648.

2. Jain, P. K.; Huang, X.; El-Sayed, I. H.; El-Sayed M. A. *Accounts Chem. Res.* **2008**, *41*, 1578-1586.

3. Sau, T. K.; Rogach, A. L.; Jäckel, F.; Klar, T. A.; Feldmann, J. *Adv. Mater.* **2010**, *22*, 1805-1825.

4. Morfa, A. J.; Rowlen, K. L.; Reilly, T. H.; Romero, M. J.; van de Lagemaat, J. *Appl. Phys. Lett.* **2008**, *92*, 013504.

5. Perassi, E. M.; Hernandez-Garrido, J. C.; Sergio Moreno, M.; Encina, E. R.; Coronado, E. A.; Midgley, P. A. *Nano Lett.* **2010**, *10*, 2097-2104.

6. Habteyes, T.; Dhuey, S.; Cabrini, S.; Schuck, P. J.; Leone, S. R. *Nano Lett.* **2011**, *11*, 1819-1825.

7. Fan, J. A.; Wu, Ch.; Bao, K.; Bao, J.; Bardhan, R.; Halas, N. J.; Manoharan, V. N.; Nordlander, P.; Shvets, G.; Capasso, F. *Science* **2010**, *328*, 1135-1138.

8. Shalaev, V. M. *Nat. Photonics* **2007**, *1*, 41-48.

9. Romero, M. J.; van de Lagemaat, J. *Phys. Rev. B* **2009**, *80*, 115432.

10. Ni, W.; Ambjörnsson, T.; Apell, S. P.; Chen, H.; Wang, J. *Nano Lett.* **2010**, *10*, 77-84.

11. Johnson, J. C.; Reilly, T. H.; Kanarr, A. C.; van de Lagemaat, J. *J. Phys. Chem. C* **2009**, *113*, 6871-6877.

12. Khatua, S.; Chang, W.-S.; Swanglap, P.; Olson, J.; Link, S. *Nano Lett.* **2011**, *11*, 3797-3802.

13. Dorfmüller, J.; Dregely, D.; Esslinger, M.; Khunsin, W.; Vogelgesang, R.; Kern, K.; Giessen, H. *Nano Lett.* **2011**, *11*, 2819-2824.

14. Alvarez-Puebla, R. A.; Agarwal, A.; Manna, P.; Khanal, B. P.; Aldeanueva-Potel, P.; Carbo-Argibay, E.; Pazos-Perez, N.; Vigderman, L.; Zubarev, E. R.; Kotov, N. A.; Liz-Marzan, L. M. *Proc. Natl. Acad. Sci. USA* **2011**, *108*, 8157-8161.

15. Hansen, P. M.; Bhatia, V. K.; Harrit, N.; Oddershede, L. *Nano Lett.* **2005**, *5*, 1937-1942.

16. Guffey, M. J.; Scherer, N. F. *Nano Lett.* **2010**, 10, 4302-4308.

17. Seol, Y.; Carpenter, A. E.; Perkins, T. T. *Optics Lett.* **2006**, *31*, 2429-2431.

18. Pelton, M.; Liu, M.; Kim, H. Y.; Smith, G.; Guyot-Sionnest, P.; Scherer, N. F. *Optics Lett.* **2006**, *31*, 2075-2077.

19. Chaikin, P.M.; Lubensky, T.C. *Principles of Condensed Matter Physics.* Cambridge University Press; Cambridge, 1995.

20. Liu, Q.; Cui, Y.; Gardner, D.; Li, X.; He, S.; Smalyukh, I. I. *Nano Lett.* **2010**, *10*, 1347-1353.

21. Khatua, S.; Manna, P.; Chang, W.-S.; Tcherniak, A.; Friedlander, E.; Zubarev, E. R.; Link, S. *J. Phys. Chem. C* **2010**, *114*, 7251-7257.

22. Ezhov, A. A.; Shandryuk, G. A.; Bondarenko, G. N.; Merekalov, A. S.; Abramchuk, S. S.; Shatalova, A. M.; Manna, P.; Zubarev, E. R.; Talroze, R. V. *Langmuir* **2011**, *27*, 13353-13360.

23. Khanal, B. P.; Zubarev, E. R. *Angew. Chem. Int. Ed.* **2009**, *48*, 6888-6891.

24. Slaughter, L. S.; Chang, W.-S.; Swanglap, P.; Tcherniak, A.; Khanal, B. P.; Zubarev, E. R.; Link, S. *J. Phys. Chem. C* **2010**, *114*, 4934-4938.

25. Koenig, G. M.; Lin, I.-H.; Abbott, N. L. *Proc. Natl. Acad. Sci. USA* **2010**, *107*, 3998-4003.

26. Smalyukh, I. I.; Kachynski, A. V.; Kuzmin, A. N.; Prasad, P. N. *Proc. Natl. Acad. Sci. USA* **2006**, *103*, 18048–18053.

27. Trivedi, R. P.; Engström, D.; Smalyukh, I. I. *J. Opt.* **2011**, *13*, 044001.

28. van de Hulst, H. C. *Light Scattering by Small Particles*. 2nd ed.; Dover Publications, Inc.; New York, 1981.

29. Koenig, G. M.; de Pablo, J. J.; Abbott, N. L. *Langmuir* **2009**, *25*, 13318-13321.

30. Wang, H.; Huff, T. B.; Zweifel, D. A.; He, W.; Low, P. S.; Wei, A.; Cheng, J.-X. *Proc. Natl. Acad. Sci. USA* **2005**, *102*, 15752–15756.

31. Zijlstra, P.; Chon, J. W. M.; Gu, M. *Nature* **2009**, *459*, 410-413.

32. Burylov, S. V.; Raikhner, Yu. L. *Phys. Lett. A* **1990**, *149*, 279-283.

33. Burylov, S. V.; Raikhner, Yu. L. *Phys. Rev. E* **1994**, *50*, 358-367.

34. Ruhwandl, R. W.; Terentjev, E. M. *Phys. Rev. E* **1997**, *56*, 5561-5565.

35. Andrienko, D.; Allen, M. P.; Skačej, G.; Žumer, S. *Phys. Rev. E* **2002**, *65*, 041702.

36. Matthias, H.; Kitzerow, H.-S. *Mol. Cryst. Liq. Cryst.* **2009**, *508*, 127-136.

37. Tkalec, U.; Škarabot, M.; Muševič, I. *Soft Matter* **2008**, *4*, 2402-2409.

38. Poulin, P.; Stark, H.; Lubensky, T. C.; Weitz, D. A. *Science* **1997**, *275*, 1770-1773.

39. Poulin, P.; Weitz, D. A. *Phys. Rev. E* **1998**, *57*, 626-637.

40. Ognysta, U.; Nych, A.; Nazarenko, V.; Muševič, I.; Škarabot, M.; Ravnik, M.; Žumer, S.;

Poberaj, I.; Babič, D. *Phys. Rev. Lett.* **2008**, *100*, 217803.

41. Gu, Y.; Abbott, N. L. *Phys. Rev. Lett.* **2000**, *85*, 4719-4722.

42. Škarabot, M.; Ravnik, M.; Žumer, S.; Tkalec, I.; Poberaj, I.; Babič, D.; Osterman, N.; Muševič, I. *Phys. Rev. E* **2008**, *77*, 031705.

43. Ognysta, U. M.; Nych, A. B.; Uzunova, V. A.; Pergamenschik, V. M.; Nazarenko, V. G.; Škarabot, M.; Muševič, I. *Phys. Rev. E* **2011**, *83*, 041709.

44. Lapointe, C. P.; Mason, T. G.; Smalyukh, I. I. *Science* **2009**, *326*, 1083-1086.

45. Grigorenko, A. N.; Roberts, N. W.; Dickinson, M. R.; Zhang, Y. *Nat. Photonics* **2008**, *2*, 365-370.

Chapter 6: Optical generation, templating, and polymerization of three-dimensional arrays of liquid crystal defects decorated by plasmonic nanoparticles

Adapted from: *Phys. Rev. E* **87**, 032503 (2013)

Chapter Overview

In the previous chapter we described using microspheres to generate defects that elastically trap GNP, here we describe a method of creating defects without the requirement of microspheres. Defects in liquid crystals are used to model topological entities ranging from skyrmions in high energy physics to early-Universe cosmic strings, as well as find practical applications in self-assembly of diffraction gratings and in scaffolding of plasmonic nanoparticles, but they are hard to control and organize into three-dimensional lattices. We laterally scan focused laser beams to produce periodic arrays of twist-stabilized defects forming either linear (fingers) or axially symmetric (torons) configurations in partially polymerizable liquid crystal films. Polymerization allows for stabilization of these structures and the formation of three-dimensional arrays of defects by stacking of the thin cholesteric films on top of each other. In the process of fabrication of such arrays, we polymerize the liquid crystal film with an array of torons or fingers and then sequentially produce and photopolymerize new liquid crystal layers on top of it, thus obtaining a three-dimensional structure of twist-stabilized defects in a layer-by-layer fashion. Templating by the polymerized layer spontaneously yields ordered organization of fingers and torons in the new cholesteric layer, thus enabling a three-dimensional ordered structure of defects. Non-destructive three-dimensional imaging of director fields by use of three-photon excitation fluorescence polarizing microscopy reveals the nature of topological singularities and physical underpinnings behind the observed novel templating effect. Three-

dimensional patterning of defects templates the self-assembly of plasmonic nanoparticles into individual singularities and their arrays, laying the groundwork for potential applications in nanophotonics, plasmonics, metamaterial fabrication, and nanoscale energy conversion.

6.1. Introduction

Topological defects in liquid crystals (LCs) provide optically imagable models of skyrmions first introduced in particle physics [1] and recently also observed in chiral magnets [2-3], phase singularities found in electron [4-5] and laser beams [6-7], and early-Universe cosmic strings [8]. In addition to regular point, line, and wall defects, LCs can support the existence of director fields in the form of Hopf fibrations, torons, merons, skyrmions [9-14] and linked and knotted disclination loops [15] stabilized by chirality, colloids, or both. Arrays of line defects enable the realization of thermodynamically stable twist grain boundary and blue phases of LCs, in which periodic arrangements of defects are found in the ground state [16]. Optical anisotropy of the LC enables a large number of potential applications, such as diffraction gratings and optical vortex generators [13,14], as well as experimental exploration of low-dimensional topology [17,18]. However, generation and stabilization of three-dimensional patterns of these defects in LCs is non-trivial and has not been achieved so far.

When a cholesteric LC is confined into a homeotropic cell with thickness on the order of the equilibrium cholesteric pitch, the system is frustrated and either remains in a purely unwound homeotropic state or forms well-defined, isolated, solitonic defects known as fingers and torons [10-14, 19, 20], which allow for local twisting of the LC director field n(r) to occur. The torons of the first type consist of two hyperbolic hedgehog point defects and a looped double-twist

cylinder that introduces energetically favorable twist while satisfying the boundary conditions set by the confining substrates and meet the vertically aligned far-field director n_0 [10]. Torons can also mediate an experimental realization of the Hopf fibration, which plays an important role in topology and is also found in toroidal DNA condensation [9, 17, 18]. Fingers of the first type resemble merons in various other condensed matter systems [21]. Similar to the so-called Lehmann clusters observed in short-pitch cholesterics [22-24], they consist of twist-stabilized quadrupoles of λ-disclinations of half-integer strengths with translational invariance along their length. Although these defects are long-term stable in non-polymerizable cholesteric LC systems, they can walk around in the LC cells due to thermal fluctuations when generated using focused beams of relatively low laser generation power (note that optical generation at high laser powers can mitigate this problem and allow for formation of large periodic arrays) [13]. The torons also can be perturbed during optical imaging as well as when the LC responds to temperature changes, mechanical stresses, and various external fields. Although this facile response of torons, fingers, and their periodic arrays to external fields can be utilized to realize optically- and electrically-tunable diffraction gratings and optical vortex generators [13, 14], some of the potential applications of toron arrays may require thin solid films that are insensitive to external fields and temperature variations in the surrounding environment. Although photopolymerization is a natural approach to achieve such structured films with arrays of defects, these films have not been experimentally realized so far and only two-dimensional arrays of torons and fingers have been demonstrated in non-polymerized systems [13, 14].

Nanoparticles possess optical and other properties that are often not observable in the bulk materials of the same chemical composition, most notably surface-plasmon resonance in metallic particles [25, 26], quantum confinement [27-29] and multiple excition generation [29] in

semiconductor nanoparticles, and increased chemical activity due to large surface area to volume ratio and rougher surfaces in a variety of different nano-sized colloids [30]. During the last several decades, chemists have developed well-controlled syntheses of anisotropic nanocrystal particles with orientation-dependent optical properties (see, for example, Refs. [25-31]). The control of alignment, orientation, and assembly of individual and small groups of such anisotropic nanoparticles is important for understanding their collective behavior for the development of approaches for fabrication of optical metamaterials, plasmonic, nanophotonic, and solar energy harvesting technologies [29-40]. The energetic cost of LC defects allows them to entrap and orient fluid-borne anisotropic nanoparticles in a reproducible manner and with well-controlled position and orientation [31]. However, these particle-defect assemblies can undergo Brownian motion in a fluid LC medium and interact with each other over time. Although these elasticity-mediated interactions can enable hierarchical self-assembly of nanoparticles and defects into colloidal superstructures defined by colloidal microparticles [31], they preclude the possibility of patterning of nanoparticles into arbitrary trap arrays defined by topological defects alone. Furthermore, the typical requirement of working with a fluid cell of thickness comparable to the cholesteric pitch often makes the exploration of three-dimensional interactions and assemblies impossible. Similar to the arrays of defects without nanoparticles, some of the applications of periodic defect-nanoparticle assemblies may benefit from converting them into solid thin films with "frozen" original structure and composition obtained by means of the optically guided self-assembly of arbitrary arrays of torons and fingers.

In this chapter, we polymerize the structures of torons and fingers as well as assemble various three-dimensional defect arrays controlled by means of scanned laser beams and soft templating. Producing these arrays in a partially polymerizable system allows for layer-by-layer templated

assembly of LC structures and post-production control of the effective optical anisotropy of the sample (e.g., via washing out most of the unpolymerized LC and subsequent infiltration of the ensuing nanoporous thin films with isotropic fluids). Polymerization stabilizes the obtained three-dimensional defect structures and ensuing n(r)-configurations against mechanical stresses, ambient temperature variations, and external fields (whenever this response is unwanted). Polymerization also eliminates Brownian motion of torons and fingers and makes the presence of confining glass substrates unnecessary, allowing for the generation of multi-layer structures with well-defined defect configurations as well as for obtaining thin flexible films with controlled n(r) and nanoparticle patterns. We demonstrate that, during the multi-layer patterning of defects, the thickness variations and director distortions associated with partially polymerized films have an interesting templating effect on the new layer, allowing for exploration of the fundamental physical underpinnings behind these topological structures and being potentially useful for large-scale production. Control of polymerization conditions can lead to the permanent capture of non-equilibrium n(r)-configurations to enable studies of toron formation and unstable non-equilibrium geometries not observed in non-polymerizable LC systems. Furthermore, our system may allow for detailed fundamental explorations of the interplay between topologies of Hopf fibrations, torons, merons, skyrmions, and various LC singularities in the form of line and point defects that may have an impact on the understanding of other condensed matter systems. Thus, the demonstrated ability of three-dimensional patterning of topological defects in the LC system and non-destructive imaging of the ensuing molecular alignment fields and defects may also enable a fertile ground for new basic science.

6.2. Materials, Methods, and Techniques

6.2.1. Sample preparation

The studied partially polymerizable cholesteric LC mixture was prepared by first mixing 69% of non-reactive nematic E7 with 30% of a diacrylate nematic (consisting of 12% of RM 82 and 18% of RM 257) and 1% initiator Irgacure 184, which was then followed by mixing of 99.8% of this nematic mixture with 0.2% of reactive chiral mesogen LC756 (Fig. 6.1). The nematic compounds have been obtained from Merck and EM Chemicals. The chiral LC756 was obtained from BASF and the photoinitiator from CIBA Specialty Chemicals. The obtained powder mixture was first dissolved in dichloromethane to homogenize, heated to 85 C for one day to remove the solvent, and cooled down to obtain a room temperature, chiral nematic mixture with the equilibrium cholesteric pitch p=9 μm. This cholesteric mixture was infiltrated into LC cells with homeotropic anchoring boundary conditions and thickness d comparable to p and optimized for stabilization of unwound director configurations at zero field while enabling generation of multistable twisted configurations, such as arrays of fingers and torons. To fabricate the cells, glass substrates with conductive indium tin oxide (ITO) coatings were spin-coated with polyimide SE1211 (Nissan) at 2700 rotations per minute for 30 seconds and then baked (5-minutes at 90°C followed by one hour at 180°C) to set strong vertical surface boundary conditions for the LC director. Electrically-controlled wedge cells with thickness d=7-10 μm were produced by separating two glass substrates with glass fiber segments of diameter 7 μm in UV curable glue at one end of the cell and segments of diameter 10 μm in UV curable glue at the opposite end of the cell. We have infiltrated the LC into the cells by capillary forces in the

isotropic phase at 80°C to prevent flow-related defects in the long-range alignment. Wire leads were attached to the ITO electrodes for electric control of the cells. When necessary, spontaneously-occurring residual defects were "erased" by applying an electric field across the cell so that large-area, purely homeotropic regions of the cell could be used for optical sculpturing of desired defect patterns.

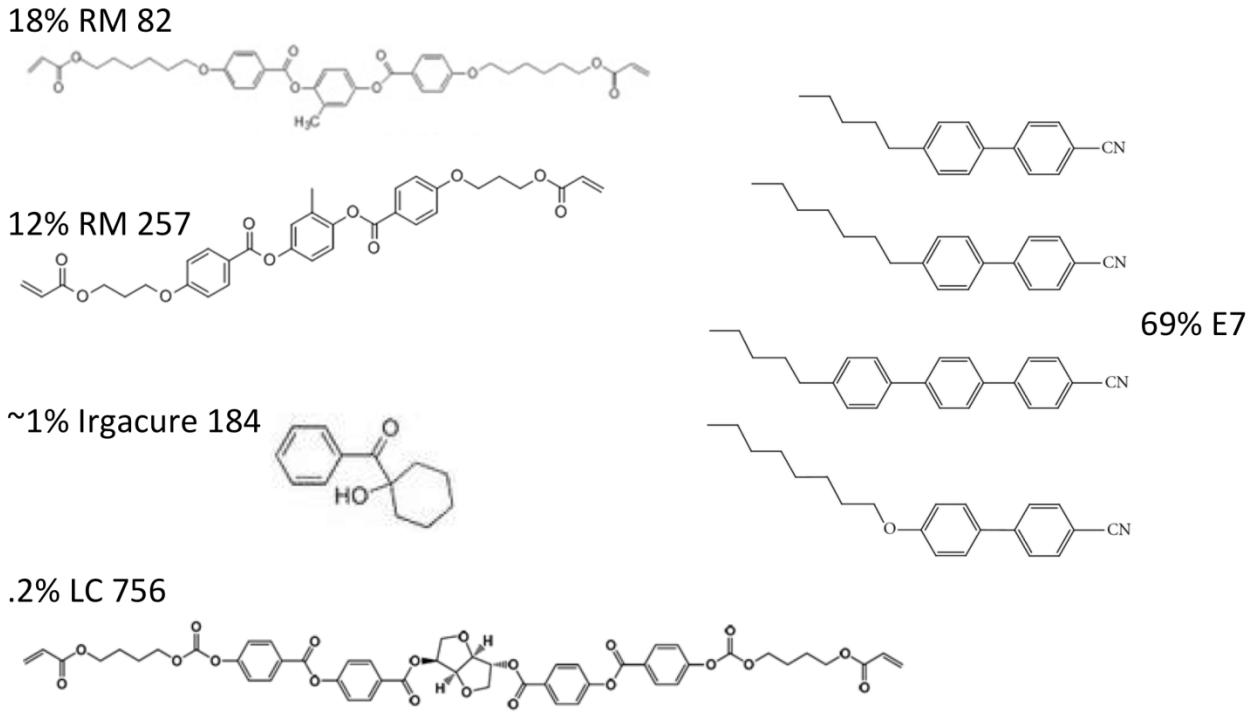

Fig. 6.1. Chemical composition of the used partially polymerizeable cholesteric mixture: 30% diacrylate reactive mesogens RM 82 and RM 257 (top left) that can cross-link to form the polymer network; 69% non-reactive nematic mixture E7 (right); 1% UV activated radical initiator Irgacure 184 (middle left). 99.8% of the above mixture is further mixed with 0.2% chiral diacrylate mesogen LC 756 to obtain a cholesteric LC of $p = 9$ μm.

Patterns of torons and fingers were first defined using a LabVIEW-based software written by us and then drawn using the laser scanning system described below. The LC cells were then polymerized under relatively weak UV exposure (by means of a setup with a 20 W mercury bulb obtained from Cinch) to avoid thermal-gradient-induced perturbations of the optically generated LC textures with torons and fingers. For comparison, we will also discuss morphology and

structure of thin cholesteric films obtained under polymerization conditions very different from these above-described optimized conditions, in particular when using a high-intensity ~200W UV illumination system (PCU-1, obtained from Specialty Coatings Systems, Inc.). In a typical experimental procedure for obtaining multi-layer films, one of the glass substrates (typically the one farther from the UV lamp in the illumination geometry) is removed to expose the polymerized cholesteric thin film. A new wedge cell is then constructed from this substrate already containing a polymerized cholesteric film and a polyimide-SE1211-coated ITO glass plate. The 7 μm and 10 μm spacers in UV glue are placed directly on top of the first layers' spacers respectively, so that the thickness d gradient directions in the two films coincide. This ensures that the regions of equal d/p overlap in the polymerized and new LC layers, thus allowing us to explore how optical generation and templating effects depend on d/p. This new cell is then infiltrated with the unpolymerized mixture to produce a second layer in which defects can be drawn and/or spontaneously form depending on the thickness of the cell and d/p. The second UV exposure is typically performed with the first polymerized layer closer to the UV source, so that the new layer can strongly adhere to the already polymerized LC film and not to the new polyimide-coated glass substrate. The removal of substrates from the partially polymerized layer does not cause noticeable damage to the partially polymerized film. The procedure of layer-by-layer polymerization of structured cholesteric films with torons and fingers can be repeated multiple times, although it soon becomes more and more technically challenging in terms of a precise control of d/p and adhesion of the polymerized cholesteric layers.

Elongated convex pentagonal and octagonal nanoprisms with length × width dimensions of 800 × 150 nm and 65 × 25 nm, respectively, (to which we also refer as gold nanorods because of

their overall rod-like shapes) were obtained as ethanol-based dispersions from Nanopartz, Inc. These nanoparticles were then re-dispersed from ethanol to the used LC host before polymerization by means of first mixing the ethanol dispersion of nanoprisms with the LC and then evaporating ethanol. Vigorous sonication of the dispersion by means of a tip sonicator (Branson Sonfier 250, obtained from Branson Ultrasonics, Inc.) was used to break apart occasional nanoparticle aggregates.

6.2.2. Laser generation and imaging setups

Torons and fingers were generated with a laser scanning system that has been described in detail elsewhere [13, 14]. Briefly, a continuous wave Ytterbium-doped collimated laser was steered by a pair of galvano mirrors powered by a digital-analog converter (NI PCI-MIO-16E-4, from National Instruments) and controlled by homemade LabVIEW-based software. The laser beam was then directed into a BX-51 upright Olympus microscope using a two-lens telescope (Fig. 2). Polarizing optical microscopy (POM) and optical manipulation were performed simultaneously while using objectives with magnifications of 10x, 20x, 50x, and 100x and numerical apertures (NA) ranging from 0.1 to 1.4.

Three-dimensional director structures in cholesteric films were probed using the non-invasive, nonlinear optical imaging technique dubbed “three-photon excitation fluorescence polarizing microscopy” (3PEF-PM) [41]. Biphenyl-containing LC molecules, such as the chemical compounds comprising the commercial mixture E7 (Fig. 6.1), have absorption and fluorescence transition dipoles along their long axis and a peak of single-photon absorption around 290nm while fluorescing in a spectral range around 400 nm [41]. We excite them via a three-photon absorption process that gives origin to a strong $\propto \cos^6\theta$ orientational dependence of the 3PEF-PM

signal intensity and inherent axial resolution in imaging of the director field n(r). The source of the 870nm pulsed excitation is a Ti:Sapphire oscillator (Coherent Chameleon Ultra-II, 680-1080nm excitation range, 140 fs pulse width, 80Mhz repetition rate). Laser polarization is controlled using a Glan-Thompson polarizer and half-wave waveplate. For imaging purposes, a low-power laser beam is focused with a 100x oil immersion objective (NA=1.4). The focal point of the focused beam is positioned and scanned in three dimensions within the sample using a scanning head consisting of two galvano mirrors (for lateral scanning) and a stepper motor (for vertical positioning). The signal is detected with a photomultiplier tube after a 417 nm bandpass filter with 60 nm bandwidth and then used to reconstruct three-dimensional images by means of computer software.

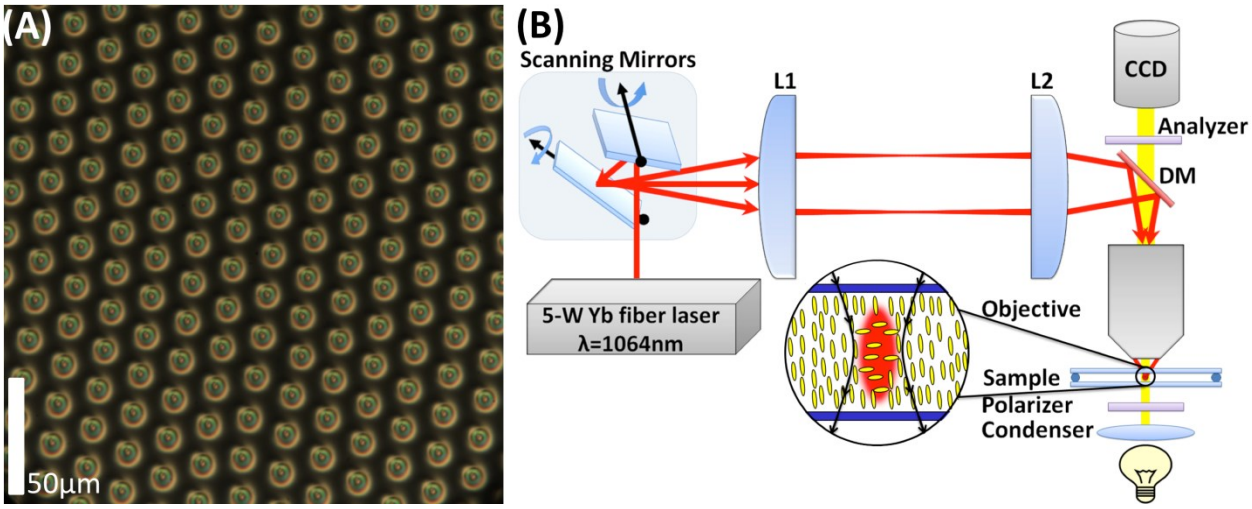

Fig. 6.2. Optical generation of torons. (A) a hexagonal array of torons drawn in a thin cholesteric cell using a scanning laser system. (B) Schematic of the scanning laser generation system built around a 5W Yb laser and Galvano mirrors used to precisely position a focused laser beam in predetermined locations within the cell; this setup allows for the generation of periodic and arbitrary patterns of torons and fingers in desired locations in the LC cell. The crossed polarizer and analyzer in (A) and in all POM textures in this article are parallel to the image edges.

6.2.3. Computer simulations

The equilibrium director structures of axially-symmetric torons and translationally-invariant fingers in single-layer cholesteric films were obtained by means of numerical minimization of elastic free energy using the director relaxation method, as described in detail elsewhere [10, 14], and then used for modeling of multi-layer structures studied in the present work. The model **n**(**r**)-configurations in the multi-layer cholesteric films were created by concatenating two single-layer director structures via superposition of **n**(**r**). The computer-simulated POM textures were then obtained for these model multi-layer **n**(**r**)-configurations using a Jones-matrix approach implemented in Mathematica and using the experimental material and cell parameters, such as optical anisotropy, equilibrium cholesteric pitch, and cell thickness.

The initial minimum-energy **n**(**r**)-configurations in the vertical cross-sections of torons and fingers were represented in the form of arrays of azimuthal and polar angles, having dimensions of 99 x 99 x 36 for the double-layer structures and 35 x 35 x 18 and 99 x 99 x 18 for the individual torons and fingers, respectively. To utilize the Jones-matrix method, we split the cell into a stack of 18 or 36 thin sub-layers while assuming that the orientation of **n**(**r**) is constant across the thickness of one of these sub-layers. The corresponding coordinate-dependent Jones matrices had an optical axis defined by orientation of **n**(**r**) and the phase retardation defined by the optical anisotropy of the LC and polar angle of the director. The resulting POM texture was obtained as a result of successive multiplication of Jones matrices corresponding to a polarizer, a series of thin LC slabs each equivalent to a phase retardation plate with spatially varying optical axis and retardation, and an analyzer. A two-dimensional POM image was then obtained by performing such a Jones-matrix calculation for each pixel and then composing a two-dimensional texture with coordinate-dependent POM intensity analogous to the experimental

images. To properly account for the achromatic nature of our experimental POM observations, we calculated these textures separately for three different wavelengths spanning the entire visible spectrum (475 nm, 510 nm, and 650 nm) and then superimposed them to obtain the achromatic simulated POM image. Computer-simulated vertical 3PEF-PM cross-sections were obtained for the same equilibrium director structures by first finding the coordinate-dependent angles θ between **n**(**r**) and the linear polarization of the probing laser light and then plotting the normalized signal intensity as $I_{3PEF\text{-}PM} = \cos^6\theta$ [41]. All experimental and computer-simulated images of **n**(**r**)-structures in single and multi-layer cholesteric films closely match each other and strongly support the interpretation of experimental findings that we describe below.

6.3. Results

6.3.1. Preparation of single-layer cholesteric cells

The generation of fingers and torons in non-reactive confined cholesteric LCs has been demonstrated in our previous publications [10-14] and implemented using both Gaussian and vortex laser beams. In partially reactive cholesteric systems studied in this work, the generation of torons occurs through the same procedure of focusing a Gaussian, 1064-nm beam in the desired location for around 0.1 s (Fig. 6.2). The used, partially-polymerizable mixture (Fig. 6.1) was chosen due to its positive dielectric anisotropy, room-temperature nematic state, and its strong homeotropic surface anchoring that can be set on confining substrates by use of polyimides. The ground-state configuration of the LC director is sensitive to the ratio of cell thickness d to pitch p. A 7-10 μm wedge cell having width of 1-2 cm typically gives a uniformly unwound 2 mm x 2 mm homeotropic region with d/p=0.7-1, in which one can optically generate

the toron and finger structures [10-14]. The thicker part of this wedge cell ($d/p>1$) contains spontaneously occurring fingers and other localized structures while the thinner part ($d/p<0.6$) contains a fully unwound homeotropic state in which optically generated localized structures are unstable and relax back to the uniform configuration with vertical director. Although the wedge geometry of the cells is unnecessary and similar results can be obtained for flat cells of constant thickness and well-controlled values of d/p, wedge cells allow for a facile exploration of how the studied optical generation and templating effects depend on d/p.

6.3.2. Partial polymerization of the structured cholesteric films

One of the main challenges in photopolymerization of cholesteric configurations is to preserve the director field of the LC during the polymerization process. Because of the absorption of UV light as it traverses the LC medium, the polymerization of a partially polymerizable mixture occurs faster near the UV source and typically causes the non-reactive components of the mixture to concentrate farther away from the UV source. If the chiral dopant is fully reactive, this process causes the cholesteric pitch gradients with the shortest pitch being at the cell substrate closer to the UV illumination source. If the chiral dopant is non-reactive, however, this process causes the pitch to decrease in the polymerized parts, thus resulting in pitch gradients analogues to pitch-gradient cholesteric polymers formed by polymerizing chiral and nematic monomers with unequal reactivity [42]. The UV exposure can also cause significant amounts of heating and lead to potential phase changes, gradients of pitch due to the temperature dependence of helical twisting power of the used chiral dopants, or even gradients of the scalar order parameter. Heating and decreasing the pitch can lead to the development of the translationally invariant configuration (TIC) from the initially homeotropic regions [12-14], as

well as tilting and merging of torons with the TIC in the cell mid-plane. Although the director configurations of polymerized cholesteric films in this case significantly differ from the ones in the fluid LC samples and would not be stable in non-polymerized systems, these TIC-embedded toron structures have not been achieved before in non-polymerizable systems and show how this polymerizable system can potentially be used for the exploration of non-equilibrium configurations of polymerized confined cholesteric LCs.

We have optimized the polymerization process by selecting a reactive chiral dopant and using relatively low light exposure for cross-linking of the cholesteric films, so that the three-dimensional structures of torons and fingers can be "frozen" by polymerization in a solid film without altering their initial director configuration (Fig. 6.3). We verify this by obtaining 3PEF-PM cross-sectional images before (Fig. 6.3(e,f)) and after (Fig. 6.3(h,i)) the polymerization. The unpolymerized E7 in this partially cross-linked system can be partially removed by addition of isopropanol. This allows for the reduction of the medium's effective birefringence by up to approximately one order of magnitude without disrupting the director structure of this partially polymerized system (Figs. 6.3 and 6.4). The residual birefringence is primarily due to the cross-linked part of the partially polymerized cholesteric film and small amounts of unwashed E7 entrapped within the partially polymerized film in the LC state.

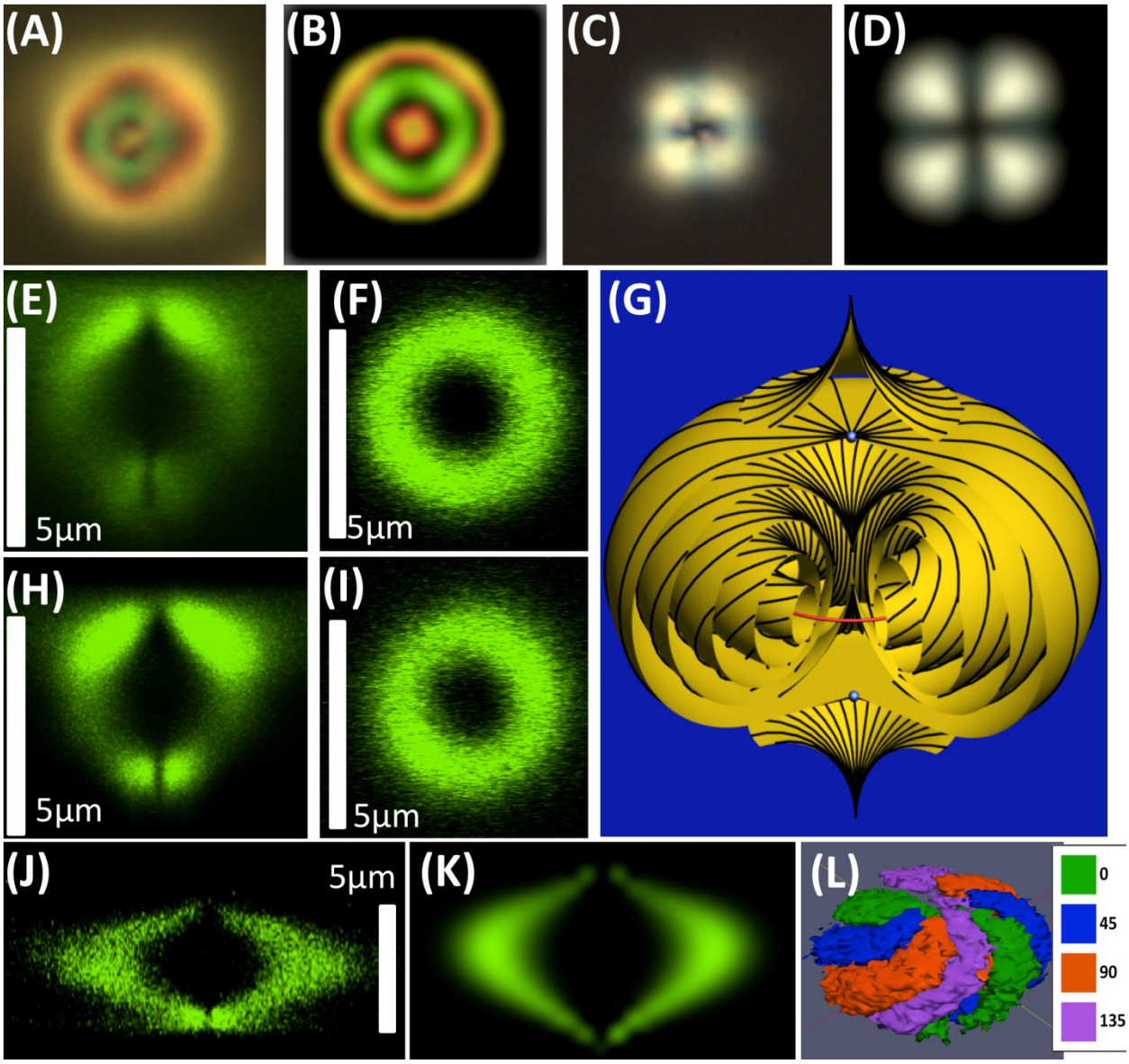

Fig. 6.3. Imaging and computer simulations of polymerized and unpolymerized torons. (a) An experimental POM image of a polymerized toron. (b) A computer-simulated POM image of a toron obtained using experimental parameters. (c) A POM image of a polymerized toron after washing away the unpolymerized LC with IPA and (d) a computer-simulated POM image of a toron with reduced birefringence produced by adjusting the residual birefringence value to match the appearance of the experimental POM image. (e-k) In-plane xy (f,i) and vertical xz (e,h,j,k) 3PEF-PM cross-sectional images of the toron obtained before (e,f) and after (h,i) polymerization show that the three-dimensional n(r) structure of the toron is unchanged during the polymerization process. (g) Schematic of the n(r) structure of a toron [10]. (j) A 3PEF-PM vertical cross-section of a polymerized toron after the unpolymerized E7 was replaced by an immersion oil shows a much more symmetric cross-section (j) as compared to (e, h) due to the large reduction in birefringence and consequent sample lensing and scattering that typically

cause imaging artifacts; this experimental image closely matches its computer-simulated counterpart shown in (k). The 3PEF-PM images shown in (e, f, h, i, j, k) were obtained using circularly polarized excitation light. (l) Three-dimensional visualization of the toron structure obtained by combining four three-dimensional images of this polymerized toron (in which E7 was replaced by an immersion oil), where high-intensity regions of fluorescence textures are depicted by colors that depend on the orientation of linear polarization of the excitation light at 0, 45, 90, and 135 degrees with respect to the x-direction.

The asymmetry of the vertical cross-sections shown in Fig. 6.3(e,h) with respect to the cell midplane is due to the absorption, scattering, and defocusing of the 3PEF-PM laser excitation light as it traverses farther away from the objective in the LC medium of high optical birefringence. Because of the reduced birefringence, the 3PEF-PM vertical cross-sections of samples with E7 partially replaced by an isotropic solvent become significantly less asymmetric with respect to the cell midplane (since the scattering- and defocusing-related artifacts are partially mitigated) and closely match the corresponding computer-simulated 3PEF-PM images (Fig. 6.3(j,k)). This artifact-free three-dimensional 3PEF-PM imaging using four different linear polarization states of excitation light also for visualization of topology of the toron structure in a ParaView presentation (Fig. 6.3(l)) resembling the so-called Pontryagin-Thom construction [9].

6.3.3. Preparation of multi-layer polymerized structures

To obtain three-dimensional patterns of torons and fingers, we first fabricate two-layer cells with collocated regions of d/p of interest (Fig. 6.4). A single-layer cell with a partially polymerized cholesteric film (obtained as described above) is split apart so that the cholesteric film remains attached to one of the two substrates. This substrate with the partially polymerized thin film is then used to form a new two-layer cholesteric cell. The process of polymerizing and opening of a

single-layer cell produces slight thickness variations in the polymerized film (visible in vertical 3PEF-PM cross-sections such as the one in Fig. 6.4(c)) due to the presence of topological defects and spatially varying n(r). This then results in the corresponding slight thickness variations of the new cholesteric layer, being complementary to the thickness profile of the polymerized film. The ensuing interaction of cholesteric structures then results in templating of certain well-defined director configurations in the new LC layer, which are highly dependent on d/p and the particular localized structures formed within the polymerized and unpolymerized LC layers in contact. When we use laser tweezers to optically "draw" an array of torons in the fluid layer initially laterally offset from the polymerized-layer's toron array, we observe little or no lateral movement of defects and structural changes in the newly generated array of torons in the fluid LC part of the cell (Fig. 6.4). However, if we draw the new torons directly on top of the torons of the templating polymerized layer, they shift off (so that the toron arrays in the two layers are eventually offset with respect to each other), although even in this case there is a small window of d/p values for which coaxial alignment of torons in the two layers is possible (Fig. 6.5).

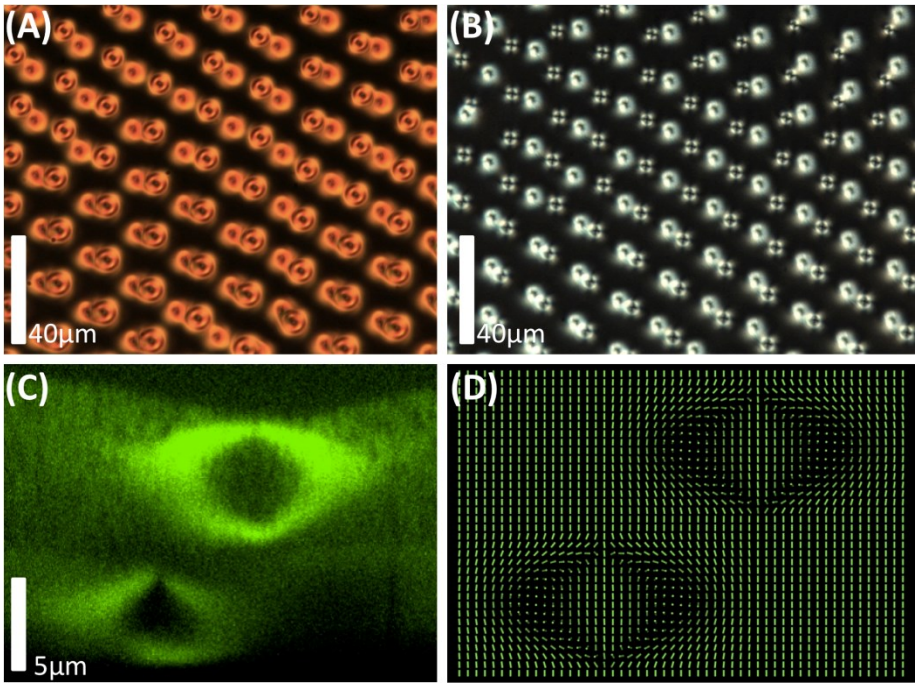

Fig. 6.4. Two-layer arrays of optically generated torons. (a) A POM image of polymerized torons in a two-layer cholesteric film; to obtain it, an optically generated hexagonal array of torons in the first layer was used as a template for localization of torons in the second layer, and was then followed by polymerization of the second layer. (b) A similar two-layer array of torons imaged after the E7 was washed out by solvent and the nanoporous cholesteric film was infiltrated with an immersion oil. (c) A vertical cross-section of the sample with two torons in different cholesteric layers obtained by means of 3PEF-PM imaging with circularly polarized excitation light. (d) A numerical model of the director field showing how the use of a first layer with a toron array causes an offset of optically generated torons in the second layer before its polymerization; the spatial variations of the director field are shown using cylinders.

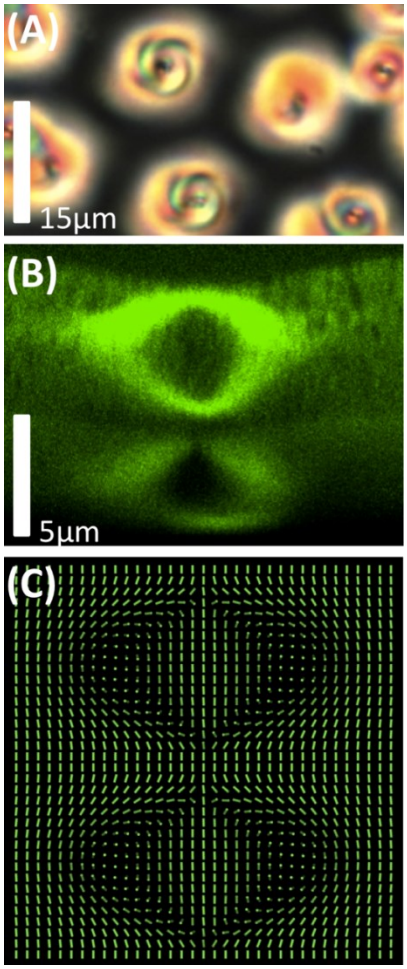

Fig. 6.5 Coaxial arrangement of torons in a two-layer polymerized cholesteric film. (a) A POM image of the two-layer structure with a toron located directly on top of another toron in the templating cholesteric layer. (b) Vertical cross-section of a two-layer film having torons in the second layer positioned directly on top of torons of the first layer obtained using 3PEF-PM with circularly polarized excitation light. (c) A numerical model of the director field shows that the first cholesteric layer with a toron can also cause a localization of an optically generated toron in the second layer before its polymerization that is coaxial with the toron in the polymerized templating layer.

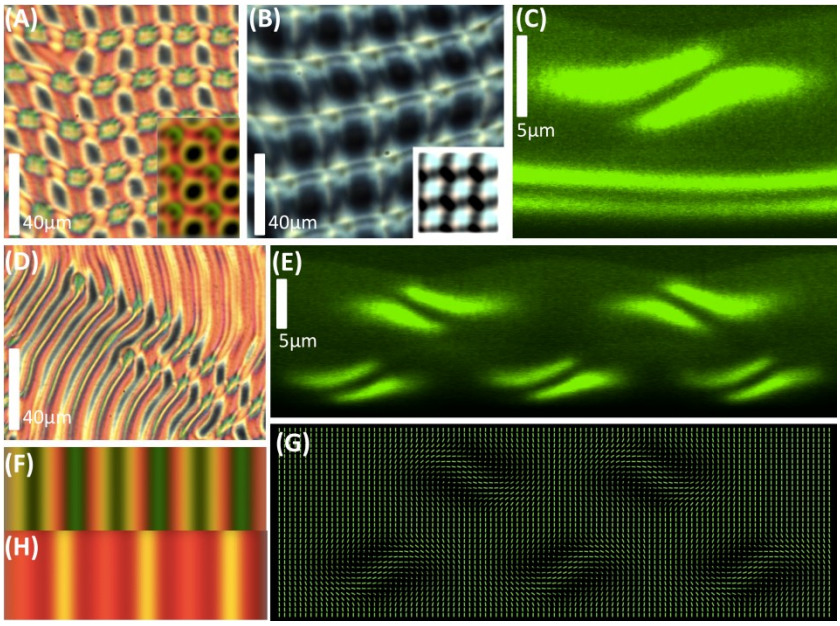

Fig. 6.6 Two-layer polymerized structures with cholesteric fingers. (a, b) Cholesteric fingers that nucleate in a second fluid cholesteric layer (before its polymerization) on top of a polymerized cholesteric layer with fingers typically spontaneously align perpendicular to the fingers in the first templating layer, as observed in POM images (a) before and (b) after replacing E7 of the partially polymerized LC with an immersion oil. The corresponding computer-simulated POM textures are shown as bottom-left insets of (a) and (b). The values of cell thickness and effective optical anisotropy used to obtain these computer-simulated images correspond to experimental values, (e.g. $\Delta n_{eff} \approx 0.03$ for the film with the E7 replaced by immersion oil, almost an order of magnitude lower than the optical anisotropy of $\Delta n = 0.022$ of E7) at which the experimental and computer-simulated images closely match each other, as shown in (b). (c) A vertical 3PEF-PM cross-section of the sample along a finger in the bottom templating layer and corresponding to the POM texture shown in (b); the linear polarization direction of laser excitation light in 3PEF-PM is perpendicular to the image. (d) A POM image showing that the fingers in the second layer can also align parallel to the fingers in a templating polymerized layer. (e) Vertical 3PEF-PM cross-section reveals that the helical axes of twist in fingers that align parallel to each other in the two layers always tilt in opposite directions with respect to the cell normal; the linear polarization direction of laser excitation light in 3PEF-PM is perpendicular to the image. (f,h) POM textures for parallel fingers obtained for two different shifts of fingers in the two layers on top of each other. As the parallel fingers in the top layer slightly shift with respect to the bottom layer, they produce dramatically different POM textures, as seen in the various regions of (d) and simulated in (f) for a $\approx p/3$ lateral shift and (h) $\approx p/2$ lateral shift. (g) A numerical model of the director field in the two-layer cholesteric film corresponding the 3PEF-PM cross-section shown in (e); the spatial variations of the director field are shown using cylinders.

Interactions between director structures of polymerized and unpolymerized layers are also present in cholesteric films containing either optically drawn and spontaneously occurring,

translationally invariant configurations of fingers (Figs. 6.6,7,8). Multiple different types of finger-finger and finger-toron interactions can occur depending on the d/p ratio. When we optically draw torons on top of fingers in the polymerized templating layer, we observe a strong attraction of these torons to well-defined equilibrium lateral positions with respect to fingers; this interaction transforms the initially periodic lattice of laser-drawn torons to a pattern template by the location of fingers in the polymerized layer (Fig. 6.8 (d,e)). When the unpolymerized layer with d/p ratio between 0.9 and 1 is somewhat thicker than the polymerized one, fingers in the unpolymerized layer can spontaneously grow and follow the patterning set by cholesteric structures in a polymerized layer. If the polymerized layer contains fingers, the new fingers grow predominantly perpendicular (Fig. 6.6(a,b)), and sometimes parallel to the polymerized-layer fingers (Fig. 6.6(d)), but not at intermediate angles between 0 and $\pi/2$. When the fingers grow parallel to the polymerized fingers, the helical axes defining the directions of twist in fingers in the two layers are always tilted in opposite directions (Fig. 6.6(e,g)); they also predominantly grow out-of-phase with the polymerized-layer fingers (as seen in the upper right of Fig. 6.6(e) and confirmed in the corresponding computer simulations of POM textures shown in Fig. 6.6(f-g)), i.e., on top of homeotropic regions interspacing the fingers of the templating polymerized layer. When fingers are spontaneously growing in on top of a laser-drawn polymerized-layer periodic array of torons, they tend to pass between the toron rows along one of the hexagonal lattice axes of the underlying array (Fig. 6.7). However, within a certain well-defined range of d/p between 0.9 and 1 in the unpolymerized layer, the fingers can also grow on top of the rows of torons (Fig. 6.8 (a-c)), with the finger axis being only slightly misaligned with respect to the hexagonal lattice axis (Fig. 6.8(a)).

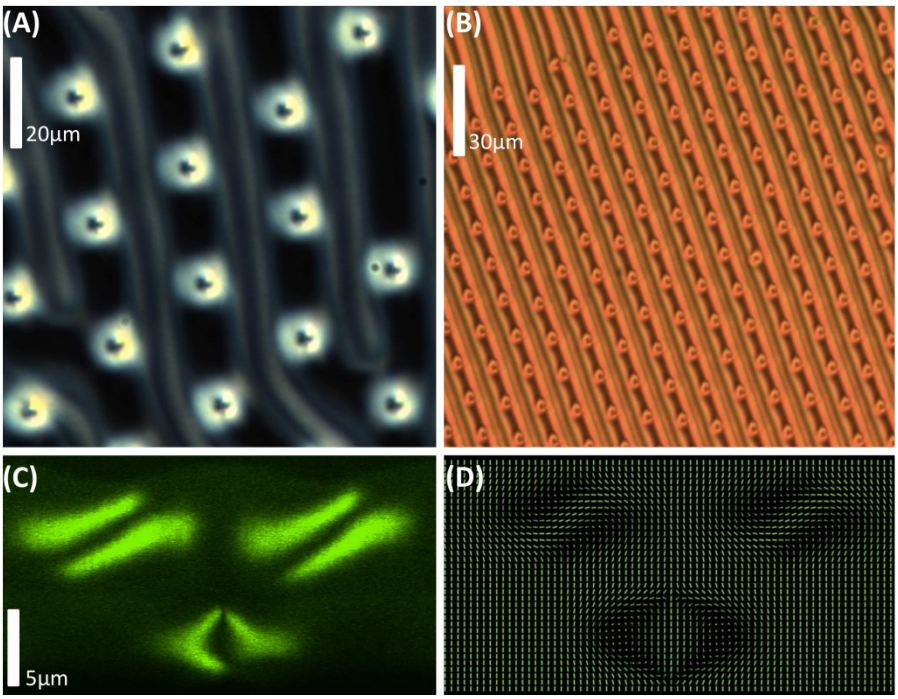

Fig. 6.7. Hybrid two-layer structure with torons in the templating layer and fingers in the second layer. (a) A POM image of the film after washing out E7 and infiltration the nanoporous structure with immersion oil. (b) A POM image for a similar film with E7 present in it. (c) Experimental 3PEF-PM vertical cross-section of the film shown in (a) obtained along a line perpendicular to the fingers. (d) A numerical model of the director field in a two-layer film corresponding to the image shown in (c). Note that the location of and orientation of fingers templated in the second cholesteric layer is pre-determined by the optically generated hexagonal lattice of torons in the polymerized templating layer.

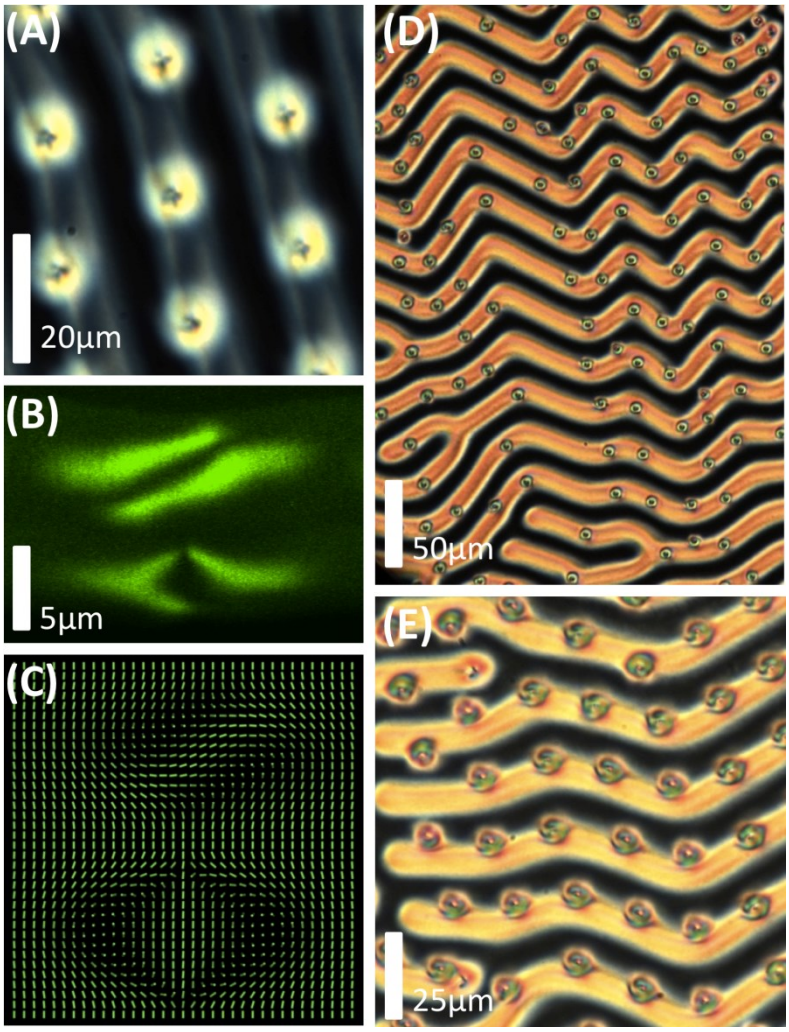

Fig. 6.8. Vertically co-located toron-finger configurations. (a) A POM image of a cholesteric two-layer film with fingers positioned on top of a row of torons and with E7 replaced by immersion oil. (b) 3PEF-PM vertical cross-section corresponding to (a) and obtained along a line perpendicular to the fingers and using excitation light with linear polarization perpendicular to the fingers. (c) Numerical model of the director field in the two-layer film corresponding to the vertical cross-section shown in (b). (d, e) POM images of a two-layer film with optically generated torons in non-polymerized layer that interact with the cholesteric fingers in a polymerized templating layer.

3PEF-PM vertical cross sections of polymerized cholesteric films with torons and fingers, show a slight bulge in the film that correlates with the spatial locations of these structures, which indicates that observed templating interactions may be caused by (a) the corresponding variations of effective thickness of unpolymerized films and (b) elastic interactions that arise from slight

variations of the LC easy axis at the interface with the polymerized layer. Our findings demonstrate that interactions between cholesteric structures of two-layer unpolymerized and partially polymerized LC films can result in templating of spontaneously occurring and optically generated structures that can be controlled via varying d/p ratios of the two films in contact. By varying d/p, one can obtain arrays of torons and fingers that are co-located, displaced, and differently oriented with respect to each other in different layers of in multi-layer partially polymerized cholesteric films. Moreover, by controlling the kinetics of the polymerization process itself (Fig. 6.9), it is also possible to obtain polymerized non-equilibrium director patterns with defects that would be unstable without using such procedures.

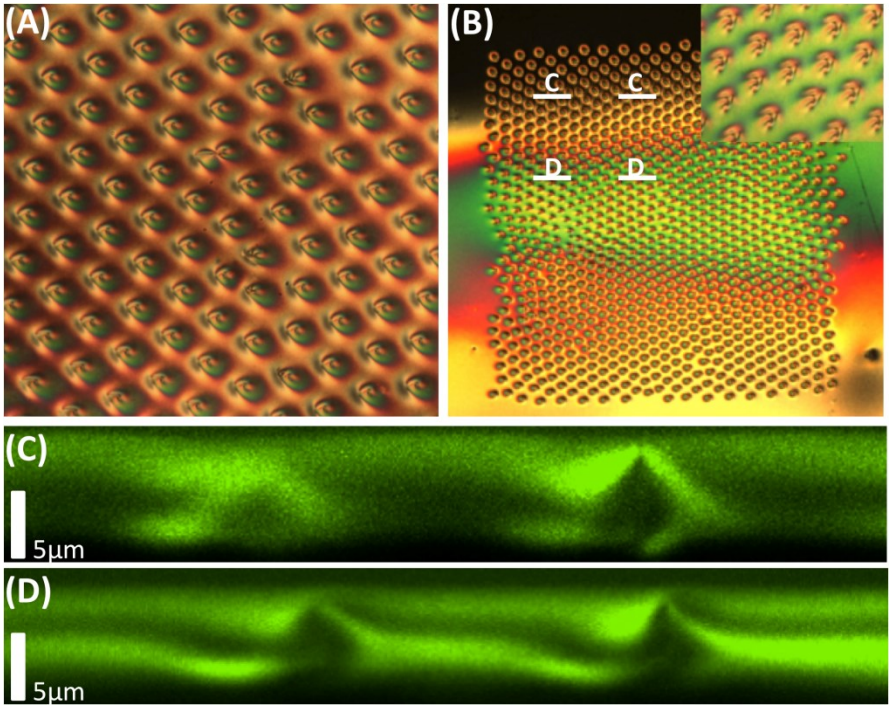

Fig. 6.9 Tilting of torons and generation of TIC caused by different polymerization procedures: (a) because of polymerization-induced gradients of chiral dopant concentration in a partially polymerizable cholesteric film with nonreactive chiral additive CB15 used instead of LC 756; (b) due to thermal effects associated with high-intensity UV exposure used for cross-linking. (c,d) 3PEF-PM vertical cross-sections of "tilted torons" from the regions of the POM image shown in (b) and marked correspondingly as C-C and D-D cross-sections on the POM image.

6.3.4. Polymerization of structures with metal nanoparticles entrapped by defects

In unpolymerized fluid LCs, topological defects spontaneously attract, spatially entrap, and align nanoparticles, so that the nanoparticles can displace energetically costly regions of defect cores with reduced order parameter and the surrounding LC with strong elastic distortions while minimizing the total free energy (Fig. 6.10(a))[31]. Dark-field imaging allows particles of size ~10 nm and larger to be detected (based on their characteristic scattering of light) and correlated with the location of singular topological defects that also scatter light (Fig. 6.10(a)). As an example, we demonstrate in Fig. 6.10(a) the observation of a 150nm x 800nm gold nanorod being attracted to the hyperbolic point defect of a toron structure (Fig. 6.10 (a,b)). Since the average size of the isotropic core of a LC defect is typically within 10-100 nm [16, 31] in non-polymerized systems, particles can be spectroscopically and microscopically observed (despite of some amount of orientational and positional averaging associated with the defect-constrained Brownian motion). Polarized dark-field imaging reveals that the nanorod orients roughly along the cell normal, as depicted in the schematic of Fig. 6.10(e). Similar oriented entrapment was also observed for the smaller studied gold nanorods with dimensions 65 × 25 nm, indicating that the demonstrated spatial patterning of anisotropic nanoparticles in defects and defect arrays can be extended to nanoparticles with a broad range of nan-scale sizes.

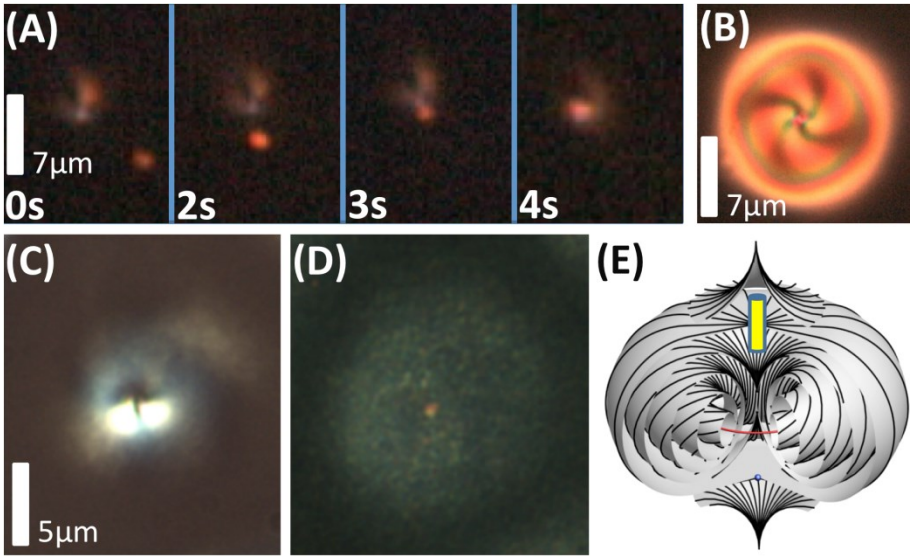

Fig. 6.10. Spatial localization of gold nanoparticles in hyperbolic point defects within a torons. (a) Dark-field microscopy time sequence showing an elongated pentagonal gold nanoprism (having length 800nm and transverse size of about 150nm) and being spontaneously attracted to the point defect of a toron structure; the elapsed time is marked on the images. (b) Co-located POM image of the same toron as shown in (a) having the gold nanoparticle entrapped by the hyperbolic point defect. (c,d) Permanently "frozen" 25 x 65 nm rod-like nanoparticle in a polymerized cholesteric film containing a toron as seen in (c) bright-field POM and (d) dark-field images and schematically depicted in (e).

Photopolymerization allows for the mitigation of the residual Brownian motion associated with a trapped nanorod and provides a stable position and orientation of the nanoparticle within the bulk of a sample, as needed for spectroscopic studies and microscopic observation (Fig. 6.10 (c,d)). Furthermore, properties of the matrix surrounding the nanoparticle entrapped by the defect can be controlled by varying the composition of unpolymerized parts of this partially-polymerized film without altering the nanoparticle's localization and orientation with respect to defects and the far-field director. For example, the infiltration with isopropanol or immersion oil (that displaces a large fraction of the unpolymerized E7 component of the film) does not disturb the

nanoparticle's orientation and relative position but allows us to significantly reduce the effective optical anisotropy of the matrix surrounding the nanoparticle (Fig. 6.10).

6.4. Discussion.

The interactions between polymerized and unpolymerized cholesteric layers in contact with each other reveal out-of-plane attractions and repulsions between localized cholesteric structures of torons and fingers that cannot be observed in conventional single-layer LC cells. These effects can potentially be used for templated layer-by-layer structural self-assembly leading to large-scale production of well-ordered films with periodic three-dimensional patterns of LC defects. A robust control of these interactions requires precise control of the d/p ratio, which can be achieved for flat LC cells with parallel substrates and well-defined cell gaps. When undesirable, these interactions can be mitigated or eliminated by using a fully polymerizable LC mixture and recoating the polymerized matrix with polyimide after the addition of each new layer. The addition of new cholesteric layers can, in principle, be carried out *ad infinitum*, however the practical realization of films with large numbers of layers is hindered by the difficulty of proper splitting of multi-layer cells, rather tenuous adhesion of new layers to the templating layers, and other technical factors. Under proper clean room conditions with an automated placement of spacer particles dispersed within UV glue to set uniform cell gap, this process could be readily used to create three-dimensional inch-scale defect arrays with and without nanoparticles decorating the LC singularities.

Localization and orientation of anisotropic nanoparticles in the energetically costly defect cores of topological structures in cholesteric LCs can be extended to a wide range of length scales and

nanoparticle material compositions, including metallic, semi-conducting, and dielectric particles. Since the localized cholesteric structures can be generated and spatially translated by the optical trap, well-controlled assemblies of one or a few nanoparticles can be generated by actively entrapping specific nanoparticles one wants to collect for a detailed analysis (e.g. for probing nanophotonic interactions between individual and small groups of plasmonic nanoparticles and quantum dots). We have previously demonstrated such entrapment of single and multiple nanoparticles using the hyperbolic hedgehog point defects induced by microspheres with homeotropic boundary conditions [31]. The present work demonstrates the feasibility of similar entrapment in LCs even without the use of microspheres and in the form of three-dimensional architectures defined by defects in multi-layer, polymerizeable cholesteric films. This type of nanoparticle patterning in defects and their arrays may provide means of exploring nanoscale energy conversion in single and small groups of quantum dots, rods, and discs, as well as plasmonic enhancement of various effects such as multiple exciton generation at precisely controlled nanoscale lengthscales. Partial polymerization of the LC in the studied multi-layer cholesteric films allows for "locking in" of desired architectures of self-assembled nanoparticles. The porous nature of such partially polymerized films allows for replacing a major fraction out of the 70% of unpolymerized E7 by various other LCs or isotropic solvents, thus controlling optical anisotropy, effective dielectric constants, and other properties of the surrounding LC matrix. This, in turn, may provide the means of probing how the interactions between defect-entrapped nanoparticles depend on the surrounding medium's optical and dielectric properties. Furthermore, combining periodic patterns of spatially varying LC optical axis and defect-entrapped arrays of plasmonic metal nanoparticles may be of interest for many photonic

applications where new photophysical properties arise from controlling the mesoscale structure and composition of organic-inorganic composites.

3PEF-PM vertical cross-sections show that the replacement of the E7 unpolymerized component of partially polymerized films by immersion oil causes the homeotropic regions of the film to swell more than the regions containing topological defects and various twisted structures, as we show in Figs. 6.4c, 6.5b, 6.6c,e, 6.7c, and 6.8b. Although the exact physical underpinnings behind such anisotropic swelling and deswelling are unknown and will be a subject of our future studies, this effect may be potentially extended to azobenzene-containing polymerizeable systems, in which surface profiles of thin films may be potentially controlled via optical illumination. The templating and anisotropic orientation-sensitive swelling effects may potentially also be extended from the flat thin-film geometry used in the present work to that of multi-layer shells, pillars, and films with grain boundaries and line defects [43-45], as well as to LC-colloidal composites containing particles with various topology and composition [46].

The use of partially polymerized LC system assures continuity of director field between different layers of the multi-layer films with defects. Therefore, our approach will enable both three-dimensional patterning and imaging of complex director configurations with defects, thus allowing for experimental exploration of relations between the topologies of LC director fields, defects, and surfaces of various colloidal inclusions [46]. The combination of optical generation of chirality-stabilized director structures, their photopolymerization, and then three-dimensional optical imaging of director fields with improved resolution brings about a set of experimental techniques that may allow researchers answering a number of open questions related to the nature and properties of LC defects [23, 46].

6.5. Conclusions

We have demonstrated that optical generation, spontaneous templating, and partial polymerization allow for the stabilization of cholesteric finger and toron structures and the formation of three-dimensional arrays of defects by the vertical stacking of thin cholesteric films. Three-dimensional patterning of defects allows for templating of plasmonic nanoparticles that decorate LC singularities and their arrays, laying the groundwork for potential applications in nanophotonics, plasmonics, nanoscale energy conversion, and metamaterial fabrication. The experimental arena that we have developed will provide researchers with a new powerful means of studying the interplay of topology of defects and director fields in confined chiral liquid crystals that will impinge on understanding defects and topologically nontrivial fields in other condensed matter systems.

6.6 References

1. T. H. Skyrme. *Proc. R. Soc. Lond. A* **260**, 127–138 (1961).

2. S. Muhlbauer, *et al. Science* **323**, 915–919 (2009)

3. S. Heinze, K. von Bergmann, M. Menzel, J. Brede, A. Kubetzka, R. Wiesendanger, G. Bihlmayer, and S. Blügel. *Nature Physics* **7**, 713-718 (2011).

4. M. Uchida and A. Tonomura. *Nature* **464**, 737–739 (2010).

5. J. Verbeeck, H. Tian and P. Schattschneider. *Nature* **467**, 301–304 (2010).

6. L. Allen, M. W. Beijersbergen, R. J. C. Spreeuw, and J. P. Woerdman. *Phys. Rev. A* **45**, 8185–8189 (1992).

7. M. R. Dennis, R. P. King, B. Jack, K. O'Holleran, and M. J. Padgett. *Nat. Phys.* **6**, 118–121 (2010).

8. I. Chuang, R. Durrer, N. Turok, and B. Yurke. *Science* **251**, 1336–1342 (1991).

9. B. G. Chen, P.J. Ackerman, G. P. Alexander, R. D. Kamien, and I. I. Smalyukh. *Phys. Rev. Lett.* (2013).

10. I. I. Smalyukh, Y. Lansac, N.A. Clark, and R. Trivedi. *Nat. Mater.* **9**, 139–145 (2010).

11. O. Trushkevych, P. Ackerman, W.A. Crossland, and I.I. Smalyukh. *Appl. Phys. Lett.* **97**, 201906 (2010).

12. I.I. Smalyukh, D. Kaputa, A. V. Kachynski, A. N. Kuzmin, P. J. Ackerman, C. W. Twombly, T. Lee, R. P. Trivedi, and P. N. Prasad. *Opt. Express* **20**, 6870-6880 (2012).

13. P. J. Ackerman, Z. Qi, and I. I. Smalyukh, *Phys. Rev. E* **86**, 021703 (2012).

14. P. J. Ackerman, Z. Qi, Y. Lin, C. Twombly, M. Laviada, Y. Lansac, and I.I. Smalyukh. *Scientific Reports* **2,** 414 (2012).

15. U. Tkalec, M. Ravnik, S. Čopar, S. Žumer, and I. Muševič. *Science* **333**, 62-65 (2011).

16. P. M. Chaikin, and T. C. Lubensky, *Principles of Condensed Matter Physics* (Cambridge University Press, Cambridge, 2000).

17. J. W. Milnor. *Topology from the Differentiable Viewpoint* (The University Press of Virginia, Charlottesville, 1965).

18. J. Charvolin and J.F. Sadoc. *Eur. Phys. J. E* **25**, 335–341 (2008)

19. P. Oswald, J. Baudry, and S. Pirkl, *Physics Reports* **337**, 67-96 (2000).

20. I. I. Smalyukh, *et al. Phys. Rev. E* **72**, 061707 (2005).

21. C. Phatak, A. K. Petford-Long, and O. Heinonen. *Phys. Rev. Lett.* **108**, 067205 (2012)

22. R. P. Trivedi, I. I. Klevets, B. Senyuk, T. Lee, and I.I. Smalyukh. *Proc. Nat. Acad. Sci. U.S.A.* **109**, 4744-4749 (2012).

23. G. Alexander, B. Chen, E. Matsumoto, and R. Kamien, *Rev. Mod. Phys.* **84**, 497 (2012).

24. I.I. Smalyukh, D. Kaputa, A.V. Kachynski, A.N. Kuzmin, and P.N. Prasad. *Opt. Express* **15**, 4359-4371 (2007).

25. J. Pérez-Juste, *et al. Coordination Chemistry Reviews* **249**, 1870–1901 (2005).

26. N. Jana, L. Gearheart, and C**.** Murphy**.** *J. Phys. Chem. B* **105**, 4065–4067 (2001).

27. A.P. Alivisatos. *Science* **271**, 933-937 (1996).

28. X. Peng, L. Manna, W. Yang, J. Wickham, E. Scher, A. Kadavanich, and A. P. Alivisatos. *Nature* **404**, 59-61 (2000).

29. A. J. Nozik. *Chem. Phys. Lett.* **457**, 3–11 (2008).

30. D. Astruc, *Nanoparticles and Catalysis* (Wiley, VCH, 2008).

31. B. Senyuk, J. S. Evans, P. Ackerman, T. Lee, P. Manna, L. Vigderman, E. R. Zubarev, J. van de Lagemaat, and I. I. Smalyukh. *Nano Lett.* **12**, 527–1114 (2012).

32. S. Lal, S. Link, and N. J. Halas. *Nat. Photonics* **1**, 641-648 (2007).

33. J. A. Fan, Ch. Wu, K. Bao, J. Bao, R. Bardhan, N. J. Halas, V. N. Manoharan, P. Nordlander, G. Shvets, and F. Capasso. *Science* **328**, 1135-1138 (2010).

34. H. Yoshida, Y. Tanaka, K. Kawamoto, H. Kubo, T. Tsuda, A. Fujii, S. Kuwabata, H. Kikuchi, and M. Ozaki. *Appl. Phys. Express* **2**, 121501 (2009).

35. H. Mertens, A. F. Koenderink, and A. Polman. *Phys. Rev. B* **76**, 115123 (2007).

36. H. Noh, S. Zelakiewicz, X. G. Feng, T. J. Gramila, L. N. Pfeiffer, and K. W. West. *Phys. Rev. B* **58**, 12621–12624 (1998).

37. Q. Liu, B. Senyuk, J. Tang, T. Lee, J. Qian, S. He, and I.I. Smalyukh. *Phys. Rev. Lett.* **109**, 088301 (2012).

38. A. J. Morfa, K. L. Rowlen, T. H. Reilly, M. J. Romero, and J. van de Lagemaat. *Appl. Phys. Lett.* **92,** 013504 (2008).

39. M. J. Romero and J. van de Lagemaat. *Phys. Rev. B* 80, 115432 (2009).

40. J. C. Johnson, T. H. Reilly, A. C. Kanarr, and J. van de Lagemaat. *J. Phys. Chem. C* 113, 6871-6877 (2009).

41. T. Lee, R. P. Trivedi, & I. I. Smalyukh. *Opt. Lett.* **35**, 3447–3449 (2010).

42. D. J Broer, J. Lub, G. N. Mol. *Nature* **378**, 467-469 (1995).

43. C. D. Modes and M. Warner. *Euro Phys. Lett* **97**, 36007 (2012).

44. C. D. Modes and M. Warner. *Phys. Rev. E* **84**, 021711 (2011).

45. Y. Sun, J. S. Evans, T. Lee, B. Senyuk, P. Keller, S. He, and I. I. Smalyukh. *Appl. Phys. Lett.* **100**, 241901 (2012).

46. B. Senyuk, Q. Liu, S. He, R. D. Kamien, R. B. Kusner, T. C. Lubensky and I. I. Smalyukh, *Nature* **493**, 200-205 (2013)

Chapter 7: Optical Manipulation of Shape-Morphing Elastomeric Liquid Crystal Microparticles Doped with Gold Nanocrystals

Adapted from: *Appl. Phys. Lett.* **100**, 241901 (2012)

Chapter Overview

In this chapter we describe the enhancement of the photothermal response of elastomeric LC colloids by dispersing large quantities of 2nm gold spheres as we have previously discussed as the simplest type of dispersion in chapter 2. We demonstrate facile optical manipulation of shape of birefringent colloidal microparticles made from liquid crystal elastomers. Using soft lithography and polymerization, we fabricate elastomeric microcylinders with weakly undulating director oriented on average along their long axes. These particles are infiltrated with gold nanospheres acting as heat transducers that allow for an efficient localized transfer of heat from a focused infrared laser beam to a submicrometer region within a microparticle. Photothermal control of ordering in the liquid crystal elastomer using scanned beams allows for a robust control of colloidal particles, enabling both reversible and irreversible changes of shape. Possible applications include optomechanics, microfluidics, and reconfigurable colloidal composites with shape-dependent self-assembly.

7.1 Introduction

Since its first demonstration, optical manipulation has always been an important research tool in physical sciences and biomedical research [1-12]. For example, in the study of soft matter systems, it allows one to explore inter-particle colloidal forces and provides insights into

physical underpinnings of colloidal self-assembly [10-12]. Although laser trapping, alignment, rotation around different axes, and other types of non-contact optical control of both shape-anisotropic and birefringent particles have been demonstrated and widely used [2-12], the efforts toward optical control of microparticle shapes are rare and the demonstrated shape transformations [8] are rather limited. For example, optical manipulation at relatively high laser powers ~100 mW allowed relatively modest stretching of red blood cells [8]. Liquid crystal elastomers (LCEs), on the other hand, have recently emerged as a new class of materials with facile control of structure and properties by means of thermal, electrical, and optical manipulation of orientational order through, for example, inducing transitions between nematic and isotropic states [13-18]. However, this shape manipulation is typically applied to centimeter-sized thin films rather than colloids. Control of elastomeric microparticles so far involved simple changes of the aspect ratio of anisotropic particles by means of thermally induced transformations between shapes of elastomeric particles pre-determined by the transition between nematic and isotropic states in the entire volume of LCE [14-18]. At the same time, dispersions of complex-shaped colloidal nano- and microparticles have recently attracted a great deal of research interest and may offer a means for fabrication of reconfigurable materials with desired optical and mechanical characteristics using shape-dictated self-assembly [10-12]. Methods for optical manipulation of colloidal shapes that would allow one to explore physical underpinnings behind such shape-dependent interactions are in a great demand.

In this chapter, we infiltrate cylindrical LCE microparticles with gold nanocrystals to enable efficient spatially localized energy transfer from a focused scanning laser beam into heat in a tiny submicrometer region of interest within the particle. Local heating alters the orientational ordering of the LCE molecules. By use of coupling between the shape and orientational ordering

in LCEs, we demonstrate laser-induced reversible and irreversible transformation of the microcylinders to a number of complex-shaped colloids.

7.2 Materials and methods

Micrometer-sized cylindrical actuators, made of side-on LCEs [17], were obtained using replica molding, a soft lithography technique developed by Whitesides *et al.* [19]. For a uniform alignment of the LCE director along the cylinder axis, particles were polymerized in a strong magnetic field of about 1 T oriented along the cylinder axis. The used LCE cylindrical particles were designed to have diameter (D) and length (L) dimensions of 2x4 μm, 17x70μm, and 20x100μm and were set free from a substrate by cutting them off using a razor blade. Dodecanethiol capped D=2 nm gold nanocrystals in toluene were prepared using the biphasic Brust Schiffrin method [20]. The LCE microparticles were infiltrated with the gold nanocrystals in this toluene dispersion for 24 hours. We replaced the solvent five times to remove non-infiltrated nanocrystals from the solvent while keeping them within the LCE. The LCE microparticles with thus embedded nanocrystals were then redispersed in water, silicone oil, or glycerol. In aqueous dispersions, surfactant sodium dodecyl sulfate (SDdS, obtained from Aldrich) was added at 1wt.% to improve colloidal stability of the fluid-borne LCE microparticles. The radius of the LCE particles slightly increases (by 5-10%) while length decreases when they are dispersed in water, silicone oil, or glycerol as compared to original dimensions of the “dry” as-fabricated microcylinders.

We use a laser tweezers system consisting of a two-axis scanning-mirror head (XLRB2, Nutfield Technology) and a continuous wave Ytterbium-doped fiber laser (1064 nm, IPG Photonics) [21].

The 1064 nm laser source was selected because this wavelength is about two times that of the peak of absorption wavelength for gold nanoparticles (thus making the two-photon absorption processes efficient) and also because infrared light can penetrate deep into the bulk of LCE due to reduced scattering as compared to the visible spectral range. The tweezers setup enables steering of a focused beam along arbitrary computer-programmed trajectories and is integrated with a polarizing optical microscope (BX-51, Olympus). A sample is placed between two crossed polarizers and viewed in a transmission-mode polarizing optical microscopy (POM) while particles are manipulated via steering the beam. Control of linear polarization of the trapping beams is performed by means of rotating a $\lambda/2$ wave plate inserted immediately before the microscope objective. Three-dimensional (3D) director structures are probed using different modalities of nonlinear optical polarizing microscopy, including coherent anti-Stokes Raman scattering polarizing microscopy (CARS-PM), built around an inverted optical microscope (IX-81, Olympus) and described in details elsewhere [22-24]. In CARS-PM imaging, the target vibration modes are the aromatic C=C stretching at wavenumbers between 1400-1600cm^{-1} [16-18], because the average stretching direction is parallel to the long molecular axes of mesogenic units and yields polarization-dependent CARS-PM signals. Broadband Stokes and 780nm pump femtosecond pulses are used for excitation and the CARS-PM signal at $w_{\text{anti-Stokes}} = 2w_{\text{pump/probe}} - w_{\text{Stokes}}$=694nm is detected with a band pass filter (BPF) having central wavelength at 700nm and 13nm bandwidth (1300-1600 cm^{-1}). We have also performed nonlinear optical imaging at the same excitation but without using a BPF, so that the images contain superimposed broadband CARS-PM signals from different chemical bonds and multiphoton excitation self-fluorescence of the LCE, as well as two-photon luminescence signals from gold nanoparticle aggregates [25-27]. For imaging and particle manipulation, we have used 10×-100× magnification microscope

objectives with 0.1-1.4 numerical apertures. POM and CARS-PM (Fig. 7.1(a-f)) reveal that the fluid-borne LCE particles have weakly undulating director field **n**(**r**) with the average director orientation along the cylinder's long axis (Fig. 7.1(g,h)). Observed undulations are likely caused by weak swelling of particles in the studied fluid hosts.

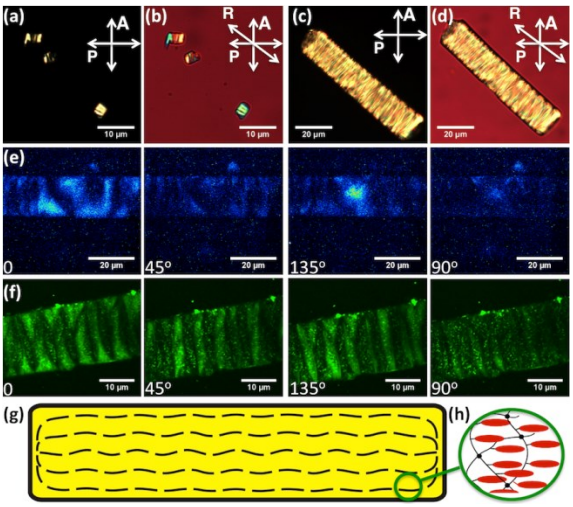

Fig. 7.1. Structure of cylindrical LCE microparticles. (a-d) POM images of LCE cylinders obtained (a,c) between crossed polarizer "P" and analyzer "A" and (b,d) with an additional full-wavelength (λ=530nm) phase retardation plate with the "fast" axis marked "R." (e,f) Broadband nonlinear optical polarizing microscopy images obtained at different angles between the linear polarization of excitation laser beams and the cylinder axis in (e) a CARS-PM imaging mode and (f) with the same excitation as in CARS-PM but without a BPF. The angles between the cylinder axis and polarization of excitation light are marked in bottom left corners of images in (e,f). (g,h) Schematics showing (g) LCE microparticle's internal structure with weakly undulating **n**(**r**) (dashed lines) and (h) local alignment of cross-linked mesogenic units.

7.3 Results and discussion

When heating in a fluid, we observe shrinking of the LCE particle's length and an increase of its diameter (Fig. 7.2(a-c)). The most dramatic change of shape takes place in the vicinity of the phase transition of LCE from nematic to isotropic phase when the particles birefringence disappears as the LCE transitions to the isotropic state (Fig. 7.2(b,c)). The absorption of the 1064nm laser light by the LCE is negligible, so that no substantial laser-induced heating and particle shape changes are observed at laser powers up to 2W in the sample, unless the LCE is heated 1-2 degrees below the nematic-isotropic transition temperature. However, embedded gold nanoparticles allow for an efficient photothermal transfer of energy into heat and control of orientational ordering at laser powers less than 200mW in the sample. When focusing the infrared laser beam into a point within the microcylinder, we observe that particle shape changes but then quickly relaxes back the original shape as the LCE cools down (Fig. 7.2(d-h)), typically within about one second. In the region of a focused laser beam, the microparticle increases in width due to the local photothermal melting of the LCE (Fig. 7.2(d-f)), consistent with experiments on heating of the entire sample, which also lead to the increase of cylinder width (Fig. 7.2(a-c)). When the laser beam is scanned unidirectionally and along the cylinder axis, we observe that the particle "swims" in the direction opposite to the direction of scanning. Symmetric scanning of the beam back-and-forth does not cause such swimming motion but rather just oscillations of particle position.

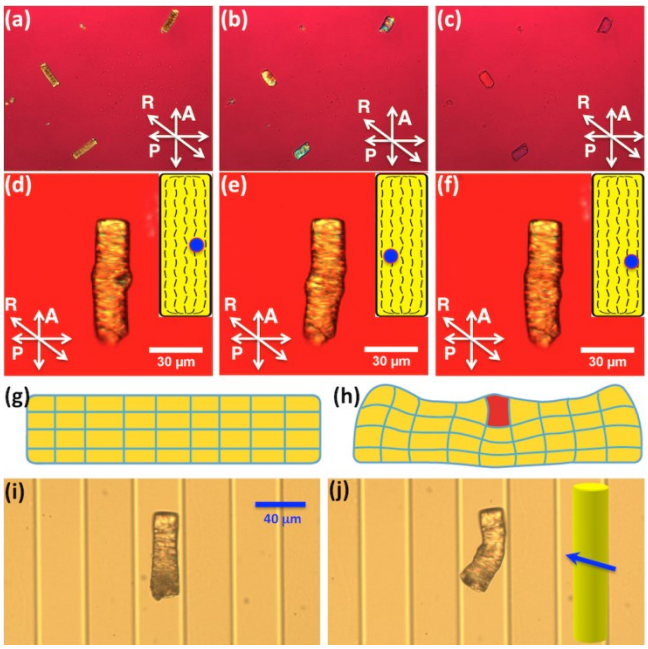

Fig. 7.2. Thermal and photothermal control of shape of LCE microparticles dispersed in glycerol. (a-f) POM images showing the change of the LCE cylinder aspect ratios as these particles are heated from (a) room temperature to (b) temperatures of about 1°C below and (c) about 1°C above the nematic-isotropic phase transition temperature of 135°C. (d-f) Local manipulation of the microparticle shape by means of a tightly-focused laser beam centered at locations shown by blue filled circles in the insets; note that these laser-induced changes of the microparticle shape are reversed after turning off the laser beam. (g,h) Schematics of initial (g) and laser-beam-modified (h) shape of the LCE microparticles deformed by local photothermal heating. (i,j) Reversible bending of the cylindrical microparticle suspended in glycerol inside a microchannel; this manipulation of the particle shape is achieved via repetitive unidirectional scanning of the focused laser beam along the direction of the blue arrow shown in the inset of (j).

Unidirectional nonreciprocal scanning of a laser beam along directions different from the microcylinder axis inevitably results in morphing of the particle shape, as demonstrated using the particle in a microchannel shown in Fig. 7.2(i,j). This unidirectionality is again essential to this effect, as bidirectional symmetric scanning along the same direction of the microparticle does not alter its shape. In all studied fluid hosts (Fig. 7.2(i,j) and Fig. 7.3), cylindrical particles bend toward the direction of scanning. Surprisingly, unlike in the case of local photothermal heating

with a focused beam simply localized within the particle volume, the shape changes induced by nonreciprocal laser beam scanning persist after scanning is discontinued and can be stable for a long period of time (several months). This indicates that the observed scanning-induced shape transformations are caused by modifications of $\mathbf{n}(\mathbf{r})$ and polymer network of the LCE microcylinders. Nonreciprocal unidirectional scanning of the laser beam results in unidirectional motion of a molten region of the LCE within the microparticle, which, subsequently, causes reorganization of the polymeric network and $\mathbf{n}(\mathbf{r})$, triggering changes of shape that persist after the laser beam is turned off. This is confirmed by CARS-PM imaging of $\mathbf{n}(\mathbf{r})$ and chemical composition of elastomeric microparticles after the laser-induced shape modification (inset of Fig. 7.3(e)). LCE microparticles without gold nanospheres do not exhibit shape transformations in response to a scanned focused laser beam, unless they are heated to elevated temperatures of about one degree below the nematic-isotropic transition, in which case their response becomes reminiscent to that of gold-nanoparticle-doped LCE microcylinders at room temperature, although still less facile. Furthermore, these shape-morphing "hot" microparticles relax to the original cylindrical shape when laser scanning is discontinued, unlike in the case of nanoparticle-doped LCEs.

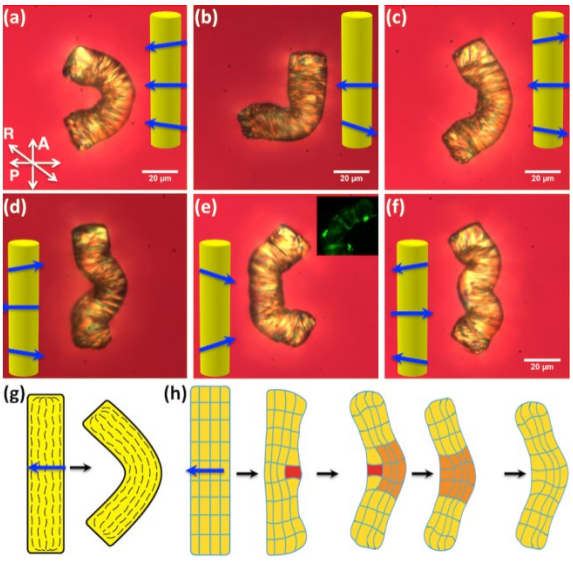

Fig. 7.3. Examples of robust reversible morphing of LCE microparticle shapes by means of unidirectional laser beam scanning along blue arrows shown in the insets of (a-f). The inset in (e) shows a typical CARS-PM image of a microparticle that was bent using a scanning laser beam. (g) Schematics of transformation of weakly undulating **n**(**r**) (shown by dashed lines) as the particle is bent due to scanning. (h) Schematic drawings show the effect of local manipulation of LCE orientational ordering by a scanned laser beam along the direction marked by the blue arrow; the scanning causes nonreciprocal unidirectional motion of a molten region (red) and in modification of the LCE polymeric network in the vicinity of the "hot" scanning region (orange), eventually leading to the stable modification of the particle shape that persists after the laser is turned off.

Although the used laser manipulation wavelength (1064nm) is far from the wavelength of absorption peak of gold nanospheres (~530nm), the photothermal laser heating is rather efficient. Nanoparticles in the LCE are likely forming small polydisperse aggregates, resulting in a sufficient light absorption at longer wavelengths, including that of the laser manipulation beam. On the other hand, two-photon absorption processes due to individual particles and their aggregates become important [25-27] at powers of the order of 100mW of tightly focused infrared laser beams. Since a large fraction of light absorbed by metal nanoparticles is converted to heat [26-27] and local laser-induced elevation temperature of >250K/W can be achieved [28], both of these processes contribute to the laser-induced local photothermal effect. Optical

trapping of LCE particles at powers of 20-30mW in the sample can achieve robust spatial control due to the refractive index difference between particles and the host media as well as rotational control of the particles due to their birefringence and shape anisotropy. This can be accomplished even when particles are trapped in an array using multiple laser beams. For example, Fig. 7.4 shows how complex-shaped LCE particles can be aligned in different directions coinciding with adjustable beam's linear polarization directions controlled by a λ/2-wave plate (Fig. 7.4).

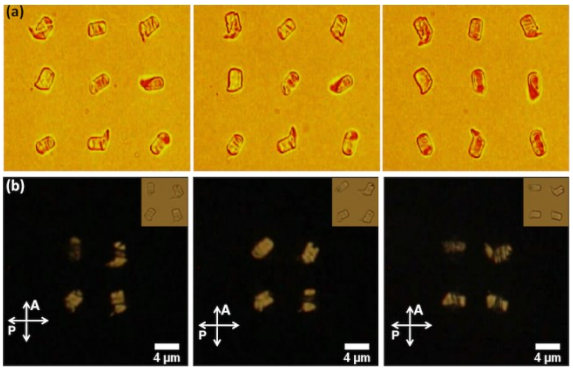

Fig. 7.4. Frames from bright-field (a) and POM (b) videos showing (a) alignment and (b) rotation of complex-shaped birefringent LCE colloids in trap arrays produced by means of holographic optical tweezers. Note that due to imperfections of colloidal shapes of arrays of trapped particles shown in (a,b), they align slightly differently with respect to the linear polarization direction of the trapping beam in (a) and rotate (b). The linear polarization directions of the trapping laser beams in (a) are marked by "$\mathbf{P}_{\mathbf{trap}}$".

7.4 Conclusions

To conclude, we have demonstrated robust manipulation of the shape of colloidal birefringent elastomeric microparticles using infrared laser beams. In addition, these particles can be spatially translated, aligned, and rotated by means of polarized-light optical tweezers, simultaneously enabling all types of non-contact optical control. In addition to infrared laser beams, one can utilize laser sources with wavelength matched to the surface plasmon resonance peak. Furthermore, extension of this approach to azobenzene-based LCEs may allow for optical

manipulation of microparticle shapes using substantially lower light intensities [15]. Possible applications include optomechanics, contact-free actuation of colloids, microfluidics, and reconfigurable colloidal composites with shape-dependent self-assembly.

7.5 References

1. A. Ashkin, J.M. Dziedzic, J.E. Bjorkholm, and S. Chu, Opt. Lett. **11**, 288 (1986).

2. K. Dholakia and T. Čižmár, Nat. Photonics **5**, 335 (2011).

3. R. C. Gauthier, M. Ashman, and C. P. Grover, Appl. Opt. **38**, 4861 (1999).

4. E. Higurashi, H. Ukita, H. Tanaka, and O. Ohguchi, Appl. Phys. Lett. **64**, 2209 (1994).

5. W. Singer, T. A. Nieminen, U. J. Gibson, N. R. Heckenberg, and H. Rubinsztein-Dunlop, Phys. Rev. E **73**, 21911 (2006).

6. H. Ukita and K. Nagatomi, Opt. Rev. **4**, 447 (1997).

7. D. B. Phillips, D. M. Carberry, S. H. Simpson, H. Schäfer, M. Steinhart, R. Bowman, G. M. Gibson, M. J. Padgett, S. Hanna, and M. J. Miles, J. Opt. **13**, 044023 (2011).

8. J. Guck, R. Ananthakrishnan, H. Mahmood, T. J. Moon, C. C. Cunningham and J. Käs, Biophys. J. **81**,767 (2001).

9. S. H. Simpson and S. Hanna, J. Opt. Soc. Am. A **28**, 850 (2011).

10. C. P. Lapointe, T. G. Mason, and I. I. Smalyukh, Science **326**, 1083 (2009).

11. M.J. Solomon, Current Opinion in Colloid & Interface Science **16**, 158 (2011).

12. J. Dontabhaktuni, M. Ravnik and S. Žumer, Soft Matter **8**, 1657 (2012).

13. P. M. Chaikin and T. C. Lubensky, *Principles of Condensed Matter Physics* (Cambridge Univ. Press, Cambridge, 2000).

14. M. Warner and E.M. Terentjev, *Liquid Crystal Elastomers* (Oxford Scientific Publications, Oxford, 2007).

15. C. Ohm, M. Brehmer and R. Zentel, Adv. Mater. **22**, 3366 (2010).

16. M.-H. Li, P. Keller, J. Yang, and P.-A. Albouy, Adv. Mater. **16**, 1922 (2004).

17. A. Buguin, M.-H. Li, P. Silberzan, B. Ladoux, P. Keller, J. Am. Chem. Soc. **128**, 1088 (2006).

18. H. Yang, A. Buguin, J.-M. Taulemesse, K. Kaneko, S. Méry, A. Bergeret and P. Keller, J. Am. Chem. Soc. **131**, 15000 (2009).

19. Y. Xia and G. M. Whitesides, Angew. Chem. Int. Ed. **37**, 550 (1998).

20. M. Brust, M. Walker, D. Bethell, D. Schiffrin and R.J. Whyman, J. Chem. Soc., Chem. Commun. **7**, 801 (1994).

21. R.P. Trivedi, D. Engström, and I.I. Smalyukh, J. Opt. **13**, 044001 (2011).

22. A.V. Kachynski, A.N. Kuzmin, P.N. Prasad, and I.I. Smalyukh, Appl. Phys. Lett. **91**, 151905 (2007).

23. T. Lee, R.P. Trivedi, and I.I. Smalyukh, Opt. Lett. **35**, 3447 (2010).

24. R.P. Trivedi, T. Lee, K. Bertness and I.I. Smalyukh, Opt. Express **18**, 27658 (2010).

25. H. Wang, T. Huff, D.A. Zweifel, W. He, P. S. Low, A. Wei and J.-X. Cheng, Proc. Natl. Acad. Sci. USA **102**, 15752 (2005).

26. F. Garwe, U. Bauerschäfer, A. Csaki, A. Steinbrück, K. Ritter, A. Bochmann, J. Bergmann, A. Weise, D. Akimov, G. Maubach, K. König, G. Hüttmann, W. Paa, J. Popp and W. Fritzsche, Nanotechnology **19**, 055207 (2008).

27. P. Zijlstra1, J. W. M. Chon and M. Gu, Nature **459**, 410 (2009).

28. A. Kyrsting, P. M. Bendix, D. G. Stamou, and L. B. Oddershede, *Nano Lett.* **11**, 888 (2011).

Chapter 8: Active shape-morphing elastomeric particles in short-pitch cholesteric liquid crystals

Adapted from: *Phys. Rev. Lett.* (2013)

Chapter Overview

In this chapter we describe the dispersion the elastomeric colloids described in the previous chapter into a polymer lyotropic LC to produce a system that allows for exploration of shape dependent distortions that can potentially inform our development of anisotropic colloids. Active elastomeric liquid crystal particles with initial cylindrical shapes are obtained by means of soft lithography and polymerization in a strong magnetic field. Gold nanocrystals infiltrated into these particles mediate energy transfer from laser light to heat, so that the inherent coupling between the temperature-dependent order and shape allows for dynamic morphing of these particles and well-controlled stable shapes. Continuous changes of particle shapes are followed by their spontaneous realignment and transformations of director structures in the surrounding cholesteric host, as well as locomotion in case of a non-reciprocal shape morphing. These findings bridge the fields of liquid crystal solids and active colloids, may enable shape-controlled self-assembly of adaptive composites and light-driven micro-machines, and can be understood by employing simple symmetry considerations along with electrostatic analogies.

8.1 Introduction

Dispersions of particles in liquid crystals (LCs) attract a constantly growing interest and exhibit many fascinating phenomena, ranging from particle-induced topological defects to novel types of elastic interactions [1-3]. Structures of LC molecular alignment around particles, typically

described by a director **n** pointing along the local average molecular orientation, give rise to elasticity-mediated colloidal self-assembly not encountered in isotropic fluid hosts. Within a far-field approximation, even spherical particles with strong boundary conditions induce dipolar or quadrupolar **n**(**r**)-distortions arising due to the anisotropic nature of the host medium and particle-induced satellite defects, such as point defects and disclination loops [1, 2]. Although many methods for self-assembly of anisotropic particles in isotropic solvents have been introduced [4], LC hosts bring a number of unique capabilities, such as the well-defined long-range alignment of anisotropic particles with respect to **n** controlled by external fields [3, 5-10]. Shape of particles dictates colloidal self-assembly [3, 7-15] and may enable practical utility of these fascinating LC-colloidal systems. Although complex-shaped particles can be fabricated using photolithography [3, 6], two-photon polymerization [10], nanocrystal growth [8], and wet chemical synthesis [7, 9], these approaches provide nematic dispersions of non-responsive colloids with no means for altering particle shape, alignment, locomotion, and self-assembly [3, 5-8].

In this chapter, we describe an optically reconfigurable double-LC colloidal system that allows for an unprecedented optical control of particle shapes and motion while being dispersed in a LC host. These active colloids are made from a nematic LC elastomer (LCE) [16-18] doped with gold nanocrystals to enable photothermal energy transfer and are morphed into low-symmetry configurations via laser-directed bending and aspect ratio control. We explore director structures in the LC host induced by these active colloids and describe them using electrostatic analogies. Finally, we discuss potential applications in reconfigurable self-assembly and controlled dynamics of active colloids in structured fluid hosts.

8.2 Materials and methods

Cylindrical particles were obtained using replica molding and polymerization in a strong magnetic field of about 1 T that aligns **n** of LCE along the cylinder axis [16, 17, 19]. Particles with diameter × length dimensions of 2 × 4 μm, 17 × 70 μm, and 20 × 100 μm were then passively infiltrated with 2 nm gold nanocrystals (obtained using wet synthesis described in Ref. [20]) by letting them soak in the dispersion of nanocrystals in toluene for 24 hours [16]. LCE microparticles with embedded gold nanocrystals were then redispersed in an aqueous cholesteric LC (CLC) solution of hydroxypropylcellulose (HPC, at 55 wt. %) [21, 22]. The sample was sheared to a partially unwound state which then relaxed to a ground-state CLC configuration with layers along the shear direction and a uniform helical axis perpendicular to it, as also observed in other studies of HPC-based LCs [21-25]. The equilibrium pitch $p \approx 350$ nm [21-25] and layer periodicity [26] $p/2 \approx 175$ nm allow for optical exploration of elastic lamellar distortions due to colloidal particles much larger than $p/2$. The LC cells were constructed from 170 μm thick glass plates optimized for high-resolution imaging and laser manipulation when using microscope objectives with high numerical aperture (NA). After shearing, the glass plates were sealed together using epoxy to form cells of thickness ranging from 100μm to 2mm.

To control particle shapes, we used laser tweezers [27-29] consisting of a two-axis scanning-mirror head (XLRB2, Nutfield Technology) and a continuous wave Ytterbium-doped fiber laser (wavelength $\lambda = 1064$ nm, IPG Photonics). The tweezers setup was integrated with an optical microscope BX-51 (Olympus). LCE particles in the LC were manipulated via steering a focused beam and monitored by polarizing optical microscopy (POM) using microscope objectives with magnifications 10×, 50×, and 100× and NA within 0.25-1.4. Linear polarization of the laser

beam was controlled by rotating a λ/2-wave plate. LCE particles were also studied using broadband coherent anti-Stokes Raman scattering polarizing microscopy (CARS-PM) [30, 31] via probing the polarized CARS-PM signals from the aromatic C=C stretching within 1400-1600 cm^{-1}. Broadband Stokes (obtained by means of a photonic crystal fiber) and 780 nm pump/probe femtosecond pulses were used for excitation. The CARS-PM signal at 694 nm was detected using a band pass filter with central wavelength at 700 nm and 13 nm bandwidth [31]. POM and CARS-PM (Fig. 8.1(a-c)) revealed weakly undulating **n**(**r**) of LCE with an average orientation along the cylinder (Fig. 8.1(d,e)) [16].

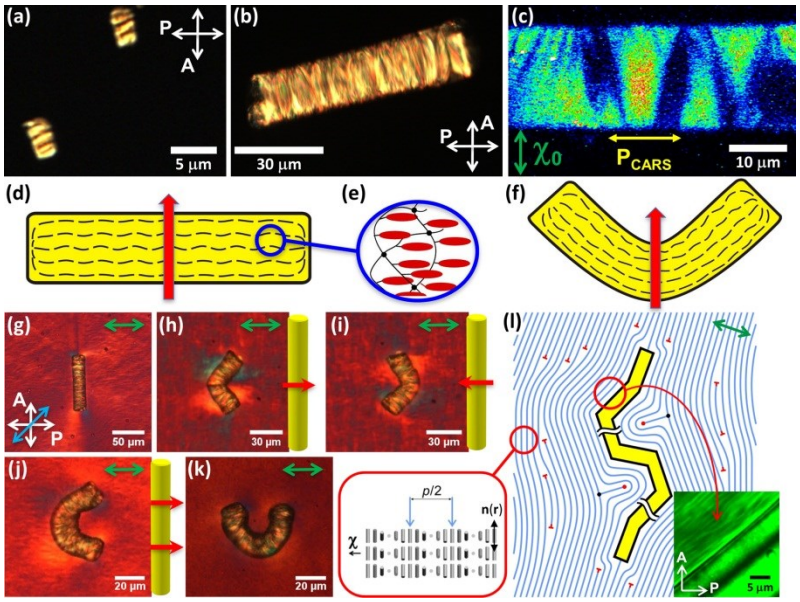

Fig. 8.1. LCE particles in isotropic and LC hosts. (a, b) POM images of LCE particles in water. (c) CARS-PM image of an LCE cylinder in a lyotropic LC obtained for a linear laser polarization marked by a yellow double arrow. (d, e, f) **n**(**r**) in LCE particles (d) before and (f) after the scanning along direction marked by red arrows. (g) LCE cylinder in a CLC. (h, i) Bent cylinders obtained by laser scanning along directions shown by red arrows in the insets. (j, k) LCE particles shaped into letters (j) "C" and (k) "U" by means of laser scanning along red arrows shown in (j). Crossed polarizer "P" and analyzer "A" are marked by white double arrows while the "slow" axis of a 530 nm retardation plate is shown by a blue double arrow in (g) and correlates with the blue color in the texture, visualizing regions where CLC layers are roughly along the blue double arrow; green double arrows mark χ_0. (l) Schematic of an optically shaped BCC distorting CLC and introducing edge dislocations (red nails); cylinders in the inset represent **n**(**r**). POM image in the inset of (l) shows that CLC layers are parallel to the BCC surface.

Unlike LCE particles, the LC host was designed to be insensitive to laser beams: (a) optical Fréedericksz transition in this system does not occur up to powers of 1 W (much higher than powers < 200mW used in experiments); (b) polymer solutions of HPC are practically insensitive to photothermal effects, as long as solvent evaporation is avoided; (c) gold nanocrystals uniformly distribute within the LCE but are immiscible with the aqueous solution of HPC, so that they do not diffuse into the surrounding host; (d) having entropic origin, tangentially

degenerate surface anchoring of the HPC-based LC is insensitive to the scanned beams. This allows for morphing particle shapes without direct coupling between $\mathbf{n}(\mathbf{r})$ of the HPC-based host and laser light (Fig. 8.1(d-l)) as well as POM imaging of the ensuing structural changes. Since the lamellar periodicity $p/2 \approx 175$ nm [21-25] of the HPC cholesteric in the ground state is smaller than the resolution of an optical microscope (≈ 300 nm when imaging with the NA = 1.4 objective and worse for lower NA), acetic acid is used as a solvent instead of water to increase p up to 3μm and directly observe cholesteric layers in POM, as shown in the inset of Fig. 8.1(l). POM textures obtained without and with a λ-retardation plate also reveal the $\boldsymbol{\chi}(\mathbf{r})$-structures.

8.3 Results and Discussion

Unidirectional laser scanning controls the particle shape via photothermal heating mediated by LCE-entrapped gold nanocrystals uniformly distributed within the particle bulk (Fig. 8.1) [32-35]. LCE microcylinders bend toward the beam scanning direction typically chosen to be orthogonal or tilted with respect to the cylinder axis (Figs. 8.1(d-l), 8.2, and 8.3) [16], giving rise to a number of low-symmetry bent-cylinder colloids (BCCs). Bidirectional scanning of a laser beam along the cylinder axis allows for both reversible and irreversible modification of the diameter-length ratio, depending on whether power of the scanning beam is reduced gradually or switched off abruptly (Fig. 8.4). POM imaging with and without a λ-plate reveals layered structures and $\boldsymbol{\chi}(\mathbf{r})$ of the surrounding LC that follow laser-guided changes of colloidal shapes (Figs. 8.2,3,4), which is due to the surface anchoring of $\boldsymbol{\chi}(\mathbf{r})$ at the LC-LCE interface (inset of Fig. 8.1(l)). In addition to smooth deformations of layers at relatively weak bending of pillars, POM textures also provide evidence for presence of dislocations (Fig. 8.1(l)) that appear to assist

in preserving layer equidistance while accommodating boundary conditions on optically controlled BCCs.

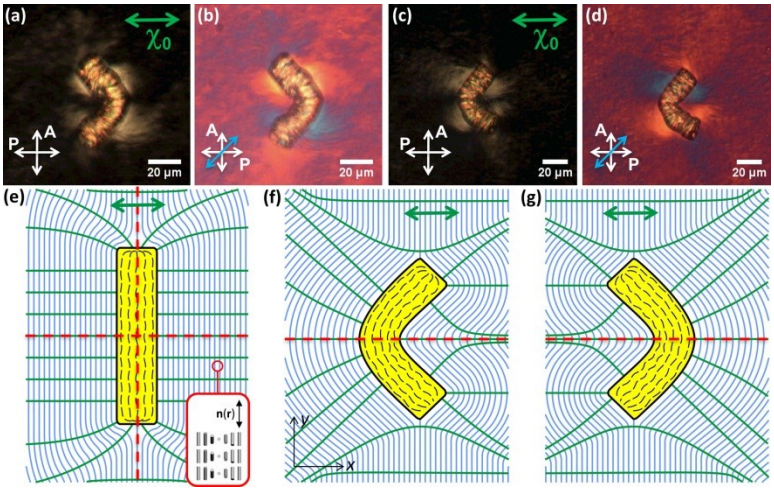

Fig. 8.2. Control of $\boldsymbol{\chi}(\mathbf{r})$- symmetry and layered structures in a CLC via optical control of BCC shapes. (a-d) POM images of BCCs obtained (a, c) without and (b, d) with a 530 nm retardation plate. (e) $\mathbf{n}(\mathbf{r})$ within the cylindrical LCE particle (black dashed lines), and the layer structures (blue lines) and $\boldsymbol{\chi}(\mathbf{r})$ (green lines) around it have mirror symmetry planes marked by dashed red lines as well as coinciding with the plane of the schematic. Cylinders in the inset represent $\mathbf{n}(\mathbf{r})$ twisting by π within each cholesteric layer. (f, g) Layer structures and $\boldsymbol{\chi}(\mathbf{r})$ induced via bending of LCE particles.

Colloid-induced perturbations of a homogeneous ground-state director $\mathbf{n}_0$ in nematic LCs have the form of a transverse two-component vector $\delta\mathbf{n}$ [36]. Along with symmetry considerations, this brings about an expansion into multipole series and electrostatic analogies between long-distance colloidal interactions and that of multipoles in electrostatics [1-11, 36]. The ground state in a CLC is strongly twisted and a direct parallel with the homogeneous nematic ground state is impossible because homogeneity of the ground state is a prerequisite of the symmetry-based considerations [11]. However, a similar approach for cholesterics is prompted by the de Gennes-Lubensky model [36], which describes a short-pitch CLC in terms of the director $\boldsymbol{\chi}$ normal to cholesteric layers. The model assumes that distortions occur over length scales much larger than p, which is the case of distortions due to our colloids of size $>>p$. The ground state $\boldsymbol{\chi}_0$ of the $\boldsymbol{\chi}$

director is homogeneous and has the same symmetry $D_{\infty h}$ as that of $\mathbf{n}_0$, and its small distortion $\delta\boldsymbol{\chi}$ is a two-component transverse vector similar to $\delta\mathbf{n}$. Hence allowed symmetries of $\boldsymbol{\chi}$ in CLCs are similar to those of $\mathbf{n}$ in nematics and this approach can be used at distances much larger than the particle size. Short-distance $\boldsymbol{\chi}(\mathbf{r})$ and $\mathbf{n}(\mathbf{r})$ and ensuing colloidal assemblies can be fully described only numerically [37].

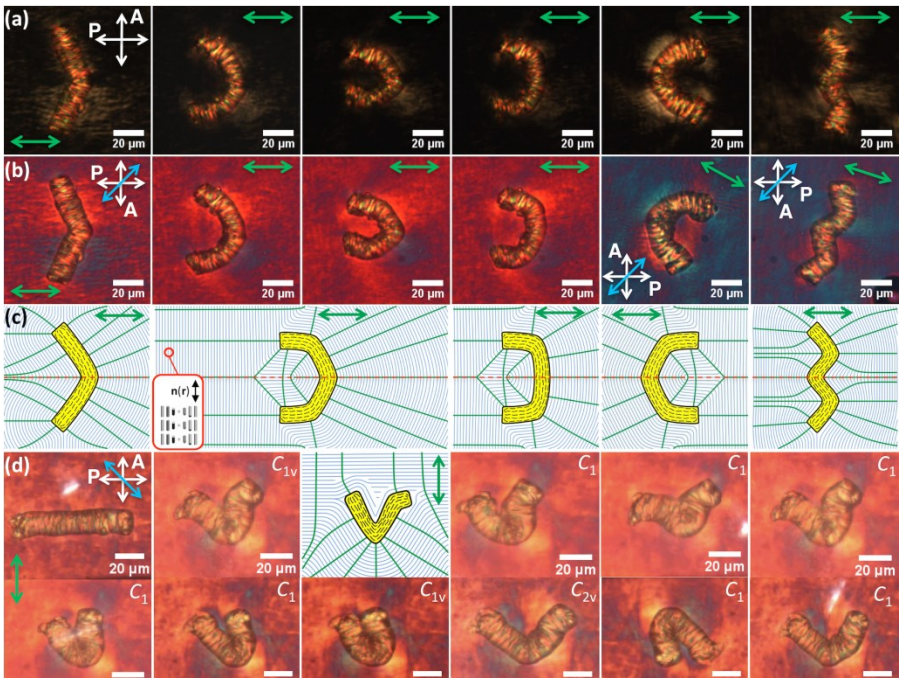

Fig. 8.3 Low-symmetry $\boldsymbol{\chi}(\mathbf{r})$-structures induced by continuous optical morphing of BCCs. (a, b) POM images of LCE particles and $\boldsymbol{\chi}(\mathbf{r})$ in the surrounding LC host obtained (a) without and (b) with a 530 nm retardation plate. (c) Schematics of cholesteric layers and $\boldsymbol{\chi}(\mathbf{r})$ around LCE particles corresponding to POM images shown in (a, b). (d) POM images obtained with a retardation plate showing examples of shapes and $\boldsymbol{\chi}(\mathbf{r})$-configurations obtained by morphing BCCs in a CLC. The last two images on the right side of (b) were taken when the sample was rotated with respect to crossed polarizers.

BCCs surface induces a normal alignment of $\boldsymbol{\chi}$ and tangential alignment of the CLC layers (inset of Fig. 8.1(l)). The unperturbed axis of LCE microcylinder is normal to $\boldsymbol{\chi}_0$ and parallel to both the CLC layers and cell substrates. $\boldsymbol{\chi}(\mathbf{r})$ around the cylinder is of the quadrupolar type (Figs. 8.1(g) and 8.2(e)) with three mirror symmetry planes: the two planes passing through the

cylinder axis, the one along χ_0 and the other one normal to χ_0, and the plane normal to the cylinder axis. Optical morphing removes some or all of these symmetry planes, thus creating different types of elastic multipoles (Figs. 8.1,2,3). One can also vary the strength of distortions without altering the symmetry of ensuing elastic configurations by changing the aspect ratio of particles (Fig. 8.4) or their fragments (Fig. 8.1(l)). Using laser scanning, we can tune the strength and geometrical distribution of elastic multipoles by controlling angles between the bent fragments of the LCE pillar, their diameters, and lengths (Figs. 8.3 and 8.4).

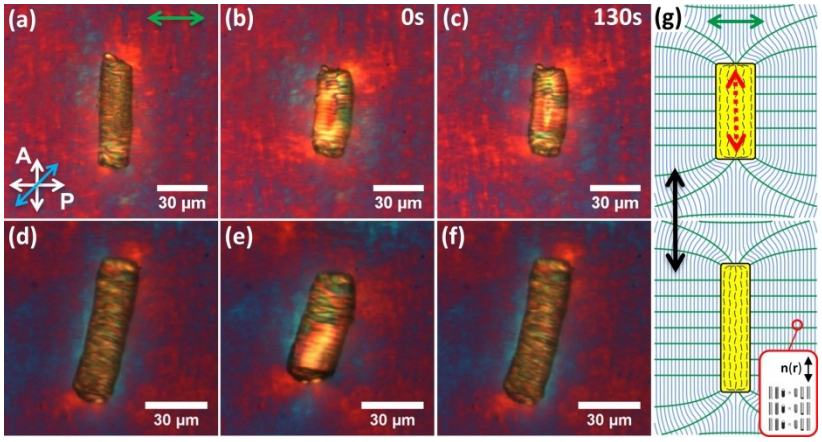

Fig. 8.4 Reversible and irreversible control of aspect ratios of LCE cylinders in a CLC. (a) LCE cylinder in a sheared CLC. (b, c) Length shrinking and diameter increase induced by bidirectional laser scanning along the cylinder axis that retains $\chi(\mathbf{r})$ symmetry and persists with time (marked in top right corners of POM images) after scanning is discontinued abruptly. (d) LCE particle in a non-sheared CLC. (e, f) Reversible shape modification induced by similar bidirectional scanning but terminated via a continuous decrease of laser power within ~2 min and accompanied by reversible change of $\chi(\mathbf{r})$ in the CLC. (g) A schematic showing changes in $\chi(\mathbf{r})$ and layer structures that follow laser-induced modification of the particle shape; the dashed red double arrow depicts bidirectional scanning of the beam. The modified shape of particle is long-term-stable if scanning is discontinued via turning laser off, but relaxes back to the original one when intensity of the beam decreases gradually.

Experimental dipolar V- and U-shaped particles with apex along χ_0 shown in Figs. 8.1(h-j), 8.2(a-d), and 8.3(a-c) and zigzag-shaped particles in the right-side parts of Figs.3(a,b) induce same-symmetry $\chi(\mathbf{r})$ shown in Figs. 8.2(f,g) and Fig. 8.3(c). Allowed symmetry elements of

these $\boldsymbol{\chi}(\mathbf{r})$-structures are those of the group C_{2v}: a rotation by an angle π about the vertical axis passing through the apex of the "V", and a vertical mirror plane lying in the plane of the particle's "V" and passing through the vertical axis [38]. The particle shown in Fig. 8.1(k) has apex of "V" pointing along layers and normal to $\boldsymbol{\chi}_0$. The symmetry elements of $\boldsymbol{\chi}(\mathbf{r})$ are those of the group D_{1h} and include a vertical mirror plane lying in the particle's plane, a horizontal mirror plane normal to it and passing through the apex of the "V", and a π rotation about the horizontal axis passing through the apex[38]. Thus, these dipolar colloids in a CLC are described by point groups C_{2v} or D_{1h}, depending on the angle the apex direction makes with $\boldsymbol{\chi}_0$. By continuous morphing particle shape, we can further lower the symmetry of $\boldsymbol{\chi}(\mathbf{r})$ around BCCs by, for example, removing symmetry elements of C_{2v}. Fig. 8.3(d) shows particles with just one vertical mirror plane coinciding with the plane of the image (symmetry group C_{1v}) and asymmetric particles with no mirror planes (trivial group C_1), as revealed by birefringent textures and defocusing of different parts of the particle. An interesting interplay between symmetries of distortions in $\mathbf{n}(\mathbf{r})$ and $\boldsymbol{\chi}(\mathbf{r})$ can be noticed when comparing like-shaped particles introduced into nematic and cholesteric LC, respectively [38]. Furthermore, since four types of pure and many hybrid elastic dipoles in nematic LCs can be identified using a tensorial description based on different symmetries of elastic distortions [11], this description can be extended to CLCs and then further classify elastic dipoles obtained in our experiments[38, 39]. In both nematic and cholesteric LCs, BCCs rotate to minimize elastic energy of the surrounding $\mathbf{n}(\mathbf{r})$ or $\boldsymbol{\chi}(\mathbf{r})$ in response to changes of particle shape (Video 1 in [38]) and even the simplest non-reciprocal dynamic morphing of the shape results in a directional locomotion (Video 2 in [38]).

8.4 Conclusions

To conclude, we have introduced a new class of active LCE colloids with light-controlled rigidly connected fragments of cylinders in fluid LCs that can be described by employing analogies with charge distributions in electrostatics. These elastomeric colloids will allow one to explore light-driven rotational and translational motion in low-viscosity nematic and cholesteric LCs of varying pitch and will bridge the fields of LC solids and active colloids. Furthermore, our double-LC colloidal system may allow one to explore the role of geometric shape in determining the complex dipolar structures, light-controlled self-assembly, reconfigurable knotting of defects, and formations of LC gels [37, 39-41]. Potential applications include laser-guided assembly of reconfigurable materials for photonic and electro-optic applications and light-driven micro-machines.

8.5 References

1. P. Poulin, H. Stark, T. C. Lubensky, and D. A. Weitz, *Science* **275**, 1170 (1997).
2. I. Muševič, M. Škarabot, U. Tkalec, M. Ravnik, and S. Žumer, *Science* **313**, 954 (2006).
3. C. P. Lapointe, T. G. Mason, and I. I. Smalyukh, *Science* **326**, 1083 (2009).
4. M. J. Solomon, *Curr. Opin. Colloid Interface Sci.* **16**, 158 (2011).
5. J. Dontabhaktuni, M. Ravnik, and S. Žumer, *Soft Matter* **8**, 1657 (2012).
6. C. P. Lapointe, S. Hopkins, T. G. Mason, and I. I. Smalyukh. *Phys. Rev. Lett.* **105**, 178301 (2010).
7. J. S. Evans, C. Beier, and I. I. Smalyukh. *J. Appl. Phys.* **110**, 033535 (2011).
8. D. Engström, R. P. Trivedi, M. Persson, K. A. Bertness, M. Goksör, and I. I. Smalyukh. *Soft Matter* **7**, 6304-6312 (2011).
9. B. Senyuk, J. S. Evans, P. J. Ackerman, T. Lee, P. Manna, L. Vigderman, E. R. Zubarev, J. van de Lagemaat, and I. I. Smalyukh. *Nano Lett.* **12**, 527-1114 (2012).

10. A. Martinez, T. Lee, T. Asavei, H. Rubinsztein-Dunlop, and I. I. Smalyukh. *Soft Matter* **8**, 2432-2437 (2012).

11. V. M. Pergamenshchik and V. A. Uzunova, *Phys. Rev. E* **83**, 021701 (2011).

12. V. A. Uzunova and V. M. Pergamenshchik, *Phys. Rev. E* **84**, 031702 (2011).

13. P. M. Phillips and A. D. Rey, *Soft Matter* **7**, 2052-2063 (2011).

14. F. Brochard and P. G. de Gennes, *J. Phys. (France)* **31**, 691-708 (1970).

15. S. V. Burylov and Yu. L. Raikhner, *Phys. Lett. A* **149**, 279-283 (1990).

16. Y. Sun, J. S. Evans, T. Lee, B. Senyuk, P. Keller, S. He, and I. I. Smalyukh, *Appl. Phys. Lett.* **100**, 241901 (2012).

17. A. Buguin, M.-H. Li, P. Silberzan, B. Ladoux, and P. Keller, *J. Am. Chem. Soc.* **128**, 1088 (2006).

18. M. Warner and E. M. Terentjev, *Liquid Crystal Elastomers* (Oxford Scientific Publications, Oxford, 2007).

19. Y. Xia and G. M. Whitesides, *Angew. Chem. Int. Ed.* **37**, 550 (1998).

20. M. Brust, M. Walker, D. Bethell, D. Schiffrin, and R. J. Whyman, *J. Chem. Soc., Chem. Commun.* **7**, 801 (1994).

21. K. Hongladarom, V. M. Hugaz, D. K. Cinader, W. R. Burghardt, and J. P. Quintana, *Macromolecules* **29**, 5346 (1996).

22. K. Hongladarom, W. R. Burghardt, *Rheol. Acta* **37**, 46 (1998).

23. R. S. Werbowyj and D. G. Gray, *Macromolecules* **17**, 1512 (1984).

24. T. Okubo, *J. Chem. Soc. Faraday Trans.* **87**, 607 (1991).

25. R. S. Werbowyj and D. G. Gray, *Macromolecules* **13**, 69 (1980).

26. P. M. Chaikin and T. C. Lubensky, *Principles of Condensed Matter Physics* (Cambridge Univ. Press, Cambridge, 2000).

27. U. Tkalec, M. Ravnik, S. Čopar, S. Žumer, and I. Muševič, *Science* **333**, 62 (2011).

28. R. P. Trivedi, D. Engström, and I. I. Smalyukh, *J. Opt.* **13**, 044001 (2011).

29. R. P. Trivedi, T. Lee, K. Bertness, and I. I. Smalyukh, *Opt. Express* **18**, 27658 (2010).

30. A. V. Kachynski, A. N. Kuzmin, P. N. Prasad, and I. I. Smalyukh, *Appl. Phys. Lett.* **91**, 151905 (2007).

31. T. Lee, R. P. Trivedi, and I. I. Smalyukh, *Opt. Lett.* **35**, 3447 (2010).

32. H. Wang, T. Huff, D. A. Zweifel, W. He, P. S. Low, A. Wei, and J.-X. Cheng, *Proc. Natl. Acad. Sci. U.S.A.* **102**, 15752 (2005).

33. F. Garwe, U. Bauerschäfer, A. Csaki, A. Steinbrück, K. Ritter, A. Bochmann, J. Bergmann, A. Weise, D. Akimov, G. Maubach, K. König, G. Hüttmann, W. Paa, J. Popp, and W. Fritzsche, *Nanotechnology* **19**, 055207 (2008).

34. P. Zijlstra1, J. W. M. Chon, and M. Gu, *Nature* **459**, 410 (2009).

35. A. Kyrsting, P. Bendix, D. Stamou, and L. B. Oddershede, *Nano Lett.* **11**, 888 (2011).

36. P. G. de Gennes and J. Prost, *The Physics of Liquid Crystals*, 2nd ed. (Oxford University Press, New York, 1995).

37. S. Copar, T. Porenta, V. S. R. Jampani, I. Musevic, and S. Zumer. *Soft Matter* **8**, 8595 (2012).

38. See Supplemental Material for supplementary text, four figs., and two videos.

39. V. M. Pergamenshchik, J. S. Evans, B. Senyuk, and I. I. Smalyukh, in preparation.

40. V. S. R. Jampani, M. Škarabot, M. Ravnik, S. Čopar, S. Žumer, and I. Muševič. *Phys. Rev. E* **84**, 031703 (2011).

41. T. A. Wood, J. S. Lintuvuori, A. B. Schofield, D. Marenduzzo, and W. C. K. Poon. *Science* **334**, 79-83 (2011).

Chapter 9: Infiltration of anisotropic solids with gold nanorods: Carbon nanotube flying carpets and microporous LC polymer networks

Adapted from: *ACS Appl. Materials & Interfaces* **3**, 3718 (2011)

Chapter Overview

In this chapter we describe a simple and versatile technique for assembly of gold nanorods on aligned macrostructures, such as thin single-walled carbon nanotube (SWNT) films, nanotube fibers, and microporous polymer LC networks. The deposition and assembly is accomplished *via* drop drying of dilute gold nanorod suspensions on macrostructures under ambient conditions. Guided by anisotropic interactions, gold nanorods and polygonal platelets spontaneously align with SWNTs, resulting in macroscopic arrays of locally ordered nanorods supported on aligned SWNT substrates. SEM reveals that the scalar order parameter of rods relative to the local average SWNT alignment is 0.7 for rods on SWNT films and 0.9 for rods on SWNT fibers. This self-alignment is enabled by anisotropic gold nanoparticle-SWNT interactions and is observed for a wide range of nanoparticles, including nanorods with aspect ratios ranging from 2–35, thin gold triangular and other polygonal platelets. Microporous polymer LC networks The plasmonic properties of aligned gold nanorods together with superior electronic, chemical and mechanical properties of SWNTs make these hybrid nanocomposites valuable for the design of self-assembled multi-functional optoelectronic materials and optical metamaterials.

9.1 Introduction

Metallic nanoparticles have been the subject of intense research owing to their unusual electro-optical properties and a broad range of potential applications.[1,2] Current research towards nanoparticles for metamaterial applications is primarily focused in two directions: synthesis and ordered assembly. Synthesis involves designing new methods for fabrication of nanoparticles from a variety of materials, with varied anisotropic shapes, sizes and aspect ratios. Particles are being tailored to possess highly tunable plasmonic and optoelectronic properties aimed for specific advanced applications. Ordered assembly entails deposition of nanoparticles on surfaces, incorporation into bulk liquid crystalline media, or chemically mediated crystallization in an organized manner so as to leverage the unique properties of individual nanoparticles collectively and attain functional behavior on macroscopic scales. Gold nanorods (GNRs) and polygonal nanoplatelets are a particularly interesting class of nanoparticles because their surface plasmon resonance (SPR) depend on polarization and can be tuned across the visible and near IR spectrum by changing the GNR aspect ratio.[3] Promising GNR applications include plasmonic enhancement of photoconversion in photovoltaics,[4-6] surface enhanced Raman scattering (SERS) based detection and imaging,[7,8] biological imaging and therapy,[9-11] and optical metamaterials;[12,13] large scale ordered assembly of GNRs is a critical step for the development of many of these applications.

Recent advances in ordered assembly and nanoscale alignment of GNRs include incorporation into lyotropic liquid crystals,[12] stretched polymer films,[14,15] electric field driven alignment in a liquid medium,[16] colloidal self-assembly,[17,18] and deposition onto patterned surfaces.[19] In most cases, however, the substrates or surrounding material (for bulk

incorporation) possess minimal or no functionality; the lack of essential properties like electrical conductivity, mechanical strength, or chemical durability often limits the range of possible applications for these hybrid materials.

Single-walled carbon nanotubes (SWNTs) offer a promising alternative in this context. SWNTs offer the functional and structural features of high performance polymers,[20] coupled with superior electro-optical properties and chemical inertness.[21] Their nanoscale diameter combined with high aspect ratio (> 1000) makes them ideal candidates for forming high performance thin films[22,23] and fibers[24-27] which in turn serve as basic functional materials for a host of engineering applications, devices and materials. For example, SWNT thin films are being developed as transparent conductive coatings for touch screens, flat electronic displays, OLEDs, electrodes for solar cells, *etc*.[28,29] High specific surface area, ~ 1300 m^2/g,[30] makes SWNT macrostructures highly desirable substrates for hosting other functional nanoparticles, for example, SWNT based supports for catalyst nanoparticles, SWNT electrodes for fuel cells, [31,32] and oriented attachment of GNRs on sidewalls of individual polymer coated MWNTs.[33]

In this chapter, we report the spontaneous ordered deposition of plasmonic GNRs and polygonal platelets on various highly aligned SWNT macrostructures. Using a simple "drop drying" method, which utilizes anisotropic interactions between GNRs and SWNT structures including capillary, entropic and van der Waals forces, "templated" deposition of GNR arrays has been achieved over large length scales (~millimeters) on planar as well as curved SWNT substrates. The superior electro-optical properties of SWNTs coupled with optical properties of plasmonic nanoparticles make SWNT-GNR composites potential candidates for a number of optoelectronic

applications like electrodes for light harvesting devices, electrochemical cells, conductive platforms for plasmon enhanced imaging.

9.2 Materials and Methods:

9.2.1 Fabrication of anisotropic gold nanoparticles

Gold Nanorod GNRs with medium (~ 5-12) and high aspect ratios (~ 12-35), were fabricated using standard seed mediated growth in the presence of CTAB (Cetyl trimethylammonium bromide).[2,17,18] Briefly, spherical gold seeds were produced by reducing chloroauric acid with sodium borohydride in the presence of CTAB. Next, three identical growth solutions were prepared with chloroauric acid, CTAB, and ascorbic acid. To produce medium length GNRs, the seed was added to the first solution and the reaction was allowed to take place progressively in each growth solution for a couple of hours, followed by pipette transfer to the next growth solution. To produce long rods, the reaction was allowed to proceed in the first two growth solutions for less than a minute and then left in the third solution overnight. In both cases, the final product was obtained in the form of a precipitate consisting of CTAB capped GNRs. The GNRs were recovered and redispersed to form dilute aqueous suspensions (1 mg/ml). Short GNRs (aspect ratio ~ 2-4) were purchased from Nanopartz Inc. (Loveland, Colorado).

High aspect ratio, polydisperse gold triangular and other polygonal platelets with up to 10 μm side lengths and about 5 nm thickness were produced using an aloe vera extract technique: 30 g of aloe vera leaf were boiled in 100 ml of de-ionized water to produce the extract, 1ml of the

extract was then added to 1 mM chloroauric acid in 9 ml of methanol and allowed to sit at room temperature for several days.[34]

9.2.2 Fabrication of aligned SWNT macrostructures

Thin films of horizontally aligned SWNTs were prepared from vertically aligned SWNT 'carpets' produced using the method described by Xu *et al*.[35] The carpets typically consisted of 20-200 μm long vertical array of SWNTs bound to Fe catalyst particles and supported on Silicon substrates, as shown in Fig. 1(a). Thin films were obtained from the SWNT carpets using a modified version of the 'roll-over' method.[36] In short, vertically aligned SWNTs were 'tilted' towards the desired direction of alignment by gentle unidirectional rubbing with a clean strip of velvet cloth, followed by the 'rolling' process which compresses the carpet into a dense, highly aligned SWNT film (Fig. 1(b)). A thin sheet of aluminum foil was used during rolling to prevent transfer of any SWNTs from the carpet on to the roller. Dipping these SWNT films in 1 M HCl solution etches away the catalyst particles, resulting in their immediate detachment from Silicon substrates; the free floating films can then be transferred onto any desired substrate.

SWNT fibers were produced by wet spinning from high concentration (> 8 wt%) SWNT-Oleum (100% sulfuric acid + 20% SO_3) solutions.[25,36-39] Polarized Raman spectroscopy of the fiber showed that for the so-called G peak (~ 1591 cm^{-1}) the ratio of intensities measured for polarizations in longitudinal vs. transverse directions is about 2.4, indicating a high degree of SWNT alignment, further confirmed by SEM (Fig. 2(a)). SEM was performed using (JEOL JSM-7401F FESEM).

9.2.3 Fabrication of Microporous Polymerized LC networks

The microporous polymerized LC networks were prepared following the mixture and cell construction techniques described in section 6.2.1, with the 69% E7 replaced by another non-reactive nematic, VALID, in order to promote phase segregation resulting in microscale regions with no reactive mesogen. Samples for SEM were prepared by dropping the unpolymerized mixture onto an untreated silicon substrate.

9.3 Results & Discussion

The GNR deposition process consisted of drop drying GNR colloidal suspensions (few microliters) on top of the aligned SWNT macrostructures; the process was demonstrated on films and fibers made of highly aligned SWNTs. Upon completion of drying under ambient conditions, the samples were further heated to ~ 90 $^{\circ}$C for 5 minutes to ensure complete removal of the solvent. The desired density of GNRs on SWNT films and fibers was achieved by repeating the drop drying procedure multiple times. GNRs with a wide range of aspect ratios (~ 2-35) were deposited on SWNT films using this procedure. The deposition on SWNT fibers was demonstrated with short GNRs suspended in two different types of medium, aqueous and an organic solvent (ethanol). Both types of suspensions yielded similar results.

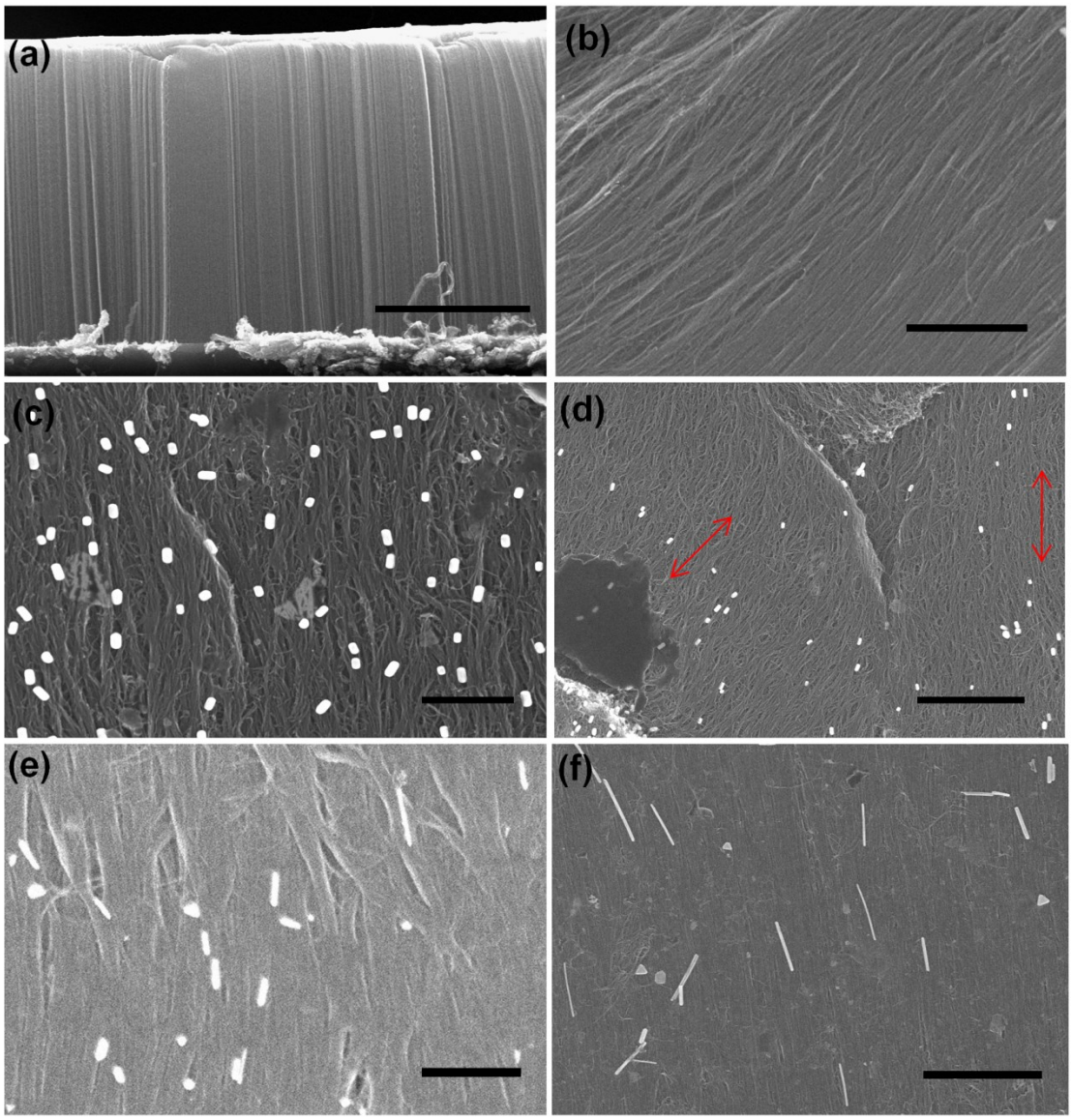

Fig. 9.1: SEM of macroscopic ordered assemblies of gold nanorods (GNRs) of varying aspect ratios, produced by drop drying on aligned SWNT films. (a) Vertically aligned SWNT carpet. (b) Aligned SWNT film fabricated from SWNT carpet. (c) Spontaneous alignment of short GNRs (aspect ratio 2-4) on SWNT film. (d) GNRs replicating the alignment defect in underlying film (shown with red arrows). (e) and (f) Alignment of medium (5-12) and long (12-35) aspect ratio GNRs with SWNTs. Scale bars: (a) 15 μm, (b) 1 μm, (c) 400 nm, (d) 1 μm, (e) 500 nm, (f) 1 μm.

The GNR-SWNT composites were analyzed using SEM imaging. Remarkably, we found that a large fraction of GNRs spontaneously align along the SWNTs in the films and fibers during the

deposition process, as shown in Figs. 9.1 (c)-(f) and Figs. 9.2 (b)-(c). In addition, the strong spontaneous alignment to the SWNT substrate was observed for all GNR aspect ratios. Most of the non-aligned GNRs were within rare aggregates. Non-uniformities (cracks, sharp protrusions, misaligned domains and domain boundaries, *etc*.) in the underlying SWNT macrostructure promoted aggregation and accumulation of GNRs, often leading to their non-uniform distribution. Employing dilute GNR suspensions limited the extent of GNR aggregation during drop drying and yielded an ordered and oriented GNR deposition.

Closer inspection of certain regions in GNR-SWNT thin films with imperfect alignment, like in Fig. 1(d), reveals that the GNRs closely follow the *local* SWNT alignment and therefore reproduce the defects and distortion patterns in their underlying SWNTs. This shows the effectiveness of this technique as a templating mechanism, which can be employed to replicate varied and intricate patterns from underlying SWNT substrates to the deposited GNR layer. Due to the same effect, the GNR arrays deposited on the films and fibers shown in Fig. 9.1 are less ordered on large length scales. In the films and fibers used here, SWNTs are aligned over large length scales (microns and higher), but show considerable waviness and undulations at shorter length scales (tens of nanometers), that can be described by a local direction of SWNT alignment, $\mathbf{N_{SWNT}(r)}$. Better unidirectional global alignment could be obtained by improving the alignment of the SWNTs and SWNT bundles in the substrates (so that $\mathbf{N_{SWNT}(r)}$ = constant).

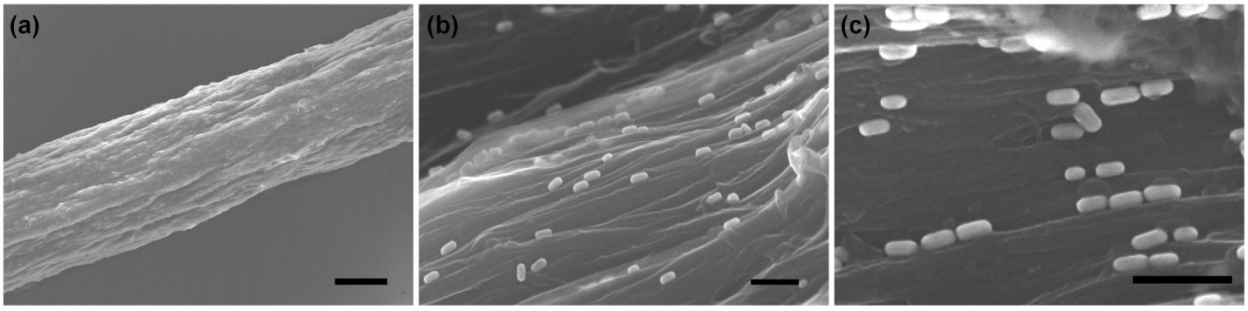

Fig. 9.2: SEM image of SWNT fiber (a) and spontaneous alignment of short GNRs with SWNTs (b-c) in the fiber. GNRs were deposited onto the fiber by drop drying as well as dip coating, both methods producing similar results. Scale bars: (a) 40 μm, (b) & (c) 200 nm.

GNR alignment on SWNT macrostructures was quantified by measuring the angular orientation of individual GNRs with respect to the aligned SWNTs in the SEM images. Multiple SEM images were analyzed for each GNR type (short, medium and long) to collect data for statistically significant number of GNRs. For example, a total of 322 short GNR particles were analyzed for SWNT films and 97 particles for short GNRs on SWNT fibers. In order to estimate the degree of relative alignment of GNRs and SWNTs, the angular orientation of individual GNRs (defined as 'α') was measured with respect to the direction of alignment $\mathbf{N}_{\mathbf{SWNT}}$ of the locally underlying SWNTs (α=0). This analysis of substrate-induced alignment of GNRs is similar to the analysis of ordering of dye molecules and anisotropic particles imposed by the elasticity of liquid crystal host media, (for example, see Refs.[41-43]) where the order parameters of aligned dye molecules or rods were also probed with respect to the local director of the surrounding liquid crystal. Fig. 9.3 shows the normalized orientation distribution function obtained for short GNRs deposited on aligned SWNT carpet films and SWNT fibers. Higher aspect ratio GNRs deposited on SWNT films showed a similar angular distribution.

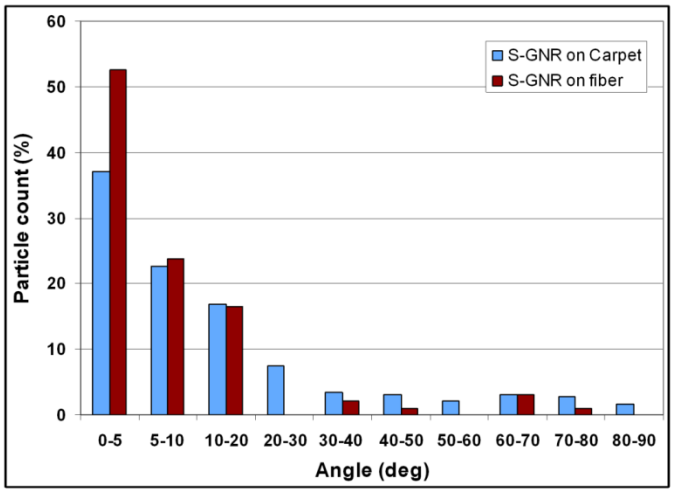

Fig. 9.3: Orientational distribution function for spontaneously aligned short GNRs (S-GNRs) on aligned SWNT macrostructures. Orientation 'angle' for each GNR was calculated with respect to the underlying SWNT/SWNT bundle. Total of 322 particles were analyzed for S-GNRs on SWNT carpets, and 97 particles for S-GNRs on SWNT fibers.

The angular orientation measurements for individual GNR particles were used to calculate the 2-D scalar order parameter (S_{2D}) for GNR arrays deposited on SWNT macrostructures. S_{2D} was obtained by evaluating $2\langle\cos^2\alpha\rangle - 1$ for each GNR and taking an average over all GNRs belonging to each aspect ratio group. S_{2D} values obtained using this method of analysis 'filter out' the effect of undulations imparted onto the GNR assembly due to alignment imperfections in the SWNT substrate, and indicate the degree of ordering achievable in a GNR array deposited on a perfectly aligned SWNT substrate with $\mathbf{N_{SWNT}(r)}$=constant. The values of S_{2D} listed in Table 9.1 further illustrate the high degree of spontaneous alignment among GNRs, imposed by the underlying ordered structures of SWNTs.

Table 9.1: 2D scalar order parameter values for ordered arrays of GNRs with varying aspect ratios, deposited on highly aligned SWNT films, and short GNRs on fibers.

Films		**Fibers**	
GNR aspect ratio	**Order Parameter**	**GNR aspect ratio**	**Order Parameter**
2 – 4	0.73	2 – 4	0.87
5 – 12	0.70	–	–
12 – 35	0.73	–	–

Interestingly, SWNT fibers produced better alignment and a higher order parameter among GNRs than the films. This is likely due to the "grooved" surface morphology of the fibers (groove width ~ tens of nanometers), which are composed of substructures of smaller diameter SWNT ropes and fibrils; the unidirectional groves can further aid in the alignment of nanoparticles. The alignment of GNRs on SWNT fibers demonstrates the portability of this technique to other SWNT macrostructures, including curved surfaces. Since the alignment behavior of GNRs on SWNT films was independent of GNR aspect ratio, the deposition on fibers was tested with only short GNRs.

The self-alignment behavior during drop drying on SWNT substrates, was investigated also using suspensions of gold nanoparticles possessing other interesting shapes, like high aspect ratio triangles and polygonal platelets (prepared using the procedure described in Ref[44]).

Interestingly, a significant number of gold triangles and polygons spontaneously aligned during deposition, with one side of polygon parallel to the SWNT alignment direction (Fig. 9.4). This demonstrates that alignment is not restricted to only rod shaped particles. The aligned triangles did not show any predominant polarity and the fraction of aligned nanoparticles was lower than that in the case of GNRs.

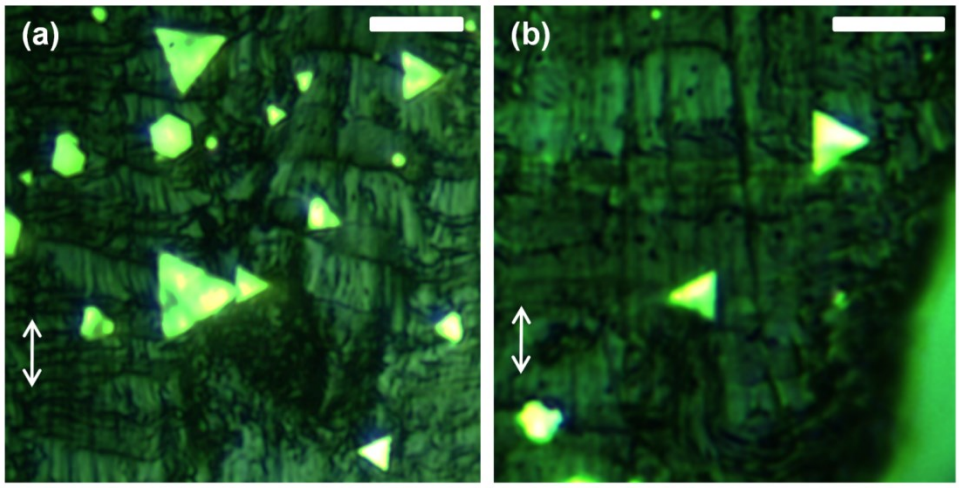

Fig. 9.4: (a-b) Optical images (reflection mode, 50x lens) showing the spontaneous alignment of 2D gold triangles and platelets, with one side of each polygon aligned parallel to underlying SWNTs in aligned SWNT films. The direction of SWNT alignment is shown by double sided arrows. Scale bar is 10 μm in both images.

3PEFPM imaging of the microporous polymer network indicates that pores run parallel to the director field of the LC allowing for engineering of the pore distribution (fig 9.5(a,b)) The microporous polymer network is significantly less absorptive than the SWNT carpets, which allows for two photon luminescence imaging to reveal the distribution of nanorods within the bulk. In fig 9.5(e) we see nanorods dispersed within the bulk with exclusion from two diagonal regions potentially corresponding to a cholesteric finger of the first kind.

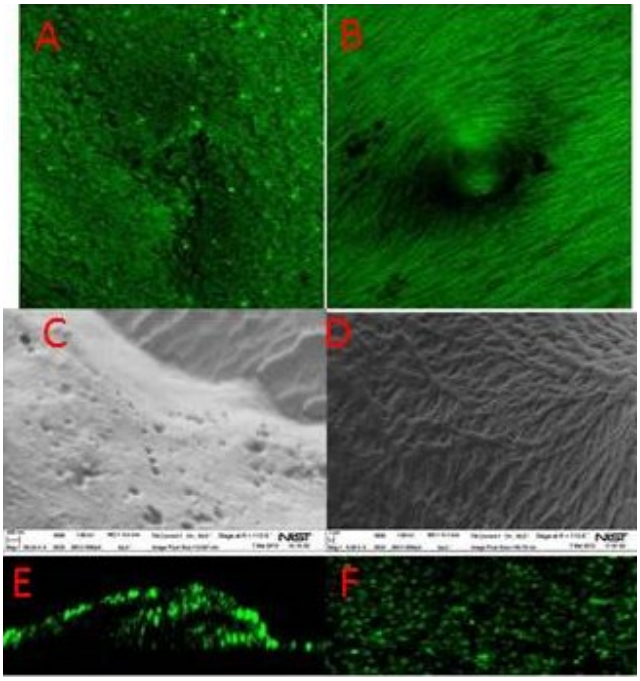

Fig. 9.5- Microporous polymerisable LC- a) Three-photon epi-fluorescence imaging of homeotropically aligned microporous polymer b) The mid-plane of a toron in TIC in microporous polymer c) SEM picture of potential homeotropic pores d) SEM picture of potential planar pores e) Two photon luminescence XZ cross section showing that the gold nanorods are infiltrating the bulk f) Two photon luminescence XY cross section showing some aggregation and some well-dispersed nanorods.

The spontaneous alignment of GNRs on aligned SWNT substrates is driven by anisotropic interactions between GNRs and SWNT structures; these interactions are a combination of capillary, entropic and van der Waals forces. During drop drying, GNRs become confined into a progressively thinning liquid film and are pushed closer to the liquid free surface as well as the anisotropic substrate. Under these circumstances, anisotropic capillary and combing forces may play an important role (Fig. 9.6(a)). Assembly of colloidal particles mediated by capillarity and receding contact lines has been reported before.[45] For drop drying on isotropic substrates, oriented assembly is typically restricted to drop edges.[43,46] In contrast, drop drying on anisotropic micro- and nanostructured surfaces can produce nanoscale orientation and uniform assembly on larger areas.[47-52] For example, minimization of surface free energy[47] and

evaporation on surfaces with patterned hydrophobicity[48] has been used for alignment and ordered deposition of nanoparticles. Strano *et al*.[49] reported the role of hydrodynamic and capillary forces in the alignment, nanoscale positioning and deposition of individual SWNTs inside a cylindrical liquid droplet. Petit and Carbeck[50] reported the molecular combing in microchannels, where DNA molecules get oriented and stretched at the interface of liquid suspension and hydrophobic capillary substrate. Anisotropic capillary forces are used for the alignment and assembly of nanowires in device fabrication.[51,52]

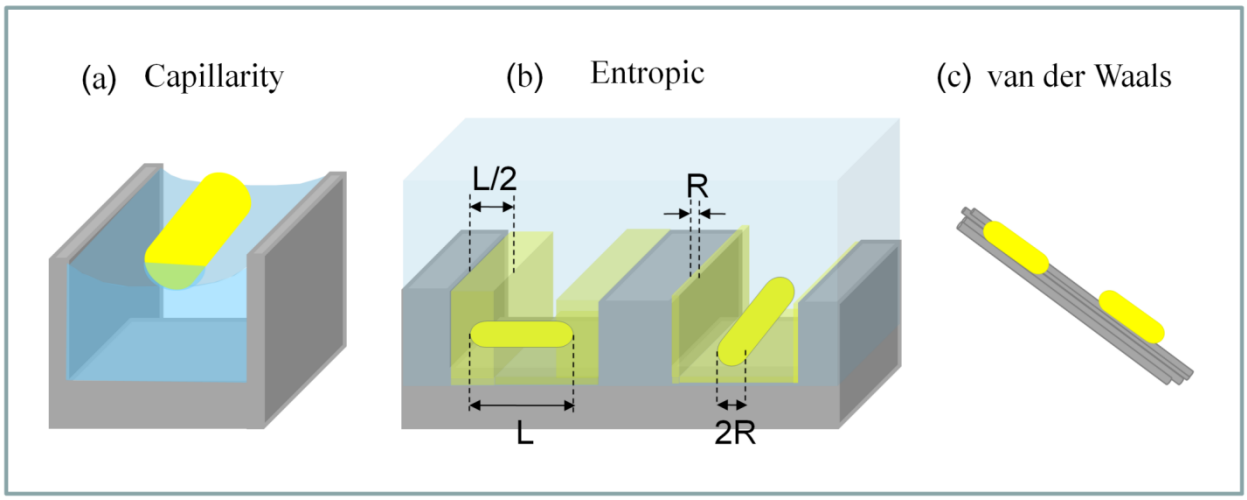

Fig. 9.6: The various forces contributing to assembly and alignment of gold nanorods on SWNT substrates. (a) Capillarity: capillary forces promote alignment of nanorods to minimize distortions in the liquid free surface. (b) Entropic forces: aligning with SWNTs and nanochannels between SWNTs minimizes excluded volume (depicted by the shaded region, which are inaccessible by the rod center of mass) and maximizes entropy. (c) Anisotropic van der Waals interactions; by aligning with the SWNTs, nanorods maximize their area of contact and reduce free energy.

In close proximity to the nanostructured SWNT substrate, overall translational and orientational entropy of GNRs is orientation dependent, which gives rise to entropic alignment forces. Spontaneous alignment on nanoscale grooved surfaces has been observed for liquid crystals as well.[53] However, there are important differences between these two systems. For thermotropic

small-molecule LCs with molecular dimensions of the order of 1 nm (typically several nanometers in length and sub-nanometer in width), the entropic effects can be neglected (the ensuing entropic interactions are much smaller than confinement-induced elastic forces and anisotropic van der Waals interactions of LC molecules with the surfaces). The entropic forces become important in lyotropic LCs composed of cylindrical micelles (surfactant-based LCs) or long molecular aggregates (chromonic LCs) that can have lengths comparable to that of our nanorods (~ 50 nm). However, the most important difference is that LCs, due to their bulk elasticity, exhibit coupling of the orientation of micelles and chromonic aggregates at the surface with the far-field director away from the surface, which is not the case for nanorods studied here. Our observations have closer resemblance to the entropy-mediated templating of patterns, from micro and nanostructured surfaces to colloidal particles in dilute suspension, observed in other systems.[54-56] Onsager theory[57] of nematic liquid crystals describes the spontaneous ordering of colloidal rigid rods for minimization of excluded volume and maximization of entropy; in our case, similar interactions between each rigid rod and the features on structured surfaces like walls of channels, protrusions and corners, help colloidal particles to attain well-defined positions and orientations. In the case of anisotropic colloids like GNRs, in unidirectional nanochannels created by SWNTs, alignment leads to reduction in their excluded volume by $\sim(L-2R)\cdot A$, where A is the surface area of channel-like substrate nanostructures, L is the length of a GNR, and R is its radius, as depicted in Fig. 9.6(b).

Finally, as GNRs deposit on the substrate, van der Waals interactions with individual SWNTs and SWNT bundles strongly affect their orientation, as depicted in Fig. 9.6(c). Aligning with SWNTs in the substrate allows GNRs to maximize their area of contact and achieve a lower energy state by means of increased van der Waals interaction. An important point to note here is

that GNRs should have stronger van der Waals attraction towards each other than to SWNTs, because gold has a higher Hamaker constant than carbon. However, a stabilization layer of micellar CTAB on GNRs prevents their self-aggregation and flocculation in suspension, while allowing them to interact with bare uncoated SWNT surfaces during deposition. Using a high concentration GNR suspension during deposition, however, can lead to deposition of multiple layers of GNRs over the same spot. The secondary and more layers of GNRs may experience much weaker templating effect of the underlying SWNT.

Further insight into the relative influence of these three forces on the oriented assembly of GNRs was obtained from the deposition of short GNRs on SWNT fibers. Short GNRs suspended in two different medium, aqueous(Fig 9.2) and in an organic solvent, were deposited on SWNT fibers using the same procedure. Due to the hydrophobic nature of SWNTs, GNRs in aqueous and organic suspensions will experience different wetting behavior, contact angle, and capillary forces. In addition, different stabilizing polymers/surfactants (proprietary, Nanopartz Inc.) were employed to suspend the GNRs in the two different solvents. However, similar degree of alignment was observed in both cases which indicate the relative dominance of entropic forces in the GNR orientated assembly process; this is especially true for the case of SWNT fibers, which possess a grooved surface morphology as mentioned before.

Similar forces are possibly in play for the case of anisotropic gold platelets and polygons (Fig. 9.4). In the simplest case, an anisotropic gold triangle or platelet (5 nm thick, 10 μm wide) approaching the SWNT film surface with its plane perpendicular to it behaves like a GNR with 5 nm diameter. Thus, the interplay of various alignment forces leads to deposition of the triangle with one of the sides parallel to SWNT orientation. The interactions and potential benefits of

alignment become more complex for other possible plane orientations, which explains the lower fraction of aligned particles observed in the case of polygonal platelets, compared to GNRs.

9.4 Conclusions

We have demonstrated a drop drying based simple and versatile technique for the ordered assembly of gold nanoparticles on highly aligned SWNT films and fibers. The method was successfully demonstrated using GNRs with aspect ratios ranging from 2–35, gold triangles with side length up to 10 μm and 5 nm thickness, and other polygonal shapes. The nanoparticles show strong interaction with SWNTs, and spontaneously align on the anisotropic substrates during deposition. These ordered arrays of plasmonic GNRs supported on strong, durable, inert and electrically conductive SWNT substrates can potentially better serve the currently existing GNR applications and act as a platform for development of advanced metamaterials.

9.5 References:

1. Daniel, M. C.; Astruc, D., *Chemical Reviews* **104** (1), 293-346 (2004).

2. Murphy, C. J.; San, T. K.; Gole, A. M.; Orendorff, C. J.; Gao, J. X.; Gou, L.; Hunyadi, S. E.; Li, T., *Journal of Physical Chemistry B***, 109** (29), 13857-13870. (2005)

3. Link, S.; Mohamed, M. B.; El-Sayed, M. A., *Journal of Physical Chemistry B***, 103** (16), 3073-3077 (1999).

4. Westphalen, M.; Kreibig, U.; Rostalski, J.; Luth, H.; Meissner, D., *Solar Energy Materials and Solar Cells* , **61** (1), 97-105 (2000).

5. Atwater, H. A.; Polman, A., *Nature Materials* **, 9** (3), 205-213 (2010).

6. Morfa, A. J.; Rowlen, K. L.; Reilly, T. H.; Romero, M. J.; van de Lagemaat, J., *Applied Physics Letters***, 92** (1), 013504 (2008).

7. Orendorff, C. J.; Gearheart, L.; Jana, N. R.; Murphy, C. J., *Physical Chemistry Chemical Physics* ,**8** (1), 165-170 (2006).

8. Nikoobakht, B.; El-Sayed, M. A., *Journal of Physical Chemistry A*, **107** (18), 3372-3378 (2003).

9. Huang, X. H.; El-Sayed, I. H.; Qian, W.; El-Sayed, M. A., *Journal of the American Chemical Society*, **128** (6), 2115-2120 (2006).

10. Huang, X. H.; El-Sayed, I. H.; Qian, W.; El-Sayed, M. A., *Nano Letters* ,**7**, 1591-1597 (2007).

11. Durr, N. J.; Larson, T.; Smith, D. K.; Korgel, B. A.; Sokolov, K.; Ben-Yakar, A., *Nano Letters* , **7** (4), 941-945 (2007).

12. Liu, Q. K.; Cui, Y. X.; Gardner, D.; Li, X.; He, S. L.; Smalyukh, I., *Nano Letters* ,**10** (4), 1347-1353 (2010).

13. Shalaev, V. M.; Cai, W. S.; Chettiar, U. K.; Yuan, H. K.; Sarychev, A. K.; Drachev, V. P.; Kildishev, A. V., *Optics Letters* ,**30** (24), 3356-3358 (2005).

14. Shenhar, R.; Norsten, T. B.; Rotello, V. M., *Advanced Materials* ,**17** (6), 657-669 (2005).

15. Murphy, C. L.; Orendorff, C. J., *Advanced Materials,* **17** (18), 2173-2177 (2005).

16. van der Zande, B. M. I.; Koper, G. J. M.; Lekkerkerker, H. N. W., *Journal of Physical Chemistry B* ,**103** (28), 5754-5760 (1999).

17. Jana, N. R.; Gearheart, L. A.; Obare, S. O.; Johnson, C. J.; Edler, K. J.; Mann, S.; Murphy, C. J., *Journal of Materials Chemistry* ,**12** (10), 2909-2912 (2002).

18. Nikoobakht, B.; Wang, Z. L.; El-Sayed, M. A., *Journal of Physical Chemistry B* ,**104** (36), 8635-8640(2000).

19. Liu, S. H.; Tok, J. B. H.; Locklin, J.; Bao, Z. N., *Small* ,**2** (12), 1448-1453 (2006).

20. Green, M. J.; Behabtu, N.; Pasquali, M.; Adams, W. W., *Polymer* ,**50** (21), 4979-4997 (2009).

21. Tans, S. J.; Devoret, M. H.; Dai, H. J.; Thess, A.; Smalley, R. E.; Geerligs, L. J.; Dekker, C., *Nature* ,**386** (6624), 474-477 (1997).

22. Dan, B.; Irvin, G. C.; Pasquali, M., *ACS Nano* ,**3** (4), 835-843 (2009).

23. Wu, Z. C.; Chen, Z. H.; Du, X.; Logan, J. M.; Sippel, J.; Nikolou, M.; Kamaras, K.; Reynolds, J. R.; Tanner, D. B.; Hebard, A. F.; Rinzler, A. G., *Science* ,**305** (5688), 1273-1276 (2004).

24. Behabtu, N.; Green, M. J.; Pasquali, M., *Nano Today* ,**3** (5-6), 24-34 (2008).

25. Davis, V. A.; Parra-Vasquez, A. N. G.; Green, M. J.; Rai, P. K.; Behabtu, N.; Prieto, V.; Booker, R. D.; Schmidt, J.; Kesselman, E.; Zhou, W.; Fan, H.; Adams, W. W.; Hauge, R. H.; Fischer, J. E.; Cohen, Y.; Talmon, Y.; Smalley, R. E.; Pasquali, M., *Nature Nanotechnology* ,**4** (12), 830-834 (2009).

26. Li, Y. L.; Kinloch, I. A.; Windle, A. H., *Science* ,**304** (5668), 276-278 (2004).

27. Miaudet, P.; Badaire, S.; Maugey, M.; Derre, A.; Pichot, V.; Launois, P.; Poulin, P.; Zakri, C., *Nano Letters* ,**5** (11), 2212-2215 (2005).

28. Hu, L.; Hecht, D. S.; Gruner, G., *Chem Rev* ,**110** (10), 5790-844 (2010).

29. Kong, B. S.; Jung, D. H.; Oh, S. K.; Han, C. S.; Jung, H. T., *Journal of Physical Chemistry C* ,**111** (23), 8377-8382 (2007).

30. Peigney, A.; Laurent, C.; Flahaut, E.; Bacsa, R. R.; Rousset, A., *Carbon* ,**39** (4), 507-514 (2001).

31. Girishkumar, G.; Vinodgopal, K.; Kamat, P. V., *Journal of Physical Chemistry B* ,**108** (52), 19960-19966 (2004).

32. Planeix, J. M.; Coustel, N.; Coq, B.; Brotons, V.; Kumbhar, P. S.; Dutartre, R.; Geneste, P.; Bernier, P.; Ajayan, P. M., *Journal of the American Chemical Society* ,**116** (17), 7935-7936 (1994).

33. Correa-Duarte, M. A.; Perez-Juste, J.; Sanchez-Iglesias, A.; Giersig, M.; Liz-Marzan, L. M., *Angewandte Chemie-International Edition* ,**44** (28), 4375-4378 (2005).

34. Chandran, S. P.; Chaudhary, M.; Pasricha, R.; Ahmad, A.; Sastry, M., *Biotechnology Progress* ,**22** (2), 577-583 (2006).

35. Xu, Y. Q.; Flor, E.; Kim, M. J.; Hamadani, B.; Schmidt, H.; Smalley, R. E.; Hauge, R. H., *Journal of the American Chemical Society* ,**128** (20), 6560-6561 (2006).

36. Pint, C. L.; Xu, Y. Q.; Pasquali, M.; Hauge, R. H., *ACS Nano* ,**2** (9), 1871-1878 (2008).

37. Ericson, L. M.; Fan, H.; Peng, H. Q.; Davis, V. A.; Zhou, W.; Sulpizio, J.; Wang, Y. H.; Booker, R.; Vavro, J.; Guthy, C.; Parra-Vasquez, A. N. G.; Kim, M. J.; Ramesh, S.; Saini, R. K.; Kittrell, C.; Lavin, G.; Schmidt, H.; Adams, W. W.; Billups, W. E.; Pasquali, M.; Hwang, W. F.; Hauge, R. H.; Fischer, J. E.; Smalley, R. E., *Science* ,**305** (5689), 1447-1450 (2004).

38. Wang, Y.; Ericson, L. M.; Kittrell, C.; Kim, M. J.; Shan, H.; Fan, H.; Ripley, S.; Ramesh, S.; Hauge, R. H.; Adams, W. W.; Pasquali, M.; Smalley, R. E., *Chemistry of Materials* ,**17** (25), 6361-6368 (2005).

39. Booker, R.; Green, M.; Fan, H.; Parra-Vasquez, A.; Behabtu, N.; Young, C.; Hauge, R.; Schmidt, H.; Smalley, R.; Hwang, W., *Proceedings of the Institution of Mechanical Engineers, Part N: Journal of Nanoengineering and Nanosystems* ,**222** (3), 101-109 (2008).

40. Davis, V. A.; Ericson, L. M.; Parra-Vasquez, A. N. G.; Fan, H.; Wang, Y. H.; Prieto, V.; Longoria, J. A.; Ramesh, S.; Saini, R. K.; Kittrell, C.; Billups, W. E.; Adams, W. W.; Hauge, R. H.; Smalley, R. E.; Pasquali, M., *Macromolecules* ,**37** (1), 154-160 (2004).

41. Yang, D.-K.; Wu, S.-T., *Fundamentals of liquid crystal devices*. John Wiley: Chichester, Eng. ; Hoboken, NJ, 2006.

42. Collings, P. J.; Ratna, B. R.; Shashidhar, R., *Physical Review E* ,**67** (2), 21705 (2003).

43. Smalyukh, II; Butler, J.; Shrout, J. D.; Parsek, M. R.; Wong, G. C. L., *Physical Review E* ,**78** (3), 30701 (2008).

44. Lapointe, C. P.; Mason, T. G.; Smalyukh, II, *Science* ,**326** (5956), 1083-1086 (2009).

45. Deegan, R. D.; Bakajin, O.; Dupont, T. F.; Huber, G.; Nagel, S. R.; Witten, T. A., *Nature* ,**389** (6653), 827-829 (1997).

46. Li, Q. W.; Zhu, Y. T.; Kinloch, I. A.; Windle, A. H., *Journal of Physical Chemistry B,* **110** (28), 13926-13930 (2006).

47. Lewandowski, E. P.; Bernate, J. A.; Searson, P. C.; Stebe, K. J., *Langmuir* ,**24** (17), 9302-9307 (2008).

48. Fan, F. Q.; Stebe, K. J., *Langmuir* ,**20** (8), 3062-3067 (2004).

49. Sharma, R.; Lee, C. Y.; Choi, J. H.; Chen, K.; Strano, M. S., *Nano Letters* ,**7** (9), 2693-2700 (2007).

50. Petit, C. A. P.; Carbeck, J. D., *Nano Letters* ,**3** (8), 1141-1146 (2003).

51. Messer, B.; Song, J. H.; Yang, P. D., *Journal of the American Chemical Society* ,**122** (41), 10232-10233 (2000).

52. Salalha, W.; Zussman, E., *Physics of Fluids* ,**17** (6) (2005).

53. Berreman, D. W., *Physical Review Letters* ,**28** (26), 1683 (1972).

54. Dinsmore, A. D.; Yodh, A. G.; Pine, D. J., *Nature* ,**383** (6597), 239-242 (1996).

55. Gupta, S.; Zhang, Q. L.; Emrick, T.; Balazs, A. C.; Russell, T. P., *Nature Materials* ,**5**, 229-233 (2006).

56. Yodh, A. G.; Lin, K. H.; Crocker, J. C.; Dinsmore, A. D.; Verma, R.; Kaplan, P. D., *Philosophical Transactions of the Royal Society of London Series a-Mathematical Physical and Engineering Sciences* ,**359** (1782), 921-937 (2001).

57. Onsager, L., *Annals of the New York Academy of Sciences* ,**51** (4), 627-659 (1949).

Chapter 10: Towards Long term stable devices: Preparation of solid materials from bulk LC phase

Chapter Overview

In the previous chapter we describe the production of gold nanorod containing materials by simply adding gold nanorods to a prepared solid. In this chapter we describe two methods of producing a solid from an LC dispersion of gold nanorods. In the first method, nematic films were precipitated from a colloidal LC composed of nanocrystalline cellulose and gold nanorods. In the second method, bulk short pitch cholesteric hydroxypropyl cellulose LC containing gold nanorods was cross-linked to produce a solid film with the same ordering as the initial fluid phase. Preparing solids from the LC phase potentially allows for significantly more control over the distribution and alignment of nanoparticles within the material than the methods discussed in chapter 9.

10.1 Introduction

LC materials offer two relatively unique material properties of elasticity mediated self-assembly and tunable response to external stimuli. Creating a solid film from a LC medium removes or limits the tunable responses it can exhibit, but significantly enhances the stability of the material and the ability to couple director structure to mechanical movement. UV curable thermotropic materials such as those discussed in chapters 6-9 can be used to create artificial muscles[1], artificial cilia[2] which respond to heat and/or light, luminescent solar concentrators[3], and a variety of other interesting applications[4]. In chapters 7 and 8 we described novel colloidal photothermal shape plasticity due to including some of our simplest nanoparticles without particular attention paid to their distribution within the materials. However the inclusion of larger

nanorods in elastomeric systems is limited by the same general issues associated with their inclusion in small molecule thermotropic LC. Lyotropic systems on the other hand can host significant numbers of nanorods without much difficulty. In this chapter we describe two types of solid structures that can be produced from controlled evaporation of nanocrystalline cellulose and polymerization of hydroxypropyl cellulose respectively.

10.2 Materials and Methods

10.2.1 Fabrication of nanocrystalline cellulose GNR cholesteric phase

Rod-shaped cellulose nanocrystals with dimensions 5nm x 100-300nm were prepared by acid hydrolysis described in detail elsewhere[5]. Briefly, 10 grams of cotton balls were added to 150ml of 65 wt% sulfuric acid and stirred for 8 hours at 45 degrees Celsius. As long as the solution remains sufficiently acidic these nanocrystals form a charge stabilized dispersion in an aqueous environment. 20nm x 50 nm mPEG coated rods in water were added to the prepared nanocrystalline cellulose and no aggregation was observed. Allowing the solution to partially evaporate concentrates the cellulose yielding the desired LC phase.

10.2.2 Production of aligned nematic nanocrystalline cellulose films

The aligned films were produced by three different methods dip-coating, gravity assisted drop drying, and shearing. The dip-coating process consisted of removing a piece of slide glass from a dilute solution of CNC at a rate of ~1mm/hr using a homemade stepper-motor driven stage controlled by a Labview program. Gravity assisted drop drying consisted of repeatedly placing a droplet of CNC GNR solution at the top of an inclined piece of slide glass and letting run down the glass until a thick enough deposit has

built up on the glass. The shearing process consisted of sandwiching the solution between two glass substrates and pulling the substrates apart along the long axis of the glass plates.

10.2.3 Hydroxypropyl cellulose dispersions

Hydroxypropyl cellulose, one of the two most commonly used polymeric lyotropic LC materials, forms a short-pitch cholesteric phase somewhere between 36% wt and 45% depending on which solvent it is dispersed in[6-7]. Simply preparing an aqueous lyotropic LC with an aqueous solution of 50nmx20nm mPEG capped gold nanorods produces a good dispersion of nanoparticles in this lyotropic system. The HPC phase can be reduced to a solid film through cross-linking it with glutaraldehyde. To produce a cross-linked film we prepared an LC phase of HPC with 2 wt% of the cross-linking agent, glutaraldehyde, and 3wt% HCl to activate the glutaraldehyde and heated to 60 degrees Celsius for 24 hrs[8].

10.3 Results

10.3.1 GNR dispersion in cellulose nanocrystal based cholesteric phase and dried nematic films

Aqueous dispersions of nanocrystalline cellulose form a chiral nematic phase above a critical concentration in accordance with a modified Onsager theory[9]. The chirality arises from minimizing the electrostatic repulsion associated with the charged sulfate groups located at the ends of the cellulose rod. mPEG capped gold nanorods can disperse and align with the director of the cholesteric phase at a second critical concentration of CNC(fig 10.1(a,b)), but are energetically costly inclusions and excluded from the cholesteric phase over time. In

fig10.1(a,b), we see a cholesteric droplet formed in the process of concentrating the cellulose with a significantly reduced amount of gold in the droplet after a fairly short time. In order to form solid films with order derived from the LC state, we must start with an isotropic phase, pass through an LC phase to order the nanorods, and deposit the material into a film before the nanorods are excluded from the phase.

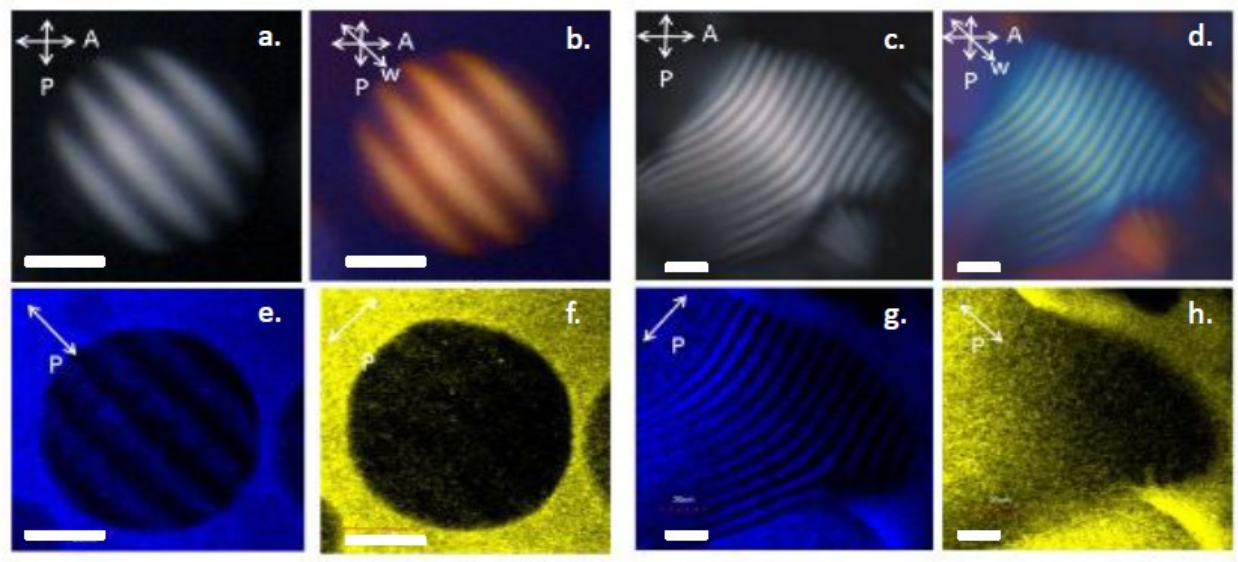

Fig. 10.1: Cellulose GNR in bulk cholesteric - a) crossed-polarized b) with red-plate images of a cholesteric droplet in an isotropic background c) cross-polarized d) with red-plate images of a cholesteric region forming during the evaporation process e-h)Two-photon luminescence imaging showing that the nanorods align with the director in the cholesteric phase, but are significantly more concentrated in the isotropic region.

The nematic films produced by gravity assisted drop-drying shown under different polarizations in fig. 10.2(a,b) show reasonably good alignment with a pink color when the polarizer is perpendicular to the cellulose director and a blue color when the polarizer is parallel to the cellulose director. The absorption spectra(fig 10.2(c,d)) show an absorption by the longitudinal plasmon is around 5 times stronger along the director of the cellulose confirming that we have achieved good, but not perfect alignment of the gold nanorods within the film. Shearing

produced aligned films of slightly worse quality than those produced by gravity assisted drop drying. Dip-coating produced films which were too thin to detect plasmonic absorption in or poorly aligned due to the accumulation of significant amounts cellulose at the water air interface which would deposit directly onto the slide without alignment.

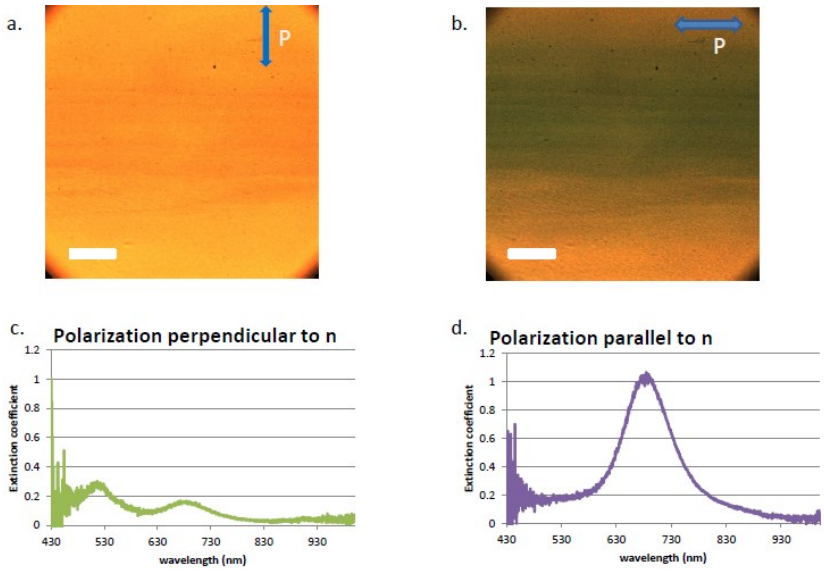

Fig. 10.2: Aligned nematic films of cellulose nanocrystals and gold nanorods produced by gravity assisted drop-drying a,b) Polarized images of a dried nematic film showing a strong blue color in the horizontally polarized picture indicating that the rods are aligned with direction the drop rolled. c,d) spectra that confirm the alignment of the rods seen in a,b).

In order to look at the material under TEM, the sample must be prepared on a copper grid with parafilm covering the grid holes which significantly limits our ability to align the sample. In fig. 10.3(a), we see a Schlieren texture associated with an unaligned nematic where the gold nanorods follow the director of the cellulose nanocrystals. Looking at a shear aligned sample of the material with an SEM reveals that the interior of the cellulose has a network like structure with the majority of the gold and cellulose rods aligned with the far-field director, but some are necessarily misaligned to provide structural support of the film. This potentially limits the quality of alignment that can be achieved.

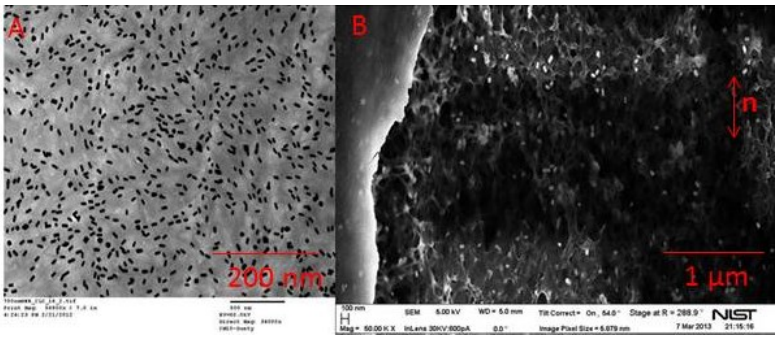

Fig. 10.3: EM characterization of dried CNC GNR phases- a)TEM micrograph of an unaligned dried sample showing the nanorods following a schlieren texture produced by the dried nematic cellulose nanocrystals. b) FIB/SEM micrograph of the interior the dried cellulose film showing a network like structure of cellulose with a significant portion of gold nanorods aligned with the far-field director $\mathbf{n_0}$. The left hand part of the SEM picture is a carbon coating that prevents the sample from charging while imaging.

10.3.2 Hydroxypropyl cellulose based lyotropic phases

Aqueous phases of hydroxypropyl cellulose containing gold nanorods are very simple to prepare and show no evidence of nanorod aggregation up to fairly high concentrations. In fig. 10.4(c,d) two photon luminescence imaging shows that individual nanorods are well dispersed with average interparticle spacing of a few hundred nanometers. Comparing the two polarizations seen in fig. 10.4 (c) and (d), individual points are brighter and darker indicating that most of the green spots are individual nanorods. Since the cholesteric pitch of the material is around 400nm, we cannot use far-field optical techniques to determine if the rods are aligning with the director of the HPC phase.

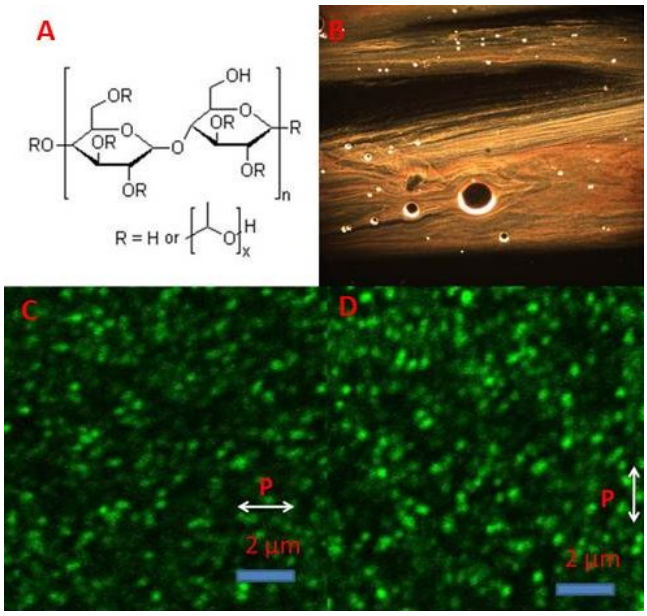

Fig. 10.4- Highly concentrated nanorods in polymer lyotropic-a) structure of hydroxypropyl cellulose which forms a short-pitch cholesteric phase above ~40wt% b) Optical darkfield image of gold nanorods c,d) Polarized Two-Photon Luminescence imaging shows that the gold nanoparticles are very well dispersed at a high concentration but cannot resolve the ~400nm pitch.

10.4 Discusssion

The production of well ordered films by depositing from an LC solution and cross-linking certain bulk LC phases are both well established techiques[10,11]. Here we have demonstrated that the inclusion of gold nanorods into these systems does not significantly interfere with these processes and the dispersion and alignment of the gold is potentially preserved in these processes. The deposition of aligned films from cellulose nanocrystal solutions is a technologically relevant way to produce plasmonic polarizers. Plasmonic polarizers have already been realized in stretched polyvinyl alcohol[12] and lyotropic LC[13]. However the dried nanocrystalline cellulose film allows for more control over the relative positions of nanorods than can be achieved in the stretched polymer case and significantly more stability than the lyotropic LC. The alignment of gold nanorods of a given aspect ratio in such a film may be fundamentally limited by the network-like structure. Working with rods of different aspect ratio and overall dimension could potentially improve the quality of such films. However without significant optimization efforts, we achieved an absorption intensity ratio of 5 to 1, which indicates a significant amount of alignment.

Hydroxypropyl cellulose based lyotropic liquid crystalline phases show the simplest and most reliable dispersion of large quantities of GNR of any material discussed in this thesis however the short pitch, opacity in an SEM and long relaxation times of the material have prevented us from properly characterizing the alignment of GNR with the director of the HPC phase. HPC as well as other polymeric lyotropic systems, such as poly benzyl glutamate, are a very promising avenue to pursue for stable concentrated dispersions of GNR in LC.

10.5 Conclusion

We have demonstrated two techniques to produce solid materials directly from LC gold nanorod composite phases. The deposition of solid films from a cellulose nanocrystal based lyotropic LC produces plasmonic polarizers with reasonably good alignment and long-term stability. The cross-linkable hydroxypropyl cellulose demonstrates that polymer lyotropic materials are very good at dispersing large amounts of gold nanorods and permanently capturing the liquid crystalline dispersion of the nanorods for potential long-term stable device application.

10.6 References

1. Madden, J.D.W., Vandesteeg, N.A., Anquetil, P.A., Madden, P.G.A., Takshi, A., Pytel, R.Z., Lafontaine, S.R., Wieringa, P.A., Hunter, I.W., *Oceanic Engineering, IEEE Journal of* , **29**, 3, 706-728 (2004).

2. C. L. van Oosten, C. W. M. Baastiansen, and D. J. Broer *Nature Mater*. **8** 677-682 (2009).

3. Verbunt, P. P. C., Kaiser, A., Hermans, K., Bastiaansen, C. W. M., Broer, D. J. and Debije, M. G., *Adv. Funct. Mater*., **19**, 2714–2719 (2009)

4. Yamada et al. *Angew. Chem. Int. Ed*., **47**, 4986–4988 (2008)

5. K. Shopowitz et. al *Nature*, **468**, 422-425 (2010).

6. K. Hongladarom, V. M. Hugaz, D. K. Cinader, W. R. Burghardt, and J. P. Quintana, *Macromolecules* **29**, 5346 (1996).

7. K. Hongladarom, W. R. Burghardt, *Rheol. Acta* **37**, 46 (1998).

8. Suto, S. and Yoshinaka, M. J. Mater. Sci. 1993, 8, 4644

9. Purdy K., Fraden S., Phys. Rev. E 70, 061703 (2004)

10. Chung, W.-J. et al. *Nature* **478,** 364–368 (2011).

11. Rokhade, A., Kulkarni, P., Mallikarjuna, N., Aminabhavi, T., *J. Microencapsul.* **26**,1,27-36.(2009).

12. Murphy C., Orendorff C., *Advanced Materials*, **17**, 2173-2177, (2005).

13.Q. Liu, Y. Cui, D. Gardner, X. Li, S. He, I.I. Smalyukh, I.I. *Nano Lett*, 10, 1347, (2010).

Chapter 11: Concluding remarks and Outlook

11.1 Conclusion

The three primary goals of this project were to understand the fundamental physics of guest-host interactions as a function of particle size and shape and mesogen size and shape, to lay the groundwork for LC based materials that access individual plasmon modes(plasmonic polarizers, nanoantennas) and to lay the groundwork of highly concentrated dispersions that access multiparticle plasmon modes (metamaterials). In this work, we have demonstrated the dispersion, alignment, and self-assembly of various gold nanoparticles in a wide variety of liquid crystalline hosts. In systems where the host mesogen and nanoparticle are of similar size, such as 50nmx20nm rods in CTAB lyotropic discussed in chapter 2, 2nm spheres in a small molecule thermotropic discussed in chapter 2, and the nanoplatelets in GGO discotic phase discussed in chapter 4, there is generally little or no self-assembly and elasticity mediated forces and we can achieve reasonably concentrated dispersions. These systems behave much like a dye-doped guest host LCD where the guest simply incorporates itself within the host director structure. As soon as the particle is one or two orders of magnitude larger than the mesogen in one or more dimensions, a continuum viscoelastic description becomes appropriate as seen in the cases of the elastic distortions around the nanostarfruit in small molecule thermotropic (Fig. 5.1.(f)), microspherical inclusions in the GGO phase(fig. 4.5), and the elastomeric pillars dispersed in HPC discussed in chapter 8. When considering such “elastic” inclusions in LC phase the absolute size of the colloid determines whether it is dragged by a phase barrier and aggregated outside of the nematic phase or allowed into the nematic phase because the particle is too large to be dragged by the phase barrier. We have observed nanorods in small molecule thermotropic

nematic phase run into each other without aggregating, but cannot achieve highly concentrated dispersions currently due to the phase transition driven aggregation.

From a device perspective, we have developed a novel method of producing plasmonic polarizers, a shape-morphing elastomer gold nanoparticle composite particle that potentially has applications in microfluidics, and concentrated dispersions of gold nanoparticles in LC, which are within 3 orders of magnitude of those ideal for producing metamaterials. Plasmonic polarizers have been previously produced using stretched polyvinyl alcohol[1] and micellar lyotropic LC[2], but the aligned cellulose films are significantly more stable than micellar lyotropic phases and allow for the particles to be more evenly distributed than stretched poly vinyl alcohol. The nanoparticle-infiltrated elastomeric pillars allow for repeatable precise optical control over shape on the microscale and could be relevant for microfluidic gates and switches.

In the effort towards metamaterials we achieved interparticle spacing of a few hundred nanometers in micellar lyotropic, and polymer lyotropic phases. However for multiparticle guided plasmonic modes to be achieved we need interparticle spacing on the order of tens of nanometers. Given the persistence length of HPC is ~10nm and the length of the micelles in the systems we work with is around ~10nm[2] such highly concentrated dispersions in these lyotropic systems are potentially not achievable. Small molecule calamitic thermotropic LCs are the most developed system for producing devices, however the small mesogen size restricts the concentrations of nanorods we can achieve using the particles available to us. Concentrated dispersions of 2nm spheres in small molecule thermotropic as described in chapter 2 are readily achievable. There are 2nm wide gold nanorods in the literature[3,4] that are potentially highly dispersable in small molecule thermotropic LCs. Using these ultrathin rods one can potentially

achieve smaller interparticle spacing at relatively low wt% and realize materials that have optical properties based upon multi-particle plasmon modes.

11.2 References

1. Murphy C., Orendorff C., *Advanced Materials*, **17**, 2173-2177, (2005).

2.Q. Liu, Y. Cui, D. Gardner, X. Li, S. He, I.I. Smalyukh, I.I. *Nano Lett*, 10, 1347, (2010).

3. Lu X., Yavuz, M., Tuan H., Korgel B., Xia Y., *J. Am. Chem. Soc.*, **130** (28), 8900–8901 (2008).

4. Feng H., Yang Y., You Y., Li G., Guo J., Yu T., Shen Z., Wu T. Xing B., *Chem. Commun.*,15,1984-1986 (2009).

Chapter 12: Bibliography

1. J.B. Pendry. *Phys Rev. Lett.*, 85, 3966, (2000).

2. J. Valentine, S. Zhang, T. Zentgraf, E. Ulin-Avila, D. Genov, G. Bartal, X. Zhang. *Nature*, 455, 376, (2008).

3. G. Colas de Francs, S. Derom, R. Vincent, A. Bouhelier, A. Dereux, *International Journal of Optics* **2012**, 175162 (2012).

4. A. V. Kabashin, P. Evans, S. Pastkovsky, W. Hendren, G. A. Wurtz, R. Atkinson, R. Pollard, V. A. Podolskiy, and A. V. Zayats *Nature Materials* **8**, 867 - 871 (2009)

5. C. Murphy, T. Sau,A. Gole, C. Orendorff, J. Gao, L. Gou, S. Hunyadi, T. Li. *J. Phys. Chem. B* **109***,* 13857-13870 (2005**).**

6. M. Grzelezak, J. Juste, P. Mulvaney, L. Liz-Marzan. *Chem. Soc. Rev.* **37**, 1783-1791 (2008).

7. C. Huang , P. Chiu, Y. Wang, W. Chen, and T. Meen *J. Electrochem. Soc*. **153**, 8, D129-D133 (2006)

8. Q. Liu, Y. Cui, D. Gardner, X. Li, S. He, I.I. Smalyukh, I.I. *Nano Lett*, 10, 1347, (2010).

9. V.G. Veselago. *Soviet Physics Uspekhi*, 10, 509, (1968).

10. D.H. Werner, D.H. Kwon, I.C. Khoo, A.V. Kildishev, V.M. Shalaev. *Optics Express,* 15, 3342, (2007).

11. A. Minovich, D.N. Neshev, D.A. Powell, I.V. Shadrivov, Y.S. Kivshar. *Appl. Phys. Lett.,* 96, 193103, 2010.

12. C.M. Soukoulis, Linden, S., Wegener, M. *Science,* 315, 47, (2007).

13. T. Li, Y.Q. Li, F.U. Wang, Q.J. Wang, H. Liu, S.N. Zhu, Y.Y. Zhu. *Appl. Phys. Lett.*, 90, 251112, (2007).

14. E. Kim, F. Wang, W. Wu, Z. Yu, Y.R. Shen. *Phys. Rev. B.*, 78, 113102, (2008).

15. A. Minovich, D.N. Neshev, D.A. Powell, I.V. Shadrivov, M. Lapine, I. McKerracher, H.T. Hattori, H.H. Tan, C. Jagadish, Y.S. Kivshar. *Phys, Rev. B.*, 81, 115109, (2010).

16. S. Zhang, W. Fan, N.C. Panoiu, K.J. Malloy, R.M. Osgood, S.R.J. Brueck. *Phys. Rev. Lett.*, 95, 1347404, (2005).

17. G. Dolling, C. Enkrich, M. Wegener, C.M. Soukoulis, S. Linden. *Science*, 312, 892, (2006).

18. W. Wu, E. Kim, E. Ponizovskaya, Y. Liu, Z. Yu, N. Fang, Y.R. Shen, A.M. Bratkovsky, W. Tong, C. Sun, X. Zhang, S.Y. Wang, R.S. William. *Appl. Phys A: Matter. Sci. Process.*, 87, 143, (2007).

19. U.K. Chettiar, A.V. Kildishev, H.K. Yuan, W. Cai, S. Xiao, V.P. Drachev, V.M. Shalaev. *Optics Letters*, 32, 1671, (2007).

20. E. Plum, J. Zhou, J. Dong, V.A. Fedotov, T. Koschny, C.M. Soukoulis, N.I. Zheludev. *Phys. Rev. B*, 79, 03540, (2009).

21. J. Yao, Z. Liu, Y. Liu, Y. Wang, C, Sun, G. Bartal, A.M. Stacy, X. Zhang, X. *Science*, *321*, 930, (2008).

22. I.C. Khoo, D.H. Werner, X. Liang, A. Diaz. *Optics Letters*, 31, 2592, (2006).

23. S. Zhang, Y.S. Park, J. Li, X. Lu, W. Zhang, X. Zhang. *Phys. Rev. Lett.*, 102, 023901, (2009).

24. V.A. Podolskiy, A.K. Sarychev, V.M. Shalaev. *J. Nonlinear Optical Phys. and Mater. Sci*, 11, 65, (2002).

25. V. Podolskiy, A. Sarychev, V. Shalaev. *Optics Express*, 11, 735, (2003).

26. V. Shalaev, W. Cai, U.K. Cettiar, H.K. Yuan, A.K. Sarychev, V.P. Drachev, A.V. Kildishev. *Optics Letters*, 30, 3356, (2005).

27. S. Linden, C. Enkrich, M. Wegener, J. Zhou, T. Koschny, C.M. Soukoulis. *Science*, 306, 1351, (2004).

28. S. Zhang, W. Fan, B.K. Minhas, A. Frauenglass, K.J. Malloy, S.R.J. Brueck. *Phys. Rev. Lett.*, 94, 037402, (2005).

29. D.R. Smith, W.J. Padilla, D.C. Vier, S.C. Nemat-Nasser, S. Schultz. *Phys. Rev. Lett.,* 84, 4184, (2000).

30. J.D. Baena, L. Jelinek, R. Marques. *Phys. Rev. B*, 76, 245115, (2007).

31. C. Lapointe, T. Mason, I.I. Smalyukh. *Science,* 326, 1083, (2009).

32. N. Liu, H. Liu, S. Zhu, H. Giessen. *Nature Photonics, 3*, 157, (2009).

33. C. Lapointe, S. Hopkins, T.G. Mason, I.I. Smalyukh. *Phys. Rev. Lett.,* 105, 178301, (2010).

34. I.I. Smalyukh. *Proc. Nat. Acad. U.S.A.,* 107*,* 3945, (2010).

35. R. Pratibha, W. Park, I.I. Smalyukh. *J. Appl. Phys.,* 107, 063511, (2010).

36. R. Pratibha, K. Park, I.I. Smalyukh, W. Park. *Optics Express*, 17, 19459, (2009).

37. K.J. Stebe, E. Lewandowski, M. Ghosh. *Science, 325*, 159, (2009).

38. A. Swami, P.R. Selvakannan, R. Pasricha, M. Sastry. *J. Phys. Chem. B., 108*, 19269, (2004).

39. M. Fukuto, R.K. Heilmann, P.S. Pershan, A. Badia, R.B. Lennox. *J. Chem. Phys., 120*, 3446, (2004).

40. R. Shenhar, T.B. Norsten, V.M. Rotello. *Advanced Materials*, *17*, 657, (2005).

41. J. Perez-Juste, B. Rodrigues-Gonzalez, P. Mulvaney, L. Liz-Marzan. *Adv. Funct. Mater.*, 15, 1065, (2005).

42. R. Elghanian, J.J. Storhoff, R.C. Mucic, R.L. Letsinger, C.A. Mirkin. *Science, 277*, 1078, (1997).

43. T. Hegmann, H. Qi, V.M. Marx. *J. Inorg. Organomet. Polym. Mater.*, *17*, 483, (2007).

44. J. Perez-Juste, L.M. Liz-Marzan, S. Carnie, D.Y.C. Chan, P. Mulvaney. *Adv. Funct. Mater*., *14*, 571, (2004).

45. M.D. Lynch, D.L. Patrick, D.L. *Nano Letters*, 2, 1197, (2002).

46. J.L. Baker, A. Widmer-Cooper, M.F. Toney, P.L. Geissler, A.P. Alivisatos. *Nano Letters*, 10, 195, (2010).

47. C. Sonnichsen, A.P. Alivisatos. *Nano Letters, 5*, 301, (2005).

48. W. Ahmed, E.S. Kooij, A. van Silfhout, B. Poelsema. *Nano Letters,* 9, 3786, (2009).

49. S. Zhang, G. Leem, L. Srisombat, T.R. Lee. J. *Am. Chem. Soc.*, *130*, 113, (2008).

50. B. Halle, P.O. Quist, I. Furó. *Phys. Rev. A*, *45*, 3763, (1992).

51. K.J. Wu, K.C. Chu, C.Y Chao, Y.F. Chen, C.W. Lai, C.C. Kang, C.Y. Chen, P.T. Chou. *Nano Letters,* 7, 1908, (2007).

52. K.T. Yong, Y. Sahoo, M. Swihart, P. Prasad. *Advanced Materials,* 18, 1978, (2006).

53. H. Yoshida, Y. Tanaka, K. Kawamoto, H. Kubo, T. Tsuda, A. Fujii, S. Kuwabata, H. Kikuchi, M. Ozaki. *Applied Physics Express*, 2, 121501, (2009).

54. J. Lydon. *Current Opin. Colloid & Interface Sci.* 3, 458, (1998).

55. A.V. Kachynski, A.N. Kuzmin, P.N. Prasad, I.I. Smalyukh, I.I. *Optics Express,* 16, 10617, (2008).

56. A. Kachynskii, A. Kuzmin, P.N. Prasad, I.I. Smalyukh. *Appl. Phys. Lett.,* 91, 151905, (2007).

57. I.I. Smalyukh, D. Kaputa, A.V. Kachynski, A.N. Kuzmin, P.N. Prasad. *Optics Express,* 15, 4359, (2007).

58. P.S. Salter, G. Carbone, E.J. Botcherby, T. Wilson, S.J. Elston, E.P. Raynes, E. P. *Phys. Rev. Lett.* 103, 257803, (2009).

59. I.I Smalyukh, S. Shiyanovskii, O.D. Lavrentovich. *Chem. Phys. Lett.* 336, 88-96, (2001).

60. T. Lee, R.P. Trivedi, I.I. Smalyukh. *Opt. Lett., 35 3447,* (2010).

61. A. Xie, D.A. Higgins. *Appl. Phys. Lett.* 84, 4014, (2004).

62. M.J. Rust, M. Bates, X. Zhuang. *Nature Methods,* 3, 793, (2006).

63. E. Betzig, G.H. Patterson, R. Sougrat, O.W. Lindwasser, S. Olenych, J.S. Bonifacino, M.W. Davidson, J. Lippincott-Schwartz, H.F. Hess. *Science,* 313, 1642, (2006).

64. P.N. Prasad. *Nanophotonics*. Wiley: Hoboken, US, (2004).

65. M. Brust, M. Walker, D. Bethell, D. Schiffrin, R.J. Whyman. J. *Chem. Soc., Chem. Commun.*, 801, (1994).

66. C. Wang, T. Wang, Z. Ma, Z. Su. *Nanotechnology*, 16, 2555, (2005).

67. N.R. Jana, L. Gearheart, C.J. Murphy. *Langmuir*, 17, 6782, (2001).

68. B. Nikoobakht, M.A. El-Sayed. *Chem. Mater.,* 15, 1957, (2003).

69. B. Pietrobon, V. Kitaev. *Chemistry of Materials*, 20, 5186, (2008).

70. S. Chandran, M. Chaudhary, R. Pasricha, A. Ahmad, M. Sastry. *Biotechnol Prog.*, 22, 577, (2006).

71. J.S. Clawson, G.P. Holland, T.M. Alam. *Phys. Chem. Chem. Phys.*, 8, 2635, (2006).

72. G. Montalvo, M. Valiente, E.J. Todenas. *Colloid Interface Sci*., 172, 494, (1995).

73. M. Zapotocky, L. Ramos, P. Poulin, T.C. Lubensky, D.A. Weitz. *Science*, 283, 209, (1999).

74. I. Koltover, T. Salditt, J.O. Radler, C.R. Safinya. *Science*, 281,78, (1998).

75. P. Poulin, H. Stark, T.C. Lubensky, D.A. Weitz. *Science* 275, 1770, (1997).

76. T.C. Lubensky, D. Pettey, N. Currier, H. Stark. *Phys Rev E* 57, 610, (1998).

77. Webb, R. H. *Rep. Prog. Phys.* **1996**, 59, 427.

78. Pawley, J. B. (ed.) *Handbook of Biological Confocal Microscopy*; Plenum Press: New York, **1995**.

79. Zipfel, W. R.; Williams, R. M.; Webb, W. W. *Nat. Biotechnol.* **2003**, 21, 1369-1377.

80. Carriles, R.; Schafer, D. N.; Sheetz, K. E.; Field, J. J.; Cisek, R.; Barzda, V.; Sylvester, A. W.;Squier, J. A. *Rev. Sci. Instrum.* **2009**, 80, 081101.

81. Chaikin, P. M.; Lubensky, T. C. *Principles of Condensed Matter Physic*; Cambridge Univ. Press: Cambridge, 2000.

82. Hendrikx, Y.; Charvolin, J.; Rawiso, M.; Liebert, L.; Holmes, M. C. *J. Phys. Chem.* **1983**, 87, 3991-3999.

83. Figueiredo Neto, A. M.; Salinas, S. R. A. *The physics of lyotropic liquid crystals*; Oxford Univ. Press: Cambridge, **2005**.

84. Lentz, B.R. *Chem. Phys. Lipids* **1993**, 64, 99-116.

85. H. Stark. *Phys Rep,* **351,** 387 (2001).

86. P. Poulin and D.A. Weitz. *Phys. Rev E* **57,** 626 (1998).

87. C. L. van Oosten, C. W. M. Baastiansen, and D. J. Broer *Nature Mater*. **8** 677-682 (2009).

88. I.I. Smalyukh, A.V. Kachynski, A.N. Kuzmin, and P.N. Prasad. *Proc. Nat. Acad. U.S.A.* **103**, 18048 (2006).

89. Y. Gu and N.L. Abbot, *Phys. Rev. Lett.* **85**, 4719 (2000).

90. C.D. Santangelo and R.D. Kamien. *Phys. Rev. Lett.* **91**, 045506-1 (2003).

91. S. J. Woltman, D. G. Jay, and G. P. Crawford. *Nature Mater.* **6**, 929-938 (2007).

92. J. Yamamoto and H. Tanaka. *Nature Mater.* **4**, 75-80 (2005).

93. I.I. Smalyukh, Y. Lansac, N. Clark, R. Trivedi. *Nature Mater.* **9**, 139-145 (2010).

94. N. Engheta. *Science* **317**, 1698 (2007).

95. D. A. Pawlak, *et al. Adv. Funct. Mater.* **20**, 1116-1124 (2010).

96. J. Xie, J. Y. Lee and D. Y. C. Wang. *J. Phys. Chem. C* **111**,10226 (2007).

97 S. Shankar, A. Rai, B. Ankamwar, A. Singh, A. Ahmad, M. Sastry. *Nature Mater.* **3**, 482-488 (2004).

98. Z. Li, A. Friedrich, A. Taubert. *Journal of Materials Chemistry* **18**, 1008-1014 (2007).

99. S. Stoeva, V. Zaikovski, B. Prasad, B. Stoimenov, C. Sorensen, K. Klabunde. *Langmuir* **21**, 10280-10283 (2005).

100. C. Lofton, W. Sigmund. *Adv. Funct. Mater.* **15**, 1197-1208 (2005)

101. T. Yamamoto, Y. Tabe, and H. Yokoyama. *Colloids and Surfaces A-Physicochemical and Engineering Aspects* **334**, 155 (2009).

102. G.M. Koenig , I.-H. Lin, N.L. Abbott. *Proc. Natl. Acad. Sci. USA* 2010, **107**, 3998–4003.

103. I. I. Smalyukh, J. Butler, J. D. Shrout, M. R. Parsek, and G.C.L. Wong. *Phys. Rev. E* **78**, 030701(R) (2008).

104. T. H. Reilly III, R.C. Tenent, T. M. Barnes, K. L. Rowlen, and J. van de Lagemaat. *ACS Nano* **2**, 615-624 (2010).

105. J. C. Johnson, T. H. Reilly III, A. C. Kanarr and J. van de Lagemaat. *J. Phys. Chem. C* **113**, 6871–6877 (2009).

106. H. A. Atwater and A. Polman. *Nature Materials* **9**, 205-213 (2010).

107. M. J. Romero, A. J. Morfa, T. H. Reilly III, J. van de Lagemaat, and M. Al-Jassim. *Nano Lett.*, **9**, 3904–3908 (2009).

108. M. R. Jones, R. J. Macfarlane, B. Lee, J. Zhang, K. L. Young, A. J. Senesi, and C. A. Mirkin. *Nature Mater*. **9**, 913-917 (2010).

109. Y. Tan, J. Lee, D. Wang. *Journal of Physical Chemistry C* **112**, 5463-5470 (2008).

110. P. de Gennes and J. Prost, *The physics of liquid crystals*, Oxford University Press, USA, 1995.

111. H. Zocher, *Zeitschrift Fur Anorganische Und Allgemeine Chemie*, 1925, **147**, 91-U15.

112. F. C. Bawden, N. W. Pirie, J. D. Bernal and I. Fankuchen, *Nature*, 1936, **138**, 1051-1052.

113. L. Onsager, *Annals of the New York Academy of Sciences*, 1949, **51**, 627-659.

114. G. J. Vroege and H. N. W. Lekkerkerker, *Reports on Progress in Physics*, 1992, **55**, 1241-1309.

115. S. Chandrasekhar, B. K. Sadashiva and K. A. Suresh, *Pramana*, 1977, **9**, 471-480.

116. S. Chandrasekhar and G. S. Ranganath, *Reports on Progress in Physics*, 1990, **53**, 57-84.

117. H. K. Bisoyi and S. Kumar, *Chemical Society Reviews*, 2010, **39**, 264-285.

118. J. D. Brooks and G. H. Taylor, *Nature*, 1965, **206**, 697-699.

119. D. Dunmur, A. Fukuda, G. Luckhurst and I. o. E. Engineers, *Physical properties of liquid crystals: nematics*, INSPEC, 2000.

120. F. M. van der Kooij, K. Kassapidou and H. N. W. Lekkerkerker, *Nature*, 2000, **406**, 868-871.

121. A. S. Sonin, *Journal of Materials Chemistry*, 1998, **8**, 2557-2574.

122. J. C. P. Gabriel and P. Davidson, *Advanced Materials*, 2000, **12**, 9-20.

123. A. B. D. Brown, C. Ferrero, T. Narayanan and A. R. Rennie, *European Physical Journal B*, 1999, **11**, 481-489.

124. F. M. van der Kooij and H. N. W. Lekkerkerker, *Journal of Physical Chemistry B*, 1998, **102**, 7829-7832.

125. D. van der Beek and H. N. W. Lekkerkerker, *Europhysics Letters*, 2003, **61**, 702-707.

126. S. Y. Liu, J. Zhang, N. Wang, W. R. Liu, C. G. Zhang and D. J. Sun, *Chemistry of Materials*, 2003, **15**, 3240-3241.

127. M. C. D. Mourad, E. J. Devid, M. M. van Schooneveld, C. Vonk and H. N. W. Lekkerkerker, *Journal of Physical Chemistry B*, 2008, **112**, 10142-10152.

128. N. Behabtu, J. R. Lomeda, M. J. Green, A. L. Higginbotham, A. Sinitskii, D. V. Kosynkin, D. Tsentalovich, A. N. G. Parra-Vasquez, J. Schmidt, E. Kesselman, Y. Cohen, Y. Talmon, J. M. Tour and M. Pasquali, *Nature Nanotechnology*, 2010, **5**, 406-411.

129. J. E. Kim, T. H. Han, S. H. Lee, J. Y. Kim, C. W. Ahn, J. M. Yun and S. O. Kim, *Angewandte Chemie International Edition*, 2011, **50**, 3043-3047.

130. Z. Xu and C. Gao, *ACS Nano*, 2011, **5**, 2908–2915.

131. L. Schmidt-Mende, A. Fechtenkotter, K. Mullen, E. Moons, R. H. Friend and J. D. MacKenzie, *Science*, 2001, **293**, 1119-1122.

132. N. Behabtu, M. J. Green and M. Pasquali, *Nano Today*, 2008, **3**, 24-34.

133. M. A. Bates and D. Frenkel, *Journal of Chemical Physics*, 1999, **110**, 6553-6559.

134. R. Eppenga and D. Frenkel, *Molecular Physics*, 1984, **52**, 1303-1334.

135. D. C. Marcano, D. V. Kosynkin, J. M. Berlin, A. Sinitskii, Z. Z. Sun, A. Slesarev, L. B. Alemany, W. Lu and J. M. Tour, *ACS Nano*, 2010, **4**, 4806-4814.

135. W. S. Hummers and R. E. Offeman, *Journal of the American Chemical Society*, 1958, **80**, 1339.

137. D. A. Dikin, S. Stankovich, E. J. Zimney, R. D. Piner, G. H. B. Dommett, G. Evmenenko, S. T. Nguyen and R. S. Ruoff, *Nature*, 2007, **448**, 457-460.

138. J. C. P. Gabriel, C. Sanchez and P. Davidson, *Journal of Physical Chemistry*, 1996, **100**, 11139-11143.

139. A. Mourchid, A. Delville, J. Lambard, E. Lecolier and P. Levitz, *Langmuir*, 1995, **11**, 1942-1950.

140. A. Mourchid, E. Lecolier, H. Van Damme and P. Levitz, *Langmuir*, 1998, **14**, 4718-4723.

141. E. E. Wahlstrom, *Optical crystallography*, John Wiley & Sons Inc., 1979.

142. M. A. Osipov and S. Hess, *Molecular Physics*, 1993, **78**, 1191-1201.

143. B. Tjiptomargo, G. T. Evans, M. P. Allen and D. Frenkel, *Journal of Physical Chemistry*, 1992, **96**, 3942-3948.

144. T. Haven, D. Armitage and A. Saupe, *Journal of Chemical Physics*, 1981, **75**, 352-364.

145. N. H. Phuong, G. Germano and F. Schmid, *Journal of Chemical Physics*, 2001, **115**, 7227-7234.

146. C. D. FavreNicolin and J. Lub, *Macromolecules*, 1996, **29**, 6143-6149.

147. Y. A. Nastishin, H. Liu, T. Schneider, V. Nazarenko, R. Vasyuta, S. V. Shiyanovskii and O. D. Lavrentovich, *Physical Review E*, 2005, **72**, 041711.

148. T. S. Perova and J. K. Vij, *Advanced Materials*, 1995, **7**, 919-922.

149. D. van der Beek, P. Davidson, H. H. Wensink, G. J. Vroege and H. N. W. Lekkerkerker, *Physical Review E*, 2008, **77**, 031708-031716.

150. F. Brochard and P. G. D. Gennes, *Journal De Physique*, 1970, **31**, 691.

151. P. Poulin, N. Frances and O. Mondain-Monval, *Physical Review E*, 1999, **59**, 4384-4387.

152. J. C. Loudet, P. Barois and P. Poulin, *Nature*, 2000, **407**, 611-613.

153. R. W. Ruhwandl and E. M. Terentjev, *Physical Review E*, 1997, **55**, 2958-2961.

154. J. S. Evans, C. N. Beier and I. I. Smalyukh, *J. Appl. Phys.* **110**, 033535 (2011)

155. P. Yeh and C. Gu, *Optics of Liquid Crystal Displays*, John Wiley & Sons, Inc., 1999.

156. Lal, S.; Link, S.; Halas, N. J. *Nat. Photonics* **2007**, *1*, 641-648.

157. Jain, P. K.; Huang, X.; El-Sayed, I. H.; El-Sayed M. A. *Accounts Chem. Res.* **2008**, *41*, 1578-1586.

158. Sau, T. K.; Rogach, A. L.; Jäckel, F.; Klar, T. A.; Feldmann, J. *Adv. Mater.* **2010**, *22*, 1805-1825.

159. Morfa, A. J.; Rowlen, K. L.; Reilly, T. H.; Romero, M. J.; van de Lagemaat, J. *Appl. Phys. Lett.* **2008**, *92*, 013504.

160. Perassi, E. M.; Hernandez-Garrido, J. C.; Sergio Moreno, M.; Encina, E. R.; Coronado, E. A.; Midgley, P. A. *Nano Lett.* **2010**, *10*, 2097-2104.

161. Habteyes, T.; Dhuey, S.; Cabrini, S.; Schuck, P. J.; Leone, S. R. *Nano Lett.* **2011**, *11*, 1819-1825.

162. Fan, J. A.; Wu, Ch.; Bao, K.; Bao, J.; Bardhan, R.; Halas, N. J.; Manoharan, V. N.; Nordlander, P.; Shvets, G.; Capasso, F. *Science* **2010**, *328*, 1135-1138.

163. Shalaev, V. M. *Nat. Photonics* **2007**, *1*, 41-48.

164. Romero, M. J.; van de Lagemaat, J. *Phys. Rev. B* **2009**, *80*, 115432.

165. Ni, W.; Ambjörnsson, T.; Apell, S. P.; Chen, H.; Wang, J. *Nano Lett.* **2010**, *10*, 77-84.

166. Khatua, S.; Chang, W.-S.; Swanglap, P.; Olson, J.; Link, S. *Nano Lett.* **2011**, *11*, 3797-3802.

167. Alvarez-Puebla, R. A.; Agarwal, A.; Manna, P.; Khanal, B. P.; Aldeanueva-Potel, P.; Carbo-Argibay, E.; Pazos-Perez, N.; Vigderman, L.; Zubarev, E. R.; Kotov, N. A.; Liz-Marzan, L. M. *Proc. Natl. Acad. Sci. USA* **2011**, *108*, 8157-8161.

168. Guffey, M. J.; Scherer, N. F. *Nano Lett.* **2010**, 10, 4302-4308.

169. Seol, Y.; Carpenter, A. E.; Perkins, T. T. *Optics Lett.* **2006**, *31*, 2429-2431.

170. Pelton, M.; Liu, M.; Kim, H. Y.; Smith, G.; Guyot-Sionnest, P.; Scherer, N. F. *Optics Lett.* **2006**, *31*, 2075-2077.

171. Khatua, S.; Manna, P.; Chang, W.-S.; Tcherniak, A.; Friedlander, E.; Zubarev, E. R.; Link, S. *J. Phys. Chem. C* **2010**, *114*, 7251-7257.

172. Ezhov, A. A.; Shandryuk, G. A.; Bondarenko, G. N.; Merekalov, A. S.; Abramchuk, S. S.; Shatalova, A. M.; Manna, P.; Zubarev, E. R.; Talroze, R. V. *Langmuir* **2011**, *27*, 13353-13360.

173. Khanal, B. P.; Zubarev, E. R. *Angew. Chem. Int. Ed.* **2009**, *48*, 6888-6891.

174. Slaughter, L. S.; Chang, W.-S.; Swanglap, P.; Tcherniak, A.; Khanal, B. P.; Zubarev, E. R.; Link, S. *J. Phys. Chem. C* **2010**, *114*, 4934-4938.

175. Trivedi, R. P.; Engström, D.; Smalyukh, I. I. *J. Opt.* **2011**, *13*, 044001.

176. van de Hulst, H. C. *Light Scattering by Small Particles*. 2nd ed.; Dover Publications, Inc.; New York, 1981.

177. Koenig, G. M.; de Pablo, J. J.; Abbott, N. L. *Langmuir* **2009**, *25*, 13318-13321.

178. Wang, H.; Huff, T. B.; Zweifel, D. A.; He, W.; Low, P. S.; Wei, A.; Cheng, J.-X. *Proc. Natl. Acad. Sci. USA* **2005**, *102*, 15752–15756.

179. Zijlstra, P.; Chon, J. W. M.; Gu, M. *Nature* **2009**, *459*, 410-413.

180. Burylov, S. V.; Raikhner, Yu. L. *Phys. Lett. A* **1990**, *149*, 279-283.

181. Burylov, S. V.; Raikhner, Yu. L. *Phys. Rev. E* **1994**, *50*, 358-367.

182. Ruhwandl, R. W.; Terentjev, E. M. *Phys. Rev. E* **1997**, *56*, 5561-5565.

183. Matthias, H.; Kitzerow, H.-S. *Mol. Cryst. Liq. Cryst.* **2009**, *508*, 127-136.

184. Tkalec, U.; Škarabot, M.; Muševič, I. *Soft Matter* **2008**, *4*, 2402-2409.

185. Ognysta, U.; Nych, A.; Nazarenko, V.; Muševič, I.; Škarabot, M.; Ravnik, M.; Žumer, S.; Poberaj, I.; Babič, D. *Phys. Rev. Lett.* **2008**, *100*, 217803.

186. Škarabot, M.; Ravnik, M.; Žumer, S.; Tkalec, I.; Poberaj, I.; Babič, D.; Osterman, N.; Muševič, I. *Phys. Rev. E* **2008**, *77*, 031705.

187. Ognysta, U. M.; Nych, A. B.; Uzunova, V. A.; Pergamenschik, V. M.; Nazarenko, V. G.; Škarabot, M.; Muševič, I. *Phys. Rev. E* **2011**, *83*, 041709.

188. Grigorenko, A. N.; Roberts, N. W.; Dickinson, M. R.; Zhang, Y. *Nat. Photonics* **2008**, *2*, 365-370.

189. T. H. Skyrme. *Proc. R. Soc. Lond. A* **260**, 127–138 (1961).

190. S. Muhlbauer, *et al. Science* **323**, 915–919 (2009)

191. S. Heinze, K. von Bergmann, M. Menzel, J. Brede, A. Kubetzka, R. Wiesendanger, G. Bihlmayer, and S. Blügel. *Nature Physics* **7**, 713-718 (2011).

192. M. Uchida and A. Tonomura. *Nature* **464**, 737–739 (2010).

193. J. Verbeeck, H. Tian and P. Schattschneider. *Nature* **467**, 301–304 (2010).

194. L. Allen, M. W. Beijersbergen, R. J. C. Spreeuw, and J. P. Woerdman. *Phys. Rev. A* **45**, 8185–8189 (1992).

195. M. R. Dennis, R. P. King, B. Jack, K. O'Holleran, and M. J. Padgett. *Nat. Phys.* **6**, 118–121 (2010).

196. I. Chuang, R. Durrer, N. Turok, and B. Yurke. *Science* **251**, 1336–1342 (1991).

197. B. G. Chen, P.J. Ackerman, G. P. Alexander, R. D. Kamien, and I. I. Smalyukh. *Phys. Rev. Lett.* (2013).

198. O. Trushkevych, P. Ackerman, W.A. Crossland, and I.I. Smalyukh. *Appl. Phys. Lett.* **97**, 201906 (2010).

199. I.I. Smalyukh, D. Kaputa, A. V. Kachynski, A. N. Kuzmin, P. J. Ackerman, C. W. Twombly, T. Lee, R. P. Trivedi, and P. N. Prasad. *Opt. Express* **20**, 6870-6880 (2012).

200. P. J. Ackerman, Z. Qi, and I. I. Smalyukh, *Phys. Rev. E* **86**, 021703 (2012).

201. P. J. Ackerman, Z. Qi, Y. Lin, C. Twombly, M. Laviada, Y. Lansac, and I.I. Smalyukh. *Scientific Reports* **2,** 414 (2012).

202. U. Tkalec, M. Ravnik, S. Čopar, S. Žumer, and I. Muševič. *Science* **333**, 62-65 (2011).

203. J. W. Milnor. *Topology from the Differentiable Viewpoint* (The University Press of Virginia, Charlottesville, 1965).

204. J. Charvolin and J.F. Sadoc. *Eur. Phys. J. E* **25**, 335–341 (2008)

205. P. Oswald, J. Baudry, and S. Pirkl, *Physics Reports* **337**, 67-96 (2000).

206. I. I. Smalyukh, *et al. Phys. Rev. E* **72**, 061707 (2005).

207. C. Phatak, A. K. Petford-Long, and O. Heinonen. *Phys. Rev. Lett.* **108**, 067205 (2012)

208. R. P. Trivedi, I. I. Klevets, B. Senyuk, T. Lee, and I.I. Smalyukh. *Proc. Nat. Acad. Sci. U.S.A.* **109**, 4744-4749 (2012).

209. G. Alexander, B. Chen, E. Matsumoto, and R. Kamien, *Rev. Mod. Phys.* **84**, 497 (2012).

210. J. Pérez-Juste, *et al. Coordination Chemistry Reviews* **249**, 1870–1901 (2005).

211. N. Jana, L. Gearheart, and C**.** Murphy**.** *J. Phys. Chem. B* **105**, 4065–4067 (2001).

212. A.P. Alivisatos. *Science* **271**, 933-937 (1996).

213. X. Peng, L. Manna, W. Yang, J. Wickham, E. Scher, A. Kadavanich, and A. P. Alivisatos. *Nature* **404**, 59-61 (2000).

214. A. J. Nozik. *Chem. Phys. Lett.* **457**, 3–11 (2008).

215. D. Astruc, *Nanoparticles and Catalysis* (Wiley, VCH, 2008).

216. B. Senyuk, J. S. Evans, P. Ackerman, T. Lee, P. Manna, L. Vigderman, E. R. Zubarev, J. van de Lagemaat, and I. I. Smalyukh. *Nano Lett.* **12**, 955-963 (2012).

217. H. Mertens, A. F. Koenderink, and A. Polman. *Phys. Rev. B* **76**, 115123 (2007).

218. H. Noh, S. Zelakiewicz, X. G. Feng, T. J. Gramila, L. N. Pfeiffer, and K. W. West. *Phys. Rev. B* **58**, 12621–12624 (1998).

219. Q. Liu, B. Senyuk, J. Tang, T. Lee, J. Qian, S. He, and I.I. Smalyukh. *Phys. Rev. Lett.* **109**, 088301 (2012).

220. D. J Broer, J. Lub, G. N. Mol. *Nature* **378**, 467-469 (1995).

221. C. D. Modes and M. Warner. *Euro Phys. Lett* **97**, 36007 (2012).

222. C. D. Modes and M. Warner. *Phys. Rev. E* **84**, 021711 (2011).

223. Y. Sun, J. S. Evans, T. Lee, B. Senyuk, P. Keller, S. He, and I. I. Smalyukh. *Appl. Phys. Lett.* **100**, 241901 (2012).

224. B. Senyuk, Q. Liu, S. He, R. D. Kamien, R. B. Kusner, T. C. Lubensky and I. I. Smalyukh, *Nature* **493**, 200-205 (2013)

225. A. Ashkin, J.M. Dziedzic, J.E. Bjorkholm, and S. Chu, Opt. Lett. **11**, 288 (1986).

226. K. Dholakia and T. Čižmár, Nat. Photonics **5**, 335 (2011).

227. R. C. Gauthier, M. Ashman, and C. P. Grover, Appl. Opt. **38**, 4861 (1999).

228. E. Higurashi, H. Ukita, H. Tanaka, and O. Ohguchi, Appl. Phys. Lett. **64**, 2209 (1994).

229. W. Singer, T. A. Nieminen, U. J. Gibson, N. R. Heckenberg, and H. Rubinsztein-Dunlop, Phys. Rev. E **73**, 21911 (2006).

230. H. Ukita and K. Nagatomi, Opt. Rev. **4**, 447 (1997).

231. D. B. Phillips, D. M. Carberry, S. H. Simpson, H. Schäfer, M. Steinhart, R. Bowman, G. M. Gibson, M. J. Padgett, S. Hanna, and M. J. Miles, J. Opt. **13**, 044023 (2011).

232. J. Guck, R. Ananthakrishnan, H. Mahmood, T. J. Moon, C. C. Cunningham and J. Käs, Biophys. J. **81**,767 (2001).

233. S. H. Simpson and S. Hanna, J. Opt. Soc. Am. A **28**, 850 (2011).

234. M.J. Solomon, Current Opinion in Colloid & Interface Science **16**, 158 (2011).

235. J. Dontabhaktuni, M. Ravnik and S. Žumer, Soft Matter **8**, 1657 (2012).

236. M. Warner and E.M. Terentjev, *Liquid Crystal Elastomers* (Oxford Scientific Publications, Oxford, 2007).

237. C. Ohm, M. Brehmer and R. Zentel, Adv. Mater. **22**, 3366 (2010).

238. M.-H. Li, P. Keller, J. Yang, and P.-A. Albouy, Adv. Mater. **16**, 1922 (2004).

239. A. Buguin, M.-H. Li, P. Silberzan, B. Ladoux, P. Keller, J. Am. Chem. Soc. **128**, 1088 (2006).

240. H. Yang, A. Buguin, J.-M. Taulemesse, K. Kaneko, S. Méry, A. Bergeret and P. Keller, J. Am. Chem. Soc. **131**, 15000 (2009).

241. Y. Xia and G. M. Whitesides, Angew. Chem. Int. Ed. **37**, 550 (1998).

242. R.P. Trivedi, T. Lee, K. Bertness and I.I. Smalyukh, Opt. Express **18**, 27658 (2010).

243. F. Garwe, U. Bauerschäfer, A. Csaki, A. Steinbrück, K. Ritter, A. Bochmann, J. Bergmann, A. Weise, D. Akimov, G. Maubach, K. König, G. Hüttmann, W. Paa, J. Popp and W. Fritzsche, Nanotechnology **19**, 055207 (2008).

244. A. Kyrsting, P. M. Bendix, D. G. Stamou, and L. B. Oddershede, *Nano Lett.* **11**, 888 (2011).

245. C. J. Smith and C. Denniston, *J. Appl. Phys.* **101**, 014305 (2007).

246. C. Lapointe, *et al*., *Science* **303**, 652 (2004).

247. Daniel, M. C.; Astruc, D., *Chemical Reviews* **104** (1), 293-346 (2004).

248. Link, S.; Mohamed, M. B.; El-Sayed, M. A., *Journal of Physical Chemistry B***, 103** (16), 3073-3077 (1999).

249. Westphalen, M.; Kreibig, U.; Rostalski, J.; Luth, H.; Meissner, D., *Solar Energy Materials and Solar Cells* , **61** (1), 97-105 (2000).

250. Orendorff, C. J.; Gearheart, L.; Jana, N. R.; Murphy, C. J., *Physical Chemistry Chemical Physics* ,**8** (1), 165-170 (2006).

251. Nikoobakht, B.; El-Sayed, M. A., *Journal of Physical Chemistry A*, **107** (18), 3372-3378 (2003).

252. Huang, X. H.; El-Sayed, I. H.; Qian, W.; El-Sayed, M. A., *Journal of the American Chemical Society*, **128** (6), 2115-2120 (2006).

253. Huang, X. H.; El-Sayed, I. H.; Qian, W.; El-Sayed, M. A., *Nano Letters* ,**7**, 1591-1597 (2007).

254. Durr, N. J.; Larson, T.; Smith, D. K.; Korgel, B. A.; Sokolov, K.; Ben-Yakar, A., *Nano Letters* , **7** (4), 941-945 (2007).

255. Murphy, C. L.; Orendorff, C. J., *Advanced Materials,* **17** (18), 2173-2177 (2005).

256. van der Zande, B. M. I.; Koper, G. J. M.; Lekkerkerker, H. N. W., *Journal of Physical Chemistry B* ,**103** (28), 5754-5760 (1999).

257. Jana, N. R.; Gearheart, L. A.; Obare, S. O.; Johnson, C. J.; Edler, K. J.; Mann, S.; Murphy, C. J., *Journal of Materials Chemistry* ,**12** (10), 2909-2912 (2002).

258. Nikoobakht, B.; Wang, Z. L.; El-Sayed, M. A., *Journal of Physical Chemistry B* ,**104** (36), 8635-8640(2000).

259. Liu, S. H.; Tok, J. B. H.; Locklin, J.; Bao, Z. N., *Small* ,**2** (12), 1448-1453 (2006).

260. Green, M. J.; Behabtu, N.; Pasquali, M.; Adams, W. W., *Polymer* ,**50** (21), 4979-4997 (2009).

261. Tans, S. J.; Devoret, M. H.; Dai, H. J.; Thess, A.; Smalley, R. E.; Geerligs, L. J.; Dekker, C., *Nature* ,**386** (6624), 474-477 (1997).

262. Dan, B.; Irvin, G. C.; Pasquali, M., *ACS Nano* ,**3** (4), 835-843 (2009).

263. Wu, Z. C.; Chen, Z. H.; Du, X.; Logan, J. M.; Sippel, J.; Nikolou, M.; Kamaras, K.; Reynolds, J. R.; Tanner, D. B.; Hebard, A. F.; Rinzler, A. G., *Science* ,**305** (5688), 1273-1276 (2004).

264. Davis, V. A.; Parra-Vasquez, A. N. G.; Green, M. J.; Rai, P. K.; Behabtu, N.; Prieto, V.; Booker, R. D.; Schmidt, J.; Kesselman, E.; Zhou, W.; Fan, H.; Adams, W. W.; Hauge, R. H.; Fischer, J. E.; Cohen, Y.; Talmon, Y.; Smalley, R. E.; Pasquali, M., *Nature Nanotechnology* ,**4** (12), 830-834 (2009).

265. Li, Y. L.; Kinloch, I. A.; Windle, A. H., *Science* ,**304** (5668), 276-278 (2004).

266. Miaudet, P.; Badaire, S.; Maugey, M.; Derre, A.; Pichot, V.; Launois, P.; Poulin, P.; Zakri, C., *Nano Letters* ,**5** (11), 2212-2215 (2005).

267. Hu, L.; Hecht, D. S.; Gruner, G., *Chem Rev* ,**110** (10), 5790-844 (2010).

268. Kong, B. S.; Jung, D. H.; Oh, S. K.; Han, C. S.; Jung, H. T., *Journal of Physical Chemistry C* ,**111** (23), 8377-8382 (2007).

269. Peigney, A.; Laurent, C.; Flahaut, E.; Bacsa, R. R.; Rousset, A., *Carbon* ,**39** (4), 507-514 (2001).

270. Girishkumar, G.; Vinodgopal, K.; Kamat, P. V., *Journal of Physical Chemistry B* ,**108** (52), 19960-19966 (2004).

271. Planeix, J. M.; Coustel, N.; Coq, B.; Brotons, V.; Kumbhar, P. S.; Dutartre, R.; Geneste, P.; Bernier, P.; Ajayan, P. M., *Journal of the American Chemical Society* ,**116** (17), 7935-7936 (1994).

272. Correa-Duarte, M. A.; Perez-Juste, J.; Sanchez-Iglesias, A.; Giersig, M.; Liz-Marzan, L. M., *Angewandte Chemie-International Edition* ,**44** (28), 4375-4378 (2005).

273. Xu, Y. Q.; Flor, E.; Kim, M. J.; Hamadani, B.; Schmidt, H.; Smalley, R. E.; Hauge, R. H., *Journal of the American Chemical Society* ,**128** (20), 6560-6561 (2006).

274. Pint, C. L.; Xu, Y. Q.; Pasquali, M.; Hauge, R. H., *ACS Nano* ,**2** (9), 1871-1878 (2008).

275. Ericson, L. M.; Fan, H.; Peng, H. Q.; Davis, V. A.; Zhou, W.; Sulpizio, J.; Wang, Y. H.; Booker, R.; Vavro, J.; Guthy, C.; Parra-Vasquez, A. N. G.; Kim, M. J.; Ramesh, S.; Saini, R. K.; Kittrell, C.; Lavin, G.; Schmidt, H.; Adams, W. W.; Billups, W. E.; Pasquali, M.; Hwang, W. F.; Hauge, R. H.; Fischer, J. E.; Smalley, R. E., *Science* ,**305** (5689), 1447-1450 (2004).

276. Wang, Y.; Ericson, L. M.; Kittrell, C.; Kim, M. J.; Shan, H.; Fan, H.; Ripley, S.; Ramesh, S.; Hauge, R. H.; Adams, W. W.; Pasquali, M.; Smalley, R. E., *Chemistry of Materials* ,**17** (25), 6361-6368 (2005).

277. Booker, R.; Green, M.; Fan, H.; Parra-Vasquez, A.; Behabtu, N.; Young, C.; Hauge, R.; Schmidt, H.; Smalley, R.; Hwang, W., *Proceedings of the Institution of Mechanical Engineers, Part N: Journal of Nanoengineering and Nanosystems* ,**222** (3), 101-109 (2008).

278. Davis, V. A.; Ericson, L. M.; Parra-Vasquez, A. N. G.; Fan, H.; Wang, Y. H.; Prieto, V.; Longoria, J. A.; Ramesh, S.; Saini, R. K.; Kittrell, C.; Billups, W. E.; Adams, W. W.; Hauge, R. H.; Smalley, R. E.; Pasquali, M., *Macromolecules* ,**37** (1), 154-160 (2004).

279. Yang, D.-K.; Wu, S.-T., *Fundamentals of liquid crystal devices*. John Wiley: Chichester, Eng. ; Hoboken, NJ, 2006.

280. Collings, P. J.; Ratna, B. R.; Shashidhar, R., *Physical Review E* ,**67** (2), 21705 (2003).

281. Deegan, R. D.; Bakajin, O.; Dupont, T. F.; Huber, G.; Nagel, S. R.; Witten, T. A., *Nature* ,**389** (6653), 827-829 (1997).

282. Li, Q. W.; Zhu, Y. T.; Kinloch, I. A.; Windle, A. H., *Journal of Physical Chemistry B,* **110** (28), 13926-13930 (2006).

283. Lewandowski, E. P.; Bernate, J. A.; Searson, P. C.; Stebe, K. J., *Langmuir* ,**24** (17), 9302-9307 (2008).

284. Fan, F. Q.; Stebe, K. J., *Langmuir ,***20** (8), 3062-3067 (2004).

285. Sharma, R.; Lee, C. Y.; Choi, J. H.; Chen, K.; Strano, M. S., *Nano Letters* ,**7** (9), 2693-2700 (2007).

286. Petit, C. A. P.; Carbeck, J. D., *Nano Letters* ,**3** (8), 1141-1146 (2003).

287. Messer, B.; Song, J. H.; Yang, P. D., *Journal of the American Chemical Society* ,**122** (41), 10232-10233 (2000).

288. Salalha, W.; Zussman, E., *Physics of Fluids* ,**17** (6) (2005).

289. Berreman, D. W., *Physical Review Letters* ,**28** (26), 1683 (1972).

290. Dinsmore, A. D.; Yodh, A. G.; Pine, D. J., *Nature* ,**383** (6597), 239-242 (1996).

291. Gupta, S.; Zhang, Q. L.; Emrick, T.; Balazs, A. C.; Russell, T. P., *Nature Materials* ,**5**, 229-233 (2006).

292. Yodh, A. G.; Lin, K. H.; Crocker, J. C.; Dinsmore, A. D.; Verma, R.; Kaplan, P. D., *Philosophical Transactions of the Royal Society of London Series a-Mathematical Physical and Engineering Sciences* ,**359** (1782), 921-937 (2001).

293. Madden, J.D.W., Vandesteeg, N.A., Anquetil, P.A., Madden, P.G.A., Takshi, A., Pytel, R.Z., Lafontaine, S.R., Wieringa, P.A., Hunter, I.W., *Oceanic Engineering, IEEE Journal of* , **29**, 3, 706-728 (2004).

294. Verbunt, P. P. C., Kaiser, A., Hermans, K., Bastiaansen, C. W. M., Broer, D. J. and Debije, M. G. (2009), *Adv. Funct. Mater*., 19: 2714–2719

295. Yamada et al. *Angew. Chem. Int. Ed*., **47**, 4986–4988 (2008)

296. K. Shopowitz et. al *Nature*, **468**, 422-425 (2010).

297. K. Hongladarom, V. M. Hugaz, D. K. Cinader, W. R. Burghardt, and J. P. Quintana, *Macromolecules* **29**, 5346 (1996).

298. K. Hongladarom, W. R. Burghardt, *Rheol. Acta* **37**, 46 (1998).

299. Suto, S. and Yoshinaka, M. J. Mater. Sci. 1993, 8, 4644

300. Purdy K., Fraden S., Phys. Rev. E 70, 061703 (2004)

301. Chung, W.-J. et al. *Nature* **478,** 364–368 (2011).

302. Rokhade, A., Kulkarni, P., Mallikarjuna, N., Aminabhavi, T., *J. Microencapsul.* **26**,1,27-36.(2009).

303. Lu X., Yavuz, M., Tuan H., Korgel B., Xia Y., *J. Am. Chem. Soc.*, **130** (28), 8900–8901 (2008).

304. Feng H., Yang Y., You Y., Li G., Guo J., Yu T., Shen Z., Wu T. Xing B., *Chem. Commun.*,15,1984-1986 (2009).

Appendix A- Self-alignment of dye molecules decorating the spatial patterns of n(r) in lyotropic mesophases

Adapted from: *Langmuir* **27**, 7446 (2011)

The cationic amphiphilic fluorescent chromophore $DiOC_{18}(3)$ is widely used as a lipophilic tracer of cell membranes and readily incorporates into surfactant monolayers and bilayers (Fig. A.1).[1-4] Its two long hydrocarbon chains are on the same side of the rod-like aromatic part of the chromophore (Fig. A.1(l)). When used as a membrane dye, the two carbocyanines of the $DiOC_{18}(3)$ molecules localize at the aqueous interface region of the membranes. Conjugated carbocyanines of this molecule have absorption/fluorescence transition dipole moments oriented parallel to the aromatic part of the chromophore, which enables direct molecular orientation study of the chromophore in membranes by means of polarized excitation and fluorescence detection.

Fig. A.1 demonstrates the schematic representation of $DiOC_{18}(3)$ molecules incorporated into different types of micelles. When intercalating into the highly-curved structure of a cylindrical micelle (Fig. A.1(a)), the rod-like rigid aromatic part of the dye molecule aligns along the micelle to fit its structure without locally disrupting the intrinsic curvature, while the hydrocarbon tails of the dye (about two times longer than that of the used surfactant molecules) span across the micelle. Because the surface of cylindrical micelles with the diameter of about 2.6 nm is highly curved compared with the size of rod-like rigid aromatic part of the dye molecule (which is about 1.3 nm in length), the alignment is robust and observed in different studied mesophases formed by these micelles (nematic, cholesteric, and columnar hexagonal)[5]. According to many of the literature studies, the size of the micelle in calamtic nematic phase is about 2.6 nm in diameter and 6.0 nm long while the size of the micelle in the discotic nematic phase is about 5.7 nm in diameter and 2.0 nm in thickness.[6] Another model (based on the

profile of the X-ray diffraction bands obtained in the nematic phases of potassium laurate/decanal/water ternary system) suggests that, at least in some of the lyotropic systems, the micelles might have orthorhombic shapes; the typical dimensions of the micelle estimated within the framework of this model are 8.5 nm by 5.5 nm in the plane perpendicular to the bilayer with the thickness of the bilayer being 2.6 nm, Fig. A.1(g).[7,8] In addition to the curvature-induced orientational alignment and hydrophobic-hydrophilic interactions that cause incorporation of the dye molecules into micelles, an important role might be played by electrostatic interactions between the charged molecules composing these building blocks of the lyotropic LC and the charged dye molecules.

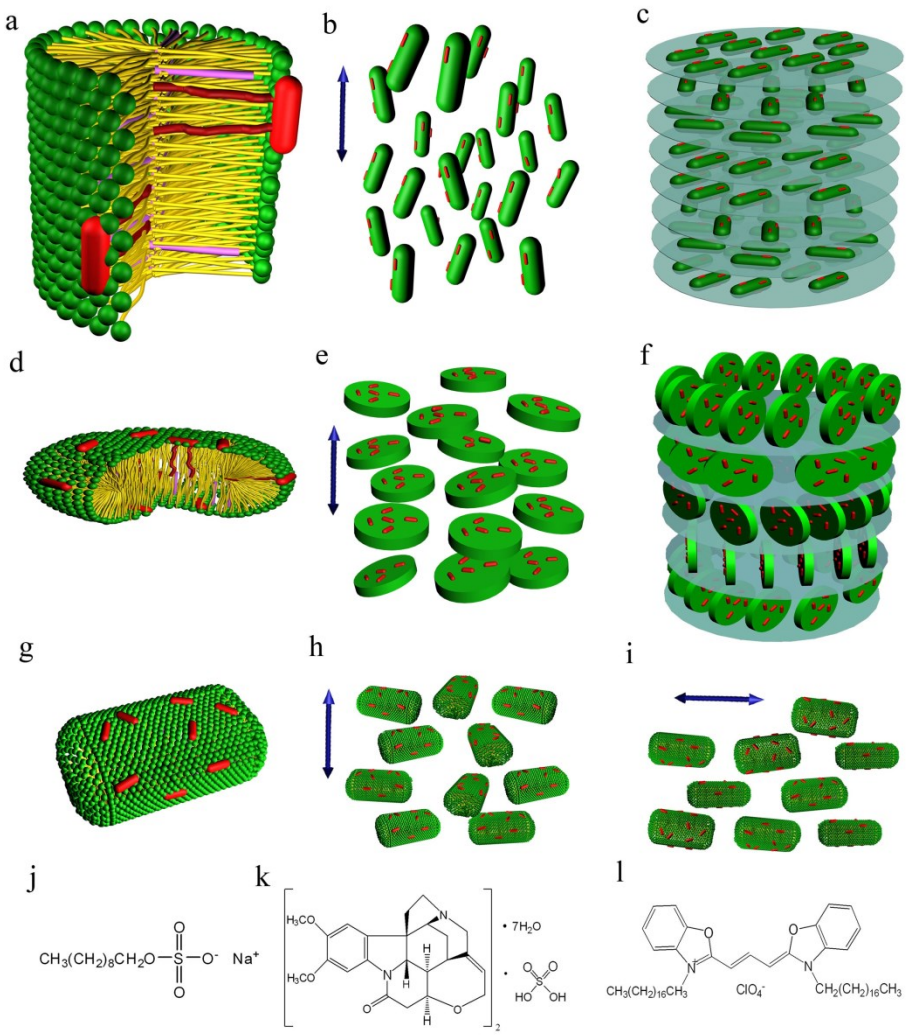

Fig. A.1. Alignment of amphiphilic dye molecules in the calamitic and discotic micelles. (a) A schematic of the self-oriented $DiOC_{18}(3)$ dye molecules (red) having anisotropic aromatic cores along the axis of a cylindrical SDS/1-decanol micelle. (b) A schematic of alignment of the dye molecules along **n**(**r**) in the calamitic nematic phase. (c) A schematic of alignment of the dye molecules along **n**(**r**) in the cholesteric phase formed by the cylindrical micelles. (d) A schematic of the oriented self-assembly of $DiOC_{18}(3)$ dye molecules (red) in a discoid SDS/1-decanol micelle (note that the hydrocarbon chains of the dye molecule are about two times longer than those of SDS). (e) A schematic of alignment of the dye molecules in the discotic nematic phase. (f) A schematic of alignment of the dye molecules in the cholesteric phase formed by the discoid micelles. (g) The orthorhombic micelles of nematic liquid crystals originate the different nematic phases by different orientational fluctuations, giving rise to (h) discotic nematic phase and (i) calamitic nematic phase. Molecular structures of (j) the amphiphilic molecule of sodium decyl sulfate (SDS), (k) chiral agent molecule of brucine sulfate heptahydrate, and (l) the dye molecule of $DiOC_{18}(3)$. We note that the schematics a-i represent highly idealized models of micelles and their self-organization into mesomorphic structures, however, the micelles in the real lyotropic

systems have rather imperfect geometric shapes and the alignment of used dye molecules is also much less perfect than what is depicted on the schematics.

The alignment of the dye molecules leads to the transition dipole moments of absorption and fluorescence of the dye following the local orientations of micelles and the mesoscopic spatial patterns of **n**(**r**), as schematically demonstrated for the examples of the ground-state nematic and cholesteric structures shown in Fig. A.1(b,c). When introduced into the same ternary system in a lamellar phase, or in a nematic phase formed by disk-shaped micelles, the amphiphilic molecules of $DiOC_{18}$(3) intercalate into the flat bilayers or prolate micelles of the surfactant molecules so that their rod-like aromatic parts of molecules and absorption/fluorescence transition dipoles are parallel to the planes of lamellae or prolate micelle but show random ordering within them, Fig. A.1(d-f). By detecting the polarization-dependent fluorescence of chromophore molecules, the collinear orientation of transition dipoles of fluorescence and absorption of the chromophore can be determined and used to reconstruct the 3D patterns of **n**(**r**). In the case of the model of orthorhombic micelles of the surfactant-based nematic LCs, orientational fluctuations of micelles that pre-determine the symmetry axis of the phase, perpendicular to the largest micellar surface, give rise to the average orientation of transition dipoles of fluorescence and absorption of the chromophores perpendicular to the director of discotic nematic LC. The orientational fluctuations that define the symmetry axis in the plane of the largest micellar surface, along the longest axis of the flattened ellipsoid, give rise to the average orientation of transition dipoles of fluorescence and absorption of the chromophore parallel to the director of the uniaxial calamtic nematic LC, Fig. A.1(h,i). Therefore, **n**(r) can also be reconstructed by use of the polarization-dependent fluorescence of the used chromophore. However, in the case of possible biaxial nematic phases, one would need to utilize more than one type of dyes in order to elucidate the 3D structures of different directors of biaxial nematic LCs.

A.2 Three-Dimensional Imaging of director fields and defects

Well-defined alignment of anisotropic amphiphilic dye molecules with respect to the anisotropic building blocks of lyotropic LCs allows for high-contrast 3D imaging of **n**(**r**) and defects by use of FCPM and 2PEFPM. Fig. A.2 shows images of the **n**(**r**)-structures and defects in nematic tactoids formed by cylindrical micelles. The tactoidal nematic droplet touches the two opposite glass plates of the sample cell and shows polarization dependent fluorescence textures (Fig. A.2(b-f)). The analysis of the images obtained in both FCPM and 2PEFPM modes and at different polarizations of probing light reveals the toroidal director structure with a twist-escaped +1 nonsingular disclination inside the nematic tactoid running across the cell and along the tactoid's diameter (Fig. A.2(a-f)), as schematically shown in Fig. A.2(c). The FCPM images obtained for the ternary lyotropic system fully in a nematic phase are shown in Fig. A.2(h,i) and reveal four half-integer singular disclinations (two of strength -1/2 and two of strength +1/2) running across the LC cell. The FCPM and 2PEFPM images are consistent with the corresponding PM texture shown in Fig A.2(a,g) (note that the PM textures have been obtained by use of the monochromatic laser light in a transmission mode). We note that the demonstrated mapping of **n**(**r**) in the plane perpendicular to the LC cell would be impossible by means of conventional imaging techniques such as optical polarizing microscopy, both for nematic and biphasic parts of the phase diagram.

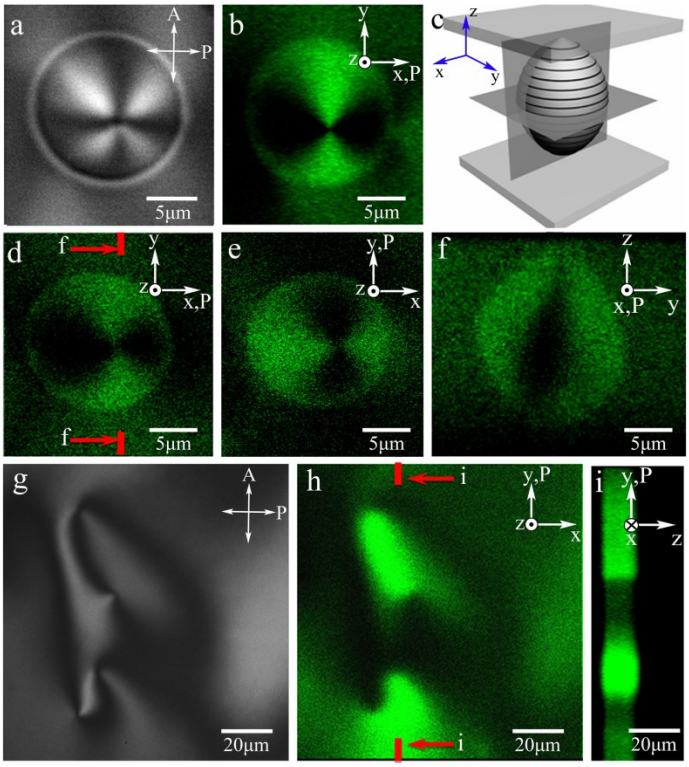

Fig. A.2 Comparative 3D imaging and analysis of nematic director structures formed by cylindrical micelles. (a) PM and (b) 2PEFPM cross-section images in the cell midplane of a nematic tactoid, a biphasic system with droplets of nematic composed of calamitic micelles surrounded by an isotropic surrounding, confined between two glass plates, as schematically shown in (c); the black concentric lines in (c) depict **n**(**r**). Similar FCPM images obtained for (d,e) in-plane cross-section with two orthogonal polarizations **P** of probing light (as marked on the images) and (f) vertical cross-section of the sample. (g) PM and (h,i) FCPM images of **n**(**r**)-structures and defects in the calamitic lyotropic nematic phase obtained for both (h) in-plane xy and (i) vertical yz cross-section, as marked on the images. The red lines in d and h indicate locations where the cross sections f and i are taken. Crossed polarizer "**P**" and analyzer "**A**" are marked in (a,g).

Fig. A.3 shows FCPM imaging of a lyotropic columnar hexagonal LC that, in addition to long-range orientational ordering, possesses the long-range two-dimensional positional ordering of the constituent building blocks (micelles). The used sample contains the so-called developable domains, the most typical defects in the columnar hexagonal LCs. Dye molecules of $DiOC_{18}(3)$ are again used as a fluorescent probes and align along the SDS/1-decanol cylindrical micelles

and **n**(**r**) of this phase, Fig. A.3(a). Since the bend-type distortions of **n**(**r**) in this phase are compatible with the hexagonal arrangement of micelles in the phase, they are not costly in terms of elastic energy and commonly observed (Fig. A.3(c,d)). These bend distortions of **n**(**r**) form the basis of the developable domain structure within which the two-dimensional translationally-periodic hexagonal ordering of the micelles in the plane perpendicular to them is not disrupted, Fig. A.3(b). FCPM imaging readily reveals the basic structure of the developable domains (Fig. A.3(c)), which is consistent with that obtained by use of polarizing optical microscopy (Fig. A.3(d)).

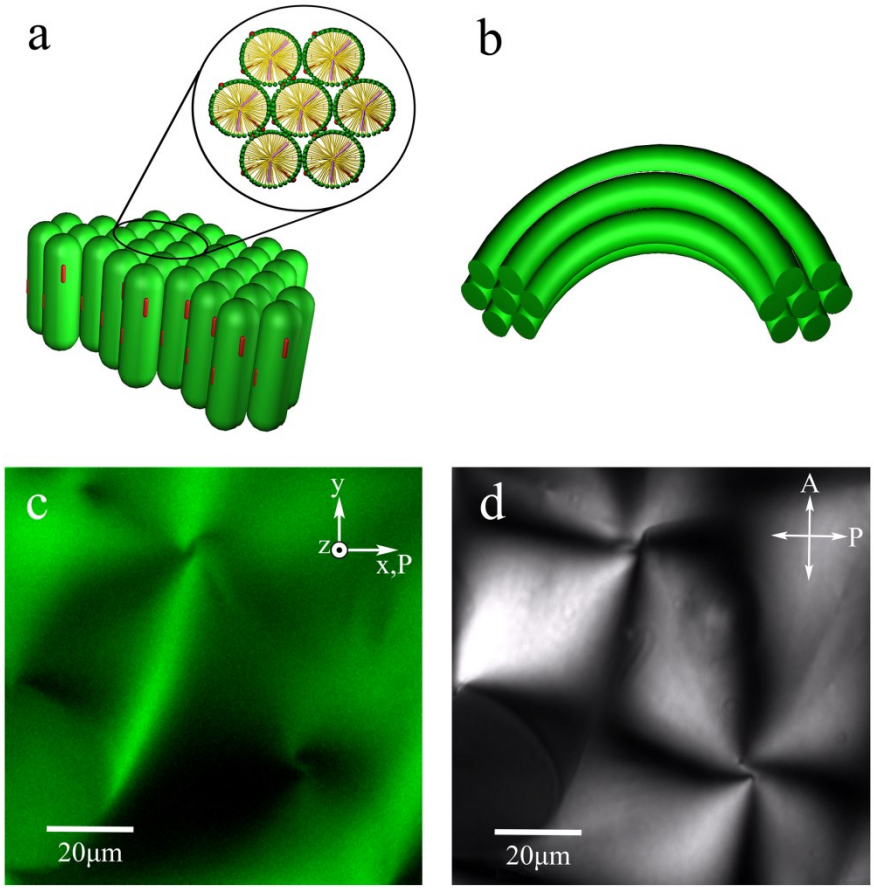

Fig. A.3 FCPM and PM imaging of **n**(**r**) in the lyotropic columnar hexagonal LC with developable domains. (a) Schematic representation of the self-assembly of cylindrical micelles with the aligned $DiOC_{18}(3)$ dye molecules incorporated into them in the columnar hexagonal phase. (b) A schematic of bend-type distortions of the columnar structure of cylindrical micelles within the developable domains. (c) FCPM and (d) PM images of the co-located columnar LC sample areas that allow one to visualize developable domains and corresponding bend-type distortions of **n**(**r**). The polarization of the FCPM probing light is marked by "**P**" in (c) and the crossed polarizer "**P**" and analyzer "**A**" are marked in (d).

A.3- References

1. Webb, R. H. *Rep. Prog. Phys.* **1996**, 59, 427.

2. Pawley, J. B. (ed.) *Handbook of Biological Confocal Microscopy*; Plenum Press: New York, **1995**.

3. Zipfel, W. R.; Williams, R. M.; Webb, W. W. *Nat. Biotechnol.* **2003**, 21, 1369-1377.

4. Carriles, R.; Schafer, D. N.; Sheetz, K. E.; Field, J. J.; Cisek, R.; Barzda, V.; Sylvester, A. W.;Squier, J. A. *Rev. Sci. Instrum.* **2009**, 80, 081101.

5. Chaikin, P. M.; Lubensky, T. C. *Principles of Condensed Matter Physic*; Cambridge Univ. Press: Cambridge, 2000.

6. Hendrikx, Y.; Charvolin, J.; Rawiso, M.; Liebert, L.; Holmes, M. C. *J. Phys. Chem.* **1983**, 87, 3991-3999.

7. Figueiredo Neto, A. M.; Salinas, S. R. A. *The physics of lyotropic liquid crystals*; Oxford Univ. Press: Cambridge, **2005**.

8. Lentz, B.R. *Chem. Phys. Lipids* **1993**, 64, 99-116.

Appendix B- Alignment of arbitrarily shaped colloids in nematic liquid crystals

Given the complexity of cholesteric elasticity and the similarities between distortions in **χ** and **n**, we adopt the electrostatic analogy approach of Brochard and de Gennes [1,2] for understanding cholesterostatic distortions. We extend their consideration of a single cylindrical particle in a nematic LC to complex-shaped particles composed of rigidly connected pillar fragments with different angles between them (Fig. B.1a), to gain quantitative insights into physics of colloidal inclusions in LC. The elastic energy cost of rotation of a rod-like particle of length L and radius R away from its equilibrium orientation is $U_{elastic} \approx \frac{1}{2} C K \gamma^2 \approx \frac{2\pi K \gamma^2 L}{\ln[2L/R]}$ [1, 2], where C is the "capacitance" and γ is the angle between the rotated particle's long axis and $\mathbf{n_0}$. In our system, cylindrical segments have different L_i and R_i and are rigidly connected to be at different angles θ_i (set by laser-induced morphing of LCE particles) with respect to the z-axis coinciding with the orientation of the first elastomeric fragment (θ_1=0). The orientation of $\mathbf{n_0}$ with respect to **z** is allowed to change to minimize the overall elastic energy due to **n**(**r**)-distortions produced by the embedded particle. We therefore need to minimize $U_{elastic} \approx \frac{1}{2} K \sum C_i (\theta_i - \theta_0)^2$ with respect to θ_0, an angle between **z** and $\mathbf{n_0}$. This is analogous to the center of mass calculation and yields equilibrium $\theta_0 = \Sigma C_i \theta_i / \Sigma C_i$ that uniquely determines equilibrium values of all θ_i. Due to the inherent nonpolar symmetry (**n**=-**n**) of the LC, angles $\theta_i - \theta_0 > \pi/2$ are replaced by $\pi - \theta_i + \theta_0$ in these calculations (since no twisting above π/2 is observed in our experiments) [3]. Although the regions in-between cylindrical fragments of bent pillars can be accounted for as segments of spheres to calculate the total free energy, they have no influence on θ_0 due to symmetry. In the case of out-of-plane bends of the particle, the equilibrium orientation can be found by

numerically minimizing $U_{elastic} \approx \frac{1}{2}K\sum C_i(\arccos[\cos\theta_i\cos\theta_0-\sin\theta_i\sin\theta_0\cos(\phi_i-\phi_0)])^2$ with respect to θ_0 and ϕ_0 (Fig. B.1a). Since the pillar fragments are rigidly connected, this problem is equivalent to that of an arbitrary asymmetric colloidal hedgehog that one obtains by spatially collocating one of the end points of each of the cylindrical fragments.

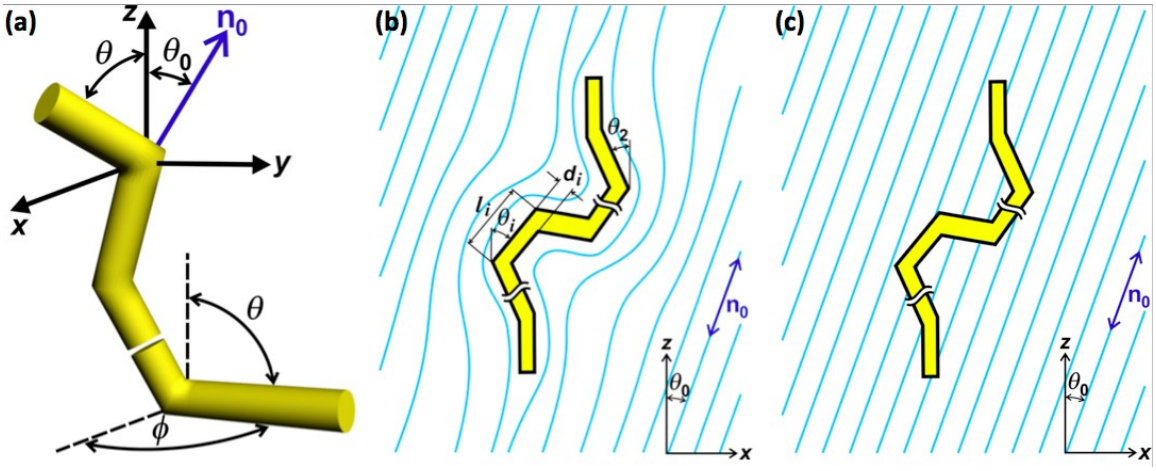

Fig. B.1. Schematic diagrams of different shape-morphing double-LC colloidal systems. (a) 3D schematic of a shape-morphing LCE particle obtained by morphing a cylinder via introducing bends and changing diameter/length of rigidly inter-connected rod-like fragments. (b,c) Two-dimensional representation of shape-morphing microparticles exerting (b) infinitely strong and (c) infinitely weak surface anchoring of **n**(**r**) of the surrounding LC. The length, diameter and polar and azimuthal angles describing the rod-like fragments are shown on the schematics.

In the limit of strong surface anchoring, the above modeling can be performed only for tangential degenerate boundary conditions (since one expects presence of bulk point and line defects around LCE colloids in the case of vertical boundary conditions). However, these calculations can be extended to cases of both vertical and tangential boundary conditions in the weak anchoring regime, in which one needs to minimize surface energy while assuming that bulk elastic distortions can be neglected (Fig. B.1c). Assuming the Rapini-Papoular surface anchoring

potential and ignoring the effect of end caps of a colloidal cylinder, we get surface energy $F=\pi RLW\sin^2\theta$ for tangential boundary conditions and $F=(\pi/2)RLW[\cos^2\theta+1]$ for vertical boundary conditions, where W is the polar surface anchoring coefficient. For rigidly connected pillar segments (Fig. B.1c), we minimize the anchoring energy for cases of both tangential and vertical boundary conditions and obtain $\tan(2\theta_0)=\sum L_i\sin(2\theta_i)/\sum L_i\cos(2\theta_i)$ for both cases. While using this expression, one has to separate the minima from maxima for both types of boundary conditions, since $\tan(2\theta_0)$ is not sensitive to a $\pi/2$ shift. Interestingly, in the small-angle approximation we obtain the same behavior as in the strong anchoring regime but with a different weighting factor: $\theta_0=\sum L_i\theta_i/\sum L_i$. One can therefore expect that this qualitative behavior and conclusions still hold even in the most common "intermediate" finite anchoring regime. Thus, the above simple model allows for finding equilibrium alignment of colloids composed of multiple rigidly connected rods with known geometric parameters and is in a good agreement with experimental observations.

B.2- References

1. F. Brochard and P. G. de Gennes, J. Phys. (France) **31**, 691-708 (1970).

2. C. J. Smith and C. Denniston, *J. Appl. Phys.* **101**, 014305 (2007).

3. C. Lapointe, *et al*., *Science* **303**, 652 (2004).